The Dissertation Committee for Avinash Krishna Murthy Certifies that this is the approved version of the following dissertation:

Surface Design and Controlled Assembly of Gold Nanoparticles into Biodegradable Nanoclusters for Biomedical Imaging Applications

Committee:

Keith P. Johnston, Supervisor

Konstantin V. Sokolov, Co-Supervisor

Jennifer Maynard

Stanislav Emelianov

Thomas M. Truskett

Surface Design and Controlled Assembly of Gold Nanoparticles into Biodegradable Nanoclusters for Biomedical Imaging Applications

by

Avinash Krishna Murthy, B.S.E.

Dissertation

Presented to the Faculty of the Graduate School of

The University of Texas at Austin

in Partial Fulfillment

of the Requirements

for the Degree of

Doctor of Philosophy

The University of Texas at Austin

August 2013

Dedication

To my parents and family, whose unflinching support during this long journey has made it all worthwhile.

Acknowledgements

This dissertation was truly a collaborative effort, both in terms of scientific content and moral support. I would first like to thank my advisor, Dr. Keith P. Johnston, for his unflagging enthusiasm for science. His passion for research drove me to accomplish much more than I had thought possible. I would also like to thank my co-advisor, Dr. Konstantin Sokolov, for his encouragement and wisdom which broadened my research horizons. Additionally I thank Dr. Thomas Truskett for his willingness to have many discussions which helped me gain a better grasp on the theory behind my results. I thank Dr. Stanislav Emelianov for his willingness to participate in an effective collaboration which allowed me to evaluate my research results through photoacoustic imaging, and thank Dr. Jennifer Maynard for her efforts in evaluating this dissertation.

I owe a great debt of gratitude to the many lab mates who have helped me grow both scientifically and personally. First, I am deeply grateful to Dr. Jasmine Tam, who showed me the ropes during my first year as a graduate student and who made my transition into graduate school life exceptionally easier. To Bobby Stover, who helped me collect data throughout the dissertation and spent countless hours with me trying to understand the science behind the results, I am truly grateful. In addition, I would like to thank my fellow current and former Johnston group members, including Leo Ma, Andrea Miller, Dan Slanac, Kiyoul Yoon, Will Hardin, Andrew Worthen, Yunshen Chen, Amro Elhag, Aileen Dinin, Bart Dear, Ameya Borwankar, Josh Laber, Jessica Hung, Csaba Kotsmar, Hitesh Bagaria, Ed Foster, and Lynn Foster, for their encouragement, scientific discussions, and moral support. Special thanks goes to our undergraduate researchers, including Robin Nguyen, Bobby Schramm, Golay Nie, Sai Gourisankar, and Miguel

Martinez, without whom this dissertation would not be nearly as complete. I would also like to express my gratitude to the Sokolov research group, especially Justina Tam and Pratixa Joshi. Their willingness to conduct cellular and animal studies involving our nanoparticles allowed me to grasp the potential impact of my work. Special thanks also goes to Soon Joon Yoon in the Emelianov group for his assistance with photoacoustic evaluation of nanoclusters. I would additionally like to thank Dr. Dwight Romanovicz and Dr. Hugo Celio for their assistance with instrumentation including TEM analysis.

Finally, I would like to thank the unwavering support of my parents, my sister, and my extended family in India. Their encouragement kept me going through long and stressful days and nights, and they have truly been instrumental in the production of this dissertation.

Surface Design and Controlled Assembly of Gold Nanoparticles into Biodegradable Nanoclusters for Biomedical Imaging Applications

Avinash Krishna Murthy, Ph.D.

The University of Texas at Austin, 2013

Supervisors: Keith P. Johnston and Konstantin V. Sokolov

Gold nanoparticles have received significant interest recently due to their utility in biomedical imaging and therapy. Nanoparticles which exhibit intense extinction in the near infrared (NIR) region, where blood and tissue absorb light weakly, are of great interest as contrast agents for biomedical imaging applications. While strong NIR extinction often requires sizes greater than ~20-30 nm, effective clearance from the body to avoid toxic accumulation necessitates sizes below ~6 nm. Moreover, effective clearance depends upon lack of adsorption of serum proteins in the bloodstream onto the particles. Herein, this conflict is addressed by assembling sub-5 nm gold nanoparticles into clusters with controlled size and morphology, in order to provide intense NIR extinction. Furthermore, the surfaces of the primary gold nanoparticles are designed such that the particles avoid the adsorption of any serum proteins. Binary ligand monolayers of anionic citrate and appropriate amounts of either cationic lysine or zwitterionic cysteine are synthesized to completely prevent serum protein adsorption from undiluted fetal bovine serum. A mechanism is proposed whereby the zwitterionic tips which are present on both the lysine and cysteine ligands limit the interactions between serum proteins and

the “buried” charges on the nanoparticle surfaces. These primary nanoparticles are subsequently assembled into biodegradable nanoclusters *via* “quenched assembly”, wherein nanoclusters are assembled and subsequently quenched by the adsorption of a biodegradable polymer on the cluster surface. The sizes of completely reversible “quenched equilibrium” nanoclusters formed from gold nanoparticles coated with a mixture of lysine and citrate are tuned from 20 nm to 40 nm, and nanocluster size is semi-quantitatively predicted by a free-energy model. Additional control over nanocluster size and extinction is demonstrated by adding NaCl, which is shown to decrease the polymer adsorption on the clusters and thus decrease polymer bridging interactions. This nanocluster formation platform is extended to nanospheres capped with citrate and the thiolated, zwitterionic cysteine ligand. A general paradigm is presented whereby the sizes and optical properties of biodegradable gold nanoclusters formed from nanospheres which do not adsorb any serum proteins are tuned *via* control over van der Waals, electrostatic, depletion, and polymer bridging colloidal interactions.

Table of Contents

List of Tables

List of Figures

Chapter 1: Introduction

A significant challenge in biomedical imaging and therapy is the development of sub-100 nm nanoparticles which not only exhibit intense imaging functionality, but also are cleared efficiently by the renal system in order to avoid toxic accumulation within the body.[1-4] Gold nanoparticles in particular have recently attracted significant interest for biomedical applications due in large part to their value as contrast agents in optical imaging modalities such as photoacoustic imaging[5-7] as well as therapeutic applications such as photothermal therapy.[8-11] For gold nanoparticles used as biomedical contrast agents, it is often desirable for nanoparticles to exhibit absorb light strongly in the near-infrared (NIR) wavelength range from 650 nm to 900 nm, where water and hemoglobin absorb weakly.[12] To date, gold nanoparticle contrast agents which exhibit intense extinction in the NIR region typically have sizes in excess of ~30 nm.[3, 9, 11, 13, 14] In order to effectively clear from the body through the renal system, however, nanoparticles must have a hydrodynamic diameter (D_h) of < 5.5 nm.[1, 15] Furthermore, in order to maintain this D_h in the body, nanoparticles must be able to resist the adsorption of serum proteins in the bloodstream, which would excessively increase the nanoparticle diameter and preclude clearance.[16, 17] Due to this conflict, the design of biodegradable contrast agents which exhibit intense NIR extinction, and can furthermore dissociate to sizes below ~5.5 nm in diameter for effective renal clearance, is of great interest.

For sub-100 nm spherical Au nanoparticles, the localized surface plasmon resonance (LSPR) created by the collective oscillation of conduction band electrons creates weak extinction in the NIR region.[18, 19] Strong NIR extinction, however, may result from the shifting of the surface plasmon resonance of the particles to the NIR region due to hybridized plasmon modes involving dipoles and quadropoles.[20, 21] This

SPR shift is commonly achieved by designing particles with asymmetric geometries, such as nanoshells,[9, 10, 22] nanorods,[11, 23, 24] nanocages,[14, 25] nanoflowers,[26-29] nanostars,[30] or nanoroses.[3, 31] The sizes of these nanoparticles are often between 30 nm and 200 nm, which is a size range ideal for high cellular uptake.[32-34] Additionally, nanoparticles in this size range have furthermore been shown to exhibit long circulation times due to an ability to avoid rapid clearance by the reticuloendothelial system (RES).[34-36] While the sizes of these nanoparticles are often desirable for imaging, cell uptake, and long circulation times, they are too large to achieve efficient renal clearance which could result in toxic accumulation of these contrast agents in the body.

In addition to asymmetric geometries, the coupling of individual spherical nanoparticles can also shift the LSPR into the NIR region.[2, 4, 6, 21, 37] For example, spherical gold nanoparticles functionalized with antibodies which recognize epidermal growth factor receptor (EGFR) have been shown to exhibit shifted extinction upon cellular uptake and endosomal capture.[37-39] The extinction exhibited by these aggregates within cells has moreover been shown to be useful for optical imaging.[2] It is often challenging, however, to control the sizes and morphologies of these nanoparticle aggregates *in vitro*. The reversibility of gold nanoclusters of controlled size, moreover, would allow for nanocluster design whereby clusters of sub-5.5 nm nanoparticles are assembled in order to provide intense NIR extinction and dissociate back to the constituent particles in order to enable clearance from the body.

An additional major barrier to the efficient clearance of nanoparticles from the body is the adsorption of serum proteins in the bloodstream, which would potentially increase the size of the nanoparticles enough to preclude renal clearance.[1, 15] In order to avoid protein adsorption, zwitterionic and nonionic coatings have been developed which minimize interactions between the proteins and the nanoparticle surfaces.[40-47] For

nanospheres coated with charged ligands, it is widely thought that significant adsorption occurs, due to electrostatic interactions between the proteins and the charged nanoparticle surfaces.[48, 49] Novel concepts would therefore be required to design moderately charged nanospheres which do not adsorb serum proteins in the bloodstream. Thus, in order to design viable contrast agents for biomedical imaging, it is critical to design reversible gold nanoclusters of controlled size which exhibit intense NIR extinction and are composed of sub-5.5 nm nanospheres which do not adsorb any serum proteins in the bloodstream.

1.1 Colloidal Nanocluster Assembly

Clusters of nanoparticles are often synthesized *in vitro* through "bricks and mortar" approaches, in which nanoparticles are assembled by taking advantage of specific interactions between nanoparticles and templating agents such as polymers, proteins, and DNA.[50-54] Moreover, nanoparticles have been assembled into constructs in the interior[53-55] and on the surface[56, 57] of polymeric micelles. The strong specific interactions between these templating agents and the nanoparticles, however, often preclude high nanoparticle loadings within the assemblies. An alternative approach to nanoparticle assembly is to tune parameters such as the pH or ionic strength of nanoparticle dispersions in order to induce aggregation.[58-61] While these assemblies exhibit relatively high metal nanoparticle loadings, it is difficult to control the nanocluster sizes and morphologies, as these methods often result in large, irregular nanoparticle aggregates.[58, 59]

Recently, the sizes and morphologies of nanoparticle clusters have been controlled by appropriately balancing the relevant colloidal interactions between primary nanoparticles.[4, 62-69] Here, clusters are often observed to form upon the reaction of precursor materials.[63] For example, nanoparticle assemblies have been observed to form upon the reaction of nanoparticle precursors have been tuned both in diethylene glycol[64] and in water via a "self-limiting" mechanism whereby short-ranged attractive van der Waals interactions balance with longer-ranged repulsive electrostatic interactions provided by charged ligands.[65] Here, nanocluster size can be tuned by varying parameters such as reaction time and the concentrations of both precursors and stabilizing ligands.[64, 65] More exquisite control over nanocluster size and morphology can be attained by clustering pre-synthesized primary nanoparticles.[63] These nanoparticles have been assembled into clusters of tunable size by modulating solvophobic interactions for iron oxide particles in ethylene glycol,[62] wherein nanocluster size was tuned by controlling the ratio of surfactant to iron oxide nanoparticles. In addition, nm gold nanospheres have been assembled into clusters in water.[69] Here, the nanoclusters were assembled by modulating steric interactions by displacing a PEG layer on the nanosphere surfaces with varying amounts of a small alkanethiol ligand.[69]

In order to mechanistically control nanocluster formation, the concept of equilibrium nanocluster assembly has been explored for both organic[66, 67] and aqueous solvents.[68] In these cases, nanocluster assembly is governed by the appropriate balancing of relatively strong, short-ranged attractions with relatively weak, longer-ranged repulsions, which can be described by a free-energy equilibrium model.[70, 71] Equilibrium nanoclusters formed in aqueous solvents are often small[72] and short-lived,[73] due to strong electrostatic repulsions between primary particles relative to the weak repulsions in organic environments with low dielectric constants.[70] Recently, however, the assembly of

small protein nanoparticles near the isoelectric point of the protein have been assembled into large (~100 nm) clusters, and the cluster sizes were described by a variation of the aforementioned free-energy model.[68] Here, short-ranged depletion attraction induced by crowder molecules added to a dispersion of protein colloids was balanced against longer-ranged electrostatic repulsion to tune nanocluster size.[68] Additionally, the nanocluster size can be predicted by the equation:

$$n^* = \frac{5aR}{6\lambda_b k_b T q^2} \quad (1.1)$$

In Equation 1.1, n^* is the equilibrium nanocluster size, a is the maginitude of the attractive force, R is the primary nanocolloid radius, k_b is Boltzmann's constant, T is the temperature, and q is the charge repulsion per primary particle.[68] These protein nanoclusters were furthermore shown to reversibly dissociate upon dilution,[68] indicating that equilibrium clusters of nanoparticles are able to reversibly dissociate to monomer upon changes in solvent conditions. It is unknown, however, whether reversible, inorganic equilibrium nanoclusters may be formed in aqueous solvents, and whether their sizes can be predicted via equilibrium theories.

Partially dissociable clusters of primary gold nanoparticles with intense NIR extinction have been reported to dissociate both in vitro and in macrophage cells.[4] Here, ~4 nm gold nanospheres capped with a mixture of lysine and citrate ligands were assembled into nanoclusters of ~80 nm in size using the biodegradable polymer PLA(1k)-*b*-PEG(10k)-*b*-PLA(1k). Upon degradation of this polymeric stabilizer, the nanoclusters were shown to partially dissociate to monomer, as shown in Figure 1.1.[4] The factors which control the size and morphology of these nanoclusters, however, were not explored in that work.[4] Systematic control over the size and morphologies of these nanoclusters is

explored in Chapter 2. Moreover, fully dissociable equilibrium gold nanoclusters of controllable sizes and morphologies are discussed in Chapter 4. The sizes of these nanoclusters are also semi-quantitatively predicted using a free-energy model[68, 70] which is adapted to gold nanoclusters. This quenched assembly mechanism for nanocluster formation is extended to nanospheres capped with varying surface ligands in Chapters 5 and 6.

1.2 Design of Nanoparticles to Prevent Serum Protein Adsorption

For gold nanospheres which have a diameter of ~4 nm, the adsorption of a single serum protein molecule in the bloodstream would potentially increase the nanoparticle size too much for renal clearance, as the adsorption of proteins such as bovine serum albumin (BSA) would increase the size to greater than the 5.5 nm diameter threshold necessary for effective clearance.[1, 15, 16] The adsorption of serum proteins onto both flat surfaces[41, 74-77] and curved nanoparticles[45-47, 78, 79] has been shown to depend on several factors, such as the orientation of ligands on the surface, the surface charge, and the surface hydrophobicity.[49, 80, 81] Numerous studies have reported relatively low adsorption of serum proteins on zwitterionic or nonionic surface coatings which exhibit zero net charge.[1, 43, 45, 46, 75, 82-84] Zwitterionic peptides on flat gold surfaces, for example, which contained equivalent amounts of cationic lysine and anionic glutamic acid exhibited minimal adsorption of lysozyme and fibrinogen.[40] Similarly, flat Au surfaces[41, 74] coated with binary ligands with equal amounts of positive and negative charges exhibit minimal protein adsorption, and curved nanoparticles with zwitterionic ligands also adsorb no protein.[45, 85]

In contrast to zwitterionic or nonionic ligands, it has been widely reported that for surfaces coated with highly charged single ligands, the adsorption of serum proteins is often significant.[48, 86, 87] For gold nanoparticles coated with highly anionic ligands such as dihydrolipoic acid (DHLA)[1] or citrate,[88-91] for example, the adsorption of serum proteins is significant, as shown by a substantial increase (on the order of ~10 nm) in hydrodynamic diameter. While nanoparticles coated with charged single ligands are known to adsorb significant amounts of serum proteins, binary or multicomponent ligand monolayers with mixed charge monolayers with net charge have received relatively little attention. Binary zwitterionic monolayers with zero net charge and equal amounts of cationic and anionic ligands, for example, have shown very little protein adsorption.[41, 74, 76, 92] When these mixed monolayers carry significant net charge, however, significant protein adsorption often occurs, as shown with mixed monolayers of lysine and glutamic acid, where the adsorption of lysozyme and fibrinogen significantly increases when the lysine to glutamic acid ratio deviates from unity.[40] For small gold nanoparticles, however, the ligand orientations in mixed charge monolayers have been designed to prevent protein adsorption, as ordered "stripes" of anionic mercaptoundecanesulfonate (MUS) and nonionic octanethiol (OT) have been shown to adsorb essentially zero serum protein upon incubation in 10% serum, even with a significantly negative zeta potential of -35 mV.[78] Here, the observed lack of serum protein adsorption was attributed to the close proximities of hydrophobic and hydrophilic groups on the nanoparticle surface.[78, 93]

While charged gold nanoparticles with appropriately designed surface ligand orientations did not adsorb protein in 10% serum, it has been demonstrated by Yang *et al.* that nanoparticles which show no protein adsorption in 10% serum can adsorb significant amounts of serum proteins in undiluted serum.[45, 75] Moreover, while low adsorption is commonly measured by techniques such as gel electrophoresis,[94, 95] surface plasmon

resonance sensing,[41, 92] or quartz crystal microbalance analysis,[96] these techniques do not offer the single protein molecule level resolution provided by techniques such as dynamic light scattering (DLS).[15, 78, 85] Novel concepts are thus required to design charged gold nanospheres which do not adsorb any serum protein in undiluted serum, as measured by DLS. Moreover, if these nanospheres could be assembled into biodegradable nanoclusters with intense NIR extinction, it would be possible to design biomedical contrast agents which can clear efficiently through the kidneys. The design of these nanospheres is discussed in Chapter 3, and the assembly of nanoclusters composed of nanospheres which do not adsorb serum proteins is discussed in Chapters 4-6.

1.3 OBJECTIVES

The use of gold nanoparticles as effective biomedical imaging contrast agents necessitates intense extinction in the NIR wavelength region as well as effective clearance from the body through the renal system. Furthermore, in order to achieve effective renal clearance, the design of nanostructures that can avoid the increase in diameter created by the adsorption of serum proteins in the bloodstream is of significant recent interest. The primary goals of this dissertation are thus: (1) to demonstrate the assembly of sub 5 nm Au nanoparticles into clusters of controlled size which exhibit intense NIR extinction, (2) to design the surfaces of ~5 nm gold nanospheres which completely avoid serum protein adsorption in undiluted serum, and (3) to design biodegradable "quenched" nanoclusters of controlled size and morphology composed of primary gold nanospheres which do not adsorb serum proteins. A biodegradable polymer, PLA(1k)-*b*-PEG(10k)-*b*-PLA(1k), will be used to modulate interparticle interactions

during nanocluster formation. Moreover, the dissociation of these nanoclusters to constituent primary nanoparticles will be discussed. The ligand monolayers on the surfaces of the constituent ~4 nm gold nanoparticles will be designed such that these nanospheres do not exhibit any serum protein adsorption in undiluted fetal bovine serum (FBS). These nanospheres will be used to form biodegradable gold nanoclusters which exhibit intense NIR extinction which reversibly dissociate to monomer. Moreover, nanocluster assembly will be conducted with nanospheres with various ligand monolayer compositions as well as a variety of surface charges, demonstrating the generality of this nanocluster formation approach.

For the first goal of this dissertation, the assembly of ~4 nm gold nanospheres capped with a mixture of lysine and citrate ligands into nanoclusters of controlled sizes from 30 nm to 100 nm is demonstrated. Here, the nanoclusters are shown to exhibit intense extinction in the NIR wavelength region due to closely-spaced constituent nanoparticles within the interior of the clusters. Nanocluster size and extinction is tuned by experimentally varying the polymer/Au ratio and the concentrations of gold nanoparticles as well as the weakly-adsorbing biodegradable polymer PLA(1k)-*b*-PEG(10k)-*b*-PLA(1k). Nanocluster formation is furthermore explained in terms of the manipulation of van der Waals, depletion, electrostatic, and steric interactions between the Au nanoparticles.

For the second goal of the dissertation, novel concepts are used to design ~5 nm gold nanospheres which exhibit essentially zero protein adsorption in undiluted fetal bovine serum (FBS). The nanosphere surfaces are coated with binary ligand monolayers of anionic citrate and either cationic lysine or zwitterionic cysteine. The nanosphere surface charge is tuned with appropriate amount of either lysine or cysteine in order to completely avoid protein adsorption upon nanosphere incubation in undiluted FBS, as

shown by a negligible change in the nanosphere hydrodynamic diameter upon FBS incubation. A mechanism is presented whereby the zwitterionic tips of either lysine or cysteine interact weakly with the serum proteins in FBS and further limit the interactions of the "buried" charges on the citrate ligands. The design of moderately charged nanospheres which nevertheless adsorb zero protein is a novel advance over previous reports of nanospheres with zero protein adsorption, which often relied upon zwitterionic or nonionic surface coatings or ordered ligand orientations on the nanosphere surface. This concept of charged gold nanospheres which adsorb zero serum protein in undiluted serum is extremely advantageous in the design of gold nanoclusters, as it enables the manipulation of colloidal interactions for nanocluster formation while allowing for potential clearance through the kidneys of primary nanospheres after nanocluster biodegradation.

For the third goal of this dissertation, gold nanospheres which do not adsorb serum protein are assembled into nanoclusters which exhibit intense NIR extinction and in some cases reversibility to monomer. Nanocluster size and morphology are initially controlled via a "quenched equilibrium" mechanism, whereby nanoclusters are quenched at an equilibrium size by the weak, slow adsorption of PLA(1k)-*b*-PEG(10k)-*b*-PLA(1k). Here, the substantial reduction in primary nanosphere surface charge, relative to the lysine/citrate nanoclusters presented in Chapter 2, both enables nanospheres to resist serum protein adsorption and enables equilibrium nanocluster formation. The equilibrium sizes of these nanoclusters formed from nanospheres capped with a mixture of lysine and citrate are semi-quantitatively predicted by the application of a free-energy model which balances short-ranged van der Waals and depletion attractions between primary particles with longer-ranged electrostatic repulsions provided by the charged surface ligands.

Additional control over nanocluster size and optical properties is achieved by the addition of the electrolyte NaCl, which both screens electrostatic repulsions between primary nanospheres as well as decreases polymer adsorption to the nanocluster surface. This decrease in polymer adsorption reduces potential polymer-induced bridging attraction between individual nanospheres, nanocluster sub-units, or nanoclusters themselves. The combination of the reduction of polymer bridging and screening of electrostatic repulsions induced by salt addition forms small (sub-30 nm) nanoclusters with intense NIR extinction. Furthermore, the dissociation of nanoclusters to constituent monomeric gold nanospheres is demonstrated upon the degradation of the polymeric quencher for nanoclusters formed with and without added NaCl. In addition to nanospheres capped with lysine and citrate, nanocluster formation is extended to nanospheres capped with citrate and the thiolated, zwitterionic cysteine ligand, as opposed to the cationic lysine ligand. Here, the addition of NaCl enables the formation of small, NIR-active nanoclusters. Thus, a general concept is presented whereby the sizes and optical properties of reversible gold nanoclusters formed from nanospheres which do not adsorb any serum protein are tuned via control of various colloidal interactions. This general platform enables the synthesis of a wide range of nanocluster contrast agents of various sizes, morphologies, and primary particle surface ligands for biomedical imaging and therapeutic applications.

1.4 Dissertation Outline

This dissertation first introduces the concept of gold nanocluster formation from primary ~4 nm constituent monomers for potential biomedical imaging applications. In

Chapter 2, gold nanoclusters with sizes from 30 nm to 100 nm are formed which exhibit intense extinction in the NIR wavelength region. The relatively small amount of polymeric stabilizer present within the nanoclusters enables the close spacings of constituent primary particles necessary for intense NIR extinction. These close spacings produce exceptionally strong extinction cross sections of up ~9×10^{-15} m^2 at a wavelength of 700 nm. Here, nanocluster sizes and optical properties are tuned by varying the volume fractions of the gold nanoparticles as well as the ratio of the biodegradable polymer PLA(1k)-*b*-PEG(10k)-*b*-PLA(1k) to gold. Nanocluster formation is also described as a function of colloidal van der Waals, depletion, electrostatic, and steric interactions, which are tuned by manipulating the particle and polymer volume fractions. This chapter was published in Langmuir in 2010 with Dr. Jasmine Tam as the first author. The author of this dissertation contributed heavily to this work in terms of both experimentation and writing, particularly with regards to the mechanistic analysis of nanocluster formation.

In Chapter 3, the surfaces of primary gold nanospheres are designed such that they adsorb zero serum proteins in undiluted fetal bovine serum (FBS). The adsorption of a single protein molecule, for example a molecules of bovine serum albumin (BSA), would increase the nanospheres size too much and preclude efficient renal clearance. The primary citrate and lysine/citrate nanospheres utilized to synthesize the nanoclusters in Chapter 2 are found to adsorb significant amounts of serum proteins, thus necessitating further design of the nanosphere surface in order to enable efficient renal clearance. Mixed charge monolayers of citrate and either cationic lysine or zwitterionic cysteine are synthesized by reacting cysteine or lysine with originally citrate-capped gold nanospheres. The ratio of lysine and cysteine to citrate on the nanosphere surface is tailored in order to lower the nanosphere surface charge and completely inhibit serum

protein adsorption in undiluted FBS. Unexpectedly, moderately charged nanospheres still completely prevent the adsorption of serum proteins. Here, the zwitterionic tips of either lysine or cysteine interact weakly with the serum proteins in FBS, whereas the increased distance between the proteins and the buried charges of citrate helps decrease the interactions between the charged sites on citrate and the interacting sites on the serum proteins. Furthermore, the ~5 nm nanospheres capped with a 1.4/1 ratio of lysine to citrate are assembled into ~20 nm nanoclusters with intense NIR extinction, which dissociate upon biodegradation of a polymeric quenching agent. These dissociated nanoclusters also do not adsorb any serum protein in undiluted FBS, making these nanoclusters potentially ideal for biomedical applications.

Tunable equilibrium nanoclusters formed from the lysine/citrate nanospheres which do not adsorb serum proteins in Chapter 3 are reported in Chapter 4. A novel concept is presented in Chapter 4 whereby equilibrium gold nanoclusters from ~20 nm to ~40 nm in diameter are formed by tuning colloidal interactions in the presence of the polymeric stabilizer PLA(1k)-*b*-PEG(10k)-*b*-PLA(1k). Nanoclusters were formed by mixing a dispersion of the lysine/citrate nanospheres described in Chapter 3 with an aqueous solution of the polymer, followed by partial evaporation of the aqueous solvent. Weak polymer adsorption to the gold surface quenches the nanoclusters at an equilibrium size and provides steric stabilization to the assembled nanoclusters. The tuning of nanocluster size is accomplished by varying the gold nanoparticle and polymer concentrations. Nanoclusters are shown to reversibly dissociate completely to monomer upon the degradation of the polymeric quencher. Here, the equilibrium cluster size is semi-quantitatively predicted via a free-energy model, which balances strong, short ranged van der Waals and depletion attractions with weak, longer-ranged electrostatic repulsions provided by the charged ligands on the nanosphere surfaces. The close

spacings of the constituent nanoparticles within the nanoclusters provide intense NIR extinction which is of great practical interest in biomedical applications such as photoacoustic imaging.

The novel quenched nanocluster formation concept presented in Chapter 4 is extended in Chapters 5 and 6 by adding a monovalent electrolyte, NaCl, to the nanocluster formation process. Chapter 5 describes the use of NaCl to systematically modulate the properties of nanoclusters formed from the lysine/citrate nanospheres which resist serum protein adsorption introduced in Chapter 3. Short-ranged attractive van der Waals, polymer bridging, and depletion interactions are balanced against longer-ranged electrostatic repulsions to tune the nanocluster diameter from ~20 nm to ~200 nm. The addition of NaCl is shown to decrease polymer adsorption and polymer bridging as well as screen electrostatic repulsions between particles. Here, a general framework is presented in which to evaluate the influence of Au nanoparticle, and polymer concentrations on van der Waals, depletion, polymer bridging, and electrostatic interactions. Moreover, the modulation of these parameters is shown to affect both nanocluster size distributions as well as the extinction spectra. Additionally, nanoclusters are shown to dissociate reversibly and completely to monomer upon degradation of the polymeric quencher, indicating that salt addition did not adversely affect nanocluster dissociation. As a result, these nanoclusters show great promise as biomedical imaging contrast agents which can potentially be effectively cleared through the kidneys.

The quenched assembly of colloidal nanoclusters is further generalized in Chapter 6, wherein nanocluster formation is extended to nanospheres capped with the zwitterionic, thiolated cysteine ligand. Nanospheres coated with a binary monolayer of citrate and cysteine ligands are assembled into nanoclusters of controlled sizes from 20 nm to 110 nm. Here, the cysteine/citrate ratio of 1.6/1 is used to prevent protein

adsorption on primary nanospheres, as demonstrated in Chapter 3. The strongly binding nature of the thiol anchoring group on cysteine enables more permanent attachment to the gold nanoparticle surface, relative to the weakly-binding lysine ligand. The addition of the monovalent salt NaCl was shown to decrease polymer adsorption and thus decrease potential polymer bridging between nanospheres, nanocluster sub-units, and nanoclusters, as in Chapter 5. Additionally, salt addition reduces electrostatic repulsion between the charged primary particles to produce densely-packed nanoclusters. As in Chapter 5, the decrease in polymer adsorption and thus decrease in polymer bridging attractions induced by NaCl addition quenches small clusters with strong NIR extinction even for sizes as small as 20 nm. Here, significant extinction is observed even for wavelengths as high as 1300 nm. The generality of the quenched nanocluster assembly platform is thus demonstrated, as this approach is shown to apply to nanospheres with surface ligands of varying charge and binding strength to gold. The strong NIR extinction and control over nanocluster size are beneficial for biomedical applications such as photoacoustic imaging. Moreover, the nanoclusters are composed of small, sub-5 nm nanospheres which do not adsorb any serum proteins, enabling the possibility of efficient clearance through the renal system.

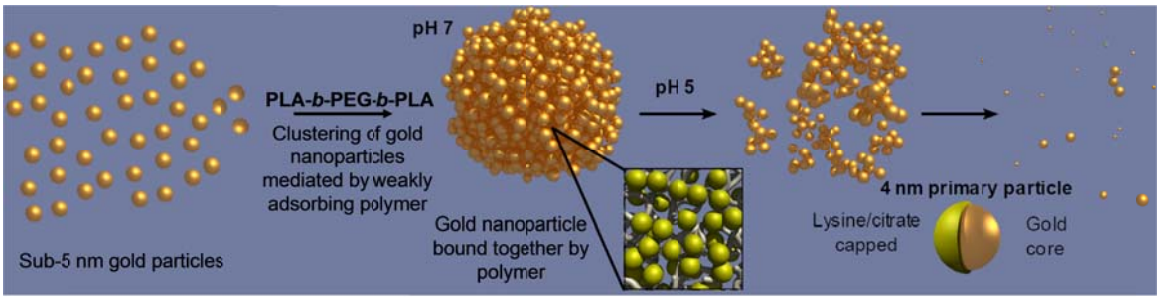

Figure 1.1:[4] Schematic illustrating the formation and partial dissociation of biodegradable gold nanoclusters.

1.5 REFERENCES

1. Choi, H. S.; Liu, W.; Misra, P.; Tanaka, E.; Zimmer, J. P.; Ipe, B. I.; Bawendi, M. G.; Frangioni, J. V. Renal Clearance of Quantum Dots. *Nature Biotechnology* **2007**, *25*, 1165-1170.
2. Aaron, J.; Travis, K.; Harrison, N.; Sokolov, K. Dynamic Imaging of Molecular Assemblies in Live Cells Based on Nanoparticle Plasmon Resonance Coupling. *Nano Letters* **2009**, *9*, 3612-3618.
3. Ma, L. L.; Feldman, M. D.; Tam, J. M.; Paranjape, A. S.; Cheruki, K. K.; Larson, T. A.; Tam, J. O.; Ingram, D. R.; Paramita, V.; Villard, J. W.*, et al.* Small Multifunctional Nanoclusters (Nanoroses) for Targeted Cellular Imaging and Therapy. *ACS Nano* **2009**, *3*, 2686-2696.
4. Tam, J. M.; Tam, J. O.; Murthy, A.; Ingram, D. R.; Ma, L. L.; Travis, K.; Johnston, K. P.; Sokolov, K. V. Controlled Assembly of Biodegradable Plasmonic Nanoclusters for near-Infrared Imaging and Therapeutic Applications. *ACS Nano* **2010**, *4*, 2178-2184.
5. Yoon, S. J.; Mallidi, S.; Tam, J. M.; Tam, J. O.; Murthy, A.; Johnston, K. P.; Sokolov, K. V.; Emelianov, S. Y. Utility of Biodegradable Plasmonic Nanoclusters in Photoacoustic Imaging. *Optics Letters* **2010**, *35*, 3751-3753.
6. Mallidi, S.; Larson, T.; Tam, J.; Joshi, P. P.; Karplouk, A.; Sokolov, K.; Emelianov, S. Multiwavelength Photoacoustic Imaging and Plasmon Resonance Coupling of Gold Nanoparticles for Selective Detection of Cancer. *Nano Letters* **2009**, *9*, 2825-2831.
7. Yoon, S. J.; Murthy, A.; Johnston, K. P.; Sokolov, K. V.; Emelianov, S. Y. Thermal Stability of Biodegradable Plasmonic Nanoclusters in Photoacoustic Imaging. *Optics Express* **2012**, *20*, 29479-29487.
8. Khlebtsov, B.; Zharov, V.; Melnikov, A.; Tuchin, V.; Khlebtsov, N. Optical Amplification of Photothermal Therapy with Gold Nanoparticles and Nanoclusters. *Nanotechnology* **2006**, 5167-5179.
9. Gobin, A. M.; Lee, M. H.; Halas, N. J.; James, W. D.; Drezek, R. A.; West, J. L. Near-Infrared Resonant Nanoshells for Combined Optical Imaging and Photothermal Cancer Therapy. *Nano Letters* **2007**, *7*, 1929-1934.
10. Hirsch, L. R.; Stafford, R. J.; Bankson, J. A.; Sershen, S. R.; Rivera, B.; Price, R. E.; Hazle, J. D.; Halas, N. J.; West, J. L. Nanoshell-Mediated near-Infrared Thermal Therapy of Tumors under Magnetic Resonance Guidance. *Proceedings of the National Academy of Sciences* **2003**, *100*, 13549-13554.

11. Huang, X.; El-Sayed, I. H.; Qian, W.; El-Sayed, M. A. Cancer Cell Imaging and Photothermal Therapy in the near-Infrared Region by Using Gold Nanorods. *Journal of the American Chemical Society* **2006**, *128*, 2115-2120.

12. Weissleder, R. A Clearer Vision for in Vivo Imaging. *Nature Biotechnology* **2001**, *19*.

13. Ma, L. L.; Borwankar, A. U.; Willsey, B. W.; Yoon, K. Y.; Tam, J. O.; Sokolov, K. V.; Feldman, M. D.; Milner, T. E.; Johnston, K. P. Growth of Textured Thin Au Coatings on Iron Oxide Nanoparticles with near Infrared Absorbance. *Nanotechnology* **2013**, *24*.

14. Chen, J.; Saeki, F.; Wiley, B. J.; Cang, H.; Cobb, M. J.; Li, Z. Y.; Au, L.; Zhang, H.; Kimmey, M. B.; Li, X.*, et al.* Gold Nanocages: Bioconjugation and Their Potential Use as Optical Imaging Contrast Agents. *Nano Letters* **2005**, *5*, 473-477.

15. Zhou, C.; Long, M.; Qin, Y.; Sun, X.; Zheng, J. Luminescent Gold Nanoparticles with Efficient Renal Clearance. *Angewandte Chemie International Edition* **2011**, *50*, 3168-3172.

16. Tirumalai, R. S.; Chan, K. C.; Prieto, D. A.; Issaq, H. J.; Conrads, T. P.; Veenstra, T. D. Characterization of the Low Molecular Weight Human Serum Proteome. *Molecular & Cellular Proteomics* **2003**, *2*, 1096-1103.

17. Striemer, C. C.; Gaborski, T. R.; McGrath, J. L.; Fauchet, P. M. Charge- and Size-Based Separation of Macromolecules Using Ultrathin Silicon Membranes. *Nature* **2007**, *445*, 749-753.

18. Kelly, K. L.; Coronado, E.; Zhao, L. L.; Schatz, G. C. The Optical Properties of Metal Nanoparticles: The Influence of Size, Shape, and Dielectric Environment *Journal of Physical Chemistry B* **2003**, *107*, 668-677.

19. Gavrilenko, V. I., *Optics of Nanomaterials*. Pan Stanford Publishing: Singapore, 2011; p 63-66.

20. Hu, Y.; Noelck, S. J.; Drezek, R. A. Symmetry Breaking in Gold-Silica-Gold Multilayer Nanoshells. *ACS Nano* **2010**, *4*, 1521-1528.

21. Halas, N. J.; Lal, S.; Chang, W.-S.; Link, S.; Nordlander, P. Plasmons in Strongly Coupled Metallic Nanostructures. *Chemical Reviews* **2011**, *111*, 3913-3961.

22. Loo, C.; Lowery, A.; Halas, N.; West, J.; Drezek, R. Immunotargeted Nanoshells for Integrated Cancer Imaging and Therapy. *Nano Letters* **2005**, *5*, 709-711.

23. Huang, X.; Peng, X.; Wang, Y.; Wang, Y.; Shin, D. M.; El-Sayed, M. A.; Nie, S. A Reexamination of Active and Passive Tumor Targeting by Using Rod-Shaped Gold Nanocrystals and Covalently Conjugated Peptide Ligands. *ACS Nano* **2010**, *4*, 5887-5896.

24. Link, S.; Mohamed, M. B.; El-Sayed, M. A. Simulation of the Optical Absorption Spectra of Gold Nanorods as a Function of Their Aspect Ratio and the Effect of the Medium Dielectric Constant. *Journal of Physical Chemistry B* **1999**, *103*, 3073-3077.

25. Song, K. H.; Kim, C.; Cobley, C. M.; Xia, Y.; Wang, L. V. Near-Infrared Gold Nanocages as a New Class of Tracers for Photoacoustic Sentinel Lymph Node Mapping on a Rat Model. *Nano Letters* **2009**, *9*, 183-188.

26. Li, L.; Weng, J. Enzymatic Synthesis of Gold Nanoflowers with Trypsin. *Nanotechnology* **2010**, *21*.

27. Wang, W.; Yang, X.; Cui, H. Growth Mechanism of Flowerlike Gold Nanostructures: Surface Plasmon Resonance (Spr) and Resonance Rayleigh Scattering (Rrs) Approaches to Growth Monitoring. *Journal of Physical Chemistry C* **2008**, *112*, 16348-16353.

28. Wang, Z.; Zhang, J.; Ekman, J. M.; Kenis, P. J. A.; Lu, Y. DNA-Mediated Control of Metal Nanoparticle Shape: One-Pot Synthesis and Cellular Uptake of Highly Stable and Functional Gold Nanoflowers. *Nano Letters* **2010**, *10*, 1886-1891.

29. Ren, Y.; Xu, C.; Wu, M.; Niu, M.; Fang, Y. Controlled Synthesis of Gold Nanoflowers Assisted by Poly(Vinylpyrrolidone)-Sodium Dodecyl Sulfate Aggregations. *Colloids and Surfaces A: Physicochemical and Engineering Aspects* **2011**, *380*, 222-228.

30. Trigari, S.; Rindi, A.; Margheri, G.; Sottini, S.; Dellepiane, G.; Giorgetti, E. Synthesis and Modelling of Gold Nanostars with Tunable Morphology and Extinction Spectrum. *Journal of Materials Chemistry* **2011**, *21*.

31. Ma, L. L.; Tam, J. O.; Willsey, B. W.; Rigdon, D.; Ramesh, R.; Sokolov, K.; Johnston, K. P. Selective Targeting of Antibody Conjugated Multifunctional Nanoclusters (Nanoroses) to Epidermal Growth Factor Receptors in Cancer Cells. *Langmuir* **2011**, *27*, 7681-7690.

32. Jiang, W.; Kim, B. Y. S.; Rutka, J. T.; Chan, W. C. W. Nanoparticle-Mediated Cellular Response Is Size-Dependent. *Nature Nanotechnology* **2008**, *3*.

33. Chithrani, B. D.; Ghazani, A. A.; Chan, W. C. W. Determining the Size and Shape Dependence of Gold Nanoparticle Uptake into Mammalian Cells. *Nano Letters* **2006**, *6*, 662-668.

34. Duan, X.; Li, Y. Physicochemical Characteristics of Nanoparticles Affect Circulation, Biodistribution, Cellular Internalization, and Trafficking. *Small* **2013**, *9*, 1521-1532.

35. Arruebo, M.; Fernandez-Pacheco, R.; Ibarra, R.; Santamaria, J. Magnetic Nanoparticles for Druge Delivery. *Nano Today* **2007**, *2*.

36. Kooi, M. E.; Cappendijk, V. C.; Cleutjens, K. B. J. M.; Kessels, A. G. H.; Kitslaar, P. J. E. H. M.; Borgers, M.; Frederik, P. M.; Daemen, M. J. A. P.; van Engelshoven, J. M. A. Accumulation of Ultrasmall Superparamagnetic Particles of Iron Oxide in Human Atherosclerotic Plaques Can Be Detected by in Vivo Magnetic Resonance Imaging. *Circulation* **2003**, *107*, 2453-2458.

37. Aaron, J.; Nitin, N.; Travis, K.; Kumar, S.; Collier, T.; Park, S. Y.; Jose-Yacaman, M.; Coghlan, L.; Follen, M.; Richards-Kortum, R.*, et al.* Plasmon Resonance Coupling of Metal Nanoparticles for Molecular Imaging of Carcinogenesis in Vivo. *Journal of Biomedical Optics* **2007**, *12*.

38. Aaron, J.; Oh, J.; Larson, T. A.; Kumar, S.; Milner, T. E.; Sokolov, K. V. Increased Optical Contrast in Imaging of Epidermal Growth Factor Receptor Using Magnetically Actuated Hybrid Gold/Iron Oxide Nanoparticles. *Optics Express* **2006**, *14*, 12930-12943.

39. Larson, T. A.; Bankson, J.; Aaron, J.; Sokolov, K. Hybrid Plasmonic Magnetic Nanoparticles as Molecular Specific Agents for Mri/Optical Imaging and Photothermal Therapy of Cancer Cells. *Nanotechnology* **2007**, *18*.

40. Chen, S.; Cao, Z.; Jiang, S. Ultra-Low Fouling Peptide Surfaces Derived from Natural Amino Acids. *Biomaterials* **2009**, *30*, 5893-5896.

41. Chen, S.; Yu, F.; Yu, Q.; He, Y.; Jiang, S. Strong Resistance of a Thin Crystalline Layer of Balanced Charged Groups to Protein Adsorption. *Langmuir* **2006**, *22*, 8186-8191.

42. Jiang, S. Y.; Cao, Z. Q. Ultralow-Fouling, Functionalizable, and Hydrolyzable Zwitterionic Materials and Their Derivatives for Biological Applications. *Advanced Materials* **2010**, *22*, 920-932.

43. Ladd, J.; Zhang, Z.; Chen, S.; Hower, J. C.; Jiang, S. Zwitterionic Polymers Exhibiting High Resistance to Nonspecific Protein Adsorption from Human Serum and Plasma. *Biomacromolecules* **2008**, *9*, 1357-1361.

44. Vaisocherova, H. Z., Z.; Yang,W.; Cao,Z.; Cheng,G.; Taylor,A.D; Piliarik,M.; Homola,J.; Jiang,S. Functionalizable Surface Platform with Reduced Nonspecific Protein Adsorption from Full Blood Plasma - Material Selection and Protein Immobilization Optimization. *Biosensors and Bioelectronics* **2008**, *24*, 1924-1930.

45. Yang, W.; Zhang, L.; Wang, S.; White, A. D.; Jiang, S. Functionalizable and Ultra Stable Nanoparticles Coated with Zwitterionic Poly(Carboxybetaine) in Undiluted Blood Serum. *Biomaterials* **2009**, *30*, 5617-5621.

46. Walkey, C. D.; Olsen, J. B.; Guo, H.; Emili, A.; Chan, W. C. W. Nanoparticle Size and Surface Chemistry Determine Serum Protein Adsorption and Macrophage Uptake. *Journal of the American Chemical Society* **2012**, *134*, 2139-2147.

47. Larson, T. A.; Joshi, P. P.; Sokolov, K. Preventing Protein Adsorption and Macrophage Uptake of Gold Nanoparticles Via a Hydrophobic Shield. *ACS Nano* **2012**, *6*, 9182-9190.

48. Brewer, S. H.; Glomm, W. R.; Johnson, M. C.; Knag, M. K.; Franzen, S. Probing Bsa Binding to Citrate-Coated Gold Nanoparticles and Surfaces. *Langmuir* **2005**, *21*, 9303-9307.

49. Lundqvist, M.; Stigler, J.; Elia, G.; Lynch, I.; Cedervall, T.; Dawson, K. A. Nanoparticle Size and Surface Properties Determine the Protein Corona with Possible Implications for Biological Impacts. *Proceedings of the National Academy of Sciences* **2008**, *105*, 14265-14270.

50. Ofir, Y. S., B.; Rotello, V.M. Polymer and Biopolymer Mediated Self-Assembly of Gold Nanoparticles. *Chemical Society Reviews* **2008**, *37*, 1814-1825.

51. Srivastava, S.; Samanta, B.; Arumugam, P.; Han, G.; Rotello, V. M. DNA-Mediated Assembly of Iron Platinum (Fept) Nanoparticles. *Journal of Materials Chemistry* **2006**, *17*, 52-55.

52. Boal, A. K.; Ilhan, F.; DeRouchey, J. E.; Thurn-Albrecht, T.; Russell, T. P.; Rotello, V. M. Self-Assembly of Nanoparticles into Structured Spherical and Network Aggregates. *Nature* **2000**, *404*, 746-748.

53. Frankamp, B. L.; Boal, A. K.; Rotello, V. M. Controlled Interparticle Spacing through Self-Assembly of Au Nanoparticles and Poly(Amidoamine) Dendrimers. *Journal of the American Chemical Society* **2002**, *124*, 15146-15147.

54. Gopidas, K. R. W., J.K.; Fox, M.A. Nanoparticle-Cored Dendrimers: Synthesis and Characterization. *Journal of the American Chemical Society* **2003**, *125*, 6491-6502.

55. Uzun, O.; Frankamp, B. L.; Sanyal, A.; Rotello, V. M. Recognition-Mediated Assembly of Nanoparticle-Diblock Copolymer Micelles with Controlled Size. *Chemistry of Materials* **2006**, *18*, 5404-5409.

56. Li, J.; He, W.-D.; Sun, X.-L. Prepartion of Poly(Styrene-B-N-Isoprpylacrylamide) Micelles Surface-Linked with Gold Nanoparticles and Thermo-Responsive Ultraviolet-Visible Absorbance. *Journal of Polymer Science Part A- Polymer Chemistry* **2007**, *45*, 5156-5163.

57. Bae, K. H.; Choi, S. H.; Park, S. Y.; Lee, Y.; Park, T. G. Thermosensitive Pluronic Micelles Stabilized by Shell Cross-Linking with Gold Nanoparticles. *Langmuir* **2006**, *22*, 6380-6384.

58. Wilcoxon, J. P. M., J.E; Schaefer, D.W. Aggregation in Colloidal Gold. *Physical Review A* **1989**, *39*.

59. Chow, M. K.; Zukoski, C. F. Gold Sol Formation Mechanisms: Role of Colloidal Stability. *Journal of Colloid and Interface Science* **1994**, *165*, 97-109.

60. Horovitz, O.; Mocanu, A.; Tomoaia, G.; Bobos, L.; Dubert, D.; Daian, I.; Yusanis, T.; Tomoaia-Cotisel, M. Lysine Mediated Assembly of Gold Nanoparticles. *Studia Universitatis Babes-Bolyai Chemia* **2007**, *52*.

61. Han, X.; Goebl, J.; Lu, Z.; Yin, Y. Role of Salt in the Spontaneous Assembly of Charged Gold Nanoparticles in Ethanol. *Langmuir* **2011**, *27*, 5282-5289.

62. Zhuang, J.; Wu, H.; Yang, Y.; Cao, Y. C. Controlling Colloidal Superparticle Growth through Solvophobic Interactions. *Angewandte Chemie International Edition* **2008**, *47*, 2208-2212.

63. Lu, Z.; Yin, Y. Colloidal Nanoparticle Clusters: Functional Materials by Design. *Chemical Society Reviews* **2012**, *41*, 6874-6887.

64. Ge, J.; Hu, Y.; Biasini, M.; Beyermann, W. P.; Yin, Y. Superparamagnetic Magnetite Colloidal Nanocrystal Clusters. *Angewandte Chemie International Edition* **2007**, *46*, 4342-4345.

65. Xia, Y. S.; Nguyen, T. D.; Yang, M.; Lee, B.; Santos, A.; Podsiadlo, P.; Tang, Z. Y.; Glotzer, S. C.; Kotov, N. A. Self-Assembly of Self-Limiting Monodisperse Supraparticles from Polydisperse Nanoparticles. *Nature Nanotechnology* **2011**, *6*, 580-587.

66. Sedgwick, H.; Egelhaaf, S. U.; Poon, W. C. K. Clusters and Gels in Systems of Sticky Particles. *J. Phys.-Condes. Matter* **2004**, *16*, S4913-S4922.

67. Buitenhuis, J.; Dhont, J. K. G.; Lekkerkerker, H. N. W. Static and Dynamic Light Scattering by Concentrated Colloidal Suspensions of Polydisperse Sterically Stabilized Boehmite Rods. *Macromolecules* **1994**, *27*, 7267-7277.

68. Johnston, K. P.; Maynard, J. A.; Truskett, T. M.; Borwankar, A. U.; Miller, M. A.; Wilson, B. K.; Dinin, A. K.; Khan, T. A.; Kaczorowski, K. J. Concentrated Dispersion of Equilibrium Protein Nanoclusters That Reversibly Dissociate into Active Monomers. *ACS Nano* **2012**, *6*, 1357-1369.

69. Larson-Smith, K.; Pozzo, D. C. Scalable Synthesis of Self-Assembling Nanoparticle Clusters Based on Controlled Steric Interactions. *Soft Matter* **2011**, *7*.

70. Groenewold, J.; Kegel, W. K. Anomalously Large Equilibrium Clusters of Colloids. *Journal of Physical Chemistry B* **2001**, *105*, 11702-11709.

71. Groenewold, J.; Kegel, W. K. Colloidal Cluster Phases, Gelation and Nuclear Matter. *J. Phys.-Condes. Matter* **2004**, *16*, S4877-S4886.

72. Stradner, A.; Sedgwick, H.; Cardinaux, F.; Poon, W. C. K.; Egelhaaf, S. U.; Schurtenberger, P. Equilibrium Cluster Formation in Concentrated Protein Solutions and Colloids. *Nature* **2004**, *432*, 492-495.

73. Porcar, L.; Falus, P.; Chen, W.-R.; Faraone, A.; Fratini, E.; Hong, K.; Baglioni, P.; Liu, Y. Formation of the Dynamic Clusters in Concentrated Lysozyme Protein Solutions. *Journal of Physical Chemistry Letters* **2010**, *1*, 126-129.

74. Holmlin, R. E.; Chen, X.; Chapman, R. G.; Takayama, S.; Whitesides, G. M. Zwitterionic Sams That Resist Nonspecific Adsorption of Protein from Aqueous Buffer. *Langmuir* **2001**, *17*, 2841-2850.

75. Yang, W.; Xue, H.; Li, W.; Zhang, J.; Jiang, S. Pursuing "Zero" Protein Adsorption of Poly(Carboxybetaine) from Undiluted Blood Serum and Plasma. *Langmuir* **2009**, *25*, 11911-11916.

76. Chen, S. F.; Cao, Z. Q.; Jiang, S. Y. Ultra-Low Fouling Peptide Surfaces Derived from Natural Amino Acids. *Biomaterials* **2009**, *30*, 5892-5896.

77. Ostuni, E.; Chapman, R. G.; Holmlin, R. E.; Takayama, S.; Whitesides, G. M. A Survey of Structure-Property Relationships of Surfaces That Resist the Adsorption of Protein. *Langmuir* **2001**, *17*, 5605-5620.

78. Verma, A.; Uzun, O.; Hu, Y.; Hu, Y.; Han, H.-S.; Watson, N.; Chen, S.; Irvine, D. J.; Stellacci, F. Surface-Structure-Regulated Cell-Membrane Penetration by Monolayer-Protected Nanoparticles. *Nature Materials* **2008**, *7*, 588-595.

79. Cedervall, T.; Lynch, I.; Lindman, S.; Berggard, T.; Thulin, E.; Nilsson, H.; Dawson, K. A.; Linse, S. Understanding the Nanoparticle-Protein Corona Using Methods to Quantify Exchange Rates and Affinities of Proteins for Nanoparticles. *Proceedings of the National Academy of Sciences* **2006**, *104*, 2050-2055.

80. Chen, S.; Li, L.; Zhao, C.; Zheng, J. Surface Hydration: Principles and Applications toward Low-Fouling/Nonfouling Biomaterials. *Polymer* **2010**, *51*, 5283-5293.

81. Markarucha, A. J.; Todorova, N.; Yarovsky, I. Nanomaterials in Biological Environment: A Review of Computer Modelling Studies. *European Biophysics Journal* **2011**, *40*, 103-115.

82. Li, L.; Chen, S.; Zheng, J.; Ratner, B. D.; Jiang, S. Protein Adsorption on Oligo(Ethylene Glycol)-Terminated Alkanethiolate Self-Assembled Monolayers: The Molecular Basis for Nonfouling Behavior. *Journal of Physical Chemistry B* **2005**, *109*, 2934-2941.

83. Liu, W.; Choi, H. S.; Zimmer, J. P.; Tanaka, E.; Frangioni, J. V.; Bawendi, M. Compact Cysteine-Coated Cdse(Zncds) Quantum Dots for in Vivo Applications. *Journal of the American Chemical Society* **2007**, *129*, 14530-14531.

84. Estephan, Z. G.; Jaber, J. A.; Schlenoff, J. B. Zwitterion-Stabilized Silica Nanoparticles: Toward Nonstick Nano. *Langmuir* **2010**, *26*, 16884-16889.

85. Jia, G.; Cao, Z.; Xue, H.; Xu, Y.; Jiang, S. Novel Zwitterionic-Polymer-Coated Silica Nanoparticles. *Langmuir* **2009**, *25*, 3196-3199.

86. Mahmoudi, M.; Lynch, I.; Ejtehadi, M. R.; Monopoli, M. P.; Bombelli, F. B.; Laurent, S. Protein-Nanoparticle Interactions: Opportunities and Challenges. *Chemical Reviews* **2011**, *111*, 5610-5637.

87. Beurer, E.; Venkataraman, N. V.; Sommer, M.; Spencer, N. D. Protein and Nanoparticle Adsorption on Orthogonal, Charge-Density-Versus-Net-Charge Surface-Chemical Gradients. *Langmuir* **2012**, *28*, 3159-3166.

88. Dobrovolskaia, M. A.; Patri, A. K.; Zheng, J.; Clogston, J. D.; Ayub, N.; Aggarwal, P.; Neun, B. W.; Hall, J. B.; McNeil, S. E. Interaction of Colloidal Gold Nanoparticles with Human Blood: Effects on Particle Size and Analysis of Plasma Protein Binding Profiles. *Nanomedicine* **2009**, *5*, 106-117.

89. De Paoli Lacerda, S. H.; Park, J. J.; Meuse, C.; Pristinski, D.; Becker, M. L.; Karim, A.; Douglas, J. F. Interaction of Gold Nanoparticles with Common Human Blood Proteins. *ACS Nano* **2010**, *4*, 365-379.

90. Dominguez-Medina, S.; McDonough, S.; Swanglap, P.; Landes, C. F.; Link, S. In Situ Measurement of Bovine Serum Albumin Interaction with Gold Nanospheres. *Langmuir* **2012**, *28*, 9131-9139.

91. Casals, E.; Pfaller, T.; Duschl, A.; Oostingh, G. J.; Puntes, V. Time Evolution of the Nanoparticle Protein Corona. *ACS Nano* **2010**, *4*, 3623-3632.

92. Chen, S.; Zhen, J.; Li, L.; Jiang, S. Strong Resistance of Phosphorylcholine Self-Assembled Monolayers to Protein Adsorption: Insights into Nonfouling Properties of Zwitterionic Materials. *Journal of the American Chemical Society* **2005**, *127*, 14473-14478.

93. Jackson, A. M.; Myerson, J. W.; Stellacci, F. Spontaneous Assembly of Subnanometre-Ordered Domains in the Ligand Shell of Monolayer-Protected Nanoparticles. *Nature Materials* **2004**, *3*, 330-336.

94. Yu, M.; Zhou, C.; Liu, J.; Hankins, J. D.; Zheng, J. Luminescent Gold Nanoparticles with Ph-Dependent Membrane Adsorption. *Journal of the American Chemical Society* **2011**, *133*, 11014-11017.

95. Liu, X.; Huang, H.; Jin, Q.; Ji, J. Mixed Charged Zwitterionic Self-Assembled Monolayers as a Facile Way to Stabilize Large Gold Nanoparticles. *Langmuir* **2011**, *27*, 5242-5251.

96. Kaufman, E. D.; Belyea, J.; Johnson, M. C.; Nicholson, Z. M.; Ricks, J. L.; Shah, P. K.; Bayless, M.; Pettersson, T.; Feldoto, Z.; Blomberg, E.*, et al.* Probing Protein Adsorption onto Mercaptoundecanoic Acid Stabilized Gold Nanoparticles and Surfaces by Quartz Crystal Microbalance and Z-Potential Measurements. *Langmuir* **2007**, *23*, 6053-6062.

Chapter 2: Kinetic Assembly of Near-IR Active Gold Nanoclusters using Weakly Adsorbing Polymers to Control the Size[1]

Clusters of metal nanoparticles with an overall size less than 100 nm and high metal loadings for strong optical functionality, are of interest in various fields including microelectronics, sensors, optoelectronics and biomedical imaging and therapeutics. Herein we assemble ~5 nm gold particles into clusters with controlled size, as small as 30 nm and up to 100 nm, which contain only small amounts of polymeric stabilizers. The assembly is kinetically controlled with weakly adsorbing polymers, PLA(1k)-*b*-PEG(10k)-*b*-PLA(1k) or PEG (MW = 3350), by manipulating electrostatic, van der Waals (VDW), steric, and depletion forces. The cluster size and optical properties are tuned as a function of particle volume fractions and polymer/gold ratios to modulate the interparticle interactions. The close spacing between the constituent gold nanoparticles and high gold loadings (80-85% w/w gold) produce a strong absorbance cross section of ~9×10-15 m^2 in the NIR at 700 nm. This morphology results from VDW and depletion attractive interactions that exclude the weakly adsorbed polymeric stabilizer from the cluster interior. The generality of this assembly platform is demonstrated for gold nanoparticles with a range of surface charges from highly negative to neutral, with the two different polymers.

[1] Reproduced in large part with permission from: Tam, J.M.; Murthy, A.K.; Ingram, D.R.; Nguyen, R.; Sokolov, K.V.; Johnston, K.P. Kinetic Assembly of Near-IR Active Gold Nanoclusters Using Weakly Adsorbing Polymers to Control the Size. *Langmuir* **2010,** *26*(11), 8988-8999. Copyright 2010 American Chemical Society.

2.1 INTRODUCTION

Optical and electronic properties of 1D[1], 2D, and 3D clusters of metal nanocrystals, 20 to 500 nm in diameter, have been studied extensively, especially for applications involving sensors, memory devices, microelectronics[2-4], and more recently, for cellular imaging and therapy[5-9]. For a variety of applications, robust and broadly applicable synthetic strategies are needed to pack high levels of functionality (i.e. high metal loadings) into clusters with an overall size smaller than ~30 to 100 nm. Most often, clusters are formed by thermodynamic self assembly. Rotello and co-workers developed a "bricks and mortar" technique for the templated assembly of metal nanoparticles into clusters using polymers, proteins, and DNA[2, 10] and Glotzer et al. and Miles et al.[11] have demonstrated assembly with polymer-tethered nanoparticles[12]. Gold nanoparticles have been assembled in the cores of block copolymer micelles[13-16] and on the surface of micelles[17, 18]. Amphiphilic gold Janus spheres, containing hydrophobic and hydrophilic domains self-assemble into clusters[19-22] upon manipulation of pH or solvent quality. For clusters formed thermodynamically, high concentrations of templating agents and strong interactions between these agents and the particles are typically required to drive the self-assembly. Consequently, these agents are usually highly retained in the final cluster and limit the metal loading, typically well below 50% w/w.

An alternative approach is to form clusters of metal nanoparticles by kinetic assembly to achieve extremely high metal loadings by manipulating van der Waals (VDW), electrostatic, and steric interactions. For example, variation of pH or ionic strength of dilute dispersions of citrate-capped gold nanoparticles screens electrostatic repulsion and induces cluster growth[23, 24]. Similarly, lysine-[25-28] and cysteine-[29] capped gold nanoparticles at high loadings aggregate reversibly in response to changes in charge

with pH. Gold nanoparticles coated with associating proteins, such as biotin and streptavidin[30], or with complementary DNA strands[31, 32] also form clusters. However, in each of these cases, uncontrolled growth often yields irregularly shaped aggregates greater than several hundred nanometers in diameter. Therefore, a conflict arises in both thermodynamically- and kinetically-controlled assembly between the need for sufficient levels of stabilizers to arrest growth to produce small sub-100 nm clusters, while simultaneously achieving high metal loadings for high functionality.

Metal nanoparticles with high NIR absorbance are of great interest in biomedical imaging and therapy because soft tissues and water are relatively transparent from 650 to 900 nm. The surface plasmon resonance (SPR) of a spherical gold particle exhibits a maximum at 530 nm, but undergoes a red shift to the NIR for particles with a hollow or non-spherical geometry, such as nanoshells[33-35], nanorods[36, 37], and nanocages[38, 39]. These particles are typically 50-100 nm in diameter. NIR absorbance has rarely been achieved for particles smaller than 50 nm, where it becomes challenging to synthesize the types of asymmetric morphologies needed for strong red-shifts[40]. Significant NIR absorbance also has been demonstrated *in vitro* and *in vivo* for the assembly of 40 nm gold spheres, conjugated with antibodies, by receptors in cancer cells into clusters[5, 6, 8, 41]. Small gold clusters that have been formed by equilibrium self assembly methods often contain high concentrations of templating agents, which result in particle separations greater than one particle diameter and thus small red shifts[42, 43].

Nanoparticle components may be assembled into clusters with properties that are challenging to achieve including, sizes below 50 nm[3, 7, 13, 44] strong optical absorbance[7, 44], multifunctionality[7], and/or biodegradability[9, 44]. Recently, there has been great interest in the development of sub-30 nm particles, which penetrate cell membranes and leaky vasculature in cancerous tumors more efficiently than particles >50 nm[45-49].

Furthermore, these small nanoparticles elicit profound changes in biological pathways in targeted cells. Sub-30 nm particles have been reported for gold nanocages[50] and multifunctional nanocluster hybrids containing gold and iron oxide, referred to as nanoroses[7]. Despite their small sizes, both types of nanoparticles absorb strongly in the NIR. The nanorose clusters, composed of nanocomposite primary particles, are formed by kinetic assembly during the reduction of gold precursors onto iron oxide nanoparticles. They exhibit intense magnetic relaxivity as well as NIR absorbance[7]. To further advance the functional properties in nanoclusters, especially biodegradability, we recently introduced a physical, rather than chemical, method for the kinetically controlled colloidal assembly of ~5 nm gold spheres into ~100 nm NIR plasmonic clusters stabilized by PLA(1k)-*b*-PEG(10k)-*b*-PLA(1k). These clusters were shown to biodegrade nearly completely in solution and in macrophage cells back to the original 5 nm primary spheres, which are small enough for renal clearance [9]. This physical, kinetic, colloidal assembly method is general and likely to enable synthesis of many types of clusters over a wide size range.

Herein we assemble kinetically sub-5 nm gold particles into clusters of controlled sizes, as small as 30 nm and up to 100 nm, stabilized by small amounts of a weakly adsorbing polymer, either PLA-*b*-PEG-*b*-PLA or PEG 3350. The physical cluster assembly process, introduced recently in Tam et al.[9], is illustrated in Figure 2.1. The gold nanoparticles are nucleated rapidly at high volume fractions in the presence of a weakly adsorbing polymer to form small clusters[9]. The nucleation and growth of the gold clusters is controlled by increasing gold and polymer concentrations simultaneously, either by solvent evaporation or by mixing of a concentrated gold dispersion with a concentrated polymer solution. A mechanism is presented to describe the cluster growth and gold particle spacing in terms of the electrostatic, VDW, steric and depletion forces.

The combination of high gold particle volume fractions and exclusion of the weakly adsorbed polymeric stabilizer from the cluster interior towards the exterior surface are utilized to produce low polymer loadings and closely spaced gold particles for strong NIR absorbance. In contrast, high polymer loadings and larger gold particle spacings are typically obtained in equilibrium assembly processes that rely on strong interactions with templating agents, such as micelles[13-18, 51, 52]. Finally, the small amount of polymer on the exterior surface provides sufficient steric stabilization to prevent unregulated cluster growth, in contrast with previous studies without polymer stabilizers[24-29]. Relative to our previous study[9], the size of the clusters is over three fold smaller, and furthermore, a wider range of ligands (to modify particle charge), polymers, and polymer/gold ratios are examined. An advantage of this kinetic assembly approach is its use of readily available polymer stabilizers and simple ligands on the gold surface, such as citrate and lysine, in contrast to templating agents that often require complicated synthetic approaches.

2.2 EXPERIMENTAL

2.2.1 Materials

$HAuCl_4 \cdot 3H_2O$ was purchased from MP Biomedicals LLC (Solon, OH) and $Na_3C_3H_5O(COO)_3 \cdot 2\ H_2O$ and $NaBH_4$ were acquired from Fisher Scientific (Fair Lawn, NJ). L(+)-lysine was obtained from Acros Chemicals (Morris Plains, NJ). PEG (MW=3350) was ordered from Union Carbide (Danbury, CT) and PLA(1k)-*b*-PEG(10k)-*b*-PLA(1k) was purchased from Sigma Aldrich (St. Louis, MO).

2.2.2 Nanocluster formation

Gold nanoparticles (3.8-nm) stabilized with citrate ligands were synthesized based on a well known method[53]. Briefly, DI water (100 mL) was heated to 97°C. While stirring, 1 mL of 1% $HAuCl_4 \bullet 3H_2O$, 1 mL of 1% $Na_3C_3H_5O(COO)_3 \bullet 2\ H_2O$, and 1 mL of 0.075% $NaBH_4$ in a 1% $Na_3C_3H_5O(COO)_3 \bullet 2\ H_2O$ solution were added in 1 minute intervals. The solution was stirred for 5 minutes and then removed to an ice bath to cool to room temperature. The gold particles were then centrifuged at 10,000 rpm for 10 minutes at 4°C to remove any large aggregates. Centrifugal filter devices (Ultracel YM-30, Millipore Co.) were used to remove unadsorbed citrate ligands as well as concentrate the gold dispersion to ~3.0 mg Au/mL. Gold concentrations were determined using flame atomic absorption spectroscopy (FAAS).

In most cases, lysine ligands were added to the citrate stabilized gold nanoparticles by adding a 1% lysine in pH 8.4 phosphate buffer (10 mM) solution to 1.2 mL of the colloidal citrate-capped gold solution to yield a final lysine and gold concentration of 0.4 mg/mL and 3.0 mg/mL, respectively. In the cases where a 1.0 mg/mL gold solution was used to produce nanoclusters, the 3.0 mg/mL stock gold solution was diluted using deionized (DI) water. The dispersion was stirred for at least 12 hours[26, 54]. PLA-*b*-PEG-*b*-PLA was added to the aqueous dispersion of ligand capped gold nanoparticles to yield polymer/gold ratios ranging from 1/10 – 40/1. The dispersions were then sonicated in a bath sonicator for 5 minutes. Unless otherwise noted, the concentration of the gold solutions used in this study to produce nanoclusters was 3.0 mg/mL with a polymer/gold ratio of 16/1.

In some cases, the polymer/gold dispersion was placed under an air stream and a certain percentage of the solvent, between 50-100%, was evaporated. The extent of solvent evaporation was determined volumetrically, by comparing the initial and final

volume of the dispersion before and after evaporation. When the dispersion was not dried to completion, it was quenched with DI water after the chosen amount of solvent evaporation Upon quenching, the concentration of the dispersion was approximately an order of magnitude lower than that of the original gold stock prior to solvent evaporation. In the case of 100% solvent evaporation, which took place over ~20-30 minutes, the dried film was redispersed with 10 mL of DI water to yield a blue dispersion of ~0.30 mg Au/mL. Nanoclusters were also formed using a mixing procedure, in which highly concentrated solutions of gold colloid and polymer were mixed together using a probe sonicator (Branson Sonifier 450, Branson Ultrasonics Corporation, Danbury, CT) with a 102 converter and tip operated in pulse mode at 35 W.

2.2.3 Nanocluster characterization

Nanocluster morphology was observed by transmission electron (TEM) and scanning electron microscopy (SEM). TEM was performed on a FEI TECNAI G2 F20 X-TWIN TEM using a high-angle annular dark field detector. TEM samples were prepared using a "flash-freezing" technique, in which a 200 mesh carbon-coated copper TEM grid was cooled using liquid nitrogen and then dipped into a dilute aqueous nanocluster dispersion. The TEM grid was dried using a Virtis Advantage Tray Lyophilizer (Virtis Company, Gardiner, NY) with 2 hours of primary drying at -40 ^{o}C followed by a 12 hour ramp to +25 ^{o}C and then 2 hours of secondary drying at 25 ^{o}C. Separation distances between primary particles within the nanoclusters were measured by analyzing TEM images using Scion Image software (Frederick, Maryland). A Zeiss Supra 40VP field emission SEM was operated at an accelerating voltage of 5−10 kV. SEM samples were prepared by depositing a dilute aqueous dispersion of the

nanoclusters onto a silicon wafer. The sample was dried in a hood, washed with DI water to remove excess polymer, and dried again. UV−visible spectra were measured using a Varian Cary 5000 spectrophotometer for a 1 cm path length. Dynamic light scattering (DLS) measurements of hydrodynamic diameter and zeta potential measurements were performed in triplicate on a Brookhaven Instruments ZetaPlus dynamic light scattering apparatus at a scattering angle of 90° and temperature of 25 °C[55]. Dispersion concentrations were adjusted with either DI water for DLS measurements or pH=7.4 buffer (10 mM) for zeta potential measurements to give a measured count rate between 300-400 kcps. For DLS measurements, all dispersions were filtered through a 0.2 μm filter and probe sonicated for 2 min prior to measurement. The data were analyzed using a digital autocorrelator (Brookhaven BI-9000AT) with a non-negative least-squares (NNLS) method (Brookhaven 9KDLSW32). A distribution of hydrodynamic diameters was obtained based on the Stokes-Einstein equation for the diffusion coefficient of a sphere. All distributions were weighted by volume. Reported average diameters correspond to the D50, or diameter at which the cumulative sample volume was under 50%. For zeta potential measurements, the average value of at least three data points was reported. Thermogravimetric analysis (TGA) was used to determine the amount of adsorbed ligand mass on the primary gold nanoparticles and the final polymer/gold ratio of the nanoclusters. TGA was performed using a Perkin–Elmer TGA 7 under nitrogen atmosphere at a gas flow rate of 20 mL/min. Excess, unadsorbed organic material, either ligands and/or polymer, was removed from particles, either colloidal gold or nanoclusters, by centrifuging the dispersions at 10,000 rpm for 5 minutes at 4^{o}C. For the colloidal gold particles, which were too small to settle efficiently during centrifugation, centrifugal filter devices were used to separate and filter the particles from the smaller unadsorbed ligands. The supernatants were discarded and the pellets were dried to a

powder. The powder samples were held at 50°C for 120 minutes to remove any moisture in the sample and then heated at a constant rate of 20 °C/min from 50°C to 800 °C and held at 800°C for 30 minutes. The loss in mass after heating accounted for the organic component of the particles. Flame atomic absorption spectroscopy (FAAS) was used to determine the gold concentration in the dispersion and the yield for the gold particles that were incorporated into the clusters. A GBC 908AA flame atomic absorption spectrometer (GBC Scientific Equipment Pty Ltd) was used to determine the amount of gold present in a sample. All measurements were conducted at 242.8 nm using an air-acetylene flame. To determine clustering efficiency, a dispersion of nanoclusters of known concentration was centrifuged at 10,000 rpm for 10 minutes at 4oC. FAAS measurements were conducted on the supernatant.

2.2.4 Determination of stability ratio and half-life for aggregation

The stability of the nanoparticles may be quantified using a stability ratio, *W*, defined as the ratio of the rate of fast, diffusion controlled aggregation to slow, kinetically-controlled aggregation[24, 56]. Alternately, *W* may also be determined using the respective half-lives for fast and slow aggregation.

$$W = \frac{k_f}{k_s} = \frac{t_{1/2,s}}{t_{1/2,f}} \qquad (2.1)$$

where k_f and k_s are the rate constants for fast and slow flocculation, respectively, and $t_{1/2,f}$ and $t_{1/2,s}$ are the half-lives for fast and slow flocculation, respectively. The half life for fast, diffusion-controlled aggregation according to Smoluchowski[24, 56] is given as:

$$t_{1/2,f} = \frac{3\eta}{4k_b T N_0} \qquad (2.2)$$

where η is the solution viscosity, and N_0 is the initial number density of nanoparticles. Slow flocculation half-lives were estimated experimentally based on the observed time required for a visual color change in the nanocluster dispersion to occur, t_{col}. The observed t_{col} may be used to estimate half-lives using the assumption that a color change corresponds to the collision of 11 particles[57] and solving the equation for second order reaction kinetics, $1/N(t) = kt + 1/N_0$, to yield:

$$t_{1/2,s} = t_{col}/10 \qquad (2.3)$$

where N is the number of particles in the system at time, t, and k is the reaction rate constant. Even though this solution is approximate for high conversions of primary particles into clusters, the deviation of the exact solution from second order kinetics is less than a factor of 2, indicating that second-order kinetics can be used to derive an approximate half-life for slow flocculation[58].

2.3 RESULTS

2.3.1 Effect of particle volume fraction on nanocluster size and optical properties

The amount of ligands on the surface of the gold particles was determined prior to the formation of nanoclusters. For the citrate-capped gold nanoparticles, the average diameter was 3.8 ± 1.0 nm (data not shown) and the zeta potential was -44.0 ± 4.7 mV (Table 2.1) at a pH of ~7.2. The citrate coverage on the gold nanoparticles was estimated to be about 6.3% w/w, based on calculations assuming saturated ligand coverage on the 4 nm gold particle surface in good agreement with the 7% w/w citrate measured by TGA(See Appendix A). The adsorption of lysine to gold did not significantly change the particle size, which was 4.1 ± 0.8 nm (Figure 2.2a), nor the pH of the gold dispersion.

Lysine contains two NH_3^+ charges and one COO^- charge over a pH range from 3 to 10 [26] (Figure A.1). The ligand exchange with the positively charged lysine increased the zeta potential to -30.1 ± 2.4 mV (Table 2.1), indicating about 30% of the adsorbed citrate was exchanged(See supplementary). The citrate/lysine-capped particles were coated with 11% total ligand, according to TGA results, compared with 7% for the citrate-only stabilized nanoparticles. The color did not vary for the citrate-only and citrate/lysine-capped gold nanoparticle dispersions for ~1 month, corresponding to a very high W of $\sim 7\times10^9$ (Table 2.2) for an N_0 of $\sim 10^{21}$ particles/m^3 and $t_{1/2,f}$ of 3.93×10^{-5} s, which is based on a gold loading of 3 mg/mL. The high stability is due to strong repulsive charges on the ligands of the particles, in good agreement with previous reports in literature[26, 59].

To form gold clusters, interactions between citrate/lysine gold particles were mediated with a weakly adsorbing polymer, either PLA-*b*-PEG-*b*-PLA, as shown in Figure 2.1, or PEG (MW=3350) homopolymer. Without any solvent evaporation, the addition of either polymer to the ligand-capped gold particles at a 16/1 polymer/gold ratio (gold concentration = 3 mg/mL) did not produce a color change over a period of one hour, indicating that clusters of closely-spaced gold were not formed[9]. After an hour, the color slowly changed. A one hour stability (t_{col} =1 hr) corresponds to a maximum W of $\sim 4\times10^5$, as determined from Eqs. 2.1-2.3 (Table 2.2). To more fully probe the kinetics of nanocluster formation, the nanocluster size was monitored as a function of solvent evaporation by quenching cluster growth with the addition of DI water after a specified level of solvent evaporation. The harvested nanoclusters were observed by TEM (Figure 2.2) and their sizes determined by DLS (Figure 2.3a). For PLA-*b*-PEG-*b*-PLA, the formation of dimers and trimers was detected, indicating nucleation, after 50% solvent evaporation (Figures 2.2, 2.3a), which occurred over ~5 minutes for a 1.4 mL sample. This time corresponds to a maximum W of $\sim 2.5\times10^5$, as $t_{1/2,s}$ could have been even

smaller than 5 minutes. These small oligomers produced a shoulder in the DLS size distribution. When the suspension, from which 50% of the solvent had been evaporated, was allowed to sit over the course of one week, still no color change was observed, indicating that the oligomers did not grow to produce larger clusters. However, additional solvent reduction to 60% evaporation, approximately one minute later, led to clusters 35-60 nm in size, as seen both by TEM and DLS. Further solvent evaporation, to 80% and 100%, produced additional growth, with D_{50} values of 60 nm and 80 nm, respectively, with low polydispersities between 1.1-1.8 (See Appendix A for calculation). From 50 to 95% evaporation, the cluster size was monotonic with the extent of evaporation. The small, but distinct secondary peaks observed in the particle size distributions for the nanoclusters were attributed to the presence of a small population of aggregates. Because the particle size distributions were weighted by volume, a small number of large aggregates can cause this small secondary peak. These large aggregates composed a very small percentage of the total nanocluster population and were easily filtered out for later experiments. Yields of gold in the clusters, or the percent of the loaded primary particles that are incorporated into clusters after quenching the growth, was determined using FAAS (Table 2.3). After 60% and 100% solvent evaporation, 95.1% and 99.7%, respectively, of the initially loaded gold nanoparticles by mass were incorporated into clusters. Therefore, cluster yields, as well as size, continued to increase with the extent of solvent evaporation. The ability to tune the cluster size over a wide range and to achieve low polydispersities is of great scientific and practical interest.

Extents of solvent evaporation greater than 60% resulted in a color change of the dispersion to blue, but it was difficult to observe the kinetics given the dark, opaque dispersions at the high volume fractions. Thus, the spectra were measured after the clusters were quenched by dilution. The increase in the NIR absorbance was consistent

with the morphologies observed by TEM and the sizes measured by DLS. Before polymer was added, the characteristic spectrum for individual gold particles exhibited a maximum at 530 nm (Figure 2.3b). For the dimers and trimers (Figure 2.2b), the red-shift was modest as expected[42, 43, 60]. A much larger increase in the NIR absorbance was observed for 60% evaporation (Figure 2.3b), where sizable clusters of 35-60 nm were observed by TEM and DLS, as expected from theoretical calculations[42, 43, 60]. The NIR absorbance continued to increase as the extent of evaporation and nanocluster size increased.

Complete solvent evaporation produced a smooth blue film on the glass surfaces of the vials, indicating a shift in the absorbance spectra of gold to the NIR. Reconstitution of the film with DI water yielded a dark blue dispersion of sub-100 nm clusters composed of primary gold nanoparticles (Figure 2.2)[9]. SEM images of nanoclusters formed after 100% solvent evaporation reveal a polymer-rich shell a few nanometers thick surrounding the exterior of each cluster. The spectra of the nanoclusters formed after 100% solvent evaporation exhibited a broad, relatively constant, absorbance in the important NIR region from 700 to 900 nm, corresponding to an extinction coefficient at the maximum absorbance, ε_{703}, of 0.017 $cm^2/\mu g$ for a 56 $\mu g/mL$ gold dispersion. Assuming that the gold nanoparticles occupy ~72% of the cluster volume (based on SEM and TEM images in Figure 2.2), characteristic of a closest-packed volume fraction, the estimated particle extinction cross section was 9.0×10^{-15} m^2 (See Appendix A), comparable to the value for nanoshells[42], nanocages[39], nanorods[42], and nanoroses[7]. The mean spacing between primary gold particles within the clusters was estimated to be 1.80 ± 0.6 nm[9], well within the range of interparticle spacing known to produce a significant red-shift in the SPR [1, 42, 43]. The ability of the gold nanoparticles to pack tightly together is supported by TGA results, which indicated that after 100%

solvent evaporation, nanoclusters contained only 20 ± 5% organic material. From the known amount of ligand reported above, 10-15% of this material was polymer. The ability to reproducibly produce nanoclusters using 100% evaporation, with respect to both size and optical properties, is shown in Figure A.2. Furthermore, these nanoparticles exhibited excellent stability in terms of particle size and optical properties over the course of 3 weeks, as determined by DLS and UV-vis measurements (data not shown). Nanoclusters were stored in a refrigerator at 4˚C between measurements.

The zeta potentials of the resultant nanoclusters of citrate-only and citrate/lysine-capped nanoparticles were -13.0 ± 3.3 mV and -16.3 ± 4.0 mV, respectively, approximately half that of the initial colloidal gold nanoparticles (Table 2.1). Interestingly, the zeta potential of clusters formed using citrate-only and citrate/lysine-capped gold, stabilized with PLA-b-PEG-b-PLA, had similar zeta potential values, somewhat larger than that of the pure polymer. The value of -8.0 ± 0.2 mV for the PLA-b-PEG-b-PLA polymer is attributed to the ionized PLA end groups.

Nanoclusters were also formed using PEG (MW=3350), instead of PLA-*b*-PEG-*b*-PLA, as the stabilizing polymer. The PEG-stabilized clusters were, on average, ~1.5 times larger than those stabilized using PLA-*b*-PEG-*b*-PLA, as reported by DLS and TEM (Figures 2.4a-c). Similar to observations for PLA-*b*-PEG-*b*-PLA-stabilized clusters, a reduction in solvent evaporation from 100% to 60% yielded a ~30% reduction in cluster size and slightly lower NIR absorbances. The strong NIR absorbance of the PEG-stabilized clusters indicated that tight packing of gold nanoparticles within the cluster was achieved (Figure 2.4d). In fact, the clusters formed at 60% solvent evaporation show a slightly stronger NIR absorbance than the clusters formed after 60% solvent evaporation using PLA-*b*-PEG-*b*-PLA, likely due to the larger cluster size.

Similar trends were obtained for nanoclusters produced using citrate-only capped gold nanoparticles and PEG 3350 (data not shown).

2.3.2 Clusters of lysine/citrate particles with PLA-*b*-PEG-*b*-PLA formed by mixing

Assembly of nanoclusters was also demonstrated without solvent evaporation by mixing together highly concentrated gold and polymer solutions. The resulting concentrations of gold particles and polymer corresponded to those achieved by certain solvent evaporation extents. For example, a 6 mg/mL dispersion of gold nanoparticles was mixed with a 100 mg/mL polymer solution to produce clusters that were equivalent to the concentrations achieved after 50% evaporation. However, the cluster sizes were at least 2.5 times larger than those where the particle volume fractions were increased gradually by solvent evaporation (Figure 2.5a). Furthermore, nanoclusters formed by mixing, instead of solvent evaporation, tended to form a larger amount of aggregates of nanoclusters, as indicated by the more prominent secondary peaks in the particle size distributions. Because of their larger sizes, nanoclusters produced by this method displayed even more shifted NIR absorbance (Figure 2.5b). Similar trends in optical properties were observed when clusters of citrate-only-capped gold nanoparticles were produced using this mixing method (Figure A.3). The high viscosities of the extremely concentrated polymer solutions, ranging from 9×10-4 Pa s (~10 times that of water) to 0.8 Pa s (~900 times that of water) for solutions corresponding to 60% and 90% solvent evaporation (Figure A.4), respectively, resulted in inadequate mixing rates, poorer polymer diffusion, and thus the larger clusters with an increased propensity to form aggregates.

2.3.3 Clusters formed with citrate-only capped particles and PEG-SH coated particles

Nanoclusters were produced using gold nanoparticles capped with two other types of ligands: negatively charged citrate, and neutral PEG-SH to compliment the above studies which used lysine (positively charged) and citrate ligands, simultaneously. Clusters of gold primary particles capped with either citrate or a citrate/lysine mixture exhibited strong NIR absorbance (Figure 2.6). However, nanoparticles capped with PEG-SH did not produce a significant red-shift, although the shift was larger for PEG-SH with a MW of 0.13K versus 5K. PEG-SH 5K has a reported radius of gyration of 3.1 nm[61]. Therefore, the corresponding particle separations between two PEG-SH coated particles of at least 6.2 nm is larger than the diameter of a gold primary particle and the strongly bound PEG-SH 5K ligands prevented the gold nanoparticles from packing together tightly enough for a strong red shift.

Relative to citrate/lysine-capped particles, very similar behavior was observed for clusters assembled with citrate-only capped gold nanoparticles and PLA-*b*-PEG-*b*-PLA upon solvent evaporation, according to DLS, TEM, and UV-vis/NIR measurements (Figure A.5). Again, there was a very strong correlation between cluster size and NIR absorbance. However, the clusters did not form until ~ 85% solvent evaporation, as compared to 60% for citrate/lysine capped gold (Figure 2.7). The greater repulsion for the citrate-only-capped particles, as is evident in the larger zeta potentials, appeared to delay cluster formation. The slightly smaller sizes and larger SPR red-shifts of the nanocluster composed of citrate/lysine nanoparticles may be influenced by the attractive electrostatic attraction between the positive and negative charges on the lysine (Figure A.1)[26]. These interactions may further promote polymer exclusion from the cluster interior.

2.3.4 Tuning cluster size with polymer/gold ratio

To demonstrate the ability to tune the cluster size, the gold loading was lowered to 1.0 mg/mL, compared to 3.0 mg/mL in our previous study[9], and the polymer/gold ratio was varied over a wide range for 100% solvent evaporation. Cluster sizes decreased considerably as polymer/gold ratios were reduced from 16/1 to 1/1 (Figure 2.8a), with an average diameter of 28.4 nm for the 1/1 ratio. Despite the reduction in cluster size, clusters produced at a polymer/gold ratio between 1/1 to 16/1 still exhibited a broad and intense NIR absorbance, similar to that shown in Figure 2.3b. However, for polymer/gold ratios below 1/1, the absorbance did not shift significantly from that of colloidal gold (Figure 2.8b). For a given polymer/gold ratio, similar results were obtained for the cluster size and spectra for the higher gold loading of 3.0 mg/mL, as shown in Figure A.6, although the sizes were slightly smaller for the 1.0 versus the 3.0 mg/mL loading. As an example of the extent by which the cluster sizes could be tuned, the much smaller clusters formed with a 1/1 polymer/gold ratio at a gold loading of 1.0 mg/mL versus a 16/1 polymer/gold ratio at a 3.0 mg/mL loading is shown in TEM micrographs (Figures 2.8c-d). Additionally, a small decrease in the absorbance spectra was observed for clusters formed at a 40/1 polymer/gold ratio and a 3.0 mg/mL gold loading (Figure A.6b). Here, an extremely high polymer concentration of 1200 mg/mL was generated when the level of solvent evaporation reached 90%, resulting in excessive polymer that likely interfered with close-spacing between the gold nanoparticles, and thus, lowered the red shift[43]. This interference was not present for lower polymer/gold ratios. Further decreasing gold loadings as low as 0.19 mg/mL and increasing the polymer/gold ratio up to 260/1 led to the formation of increasingly larger clusters with reduced NIR absorbance (Table A.1, Figure A.7). Nanoclusters produced at a 1/1 gold/polymer ratio and a 1.0 mg/mL gold concentration were approximately 85% gold

w/w, comparable to 80% w/w gold in nanoclusters formed with a 16/1 gold/polymer ratio and a starting gold concentration of 3.0 mg/mL, as determined by TGA.

2.4 DISCUSSION

2.4.1 Interaction potential and stability ratio

The kinetic assembly of nanoparticles into clusters may be controlled by adjusting the stability ratio for a pair of particles, which is dependent upon the total interaction potential between particles:

$$V_{total} = V_{electrosta\ tic} + V_{VDW} + V_{steric} + V_{depletion} \quad (2.4)$$

The first two terms are described by DLVO theory, as discussed in the supplementary section. The addition of a weakly or non-adsorbing polymer introduces attractive depletion interactions, which arise from the exclusion of polymer from the gap region between two particle surfaces. The depletion potential for hard sphere colloids and polymers treated as "penetrable hard spheres" is given by[62-64]:

$$\frac{V_{depletion}(H)}{k_b T} = -\rho_\infty \pi \left[\frac{4}{3} r^3 + 2r^2 a - r^2 H - 2raH + \frac{aH^2}{2} + \frac{H^3}{12} \right], 0 \le H < 2r \quad (2.5)$$

where H is the distance between particle surfaces, r is the polymer radius, a is the nanoparticle radius, and ρ_∞ is the number density of polymer particles in solution. If the polymer forms micelles, the micellar properties are used (See Appendix A). The ability of depletion forces to cause particle flocculation, and even phase separation, in colloid-polymer mixtures is well known both experimentally and theoretically[65-67]. The kinetic stability ratio, in terms of V_{total}, is described by [55]

$$W = 2a\int_{2a}^{\infty} \frac{\frac{D_\infty}{D(u)}\left[\exp\left(\frac{V_{total}}{k_b T}\right)\right]}{H^2} dH \qquad (2.6)$$

where u is a dimensionless variable defined as $(H-2a)/a$, and the ratio $D_\infty/D(u)$ is the hydrodynamic correction factor:

$$\frac{D_\infty}{D(u)} = \frac{6u^2 + 13u + 2}{6u^2 + 4u} \qquad (2.7)$$

The first parts of the discussion section compare the kinetically controlled nanocluster assembly with previous studies based on the terms for V_{total} and the manipulation of the particle concentrations. A quantitative expression is not presented herein for V_{steric}, given the complexity of hydration of PEG at high concentrations where gels are formed.

2.4.2 Cluster assembly in the absence of polymer (VDW and electrostatic forces)

In the absence of a polymer, the VDW and electrostatic terms play a primary role in cluster formation, whereas steric and depletion interactions are small. Electrostatic repulsion of the nanoparticles may be weakened by a change in pH or salinity to reduce the charge. For dilute dispersions of gold coated with citrate (0.1 mg gold/mL), the growth from attractive VDW forces may be controlled over a period of hours to form clusters >100 nm in size[23, 24]. For these dilute conditions, the clusters are typically relatively low density with a low fractal dimension. In contrast, clusters formed at high particle concentrations are more likely to be composed of gold particles with close spacing that favors strong NIR absorbance. However, for concentrated gold dispersions (20-50 mg/mL), it becomes difficult to balance the electrostatic repulsion and VDW attraction to control the growth, and substantial aggregation has been observed over a

period of several minutes[26]. For instance, when gold nanoparticles are capped with lysine ligands, a change in pH simultaneously produces both positive and negative charges (Figure A.1) that result in electrostatic attraction and irregularly shaped aggregates up to several microns in diameter[23, 25-28]. Additional concepts in kinetic assembly are needed to better control Vtotal and thus the particle size and gold spacing.

2.4.3 Cluster assembly in the presence of polymer

The key challenge in this study was to control nanocluster size and gold particle spacing within the clusters by manipulation of the particle concentration pathways and V_{total}. High gold particle concentrations (>>0.1 mg/mL) were utilized in order to achieve sufficiently close gold particle spacing for strong NIR absorbance. However, they can also cause unmitigated cluster growth. This dilemma was addressed by the addition of a weakly adsorbing polymer to manipulate the electrostatic, steric, and depletion forces. The polymer initiates nucleation and growth, while simultaneously providing steric stabilization, but with low final polymer loadings.[2, 18, 51]

The initial citrate-only and citrate/lysine-capped gold nanoparticles in this study were extremely stable, evidenced by large negative zeta potentials of -44 and -30 mV, respectively, and a V_{total} of at least 23 k_BT (Figure 2.9) (See Appendix A). Nanocluster formation was initiated by raising the polymer and gold particle concentrations either by solvent evaporation or mixing to raise the adsorption of the polymer on gold. The weakly adsorbed polymer decreases the local dielectric constant near the charged ligands and thus weakens the ion hydration, causing ion pairing. This decrease in particle charge is directly evident in the decrease in the zeta potential with the addition of polymer (Table 2.1). The decrease in electrostatic repulsion causes a marked decrease in the

experimentally determined W (Table 2.2) from ~10^{10} for the citrate/lysine-capped primary particles to ~10^5 after the addition of polymer and 50% solvent evaporation. At this condition, the polymer adsorption did not reduce the particle charge enough to produce clusters larger than dimers or trimers within several hours.

At an extent of 50% solvent evaporation, the charge on an individual gold particle was regressed from the theoretical W in Eq. 2.6, given the known experimental W described above (Table 2.2). In this regression, V_{total} included electrostatic, VDW, and depletions terms, as described in the supplementary section. V_{steric} was not included in the regression because its role during the aggregation process was assumed to be relatively small, given the much larger magnitude of the electrostatic repulsion for the weakly adsorbed polymer. However, the role of steric stabilization for the fully formed nanoclusters is more significant because the polymer is excluded toward the outside of the clusters. All of the properties were known except the surface potential (and thus surface charge) on a gold nanoparticle. The reduction in the regressed surface charge of 1.6 after 50% solvent evaporation, relative to that of the initial colloidal gold particles, was found to be comparable to the reduction in zeta potential given in Table 2.1. The loss in charge is further characterized by the large decrease in V_{total} to about 11 k_BT (Figure 2.9), which may be attributed to the significant drop in $V_{electrostatic}$ upon charge reduction caused by the polymer, as V_{VDW} did not change. Thus, this large decrease in $V_{electrostatic}$, and consequently V_{total}, produced a decrease in W at 50% solvent evaporation of 5 orders of magnitude, relative to the initial colloidal gold particles (Figure 2.10). It was not possible to regress any changes in the particle charge with higher extents of solvent evaporation because the dispersions were too turbid to determine W experimentally. The regressed charge at 50% was used to calculate the V_{total} and thus W for greater solvent evaporation levels. V_{total} decreased as solvent evaporation increased,

primarily due to a reduction in $V_{electrostatic}$. Using Eq. 2.6, the steady decrease in $V_{electrostatic}$, and thus V_{total}, with solvent evaporation (i.e. increasing particle volume fraction) was found to cause a further decrease in W (Figure 2.10). The $V_{electrostatic}$ decreases with an increase in the number density of charged gold nanoparticles as the extent of evaporation increases. For electro-neutrality, the resulting increase in counter-ion concentration reduces the Debye length according to Eq. A.12. However this change in $V_{electrostatic}$ changes W by less than an order of magnitude, significantly smaller than the changes observed with polymer induced ion pairing. Therefore, the initial cluster growth is driven primarily by the attractive VDW forces upon reduction of particle charge and electrostatic repulsion upon weak polymer adsorption[65, 68]. As the number of closely-spaced gold particles in the cluster increases, the number of water molecules in the coordination shells about each particle decreases, given that the gold surface is hydrophobic. This decrease in hydration may further contribute to ion pairing and weakened electrostatic repulsion.

The smaller clusters produced using PLA-*b*-PEG-*b*-PLA as a stabilizer versus PEG homopolymer may be attributed to the stronger adsorption of the more hydrophobic PLA-*b*-PEG-*b*-PLA[16, 69], which produces greater charge reduction and thus more rapid nucleation. The larger number of nuclei and greater steric stabilization for reduced growth would lead to small clusters. Furthermore, the presence of micelles for PLA-*b*-PEG-*b*-PLA may provide greater steric stabilization than the homopolymer in the early stages of growth. Similarly, smaller clusters formed for the less charged citrate/lysine-capped gold versus citrate-only capped gold (Figure 2.7) may also be attributed to more rapid nucleation. In addition, the attractive electrostatic interactions between the lysine ligands may enhance polymer exclusion from the cluster interior.

The decrease in $V_{electrostatic}$ to drive cluster growth may also be achieved simply by adding salts. However, without the steric and depletion contributions to the potential, control over the final cluster size for high initial gold particle concentrations has not been successful[23, 24]. Thus, manipulation of these additional terms with polymer concentration and structure is important to achieve greater control over kinetic self-assembly. The nucleation of clusters via an adsorbed polymer to reduce the surface charge and simultaneously provide steric stabilization enables significantly improved control over cluster growth even with the high gold particle concentrations.

2.4.4 Spacing between gold particles in the nanoclusters

The final polymer weight fraction in the clusters was only on the order of 10 to 15% w/w according to TGA, even with starting polymer/gold ratios well above unity, for example our most common case of 16/1. The small spacing between the gold particles of only 1.80 nm[9] for PLA-*b*-PEG-*b*-PLA stabilized nanoclusters is considerably smaller than the size of a PLA-*b*-PEG-*b*-PLA polymer micelle, measured to be 10-14 nm (Figure A.8) or the R_g of the PEG homopolymer of 6.1 nm[70]. Thus, the polymers were excluded from the cluster interior. Various properties of gold contribute to the low polymer loadings, which favor small interparticle distances. The Hamaker constant is 60 k_BT for Au versus only 0.6 k_BT for the PEG, calculated using Lifshitz theory[12]. The gold surface is not highly hydrophilic given that polypropylene oxide adsorbs more strongly to gold than PEG[69]. Thus, the gold particles are strongly attracted to each other by VDW and hydrophobic forces. Additionally, the polymer chains are depleted from the overlap regions in the interior of the clusters towards the cluster exterior in order to raise their

conformation entropy, as described by Eq. 2.5. These depletion forces, along with the propensity for hydrophilic PEG segments to orient towards the aqueous exterior, drive the weakly adsorbed and hence highly mobile polymer away from the cluster interior and towards the exterior cluster interface with water and into bulk water. This mechanism is supported by the polymer shell observed in the SEM image (Figure 2.2f), as well as the low polymer loadings. Thus, the hydrophilic PEG segments of the polymer, which are oriented preferentially towards the exterior cluster interface, extend into the aqueous environment and provide steric stabilization. In essence, the close spacing of the gold particles is driven by the strong VDW attraction between the gold particles and the depletion forces which exclude the polymer.

In the case where a strongly adsorbing polymer is used to regulate cluster formation and growth, the polymer is often retained at significantly higher levels within the final cluster than in the present study. Prud'homme et al. have developed a "flash nanoprecipitation" method to mix an organic dispersion of gold and and aquous phase containing a polymeric stabilizer. The process resulted in relatively high 35% w/w particle loadings in clusters by inducing high supersaturation with rapid "micro-mixing" to kinetically control nucleation and growth[51, 52]. The polymer adsorption was sufficiently strong to passivate the surface of nucleating particles under high supersaturation conditions to produce clusters as small as 80 nm[51]. However, the resultant clusters did not exhibit a shift into the NIR. It is possible that the interactions between the polymer and the gold were too strong to achieve close-packing between the gold particles. In addition, the organic phase may have attracted too much polymer to the gold.

2.4.5 Condensation versus coagulation

Size distribution moments calculated from DLS results (Figure 2.3a) suggest that the nanoclusters were formed more by condensation than by coagulation, yet some coagulation was present (See Appendix A, Table 2.3). A high yield of 95% of gold in the cluster was observed after only 60% solvent evaporation. Here, exhaustion of primary particles slows down nanocluster growth by condensation. The substantial growth in cluster size from 60% to 100% solvent evaporation cannot be caused by the remaining 5% gold, since the mass of the clusters is proportional to the diameter cubed. Thus, coagulation was the primary cause of growth at this stage. Close inspection of the TEM images in Fig. 2.2 shows that the larger nanoclusters, formed after larger extents of evaporation (i.e. greater than 60%), are more irregular in shape relative to a spherical geometry. In fact, one may even discern that the larger clusters are partially composed of smaller, 35-60 nm, clusters, indicating a small degree of coagulation. By quenching the nanocluster dispersion with DI water soon after cluster formation, after only 60% solvent evaporation, the potential for additional coagulation was reduced, thus preserving smaller nanocluster sizes and low polydispersities.

2.4.6 Tuning cluster size with polymer/gold ratio

A reduction in the polymer/gold ratio from 16/1 to 1/1 resulted in a marked decrease in cluster size from ~80 nm to ~30 nm (Figure 2.8), as well as a reduction in polymer loading from 20 to 15%, as shown by TGA. This decrease is the opposite of what is expected for steric stabilization alone, indicating other factors were operative. For lower initial polymer/gold ratios and thus polymer concentrations, the lower

adsorption onto gold produces a smaller degree of ion pairing and thus a larger $V_{electrostatic}$. The greater repulsion will favor slower growth as observed. Furthermore, the lower polymer concentration reduces the collision frequency between polymer chains and gold clusters, leading to less trapping of polymer in the clusters. Rheological factors are also present. The viscosity of PLA-b-PEG-b-PLA solutions increases markedly with concentration in the dilute to semi-dilute transition (Figure A.4). During gold cluster formation via solvent evaporation, the viscosity of the dispersion will increase sooner for higher polymer/gold ratios, increasing the amount of entangled polymer that may get trapped within the gold clusters. This behavior was observed as the polymer/gold ratio was raised from 1/1 to 16/1, and was even more prevalent for the 40/1 polymer/gold ratio (Figure A.6). Coagulation was particularly evident at this highest ratio, according to size distribution moment calculations ($\mu1=1.55$, $\mu3=0.81$). To examine the effect of polymer gelation, a 50 mg/mL solution of PLA-b-PEG-b-PLA without gold particles was dried by solvent evaporation. The precipitate was redispersed to give large aggregates (> 500 nm) that did not break up into block copolymer micelles, indicating that gelation was not fully reversible (Figure A.8). For the formation of gold clusters, the gelation of the polymer may make the polymer less available for steric stabilization. Finally, the depletion attraction forces mediate cluster growth both during condensation and coagulation. For smaller polymer/gold ratios, the depletion attraction will decrease, which would favor smaller clusters, as observed (Figure 2.8a). As the volume of the gap region increases between particles, the depletion attraction also increases. Thus, the depletion attraction will be larger for two 20 nm, growing clusters than for two primary colloidal 5 nm gold particles. Thus depletion attraction may play a larger role in the later coagulation stage than for the initial growth of the smallest embryos.

2.4.7 Comparison to thermodynamic self assembly methods

The mechanism by which our nanoclusters are formed is fundamentally different from equilibrium-based processes, in which particles are assembled into the cores of micelles or at the interface between the core and the corona. In the case of thermodynamic self-assembly, the polymer-gold interactions are inherently stronger and play a much more dominant role, leading to higher polymer loadings and larger gold spacings.

The loadings into micelles are governed by entropic and enthalpic interactions between the solute and the micelle core, as well as the interfacial free energy between the core and corona of a micelle, $\Delta\overline{F_{int}}$ [71]. The change in free energy for mixing solute molecules and micelles is given by [71]

$$\Delta\overline{F_1} = -\Delta S_m + \Delta H_m + \Delta\overline{F_{int}} \quad (2.8)$$

where ΔS_m and ΔH_m are the change in entropy and enthalpy upon mixing, respectively. The amount of work required for expansion of the interface between the core and corona upon imbibing a solute molecule increases as the micelle size decreases, due to larger Laplace pressures. This interfacial term becomes especially significant for micelles smaller than 200 nm[71]. The loadings of small molecules such as pharmaceuticals in the cores of micelles are often less than 25% by weight[71] and typically less than 10%. The loading of a gold particle in a micelle will be even lower because ΔS_m will be less favorable, given the high molecular weight of the particle . For example, loadings of only < 2% w/w of ~2.4 nm gold particles in ~20 nm polymer micelles has been observed using small angle x-ray scattering (SAXS)[72]. Thus,

thermodynamic assembly methods are not likely to incorporate sufficient gold loadings to yield a strong red-shift in the SPR for clusters, especially for sizes smaller than 50 nm.

The kinetic nanocluster assembly method in the present study is not restricted by the thermodynamic constraints of micelle encapsulation. Clusters were formed by purposely aggregating gold nanoparticles with a weakly adsorbing polymer to control nucleation and growth by manipulation of the electrostatic, steric, and depletion interactions. The strong van der Waals interactions between the gold particles were the primary driving force for cluster growth. Furthermore, depletion effects promote exclusion of the polymer to the cluster surface. These interactions lead to much higher loadings than for thermodynamic assembly of gold particles with micelles.

2.4.8 Application to biomedical imaging and therapeutics

Gold nanoparticles with intense NIR absorbance, including nanoshells[33-35], nanorods[36, 37], and nanocages[38, 39], have received extensive attention as biomedical imaging and therapeutic agents. However, while these particles are within the optimal size range of 6-100 nm to exhibit sufficiently long blood residence times for accumulation at disease sites, they are above the threshold size of 5.5 nm required for efficient clearance by the kidneys [73-75]. Furthermore, the metallic bonds between the gold atoms in these particles do not biodegrade. In contrast, our gold nanoclusters, using PLA-b-PEG-b-PLA as the stabilizer , were shown to biodegrade nearly completely in solution and in macrophage cells back to the original 5 nm gold spheres[9]. The ability to further tune the size to 30 nm and to vary composition, as demonstrated in the current study, broadens the scope of biodegradable nanoclusters significantly.

2.5 CONCLUSIONS

A general kinetic self-assembly method has been introduced to tune the size of hybrid polymer/gold nanoclusters, as small as 30 nm, with closely-spaced gold particles along with unusually low polymer loadings. These properties are achieved by the combination of high initial gold particle volume fractions and the depletion of the weakly adsorbed polymeric stabilizer from the cluster interior. Either evaporation or mixing may be utilized to produce high initial gold particle and polymer concentrations simultaneously to manipulate growth. Here, the polymer adsorbs weakly on the gold and thereby reduces the electrostatic repulsion to nucleate cluster growth. The growth is arrested by small amounts of polymer on the exterior cluster surface, as characterized by SEM and TGA, which provide steric stabilization and minimize coagulation. The closely-spaced particles provide intense NIR absorbance even in clusters as small as 30 nm, a size which is of great interest for manipulation of biological pathways and signaling at the cellular level[76]. This kinetic assembly platform may be used to tune the size, morphology, and optical properties of a widespread variety of clusters with high metal loadings, simply by varying the particle concentration pathways to adjust the colloidal forces. Additionally, the method has been generalized for initial gold particles with varying surface charge. In contrast, higher polymer loadings along with more widely spaced metal particles are often obtained in nanoclusters formed by thermodynamic self-assembly, which requires stronger metal particle-polymer interactions. Kinetically-controlled nanocluster assembly using physical methods offers broad opportunities for the design of nanoclusters for sensors, optoelectronics and biomedical applications, including multi-modal imaging/therapeutic systems, cell-specific targeting, and biodegradable clusters for rapid clearance from the body.

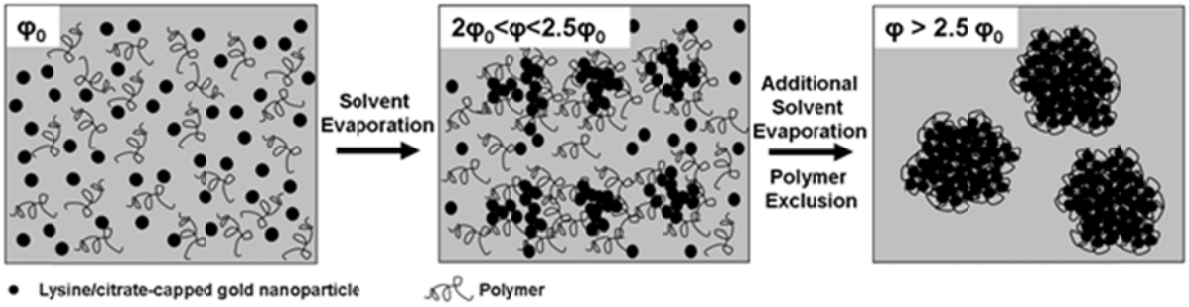

Figure 2.1 Schematic of kinetically controlled assembly process of nanocluster formation, in which primary gold nanoparticles aggregate in the presence of a weakly adsorbing polymer, PLA-*b*-PEG-*b*-PLA micelles, in a controlled manner to yield sub-100 nm clusters. Weak polymer adsorption increases counter ion binding and reduces the surface charge on the gold nanoparticles to facilitate cluster nucleation. Cluster growth is facilitated by increasing the volume fraction of particles,φ, via solvent evaporation. PEG blocks on the polymer extend into the aqueous environment and provide steric stabilization to clusters.

Table 2.1: Zeta potentials of gold primary particles and nanoclusters capped with citrate or a combination of citrate and lysine ligands.

Ligand	Zeta potential (mV)
Citrate (primary particle)	-44.0 ± 4.9
Citrate/lysine (primary particle)	-30.1 ± 2.4
PLA(1k)-*b*-PEG(10k)-*b*-PLA(1k)	-8.0 ± 0.2
Citrate/lysine 16/1 PLA-*b*-PEG-*b*-PLA /Au (nanocluster – 100% evaporation)	-16.3 ± 4.0
Citrate 16/1 PLA-*b*-PEG-*b*-PLA /Au (nanocluster – 100% evaporation)	-13.0 ± 3.3

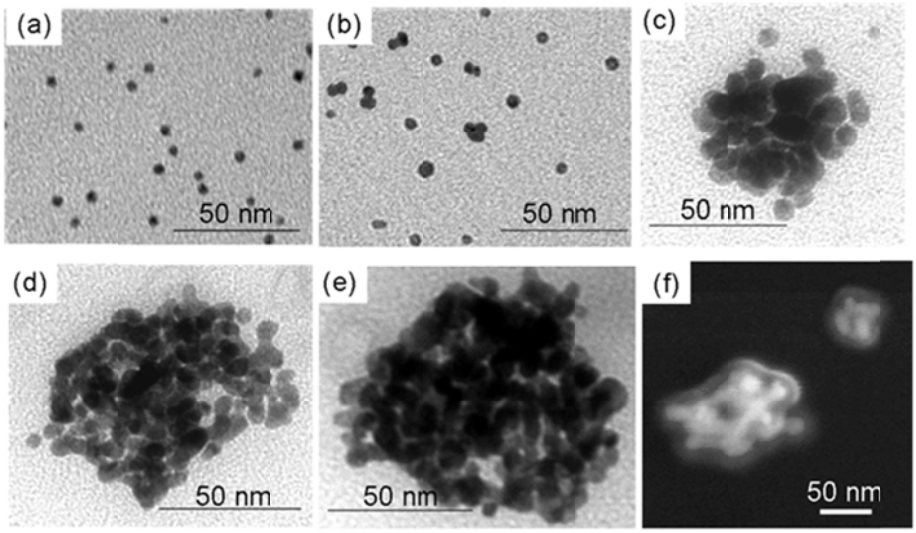

Figure 2.2: TEM images of nanoclusters produced after (a) 0%, (b) 50%, (c) 60%, (d) 80%, (e) 100% solvent evaporation. (f) SEM image of nanoclusters produced after 100% solvent evaporation. The nanoclusters were formed at an initial gold concentration of 3 mg/mL and a PLA-b-PEG-b-PLA concentration of 50 mg/mL.

Table 2.2: Calculated stability ratios for nanoclusters produced using citrate/lysine-capped nanoparticles at a 16/1 PLA-*b*-PEG-*b*-PLA /Au ratio and a starting gold concentration of 3 mg/mL.

Evaporation Extent (%)	N_0 (particles/m^3)	$t_{1/2,f}$ (s)	t_{col} (s)	$t_{1/2,s}$ (s)	W
0, no polymer	5×10^{21}	3.93×10^{-5}	2.59×10^{6}	256634	6.60×10^{9}
0, polymer	5×10^{21}	1.51×10^{-4}	3.60×10^{3}	356	3.97×10^{5}
50	1×10^{22}	1.30×10^{-4}	300	30	2.50×10^{5}

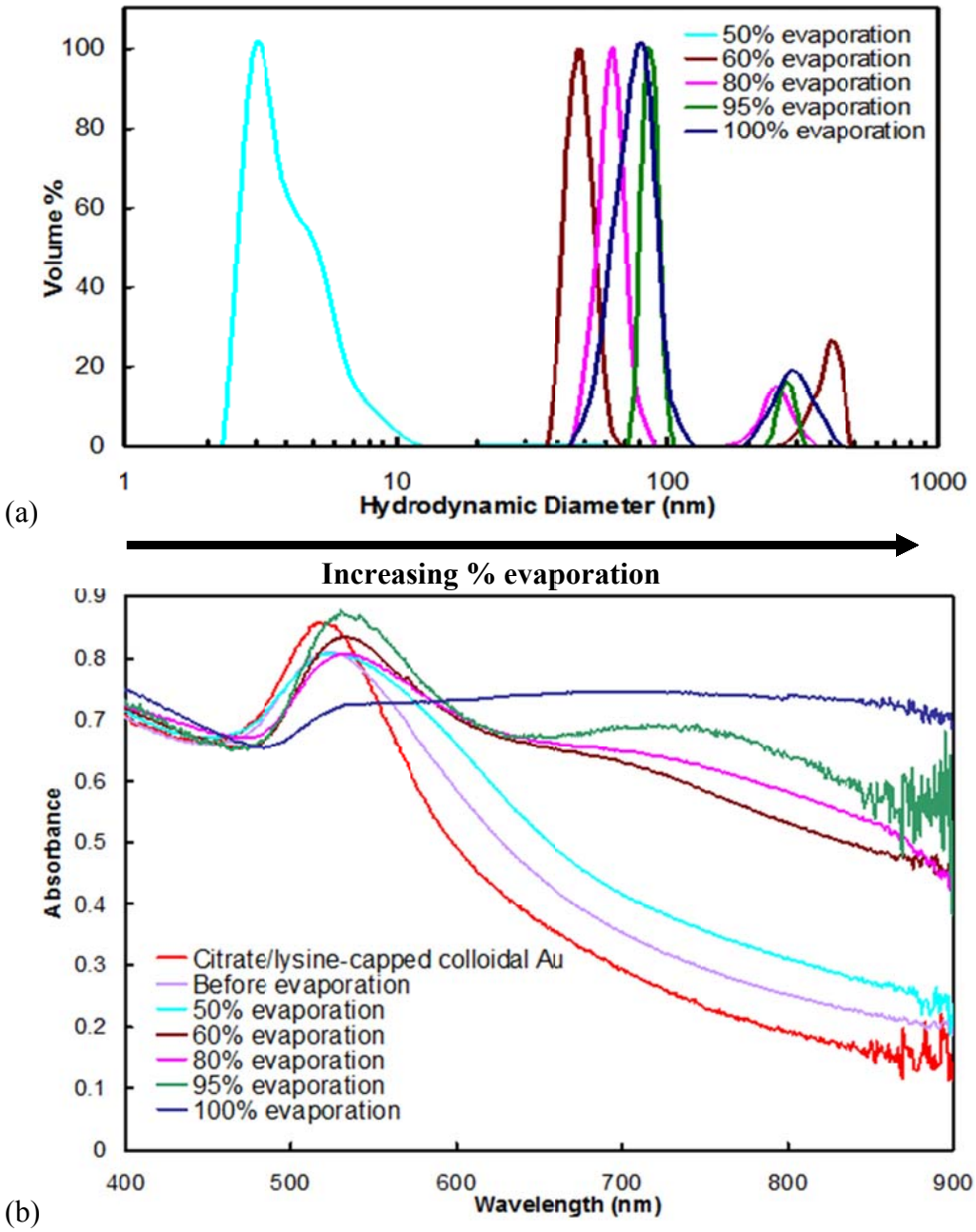

Figure 2.3: (a) Particle size measurements, by DLS, and (b) UV-vis absorbance spectra for nanoclusters composed of citrate/lysine-capped gold nanoparticles produced after different extents of evaporation. Nanoclusters were produced at a starting gold concentration of 3 mg/mL and bound together with PLA-*b*-PEG-*b*-PLA at a polymer/gold ratio of 16/1.

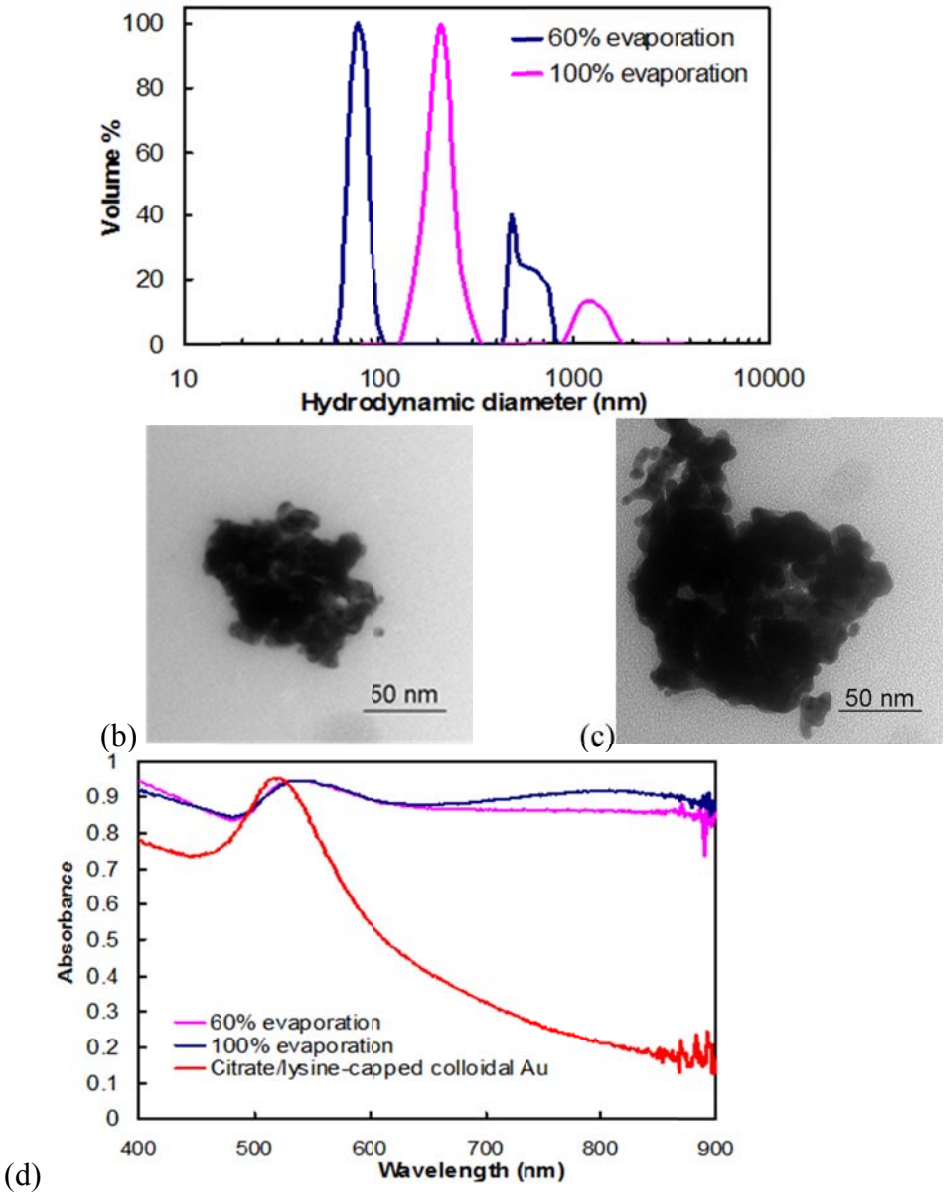

Figure 2.4: (a) Particle size measurements, by DLS, TEM images of nanoclusters after (b) 60% and (c) 100% solvent evaporation, and (d) UV-vis absorbance spectra of nanoclusters composed of citrate/lysine-capped nanoparticles assembled using PEG homopolymer (MW=3350). The starting gold and polymer concentrations were 3 mg/mL and 50 mg/mL, respectively.

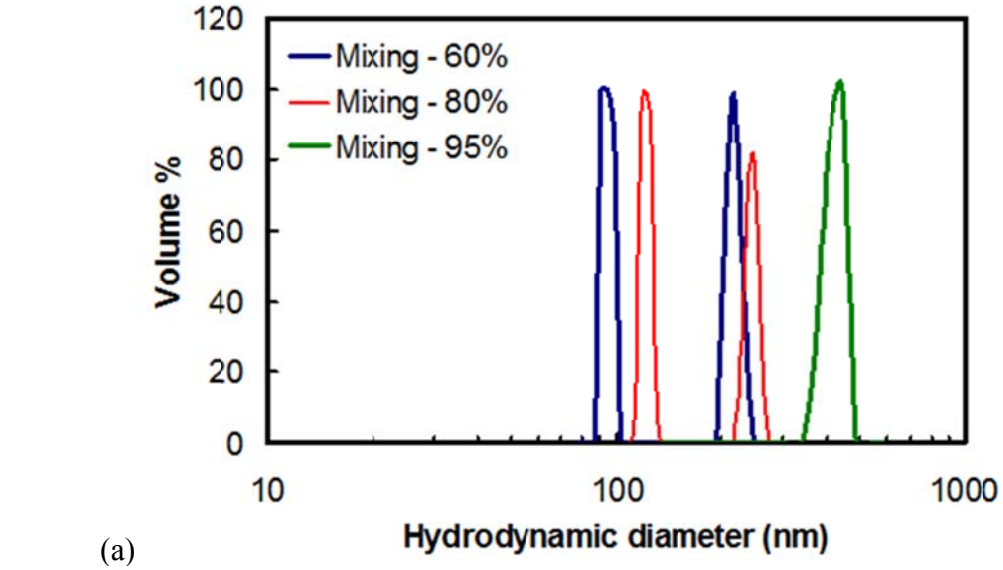

(a)

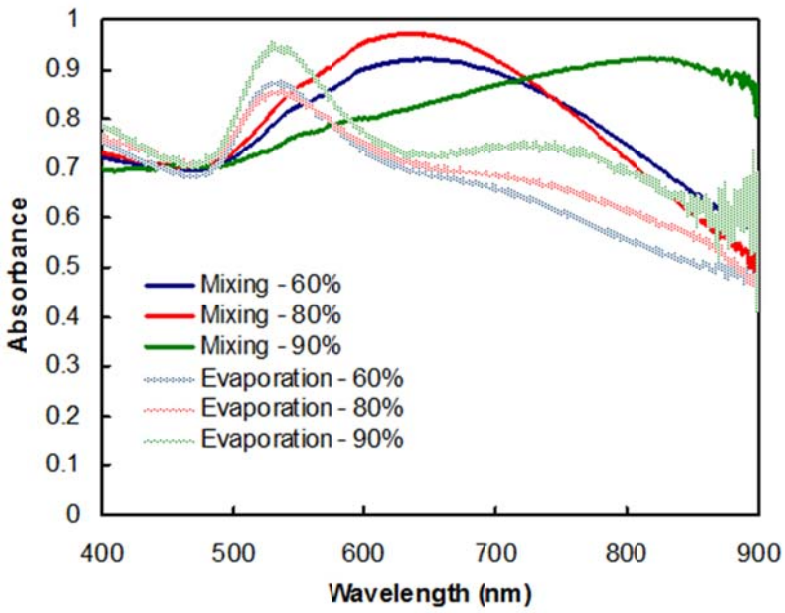

(b)

Figure 2.5: (a) Particle size distribution, as measured by DLS, and (b) UV-vis spectra of clusters of citrate/lysine-capped nanoparticles made with the mixing protocol. The conditions of cluster formation are equivalent to that for clusters formed by solvent evaporation at a starting gold concentration of 3 mg/mL and a PLA-*b*-PEG-*b*-PLA/Au ratio of 16/1. In (b), the UV-vis spectra are compared to that for nanoclusters produced using solvent evaporation.

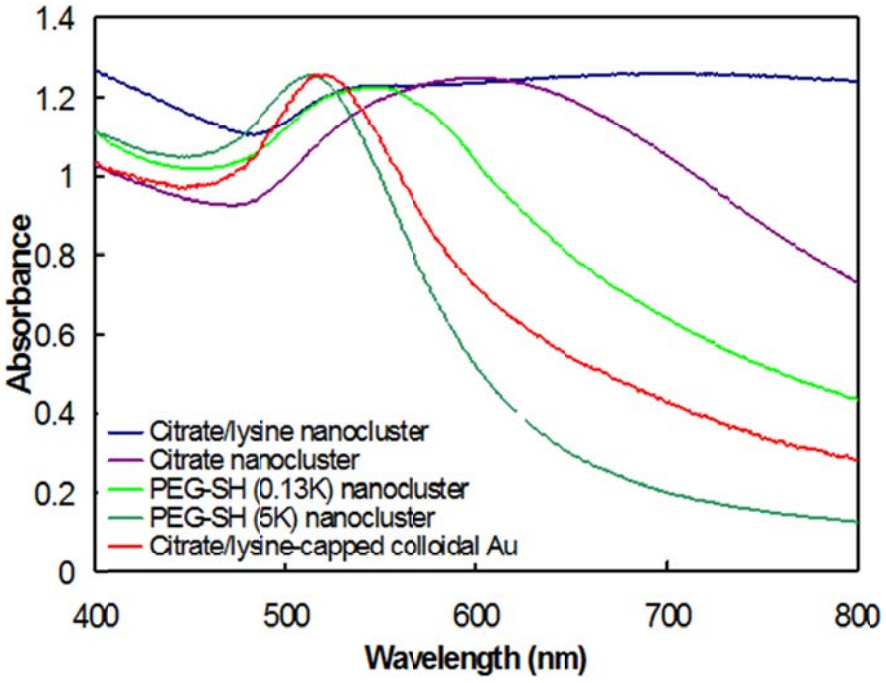

Figure 2.6: UV-vis absorbance spectra for clusters made with gold primary particles capped with different ligands. The clusters were produced using a starting gold concentration of 3 mg/mL and bound together using PLA-*b*-PEG-*b*-PLA at a 16/1 polymer/Au ratio. The clusters were formed under 100% solvent evaporation.

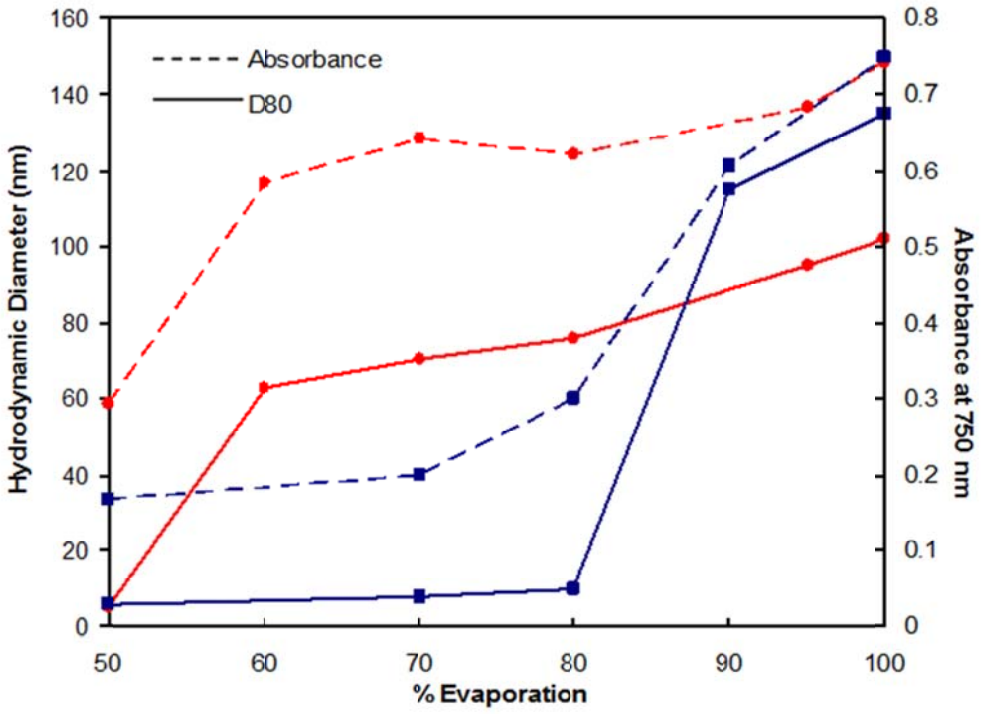

Figure 2.7: Hydrodynamic diameter (D80) and absorbance values for nanoclusters composed of primary particles capped with citrate (■) or a combination of citrate and lysine (●) ligands. The clusters were produced using a starting gold concentration of 3 mg/mL and bound together using PLA-*b*-PEG-*b*-PLA at a 16/1 polymer/Au ratio.

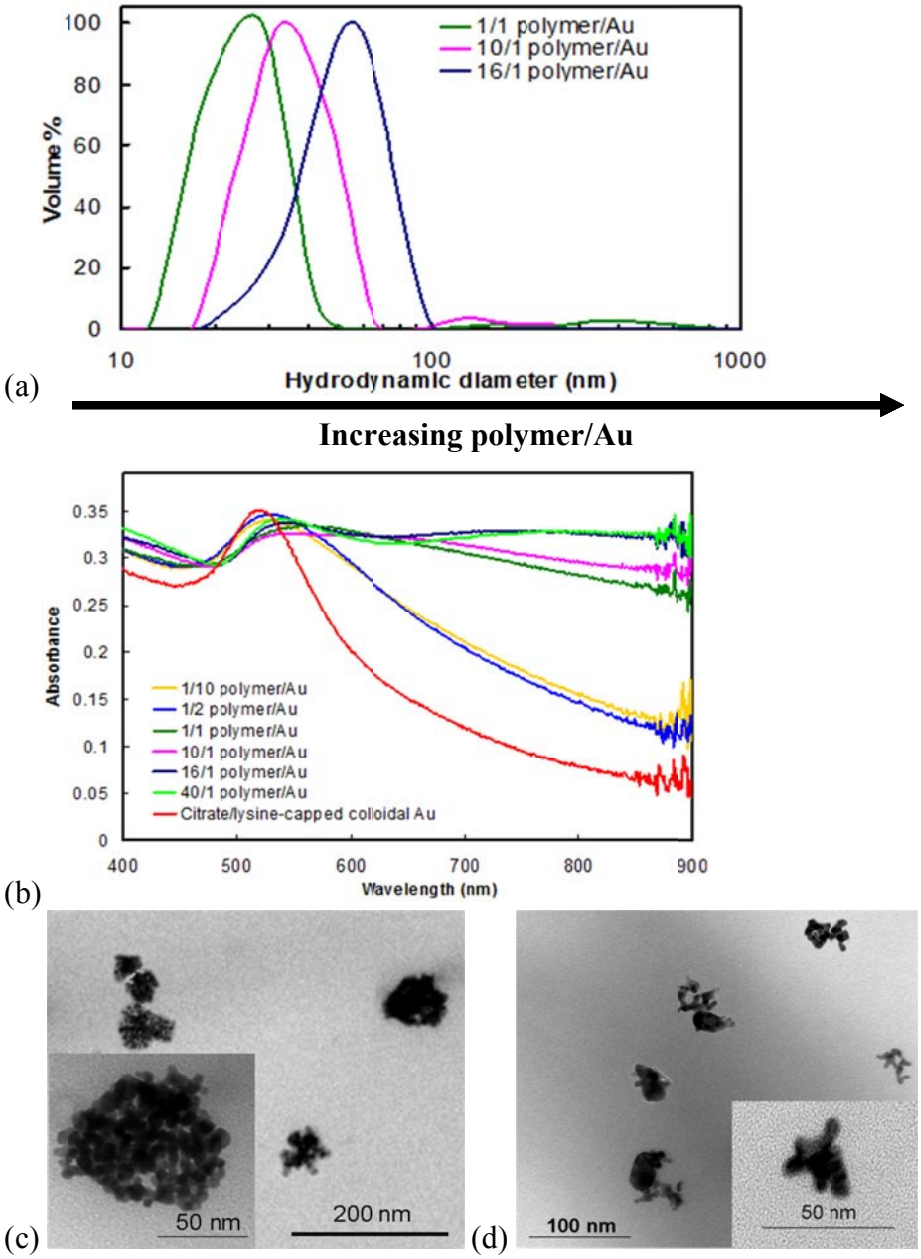

Figure 2.8: (a) Particle size distribution, as measured by DLS, and (b) UV-vis absorbance spectra of nanoclusters of citrate/lysine-capped nanoparticles produced with varying PLA-*b*-PEG-*b*-PLA/gold ratios at an initial gold concentration of 1 mg/mL and 100% solvent evaporation. TEM images of nanoclusters: (c) 16/1 polymer/gold ratio and an initial gold concentration of 3 mg/mL and (d) a 1/1 polymer/gold ratio with an initial gold concentration of 1 mg/mL after 100% solvent evaporation.

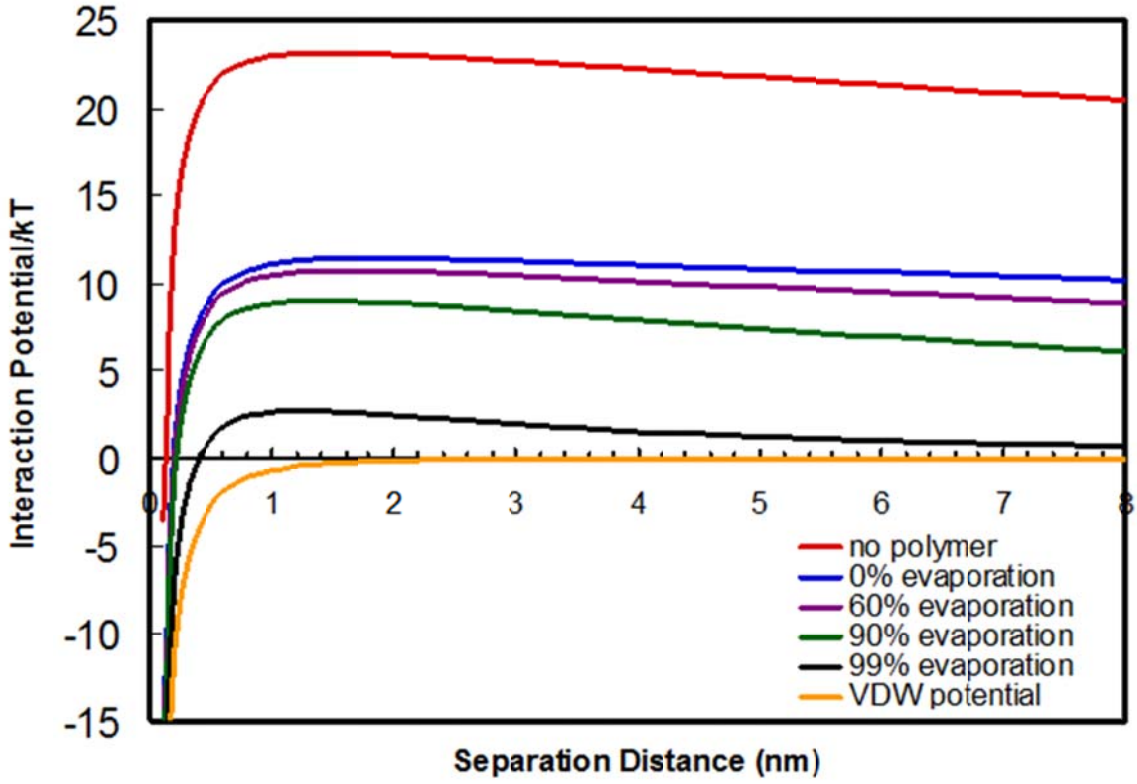

Figure 2.9: Van der Waals and total interaction potentials describing the stability of citrate/lysine- capped gold nanoparticles in the absence of PLA-*b*-PEG-*b*-PLA and after the addition of PLA-*b*-PEG-*b*-PLA. Effects of solvent evaporation on the total interaction potentials are shown.

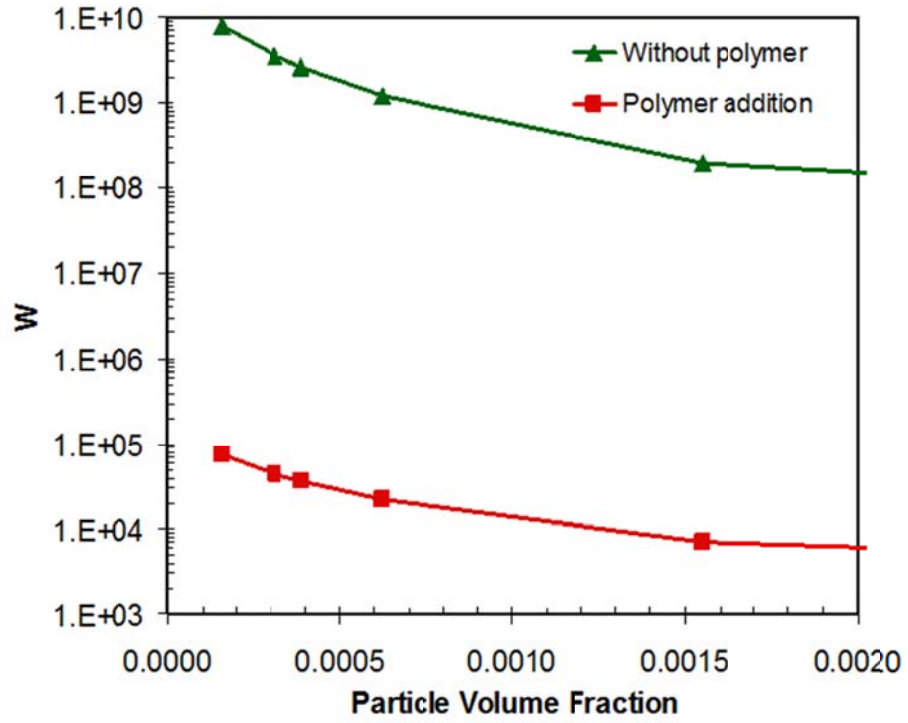

Figure 2.10: Stability ratio of a system of citrate/lysine-capped gold nanoparticles in the absence and presence of PLA-*b*-PEG-*b*-PLA determined using DLVO theory, as a function of particle volume fraction.

Table 2.3: Size distribution moments and cluster yields, as determined by FAAS, for nanoclusters produced using different extents of evaporation. The initial gold concentration was 3 mg/mL and the PLA-*b*-PEG-*b*-PLA /gold ratio was 16/1.

Sample	Cluster yield (%)	μ_1	μ_3
Citrate/lysine-capped nanoclusters 100% evaporation	99.7	1.11	0.93
Citrate/lysine-capped nanoclusters 80% evaporation	96.8	1.04	0.97
Citrate/lysine-capped nanoclusters 60% evaporation	95.1	1.09	0.93
Citrate-capped nanoclusters 100% evaporation	98.5	1.01	0.99

2.6 REFERENCES

1. DeVries, G. A.; Brunnbauer, M.; Hu, Y.; Jackson, A. M.; Long, B.; Neltner, B. T.; Uzun, O.; Wunsch, B. H.; Stellacci, F., Divalent Metal Nanoparticles. *Science* **2007**, *315*, 358-361.
2. Ofir, Y.; Samanta, B.; Rotello, V. M., Polymer and biopolymer mediated self-assembly of gold nanoparticles. *Chemical Soceity Reviews* **2008**, *37*, 1814-1825.
3. Boal, A. K.; Ilhan, F.; DeRouchey, J. E.; Thurn-Albrecht, T.; Russell, T. P.; Rotello, V. M., Self-assembly of nanoparticles into structured spherical and network aggregates. *Nature* **2000**, *404*, 746-748.
4. Ditsch, A.; Laibinis, P. E.; Wang, D. I. C.; Hatton, T. A., Controlled Clustering and Enhanced Stability of Polymer-Coated Magnetic Nanoparticles. *Langmuir* **2005**, *21*, 6006-6018.
5. Aaron, J.; Nitin, N.; Travis, K.; Kumar, S.; Collier, T.; Park, S. Y.; Jose-Yacaman, M.; Coghlan, L.; Follen, M.; Richards-Kortum, R.*, et al.*, Plasmon resonance coupling of metal nanoparticles for molecular imaging of carcinogenesis in vivo. *Journal of Biomedical Optics* **2007**, *12*, 034007/034001-034007/034011.
6. Larson, T. A.; Bankson, J.; Aaron, J.; Sokolov, K., Hybrid plasmonic magnetic nanoparticles as molecular specific agents for MRI/optical imaging and photothermal therapy of cancer cells. *Nanotechnology* **2007**, *18*, 325101/325101-325101/325108.
7. Ma, L. L.; Feldman, M. D.; Tam, J. M.; Paranjape, A. S.; Cheruku, K. K.; Larson, T. A.; Tam, J. O.; Ingram, D. R.; Paramita, V.; Villard, J. W.*, et al.*, Small multifunctional nanoclusters (Nanoroses) for targeted cellular imaging and therapy. *ACS Nano* **2009**, *3*, 2686-2696.
8. Sokolov, K. V.; Follen, M.; Aaron, J.; Pavlova, I.; Malpica, A.; Lotan, R.; Richards-Kortum, R., Real-time vital optical imaging of precancer using anti-epidermal growth factor receptor antibodies conjugated to gold nanoparticles. *Cancer Research* **2003**, *63*, 1999-2004.
9. Tam, J. M.; Tam, J. O.; Murthy, A. K.; Ingram, D. R.; Ma, L. L.; Travis, K. A.; Sokolov, K. V.; Johnston, K. P., Controlled Assembly of Biodegradable Plasmonic Nanoclusters for Near-Infrared Imaging and Therapeutic Applications. *ACS Nano* **2010**, *4*, 2178-2184.
10. Srivastava, S.; Samanta, B.; Arumugam, P.; Han, G.; Rotello, V. M., DNA-mediated assembly of iron platinum (FePt) nanoparticles. *Journal of Materials Chemistry* **2007**, *17*, 52-55.

11. Miles, W. C. G., J.D.;Huffstetler, P.P.; Reinhold, C.M.; Pothayee, N.; Caba, B.L.; Boyd, J.S.; Davis, R.M.; Riffle, J.S., Synthesis and Colloidal Properties of Polyether-Magnetite Complexes in Water and Phosphate-Buffered Saline. *Langmuir* **2009**, *25*, 803-813.

12. Iacovella, C. R.; Horsch, M. A.; Glotzer, S. C., Local ordering of polymer-tethered nanospheres and nanorods and the stabilization of the double gyroid phase. *The Journal of Chemical Physics* **2008**, *129*, 044902-044901 - 0440902-0440910.

13. Frankamp, B. L.; Uzun, O.; Ilhan, F.; Boal, A. K.; Rotello, V. M., Recognition-Mediated Assembly of Nanoparticles into Micellar Structures with Diblock Copolymers. *Journal of the American Chemical Society* **2002**, *124*, 892-893.

14. Gopidas, K. R.; Whitesell, J. K.; Fox, M. A., Nanoparticle-Cored Dendrimers: Synthesis and Characterization. *Journal of the American Chemical Society* **2003**, *125*, 6491-6502.

15. Uzun, O.; Frankamp, B. L.; Sanyal, A.; Rotello, V. M., Recognition-Mediated Assembly of Nanoparticle-Diblock Copolymer Micelles with Controlled Size. *Chemistry of Materials* **2006**, *18*, 5404-5409.

16. Sakai, T.; Alexandridis, P., Metal nanoparticle synthesis and organization in 1D, 2D and 3D structures formed by amphiphilic block copolymers. *PMSE Preprints* **2005**, *93*, 798-799.

17. Li, J.; He, W.-D.; Sun, X.-L., Preparation of poly(styrene-b-N-isopropylacrylamide) micelles surface-linked with gold nanoparticles and thermo-responsive ultraviolet-visible absorbance. *Journal of Polymer Science, Part A: Polymer Chemistry* **2007**, *45*, 5156-5163.

18. Bae, K. H.; Choi, S. H.; Park, S. Y.; Lee, Y.; Park, T. G., Thermosensitive Pluronic Micelles Stabilized by Shell Cross-Linking with Gold Nanoparticles. *Langmuir* **2006**, *22*, 6380-6384.

19. Isojima, T.; Suh, S. K.; Vander Sande, J. B.; Hatton, T. A., Controlled Assembly of Nanoparticle Structures: Spherical and Toroidal Superlattices and Nanoparticle-Coated Polymeric Beads. *Langmuir* **2009**, *25*, 8292-8298.

20. Harada, T.; Hatton, T. A., Formation of Highly Ordered Rectangular Nanoparticle Superlattices by the Cooperative Self-Assembly of Nanoparticles and Fatty Molecules. *Langmuir* **2009**, *25*, 6407-6412.

21. Isojima, T.; Lattuada, M.; Vander Sande, J. B.; Hatton, T. A., Reversible Clustering of pH- and Temperature-Responsive Janus Magnetic Nanoparticles. *ACS Nano* **2008**, *2*, 1799-1806.

22. Lattuada, M.; Hatton, T. A., Preparation and Controlled Self-Assembly of Janus Magnetic Nanoparticles. *Journal of the American Chemical Society* **2007**, *129*, 12878-12889.

23. Wilcoxon, J. P.; Martin, J. E.; Schaefer, D. W., Aggregation in colloidal gold. *Physical Review A: Atomic, Molecular, and Optical Physics* **1989**, *39*, 2675-2688.

24. Chow, M. K.; Zukoski, C. F., Gold sol formation mechanisms: role of colloidal stability. *Journal of Colloid and Interface Science* **1994**, *165*, 97-109.

25. Guo, Y.; Ma, Y.; Xu, L.; Li, J.; Yang, W., Conformational Change Induced Reversible Assembly/Disassembly of Poly-L-lysine-Functionalized Gold Nanoparticles. *Journal of Physical Chemistry C* **2007**, *111*, 9172-9176.

26. Horovitz, O.; Mocanu, A.; Tomoaia, G.; Bobos, L.; Dubert, D.; Daian, I.; Yusanis, T.; Tomoaia-Cotisel, M., Lysine mediated assembly of gold nanoparticles. *Studia Universitatis Babes-Bolyai, Chemia* **2007**, *52*, 97-108.

27. Murthy, V. S.; Cha, J. N.; Stucky, G. D.; Wong, M. S., Charge-Driven Flocculation of Poly(L-lysine)-Gold Nanoparticle Assemblies Leading to Hollow Microspheres. *Journal of the American Chemical Society* **2004**, *126*, 5292-5299.

28. Xu, L.; Guo, Y.; Xie, R.; Zhuang, J.; Yang, W.; Li, T., Three-dimensional assembly of Au nanoparticles using dipeptides. *Nanotechnology* **2002**, *13*, 725-728.

29. Lim, I. I. S.; Ip, W.; Crew, E.; Njoki, P. N.; Mott, D.; Zhong, C.-J.; Pan, Y.; Zhou, S., Homocysteine-mediated reactivity and assembly of gold nanoparticles. *Langmuir* **2007**, *23*, 826-833.

30. Aslan, K.; Luhrs, C. C.; Perez-Luna, V. H., Controlled and Reversible Aggregation of Biotinylated Gold Nanoparticles with Streptavidin. *Journal of Physical Chemistry B* **2004**, *108*, 15631-15639.

31. Lazarides, A. A.; Schatz, G. C., DNA-Linked Metal Nanosphere Materials: Structural Basis for the Optical Properties. *Journal of Physical Chemistry B* **2000**, *104*, 460-467.

32. Mirkin, C. A.; Letsinger, R. L.; Mucic, R. C.; Storhoff, J. J., A DNA-based method for rationally assembling nanoparticles into macroscopic materials. *Nature (London)* **1996**, *382*, 607-609.

33. Adler, D. C.; Huang, S.-W.; Huber, R.; Fujimoto, J. G., Photothermal detection of gold nanoparticles using phase-sensitive optical coherence tomography. *Optics Express* **2008**, *16*, 4376-4393.

34. Hirsch, L. R.; Stafford, R. J.; Bankson, J. A.; Sershen, S. R.; Rivera, B.; Price, R. E.; Hazle, J. D.; Halas, N. J.; West, J. L., Nanoshell-mediated near-infrared thermal therapy of tumors under magnetic resonance guidance. *Proceedings of the*

National Academy of Sciences of the United States of America **2003**, *100*, 13549-13554.

35. Loo, C.; Lowery, A.; Halas, N.; West, J.; Drezek, R., Immunotargeted Nanoshells for Integrated Cancer Imaging and Therapy. *Nano Letters* **2005**, *5*, 709-711.

36. Huang, X.; El-Sayed, I. H.; Qian, W.; El-Sayed, M. A., Cancer Cell Imaging and Photothermal Therapy in the Near-Infrared Region by Using Gold Nanorods. *Journal of the American Chemical Society* **2006**, *128*, 2115-2120.

37. Pissuwan, D.; Valenzuela, S. M.; Killingsworth, M. C.; Xu, X.; Cortie, M. B., Targeted destruction of murine macrophage cells with bioconjugated gold nanorods. *Journal of Nanoparticle Research* **2007**, *9*, 1109-1124.

38. Chen, J.; Saeki, F.; Wiley, B. J.; Cang, H.; Cobb, M. J.; Li, Z.-Y.; Au, L.; Zhang, H.; Kimmey, M. B.; Li, X.*, et al.*, Gold Nanocages: Bioconjugation and Their Potential Use as Optical Imaging Contrast Agents. *Nano Letters* **2005**, *5*, 473-477.

39. Skrabalak, S. E.; Chen, J.; Au, L.; Lu, X.; Li, X.; Xia, Y., Gold nanocages for biomedical applications. *Advanced Materials* **2007**, *19*, 3177-3184.

40. Kreibig, U.; Vollmer, M., *Optical Properties of Metal Clusters* Springer: Berlin, Germany, 1995 Vol. 25.

41. Kumar, S.; Harrison, N.; Richards-Kortum, R.; Sokolov, K., Plasmonic Nanosensors for Imaging Intracellular Biomarkers in Live Cells. *Nano Letters* **2007**, *7*, 1338-1343.

42. Jain, P. K.; Lee, K. S.; El-Sayed, I. H.; El-Sayed, M. A., Calculated Absorption and Scattering Properties of Gold Nanoparticles of Different Size, Shape, and Composition: Applications in Biological Imaging and Biomedicine. *Journal of Physical Chemistry B* **2006**, *110*, 7238-7248.

43. Khlebtsov, B.; Zharov, V.; Melnikov, A.; Tuchin, V.; Khlebtsov, N., Optical amplification of photothermal therapy with gold nanoparticles and nanoclusters. *Nanotechnology* **2006**, *17*, 5167-5179.

44. Troutman, T. S.; Barton, J. K.; Romanowski, M., Biodegradable plasmon resonant nanoshells. *Advanced Materials* **2008**, *20*, 2604-2608.

45. Ferrari, M., Cancer nanotechnology: opportunities and challenges. *Nature Reviews Cancer* **2005**, *5*, 161-171.

46. Zhou, Y.; Jiang, K.; Chen, Y.; Liu, S., Gold nanoparticle-incorporated core and shell crosslinked micelles fabricated from thermoresponsive block copolymer of N-isopropylacrylamide and a novel primary-amine containing monomer. *Journal of Polymer Science, Part A: Polymer Chemistry* **2008**, *46*, 6518-6531.

47. Reddy, S. T. S., M. A.; Hubbell, J. A., Targeting dendritic cells with biomaterials: developing the next generation of vaccines. *Trends in Immunology* **2006**, *27*, 573-579.

48. Wang, A. Z. B., V.; Vasilliou, C. C;Gu, F.;Alexis, F.; Zhang, L.; Shaikh, M.; Yuet, K.;Cima, M. J.; Langer, R.; Kantoff, P.W.;Bander, N.H; Jon, S.;Farokhzad, O.C., Superparamagnetic iron oxide nanopartilc-aptamer bioconjugates for combined prostate cancer imaging and therapy. *ChemMedChem* **2008**, *3*, 1311-1315.

49. Weissleder, R., Molecular Imaging in Cancer. *Science* **2006**, *312*, 1168-1171.

50. Xia, Y. In *Gold nanocages: A new class of plasmonic nanostructures for biomedical applications*, ACS National Meeting, Boston, MA, United States, August 19-23, 2007 Boston, MA, United States, 2007; pp COLL-528.

51. Gindy, M. E.; Panagiotopoulos, A. Z.; Prud'homme, R. K., Composite Block Copolymer Stabilized Nanoparticles: Simultaneous Encapsulation of Organic Actives and Inorganic Nanostructures. *Langmuir* **2008**, *24*, 83-90.

52. Gindy, M. E.; Prud'homme, R. K.; Ji, S.; Hoye, T. R.; Macosko, C. W., Functional block copolymer nanoparticles for targeted drug delivery and imaging. *PMSE Preprints* **2006**, *95*, 989-990.

53. Grabar, K. C.; Allison, K. J.; Baker, B. E.; Bright, R. M.; Brown, K. R.; Freeman, R. G.; Fox, A. P.; Keating, C. D.; Musick, M. D.; Natan, M. J., Two-dimensional arrays of colloidal gold particles: a flexible approach to macroscopic metal surfaces. *Langmuir* **1996**, *12*, 23535-22361.

54. Selvakannan, P. R.; Mandal, S.; Phadtare, S.; Pasricha, R.; Sastry, M., Capping of Gold Nanoparticles by the Amino Acid Lysine Renders Them Water-Dispersible. *Langmuir* **2003**, *19*, 3545-3549.

55. Ryoo, W., Webber, S.E., Johnston, K.P., Water-in-Carbon Dioxide Microemulsions with Methylated Branched Hydrocarbon Surfactants. *Industrial & Engineering Chemistry Research* **2003**, *42*, 6348-6358.

56. Hiemenz, P. C.; Rajagopalan, R., *Principles of Colloid and Surface Chemistry*. 3 ed.; Taylor & Francis: New York, 1997.

57. Kim, T.; Lee, C.-H.; Joo, S.-W.; Lee, K., Kinetics of gold nanoparticle aggregation: Experiments and modeling. *Journal of Colloid and Interface Science* **2008**, *318*, 238-243.

58. Friedlander, S. K., *Smoke, Dust, and Haze: Fundamentals of Aerosol Dynamics*. Oxford University Press: New York, 2000.

59. Brewer, S. H.; Glomm, W. R.; Johnson, M. C.; Knag, M. K.; Franzen, S., Probing BSA Binding to Citrate-Coated Gold Nanoparticles and Surfaces. *Langmuir* **2005**, *21*, 9303-9307.

60. Blatchford, C. G.; Campbell, J. R.; Creighton, J. A., Plasma Resonance-Enhanced Raman Scattering by Adsorbates on Gold Colloids: The Effects of Aggregation. *Surface Science* **1982**, *120*, 445-455.

61. Riley, T.; Stolnik, S.; Heald, C. R.; Xiong, C. D.; Garnett, M. C.; Illum, L.; Davis, S. S., Physicochemical Evaluation of Nanoparticles Assembled from Poly(lactic acid)-Poly(ethylene glycol) (PLA-PEG) Block Copolymers as Drug Delivery Vehicles. *Langmuir* **2001**, *17*, 3168-3174.

62. Kleshchanok, D.; Tuinier, R.; Lang, P. R., Direct measurements of polymer-induced forces. *Journal of Physics: Condensed Matter* **2008**, *20*, 073101/073101-073101/073125.

63. Mondain-Monval, O.; Leal-Calderon, F.; Phillip, J.; Bibette, J., Depletion Forces in the Presence of Electrostatic Double Layer Repulsion. *Physical Review Letters* **1995**, *75*, 3364-3367.

64. Vrij, A., Polymers at Interfaces and the Interactions in Colloidal Dispersions *Pure and Applied Chemistry* **1976**, *48*, 471-483

65. Gögelein, C.; Nägele, G.; Buitenhuis, J.; Tuinier, R.; Dhont1, J. K. G., Polymer depletion-driven cluster aggregation and initial phase separation in charged nanosized colloids. *The Journal of Chemical Physics* **2009**, *130*, 204905-204901 - 204905-204915.

66. Mutch, K. J.; Duijneveldt, J. S. v.; Eastoe, J., Colloid–polymer mixtures in the protein limit. *Soft Matter* **2007**, *3*, 155-167.

67. Mutch, K. J.; Duijneveldt, J. S. v.; Eastoe, J.; Grillo, I.; Heenan, R. K., Small-Angle Neutron Scattering Study of Microemulsion Polymer Mixtures in the Protein Limit. *Langmuir* **2008**, *24*, 3053-3060.

68. Kline, S. R.; Kaler, E. W., Aggregation of Colloidal Silica by n-Alkyl Sulfates. *Langmuir* **1996**, *12*, 2402-2407.

69. Sakai, T.; Alexandridis, P., Mechanism of Gold Metal Ion Reduction, Nanoparticle Growth and Size Control in Aqueous Amphiphilic Block Copolymer Solutions at Ambient Conditions. *Journal of Physical Chemistry B* **2005**, *109*, 7766-7777.

70. Agrawal, S. K.; Sanabria-DeLong, N.; Tew, G. N.; Bhatia, S. R., Structural Characterization of PLA-PEO-PLA Solutions and Hydrogels: Crystalline vss Amorphous PLA Domains. *Macromolecules* **2008**, *41*, 1774-1784.

71. Varun, K.; Robert, K. P. h., Thermodynamic limits on drug loading in nanoparticle cores. *Journal of Pharmaceutical Sciences* **2008**, *97*, 4904-4914.

72. Huang, C.-M.; Wei, K.-H.; Jeng, U. S.; Liang, K. S., Structural Evolution of Poly(styrene-b-4-vinylpyridine) Diblock Copolymer/Gold Nanoparticle Mixtures from Solution to Solid State. *Macromolecules* **2007**, *40*, 5067-5074.

73. Betancourt, T.; Brown, B.; Brannon-Peppas, L., Doxorubicin-loaded PLGA nanoparticles by nanoprecipitation: preparation, characterization and *in vitro* evaluation. *Nanomedicine* **2007**, *2*, 220-232.

74. Kooi, M. E. C., V. C.;Cleutjens, K. B. J. M;Kessels, A. G. H;Kitsllar, P.J.E.H. M.; Borgers, M.; Frederik, P. M.; Daemen, M.J.A.P.; Engelshoven, J.M.A. v., Accumulation of Ultrasmall Superparamagnetic Particles of Iron Oxide in Human Atherosclerotic Plaques Can Be Detected by In Vivo Magnetic Resonance Imaging. *Circulation* **2003**, *107*, 2453-2458.

75. Choi, H. S.; Liu, W.; Misra, P.; Tanaka, E.; Zimmer, J. P.; Ipe, B. I.; Bawendi, M. G.; Frangioni, J. V., Renal clearance of quantum dots. *Nature Biotechnology* **2007**, *25*, 1165-1170.

76. Jiang, W.; Kim, B. Y. S.; Rutka, J. T.; Chan, W. C. W., Nanoparticle-mediated cellular response is size-dependent. *Nature Nanotechnology* **2008**, *3*, 145-150.

Chapter 3: Charged Gold Nanoparticles with Essentially Zero Serum Protein Adsorption in Undiluted Fetal Bovine Serum[2]

The adsorption of even a single serum protein molecule on a gold nanosphere used in biomedical imaging may increase the size too much for renal clearance. Herein, we design charged ~5 nm Au nanospheres coated with binary mixed charge ligand monolayers that do not change in size upon incubation in pure fetal bovine serum (FBS). This lack of protein adsorption is unexpected given the Au surface is moderately charged. The mixed charge monolayers are comprised of anionic citrate ligands modified by place exchange with naturally-occurring amino acids: either cationic lysine or zwitterionic cysteine ligands. The zwitterionic tips of either the lysine or cysteine ligands interact weakly with the proteins and furthermore increase the distance between the "buried" charges closer to the Au surface and the interacting sites on the protein surface. The ~5 nm nanospheres were assembled into ~20 nm diameter nanoclusters with strong NIR absorbance (of interest in biomedical imaging and therapy) with a biodegradable polymer, PLA(1k)-*b*-PEG(10k)-*b*-PLA(1k). Upon biodegradation of the polymer in acidic solution, the nanoclusters dissociated into primary ~5 nm Au nanospheres, which also did not adsorb any detectable serum protein in undiluted FBS.

[2] Reproduced in large part with permission from: Murthy, A.K.; Stover, R.J.; Hardin, W.G.; Schramm, R.; Nie, G.D.; Gourisankar, S.; Truskett, T.M.; Sokolov, K.V.; Johnston, K.P., Charged Gold Nanoparticles with Essentially Zero Serum Protein Adsorption in Undiluted Fetal Bovine Serum. *Journal of the American Chemical Society* **2013**, *135,* 7799-7802. Copyright 2013 American Chemical Society.

3.1 INTRODUCTION

For Au nanoparticles of interest in biomedical imaging, the hydrodynamic diameter (D_h) must be less than ~6 nm for efficient renal clearance.[1, 2] As these nanoparticles are exposed to blood, the adsorption of even a single protein molecule on their surface, particularly the highly prevalent serum albumin (D_h = ~ 7 nm),[3, 4] may increase the size too much for clearance. The adsorption of serum proteins on flat surfaces[5-9] and curved nanoparticles[10-14] coated with nonionic, zwitterionic, or charged ligands depends in a complex manner on the ligand orientation on the surface, charge, and hydrophobicity.[15-17] Remarkably, precisely defined experiments to study renal clearance indicated that protein adsorption from 10% fetal bovine serum (FBS) was fully prevented for neutral (PEG) or zwitterionic (cysteine) ligands, but was high for charged anionic and cationic ligands such as dihydrolipoic acid (DHLA) and cysteamine, respectively.[1] In numerous other studies, serum protein adsorption has been found to be relatively low on zwitterionic and nonionic surface coatings with zero net charge.[1, 7, 11, 13, 18-21] For example, zwitterionic peptide ligands on flat Au surfaces synthesized from equal amounts of lysine (q = +1) and glutamic acid (q = -1) were shown to adsorb minimal amounts (< 0.3 ng protein/cm^2) of the model serum proteins lysozyme and fibrinogen.[8] Similar low adsorption levels of these proteins were found for flat Au surfaces tailored with binary ligands with equal amounts of positive and negative charges.[5, 6] The close spacings between the positive and negative charges on single zwitterionic ligands favor hydration and essentially zero protein adsorption on nanoparticles, as measured by dynamic light scattering (DLS).[11, 22]

For Au nanoparticles coated with charged ligands, electrostatic interactions, as well as charge-dipole interactions and specific interactions with hydrogen bond donor and acceptor sites raise adsorption, relative to nonionic and zwitterionic ligands.[1, 5, 23, 24]

However, the roles of net charge and the topology of charge on the Au and protein surfaces on adsorption are not well understood. For nanoparticles coated with highly charged citrate, DHLA, or cysteamine ligands, adsorption of serum proteins has been found to increase the D_h significantly, on the order of 10 nm.[1, 25, 26] For highly anionic citrate-capped Au nanoparticles with zeta potentials (ζ) of ~-40 mV, the D_h grew from 30 to ~80 nm upon incubation in undiluted human plasma.[25] Interestingly, very small ~3 nm highly charged Au nanospheres coated with glutathione (GSH), with two negative and one positive charge at neutral pH, were shown to clear efficiently through the kidneys.[2] While very low adsorption is typically measured with techniques such as gel electrophoresis,[27, 28] surface plasmon resonance sensing,[6, 29] and quartz crystal microbalance analysis,[30] these techniques do not have the sensitivity to measure the adsorption at the single protein molecule level, as can be done by DLS[2, 10, 11, 22] or gel filtration chromatography.[1]

Although charged monolayers on nanoparticles composed of single ligands are not thought to resist protein adsorption,[1, 25, 26, 31] relatively little is known about the behavior for binary and multicomponent mixed charge monolayers. For binary zwitterionic mixtures with equal amounts of cationic and anionic ligands, adsorption is very low.[5, 6, 8, 29] However, mixed monolayers of charged ligands, such as peptides on Au composed of lysine and glutamic acid, bind significant amounts of proteins (> 50 ng/cm^2) such as fibrinogen and lysozyme when the lysine to glutamic acid ratio deviates from unity and the surface becomes charged.[8] Verma *et al.,* however, reported that Au nanospheres with ordered "stripes" of anionic mercaptoundecanesulfonate (MUS) and nonionic octanethiol (OT) adsorbed nearly zero serum protein upon incubation in 10% serum, as shown by a negligible change in D_h via DLS, despite a highly negative ζ of ~-35 mV.[10] Here, the inhibition of protein adsorption was attributed to the close proximities

(~5 Å) of hydrophobic and hydrophilic groups on the nanosphere surface.[10, 32] However, Yang *et al.* have demonstrated that Au nanoparticles and flat Au surfaces which do not adsorb protein in 10% human blood serum may adsorb significant amounts of protein in 100% serum.[7, 11] Novel concepts are required to determine if it is possible to form charged mixed monolayers for essentially zero protein adsorption, even in undiluted serum.

Herein, we design charged ~ 5 nm Au nanospheres that adsorb essentially zero protein from undiluted fetal bovine serum, as shown by a negligible increase in the D_h by dynamic light scattering. The charged surfaces were tailored with binary ligand monolayers composed of two naturally occurring, relatively hydrophilic ligands, citrate (q = -3) and either cationic lysine (q = +1) or zwitterionic cysteine (q = 0). The Au surface charge was tuned by place exchange of the citrate ligands with each amino acid, as characterized by the zeta potential and X-ray photoelectron spectroscopy (XPS). Relatively hydrophilic ligands were used to attempt to limit hydrophobic interactions that may increase adsorption.[12, 23, 33] For pure citrate or highly charged mixed charge monolayers with high citrate levels, the D_h increased ~3 nm or more with protein adsorption. However, the change in D_h was negligible for lower citrate fractions, even for a moderate ζ of -22 mV in undiluted fetal bovine serum. The zwitterionic tips of the lysine and cysteine ligands interact weakly with the protein and, furthermore, mitigate the interactions of the "buried" charges on the anchor groups at the Au surface. Upon assembly of the Au nanospheres into ~20 nm nanoclusters of closely spaced primary particles, following an earlier methodology,[34-36] they exhibited intense NIR extinction that is of interest in biomedical applications including photoacoustic imaging.[37] Upon biodegradation of PLA(1k)-*b*-PEG(10k)-*b*-PLA(1k) on the surface of the nanoclusters,

they dissociated into the original ~5 nm constituent nanospheres, which will now be shown to totally resist adsorption of serum proteins.

3.2 EXPERIMENTAL

3.2.1 Materials

$HAuCl_4 \cdot 3H_2O$ was purchased from MP Biomedicals LLC (Solon, OH), and $Na_3C_3H_5O(COO)_3 \cdot 2H_2O$ as well as $NaBH_4$ were obtained from Fisher Scientific (Fair Lawn, NJ). L-(+)-lysine and cysteine were acquired from Acros Chemicals (Morris Plains, NJ), and PLA(1k)-*b*-PEG(10k)-*b*-PLA(1k) was purchased from Sigma-Aldrich (St. Louis, MO). Fetal bovine serum was obtained from Hyclone (Logan, UT).

3.2.2 Synthesis of Citrate-Capped Primary Au Nanospheres

Citrate-coated gold nanoparticles were synthesized by adapting a method described previously.[34] Briefly, 3 L of deionized water was heated to ~97 °C. Aqueous solutions of 1% $HAuCl_4 \cdot 3H_2O$, 1% $Na_3C_3H_5O(COO)_3 \cdot 2H_2O$, and 0.075% $NaBH_4$ in 1% $Na_3C_3H_5O(COO)_3 \cdot 2H_2O$ were prepared, and 30 mL of each solution was added successively in 1 min intervals while the solution was vigorously stirred. The gold nanoparticle solution was allowed to cool to room temperature and then was centrifuged in 250 mL centrifuge tubes at 10000 rpm for 10 min at 4 °C in order to remove ~100 ml of the 3 L solution as large particles. The remaining supernatant (~0.02 mg Au/ml) was then passed through a tangential flow filtration (TFF) device (Krosflo Research II, Spectrum Labs, Rancho Domingo, CA) using a polystyrene filter with a pore size of 10 kDa and filter surface area of 1050 cm^2 in order to remove water and excess reaction reagents. The TFF process concentrated the gold solution to a concentration of ~1

mg/ml. 15 mL centrifugal filter devices with a 30000 Da MW cutoff (Ultracel YM-30, Millipore Co., Billerica, MA) were used to additionally concentrate gold particles by centrifuging the gold solution at 6000 rpm for 5 min to remove water through the filter. The concentration of the aqueous citrate-capped gold nanoparticle dispersion was then adjusted with DI water to 3.0 ± 0.1 mg/ml Au, as measured by FAAS.

3.2.3 Place exchange with lysine and cysteine ligands

The lysine place exchange of ligands was carried out by adding freshly prepared aqueous solutions of lysine (1% or 5% w/v) to dispersions of citrate-capped Au nanospheres at ambient temperature. The initial amount of citrate coated on the Au nanospheres was ~4% w/w citrate, measured by thermogravimetric analysis (TGA), as described below. Given an Au concentration of 3 mg/ml, measured by FAAS, the citrate concentration was thus ~0.12 mg/ml. For a 4.5/1 lysine/citrate feed ratio, 50 µl of freshly prepared 1% (w/v) lysine was added to 1.2 ml of a ~3 mg/ml citrate-capped gold nanoparticle dispersion to form nanospheres. Here the addition of the basic lysine ligand increased the pH of the citrate-capped Au nanoparticle dispersion to pH ~8.3. For a lysine/citrate feed ratio of 9/1, 20 µl of 50 mg/ml (5%) aqueous lysine was added to 1.2 ml of a ~3 mg/ml citrate-capped gold nanoparticle solution. Here the pH of the dispersion increased from pH ~7 to pH ~8.8 upon adding the basic lysine ligand. Place exchange reactions were also performed with cysteine ligands using a 1% (w/v) solution of cysteine. For the 0.3/1 cysteine/citrate ratio, 1.4 µl of aqueous cysteine was added to 0.6 ml of a ~3 mg/ml citrate-capped Au nanosphere dispersion, and for the 0.7/1 cysteine/citrate feed ratio, 3.2 µl of 1% cysteine was added to 0.6 ml of the citrate-capped Au nanosphere dispersion. In each ligand exchange reaction, the mixtures were stirred for

15 min at room temperature. Immediately after reaction, aliquots of the samples were diluted in DI water to a concentration of ~0.02-0.04 mg/ml and analyzed by dynamic light scattering (DLS) and zeta potential (ζ) analysis. The undiluted mixtures not used for DLS and ζ analysis were used to form nanoclusters as described below.

3.2.4 Nanosphere Characterization

After place exchange, nanospheres were analyzed by dynamic light scattering (DLS), ζ analysis, and thermogravimetric analysis (TGA), X-ray photoelectron spectroscopy (XPS) and UV-Vis-NIR spectroscopy. DLS measurements were taken at a scattering angle of 45° using an avalanche photodiode at ~25 °C. DLS sample concentrations were adjusted such that the measured count rate was between 100 and 300 kcps. Data were analyzed using a digital autocorrelator (Brookhaven BI-9000AT) and the CONTIN method. The Stokes-Einstein equation was then used in order to obtain a volume-weighted distribution of particle hydrodynamic diameters (D_h). For lysine/citrate nanospheres, the average of 3 separate samples is reported (as shown in Tables B.4-B.7), whereas for cysteine/citrate nanospheres, the average of 2 separate samples is reported (Tables B.4-B.7). As a control experiment, DLS was conducted on pure FBS without any added Au nanospheres. The average D_h of pure FBS was 8.6 ± 5.2 nm, as shown in Figure B.3. Here, the average DLS count rate was 39 ± 6 kcps, substantially lower than the average count rate with added nanospheres (1.4 lysine citrate) of 257 ± 2 kcps. Thus, the vast majority of scattering for DLS comes from Au nanospheres, and we conclude that the DLS D_h distributions primarily reflect the sizes of Au nanospheres. As a result, we do not separately consider the different refractive indices and absorbance of the proteins and nanoparticles in the calculation of DLS volume-weighted D_h distributions.

Additionally, for 1.4 lysine/citrate and 1.6 cysteine/citrate nanospheres, the extremely small (~3% by volume) portion of the size distribution ~10 nm in size (Tables B.8 and B.9) may be attributed to the above scattering from the free protein, as this size agrees with the D_h distribution of pure FBS (Figure B.3). Due to the fact that Au nanospheres scatter 6 times more intensely than free proteins (as shown by count rate measurements), the free proteins in FBS provide only a small perturbation in the overall size distributions in the 5 to 10 nm range. The dynamic light scattering technique is particularly effective for particles smaller than 10 nm where the adsorption of a single protein molecule produces a significant change in hydrodynamic diameter. Future studies would be warranted with larger particle diameters and with other experimental techniques to determine the role of Au particle diameter and curvature.

ζ analysis was performed using a Brookhaven ZetaPALS zeta potential analyzer, and the average and standard deviations of at least three measurements were reported. For lysine/citrate nanospheres, the average for 3 separate samples is reported in Table 3.1, whereas for cysteine/citrate nanospheres, the average of 2 separate samples is reported. Nanosphere samples were ultracentrifuged for 45 min at 45000 rpm in order to remove excess citrate and lysine ligands, and the resulting pellet was dried for XPS analysis. UV-vis-NIR extinction spectra were measured with a Varian Cary 3E spectrophotometer with a path length of 1 cm.

XPS was performed with a Kratos AXIS Ultra DLD spectrometer with a monochromatic Al X-ray source (Al α, 1.4866 eV). Elemental analysis was performed on the Au 4f, C 1s, N 1s, and O 1s regions with pass energies of 30 eV, 20 eV, 40 eV, and 20 eV, respectively. A 0.1 eV step and a 4 s dwell time was used in all cases. Charge compensation was not used due to the conductivity of the samples. Peak positions and

areas were calculated using a Gaussian + Lorentzian fit and a Shirley background correction.

3.2.5 Centrifugation to Support DLS Measurements

Centrifugation of mixed monolayer nanosphere samples was performed after incubating samples in either 100% FBS or DI water. In a typical experiment, 50 ul of 3 mg/ml Au nanosphere solution was incubated in 5 ml of either pure FBS or DI water for 4 h at 37 °C. Samples were then centrifuged at 10000 rpm for 15 min in an Eppendorf 5810R centrifuge in order to form a nanosphere pellet. The mass of Au in the pellet was then determined from FAAS in order to calculate the Au mass yield of each sample.

3.2.6 Nanocluster Formation

Immediately after 15 min of lysine place exchange, clusters of nanoparticles were formed with a procedure modified from our previous work.[34-36] An aqueous 120 mg/ml solution of PLA(1k)-b-PEG(10k)-PLA(1k) was initially prepared. The 3 mg/ml lysine/citrate capped gold nanoparticle dispersion was diluted to 0.5 mg/ml with deionized water. 250 µl of the PLA(1k)-b-PEG(10k)-b-PLA(1k) solution was then added to 3 ml of the nanosphere dispersion in 5 iterations of 50 µl each over 10 min under vigorous stirring. After 10 min, this mixture was placed in a 19 x 48 mm glass vial, and the vial was placed in a 40 °C water bath and stirred using a magnetic stirrer. Using a small tube inserted into the vial, dried air was blown gently over the sample. The combination of water bath and airflow kept the sample temperature at 25 ± 3 °C, and the sample was evaporated to 50% of its original volume over ~40 min. After sample evaporation, cluster formation was terminated by adding 30 ml of DI water to the sample.

The solution was then centrifuged at 10000 rpm for 10 min in order to separate unclustered and loosely-clustered particles from the dense gold nanoclusters.

3.2.7 Nanocluster Characterization

The morphology of nanoclusters was observed by transmission electron microscopy (TEM) performed on a FEI TECNAI G2 F20 X-TWIN TEM using a high-angle annular dark-field detector. Samples were prepared by dipping 200 mesh copper-coated carbon TEM grids (Electron Microscopy Sciences) into liquid nitrogen and then pipetting 5 µl of a dilute NC dispersion onto the grid. The grid was then dried using a VirTis AdVantage tray lyophilizer (VirTis, Gardiner, NY). Unless noted, the characterization techniques were the same as for the nanospheres. The scattering angle for DLS was 90°. Flame atomic absorption spectroscopy (FAAS) (GBC Scientific Equipment Pty Ltd., GBC 908AA) was used to determined Au concentrations of primary citrate-capped nanoparticles as well as gold nanoclusters. Measurements were conducted at 242.8 nm using an air-acetylene flame on samples diluted in aqua regia to between 1 ppm and 5 ppm of gold.

3.2.8 Nanocluster Dissociation and Characterization

After nanocluster formation, nanocluster dissociation was monitored by adding ~100 µl of ~1 mg/ml nanocluster dispersion to 2 mL of pH 5 HCl to degrade the polymer. Addition of the nanocluster dispersion did not change the pH of the HCl solution from pH 5. After incubation in pH 5 HCl for 48 h, nanoclusters dissociated to primary Au nanospheres, and these dissociated nanoclusters were characterized by UV-Vis-NIR spectroscopy and DLS. For DLS, the scattering angle was 45°.

3.2.9 Protein Adsorption Studies

Mixed monolayer-capped nanospheres, as well as dissociated nanoclusters, were incubated in 100% fetal bovine serum (FBS) at a concentration of ~0.03 mg/ml Au at 37 °C in a water bath for 4 h and subsequently characterized by DLS at a scattering angle of 45°.

3.3 Results and Discussion

In order to form the binary mixed charge monolayers on the surface of ~5 nm Au nanospheres, citrate-capped nanospheres were first synthesized and place exchange reactions were conducted with either lysine or cysteine ligands (schematically depicted in Figures 3.1a and 3.1b). In order to determine the final ligand ratio on the nanosphere surface, excess ligands were removed by ultracentrifugation, and XPS was conducted on the dried nanosphere pellet, as described in detail in the supplemental section. For lysine/citrate molar feed ratios from 4.5 to 9, place exchange led to final ligand ratios of 0.5 to 1.4 according to XPS (Table 3.1, Figure B.1). The initial D_h value of 4.3 ± 0.8 nm (Table 3.1) increased only slightly for both lysine/citrate ratios after place exchange (Table 3.1, Figure 3.1c). This result is expected given the very small difference in the size of these two ligands relative to the diameter of the Au core. The increase in the amount of lysine from lysine/citrate ratios of 0.5 to 1.4 raised the ζ to -28.9 ± 3.9 mV and -16.1 ± 2.9 mV, compared with a strongly negative value of -58.4 ± 5.3 mV for pure citrate (Table 3.1). The ratios of each of these zeta potentials relative to that of citrate were 49 and 28% in good agreement of estimated ratios of 56 and 22%, respectively, from the number of charges on the ligands and known ratio from XPS. (Table B.1, see Appendix B for calculations and for reproducibilities in D_h and ζ, Tables B.4-B.7) incubation. For the place exchange of citrate with zwitterionic cysteine, smaller feed ratios were used than

for lysine, given the stronger binding of the thiol group on cysteine to Au relative to the amino group on lysine. Again the increase in D_h was negligible (Table 3.1, Figure 3.1d). The final cysteine/citrate ligand ratios, as determined by XPS, were 1.0 and 1.6 for feed ratios of 0.3 and 0.7, respectively. (Table 3.1, Figure B.1), and the ζ values were -28.8 ± 3.2 mV to -21.6 ± 1.7 mV. The corresponding zeta potential ratios of 49 and 37% relative to pure citrate-coated nanospheres were in good agreement with the calculated ratios of 49 and 39%, respectively, from the stoichiometries *via* XPS (Table B.1).

The resistance of the charged mixed monolayer nanospheres to serum protein adsorption was evaluated in 100% fetal bovine serum (FBS). Here, even adsorption of a single 7 nm BSA or 14 nm immunoglobulin G molecule,[4] would produce a substantial change in D_h. The adsorption of one BSA molecule would correspond to ~ 0.1 μg/cm^2 BSA, for a 5 nm Au nanosphere. For highly charged nanospheres with single ligands, the D_h increased significantly, by 16 nm for citrate-capped nanospheres (Table 3.1, Figure 3.1c) and 13 nm for glutathione-capped nanospheres (Figure B.2). In control experiments with DLS reported in the supporting information, it was found that scattering from FBS solutions without added Au nanospheres was weak relative to the scattering by the Au nanospheres. For incubation in 100% FBS for lysine/citrate nanospheres with the lower ratio of 0.5, the D_h increased only modestly, by 3 nm as shown in Table 3.1. With a greater lysine/citrate ratio of 1.4 and ζ of only -16.1 mV, serum protein adsorption was completely inhibited, as the change in D_h was less than 1 nm, within experimental error (Table 3.1, Figure 3.1c). Similar behavior was observed in the case of the cysteine/citrate mixed monolayers. For the lower cysteine/citrate ratio of 1.0, D_h increased only 4 nm (Table 3.1). For a larger ratio of 1.6, however, protein adsorption was completely inhibited, as the nanosphere D_h change from 3.4 ± 2.5 nm to 3.4 ± 2.7 nm was within experimental error (Table 3.1, Figure 3.1d). Remarkably, not a single protein molecule

was adsorbed, despite the substantial nanosphere surface charge ($\zeta = 21.6 \pm 1.7$ mV). If protein molecules adsorb they may produce aggregation of Au nanospheres; however, our DLS distributions did not reveal any aggregates in the 100 nm-1000 nm size range (Tables B.8 and B.9).

To support the results by DLS, nanosphere sedimentation was measured in a centrifugal field. The Au yield by mass was measured in the pellet, after centrifugation for 15 min at 10000 rpm as described in the Experimental section. For Au nanospheres in deionized water, the yield was ~ 20% (Appendix B) in each case. For the 1.6 cysteine/citrate level a similar yield of 21% was observed in FBS consistent with the lack of protein adsorption. However, for the ratio of 1.0 where the D_h increased to 8.8 nm, the yield in the pellet increased to 39% indicating the centrifugation technique was also highly sensitive to protein adsorption. A similar trend was observed for lysine/citrate nanospheres (see Appendix B). Thus, the DLS and sedimentation techniques provide complimentary evidence that the protein adsorption was neglible for the Au nanospheres coated with either cysteine/citrate or lysine/citrate ligands at the higher ratios. To our knowledge, this study presents the first examples of moderately charged gold nanospheres coated with binary mixed charge ligands that completely prevent serum protein adsorption in undiluted serum. Furthermore, both ligands are naturally found in the body.

The significant level of protein adsorption on citrate and GSH-capped nanospheres can be partially attributed to overall electrostatic interactions between negatively charged nanosphere surfaces and positively-charged proteins, as well as local charges and hydrogen bonding sites on protein surfaces. Beurer *et al.*, for example, found that protein adsorption on surfaces with a charge gradient from positively-charged aminoundecanethiol to negatively-charged mercaptoundecanoic acid was correlated with

overall electrostatic attraction.[24] Here, negatively charged BSA and fibrinogen adsorbed mostly on the cationic quaternary ammonium section and positively-charged lysozyme adsorbed mainly on the anionic carboxylates.[24] The most prevalent protein in serum, BSA, with a pI of 4.7,[24] is negatively charged at neutral pH and thus the overall electrostatic interaction with anionic Au surfaces is repulsive. However, interactions must be considered between the charged ligands and local charges and hydrogen bonding sites on the protein surface. For example, local attraction or salt bridges between cationic lysine residues on BSA and citrate ligands on Au nanospheres contribute to adsorption.[31, 38] Thus, serum protein adsorption observed on citrate and GSH-capped nanospheres may be caused by overall electrostatic interactions with positively-charged proteins, as well as local electrostatic and hydrogen bonding interactions for both positively and negatively charged proteins.

Our observation *via* DLS of essentially zero serum protein adsorption on a moderately charged binary monolayer is unexpected, relative to previous studies with single ligand monolayers[1, 31, 38, 39] as well as mixed charge monolayers with substantial net charge.[24, 29] For the 1.4 lysine/citrate monolayers, the lack of protein adsorption suggests that the lysine screens the strong interactions of the trivalent citrate with the proteins, similar to the 1.6 cysteine/citrate monolayers. The overall electrostatic interaction between the net negative charge of the binary monolayer and positively charged serum proteins is attractive. The difference in length of the citrate ligand versus either lysine or cysteine, however, may be expected to play an important role in resisting protein adsorption. For example, the zwitterionic tips of lysine or cysteine will interact weakly with protein surfaces given the lack of net charge and strong hydration, as is known for other zwitterions.[5, 6, 29] Another important factor is that each of these amino acids is considerably longer than the citrate molecule, as shown in Figures 1a and 1b. The

amino acids in the monolayers thus provide steric hindrance by increasing the distance between the three carboxylates on citrate and the protein surface. Thus, the local "buried" charges in the ligand monolayers will interact more weakly with the local charges and hydrogen bonding sites on the protein surface. In addition, delocalization of the charge with the gold electrons for the two carboxylate anions on citrate and the protonated amine on lysine will further reduce the strength of the electrostatic interactions with the proteins.

Lysine and cysteine, as well as citrate, are all highly hydrophilic unlike hydrophobic ligands that interact with hydrophobic segments of serum proteins and facilitate adsorption of serum proteins.[33] For example, the hydrophilicity value is 3.0 for lysine, relative to 0.0 for glycine and -3.4 for highly hydrophobic tryptophan in the Hopp and Woods hydrophilicity index.[40] Cysteine is more hydrophobic than lysine (hydrophilicity value of -1.0[40]) but hydrophilic enough to resist protein adsorption when combined with citrate in our mixed monolayers. In summary, the tunability of the ligand ratio and thus surface charge for each of our mixed monolayers could be utilized to tailor the surfaces to resist protein adsorption even for moderate net charge.

Various techniques have been used to form nanoclusters with controlled properties from primary particles.[41-44] The 1.4 lysine/citrate nanospheres were assembled into nanoclusters upon solvent evaporation in the presence of a weakly adsorbing polymer, PLA-*b*-PEG-*b*-PLA, following a previously reported procedure, as discussed in the supplemental section.[34-36] The nanoclusters with a D_h of 21.7 ± 4.3 nm were composed of closely-spaced primary Au nanospheres (Figure 3.2), which shifted the extinction in the near infrared region (NIR) from 650 nm to 900 nm. Upon incubating the nanoclusters in pH 5 HCl for 24 h, the PLA(1k)-*b*-PEG(10k)-*b*-PLA(1k) on the surface was hydrolyzed, and consequently the nanoclusters dissociated to Au nanospheres with

the original nanosphere size, as seen in the UV-Vis-NIR spectrum (Figure 3.2c) as well as the DLS size distribution (Figure 3.2d). The dissociated nanoclusters did not adsorb serum proteins, as the D_h remained only 4.2 ± 2.6 nm upon incubation in 100% FBS (Figure 3.2d), a desired size for kidney clearance.

In this robust colloidal assembly approach,[34-36] the size of nanoclusters may be tuned as a function of the polymer and gold concentrations, chemical structure of the surface ligands, and the extent of solvent evaporation. The biodegradable polymer adsorbs on the surface of the nanoclusters and quenches the size *via* an equilibrium mechanism.[36] In the current study, we show for the first time that these clusters may be formed from Au particles with a large enough charge for nanocluster dissociation upon biodegradation of the polymer coating, but yet the surface charge is small enough to fully resist protein adsorption.

3.4 CONCLUSIONS

In conclusion, incubation of charged ~5 nm Au nanospheres with binary natural and relatively hydrophilic ligands in undiluted serum protein does not increase the hydrodynamic diameter according to dynamic light scattering, indicating essentially zero protein adsorption. A secondary conclusion is that the Au nanospheres may be assembled into NIR-active nanoclusters which biodegrade *in vitro* to primary Au nanospheres, again with essentially zero protein adsorption.

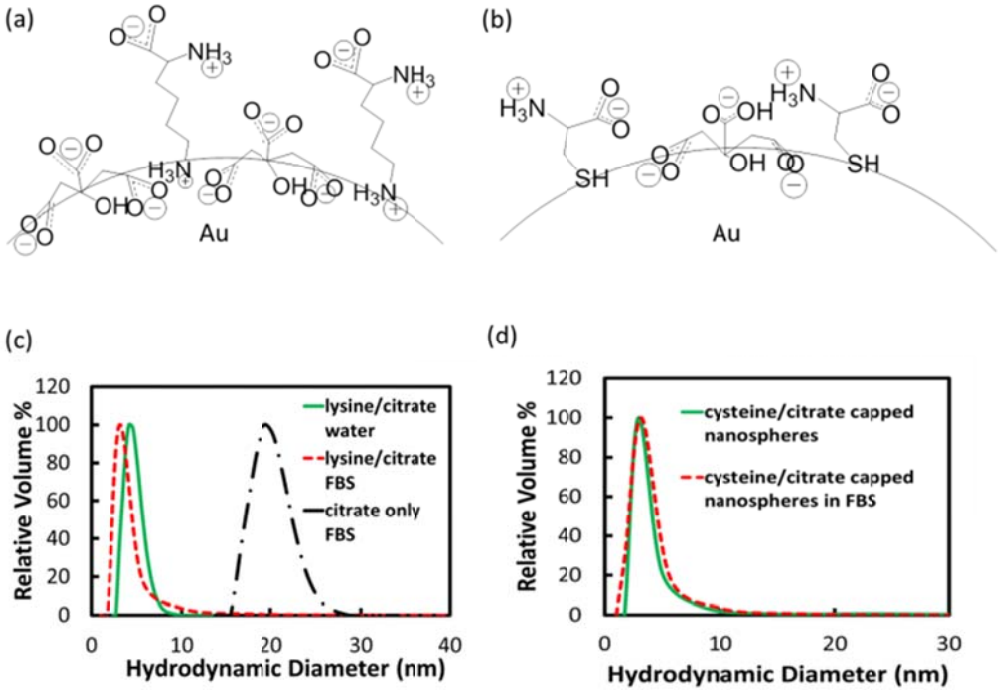

Figure 3.1: Schematics of nanosphere surfaces coated with (a) citrate and lysine, and (c) citrate and cysteine. DLS distributions in water (green curve) and FBS (red curve) for (c) 1.4 lysine/citrate nanospheres, and (d) 1.6 cysteine/citrate nanospheres. Black curve in (c) is DLS distribution of citrate only-capped nanospheres after FBS incubation.

Table 3.1: Properties of nanospheres capped with citrate or binary ligands before and after incubation in FBS.

Ligand(s)	Ligand Ratio (feed)	Ligand Ratio (XPS)	D_h (nm)	ζ (mV)	D_h in FBS (nm)
Citrate	n/a	n/a	4.3 ± 0.8	-58.4 ± 5.3	19.9 ± 2.1
Lysine/citrate	4.5	0.5	5.0 ± 1.2	-28.9 ± 3.9	7.7 ± 3.8
Lysine/citrate	9	1.4	4.6 ± 1.1	-16.1 ± 2.9	3.9 ± 2.1
Cysteine/ citrate	0.3	1.0	5.1 ± 3.9	-28.8 ± 3.2	8.8 ± 5.8
Cysteine/ citrate	0.7	1.6	3.4 ± 2.5	-21.6 ± 1.7	3.4 ± 2.7

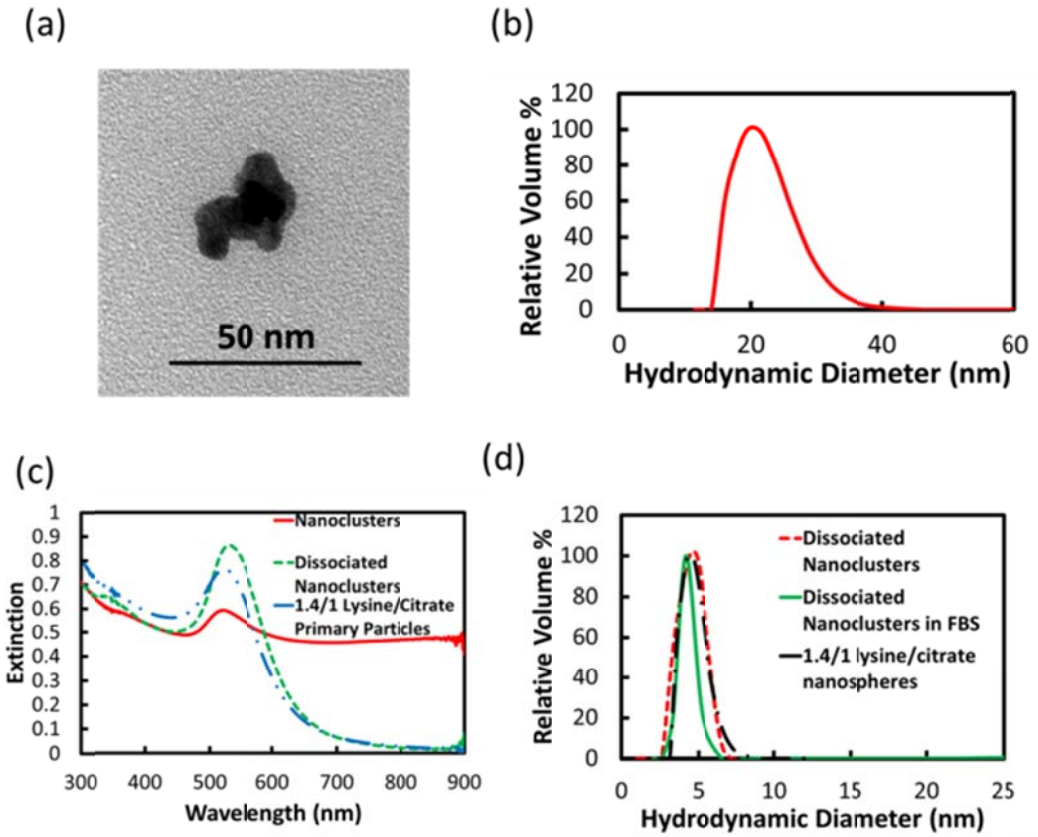

Figure 3.2: Lysine/citrate nanoclusters (a) TEM image, (b) DLS D_h distribution, and (c) UV-Vis-NIR extinction spectrum, with spectra of dissociated nanoclusters and nanospheres included, and (d) DLS D_h distributions of dissociated nanoclusters, dissociated nanoclusters in FBS, and lysine/citrate nanospheres.

3.5 REFERENCES

1. Choi, H. S.; Liu, W.; Misra, P.; Tanaka, E.; Zimmer, J. P.; Ipe, B. I.; Bawendi, M. G.; Frangioni, J. V. Renal Clearance of Quantum Dots. *Nat. Biotechnol.* **2007**, *25*, 1165-1170.
2. Zhou, C.; Long, M.; Qin, Y.; Sun, X.; Zheng, J. Luminescent Gold Nanoparticles with Efficient Renal Clearance. *Angew. Chem. Int. Ed.* **2011**, *50*, 3168-3172.
3. Tirumalai, R. S.; Chan, K. C.; Prieto, D. A.; Issaq, H. J.; Conrads, T. P.; Veenstra, T. D. Characterization of the Low Molecular Weight Human Serum Proteome. *Molecular & Cellular Proteomics* **2003**, *2*, 1096-1103.
4. Striemer, C. C.; Gaborski, T. R.; McGrath, J. L.; Fauchet, P. M. Charge- and Size-Based Separation of Macromolecules Using Ultrathin Silicon Membranes. *Nature* **2007**, *445*, 749-753.
5. Holmlin, R. E.; Chen, X.; Chapman, R. G.; Takayama, S.; Whitesides, G. M. Zwitterionic Sams That Resist Nonspecific Adsorption of Protein from Aqueous Buffer. *Langmuir* **2001**, *17*, 2841-2850.
6. Chen, S.; Yu, F.; Yu, Q.; He, Y.; Jiang, S. Strong Resistance of a Thin Crystalline Layer of Balanced Charged Groups to Protein Adsorption. *Langmuir* **2006**, *22*, 8186-8191.
7. Yang, W.; Xue, H.; Li, W.; Zhang, J.; Jiang, S. Pursuing "Zero" Protein Adsorption of Poly(Carboxybetaine) from Undiluted Blood Serum and Plasma. *Langmuir* **2009**, *25*, 11911-11916.
8. Chen, S.; Cao, Z.; Jiang, S. Ultra-Low Fouling Peptide Surfaces Derived from Natural Amino Acids. *Biomaterials* **2009**, *30*, 5893-5896.
9. Ostuni, E.; Chapman, R. G.; Holmlin, R. E.; Takayama, S.; Whitesides, G. M. A Survey of Structure-Property Relationships of Surfaces That Resist the Adsorption of Protein. *Langmuir* **2001**, *17*, 5605-5620.
10. Verma, A.; Uzun, O.; Hu, Y.; Hu, Y.; Han, H.-S.; Watson, N.; Chen, S.; Irvine, D. J.; Stellacci, F. Surface-Structure-Regulated Cell-Membrane Penetration by Monolayer-Protected Nanoparticles. *Nature Materials* **2008**, *7*, 588-595.
11. Yang, W.; Zhang, L.; Wang, S.; White, A. D.; Jiang, S. Functionalizable and Ultra Stable Nanoparticles Coated with Zwitterionic Poly(Carboxybetaine) in Undiluted Blood Serum. *Biomaterials* **2009**, *30*, 5617-5621.
12. Cedervall, T.; Lynch, I.; Lindman, S.; Berggard, T.; Thulin, E.; Nilsson, H.; Dawson, K. A.; Linse, S. Understanding the Nanoparticle-Protein Corona Using Methods to Quantify Exchange Rates and Affinities of Proteins for Nanoparticles. *Proceedings of the National Academy of Sciences* **2006**, *104*, 2050-2055.

13. Walkey, C. D.; Olsen, J. B.; Guo, H.; Emili, A.; Chan, W. C. W. Nanoparticle Size and Surface Chemistry Determine Serum Protein Adsorption and Macrophage Uptake. *Journal of the American Chemical Society* **2012**, *134*, 2139-2147.

14. Larson, T. A.; Joshi, P. P.; Sokolov, K. Preventing Protein Adsorption and Macrophage Uptake of Gold Nanoparticles Via a Hydrophobic Shield. *ACS Nano* **2012**, *6*, 9182-9190.

15. Chen, S.; Li, L.; Zhao, C.; Zheng, J. Surface Hydration: Principles and Applications toward Low-Fouling/Nonfouling Biomaterials. *Polymer* **2010**, *51*, 5283-5293.

16. Lundqvist, M.; Stigler, J.; Elia, G.; Lynch, I.; Cedervall, T.; Dawson, K. A. Nanoparticle Size and Surface Properties Determine the Protein Corona with Possible Implications for Biological Impacts. *Proceedings of the National Academy of Sciences* **2008**, *105*, 14265-14270.

17. Markarucha, A. J.; Todorova, N.; Yarovsky, I. Nanomaterials in Biological Environment: A Review of Computer Modelling Studies. *Eur. Biophys. J.* **2011**, *40*, 103-115.

18. Li, L.; Chen, S.; Zheng, J.; Ratner, B. D.; Jiang, S. Protein Adsorption on Oligo(Ethylene Glycol)-Terminated Alkanethiolate Self-Assembled Monolayers: The Molecular Basis for Nonfouling Behavior. *Journal of Physical Chemistry B* **2005**, *109*, 2934-2941.

19. Liu, W.; Choi, H. S.; Zimmer, J. P.; Tanaka, E.; Frangioni, J. V.; Bawendi, M. Compact Cysteine-Coated Cdse(Zncds) Quantum Dots for in Vivo Applications. *Journal of the American Chemical Society* **2007**, *129*, 14530-14531.

20. Ladd, J.; Zhang, Z.; Chen, S.; Hower, J. C.; Jiang, S. Zwitterionic Polymers Exhibiting High Resistance to Nonspecific Protein Adsorption from Human Serum and Plasma. *Biomacromolecules* **2008**, *9*, 1357-1361.

21. Estephan, Z. G.; Jaber, J. A.; Schlenoff, J. B. Zwitterion-Stabilized Silica Nanoparticles: Toward Nonstick Nano. *Langmuir* **2010**, *26*, 16884-16889.

22. Jia, G.; Cao, Z.; Xue, H.; Xu, Y.; Jiang, S. Novel Zwitterionic-Polymer-Coated Silica Nanoparticles. *Langmuir* **2009**, *25*, 3196-3199.

23. Mahmoudi, M.; Lynch, I.; Ejtehadi, M. R.; Monopoli, M. P.; Bombelli, F. B.; Laurent, S. Protein-Nanoparticle Interactions: Opportunities and Challenges. *Chemical Reviews* **2011**, *111*, 5610-5637.

24. Beurer, E.; Venkataraman, N. V.; Sommer, M.; Spencer, N. D. Protein and Nanoparticle Adsorption on Orthogonal, Charge-Density-Versus-Net-Charge Surface-Chemical Gradients. *Langmuir* **2012**, *28*, 3159-3166.

25. Dobrovolskaia, M. A.; Patri, A. K.; Zheng, J.; Clogston, J. D.; Ayub, N.; Aggarwal, P.; Neun, B. W.; Hall, J. B.; McNeil, S. E. Interaction of Colloidal Gold Nanoparticles with Human Blood: Effects on Particle Size and Analysis of Plasma Protein Binding Profiles. *Nanomedicine* **2009**, *5*, 106-117.

26. De Paoli Lacerda, S. H.; Park, J. J.; Meuse, C.; Pristinski, D.; Becker, M. L.; Karim, A.; Douglas, J. F. Interaction of Gold Nanoparticles with Common Human Blood Proteins. *ACS Nano* **2010**, *4*, 365-379.

27. Yu, M.; Zhou, C.; Liu, J.; Hankins, J. D.; Zheng, J. Luminescent Gold Nanoparticles with Ph-Dependent Membrane Adsorption. *Journal of the American Chemical Society* **2011**, *133*, 11014-11017.

28. Wei, H.; Insin, N.; Lee, J.; Han, H.-S.; Cordero, J. M.; Liu, W.; Bawendi, M. G. Compatct Zwitterion-Coated Iron Oxide Nanoparticles for Biological Applications. *Nano Letters* **2011**, *12*, 22-25.

29. Chen, S.; Zhen, J.; Li, L.; Jiang, S. Strong Resistance of Phosphorylcholine Self-Assembled Monolayers to Protein Adsorption: Insights into Nonfouling Properties of Zwitterionic Materials. *Journal of the American Chemical Society* **2005**, *127*, 14473-14478.

30. Kaufman, E. D.; Belyea, J.; Johnson, M. C.; Nicholson, Z. M.; Ricks, J. L.; Shah, P. K.; Bayless, M.; Pettersson, T.; Feldoto, Z.; Blomberg, E.*, et al.* Probing Protein Adsorption onto Mercaptoundecanoic Acid Stabilized Gold Nanoparticles and Surfaces by Quartz Crystal Microbalance and Z-Potential Measurements. *Langmuir* **2007**, *23*, 6053-6062.

31. Brewer, S. H.; Glomm, W. R.; Johnson, M. C.; Knag, M. K.; Franzen, S. Probing Bsa Binding to Citrate-Coated Gold Nanoparticles and Surfaces. *Langmuir* **2005**, *21*, 9303-9307.

32. Jackson, A. M.; Myerson, J. W.; Stellacci, F. Spontaneous Assembly of Subnanometre-Ordered Domains in the Ligand Shell of Monolayer-Protected Nanoparticles. *Nature Materials* **2004**, *3*, 330-336.

33. You, C.-C.; De, M.; Han, G.; Rotello, V. M. Tunable Inhibition and Denaturation of a-Chymotrypsin with Amino Acid-Functionalized Gold Nanoparticles. *Journal of the American Chemical Society* **2005**, *127*, 12873-12881.

34. Tam, J. M.; Murthy, A. K.; Ingram, D. R.; Nguyen, R.; Sokolov, K. V.; Johnston, K. P. Kinetic Assembly of near-Ir Active Gold Nanoclusters Using Weakly Adsorbing Polymers to Control the Size. *Langmuir* **2010**, *26*, 8988-8999.

35. Tam, J. M.; Tam, J. O.; Murthy, A.; Ingram, D. R.; Ma, L. L.; Travis, K.; Johnston, K. P.; Sokolov, K. V. Controlled Assembly of Biodegradable Plasmonic Nanoclusters for near-Infrared Imaging and Therapeutic Applications. *ACS Nano* **2010**, *4*, 2178-2184.

36. Murthy, A. K.; Stover, R. J.; Borwankar, A. U.; Nie, G. D.; Gourisankar, S.; Truskett, T. M.; Sokolov, K. V.; Johnston, K. P. Equilibrium Gold Nanoclusters Quenched with Biodegradable Polymers. *ACS Nano* **2013**, *7*, 239-251.

37. Yoon, S. J.; Mallidi, S.; Tam, J. M.; Tam, J. O.; Murthy, A.; Johnston, K. P.; Sokolov, K. V.; Emelianov, S. Y. Utility of Biodegradable Plasmonic Nanoclusters in Photoacoustic Imaging. *Opt. Lett.* **2010**, *35*, 3751-3753.

38. Dominguez-Medina, S.; McDonough, S.; Swanglap, P.; Landes, C. F.; Link, S. In Situ Measurement of Bovine Serum Albumin Interaction with Gold Nanospheres. *Langmuir* **2012**, *28*, 9131-9139.

39. Casals, E.; Pfaller, T.; Duschl, A.; Oostingh, G. J.; Puntes, V. Time Evolution of the Nanoparticle Protein Corona. *ACS Nano* **2010**, *4*, 3623-3632.

40. Hopp, T. P.; Woods, W. R. Prediction of Protein Antigenic Determinants from Amino Acid Sequences. *Proceedings of the National Academy of Sciences* **1981**, *78*, 3824-3828.

41. Zhuang, J.; Wu, H.; Yang, Y.; Cao, Y. C. Controlling Colloidal Superparticle Growth through Solvophobic Interactions. *Angew. Chem. Int. Ed.* **2008**, *47*, 2208-2212.

42. Ma, L. L.; Feldman, M. D.; Tam, J. M.; Paranjape, A. S.; Cheruki, K. K.; Larson, T. A.; Tam, J. O.; Ingram, D. R.; Paramita, V.; Villard, J. W.*, et al.* Small Multifunctional Nanoclusters (Nanoroses) for Targeted Cellular Imaging and Therapy. *ACS Nano* **2009**, *3*, 2686-2696.

43. Xia, Y. S.; Nguyen, T. D.; Yang, M.; Lee, B.; Santos, A.; Podsiadlo, P.; Tang, Z. Y.; Glotzer, S. C.; Kotov, N. A. Self-Assembly of Self-Limiting Monodisperse Supraparticles from Polydisperse Nanoparticles. *Nat. Nanotechnol.* **2011**, *6*, 580-587.

44. Lu, Z.; Yin, Y. Colloidal Nanoparticle Clusters: Functional Materials by Design. *Chem. Soc. Rev.* **2012**, *41*, 6874-6887.

Chapter 4: Equilibrium Gold Nanoclusters Quenched with Biodegradable Polymers[3]

Although sub-100 nm nanoclusters of metal nanoparticles are of interest in many fields including biomedical imaging, sensors and catalysis, it has been challenging to control their morphologies and chemical properties. Herein, a new concept is presented to assemble equilibrium Au nanoclusters of controlled size by tuning the colloidal interactions with a polymeric stabilizer, PLA(1k)-*b*-PEG(10k)-*b*-PLA(1k). The nanoclusters form upon mixing a dispersion of ~5 nm Au nanospheres with a polymer solution followed by partial solvent evaporation. A weakly adsorbed polymer quenches the equilibrium nanocluster size and provides steric stabilization. Nanocluster size is tuned from ~20 nm to ~40 nm by experimentally varying the final Au nanoparticle concentration and the polymer/Au ratio, along with the charge on the initial Au nanoparticle surface. Upon biodegradation of the quencher, the nanoclusters reversibly and fully dissociate to individual ~5 nm primary particles. Equilibrium cluster size is predicted semi-quantitatively with a free energy model that balances short-ranged depletion and van der Waals attractions with longer-ranged electrostatic repulsion, as a function of the Au and polymer concentrations. The close spacings of the Au nanoparticles in the clusters produce strong NIR extinction over a broad range of wavelengths from 650 to 900 nm, which is of practical interest in biomedical imaging.

[3] Reproduced in large part with permission from: Murthy, A.K.; Stover, R.J.; Borwankar, A.U.; Nie, G.D.; Gourisankar, S.; Truskett, T.M.; Sokolov, K.V.; Johnston, K.P., Equilibrium Gold Nanoclusters Quenched with Biodegradable Polymers. *ACS Nano* **2013**, *7*(1), 239-251. Copyright 2013 American Chemical Society.

4.1 INTRODUCTION

Metal nanoclusters composed of primary nanoparticles are of interest in a wide array of applications such as biomedical imaging, catalysis, sensors, and electromagnetic imaging of subsurface reservoirs.[1-6] Structure-directing agents including polymers, dendrimers, proteins, or DNA are often used to template the orientation of the primary particles within the clusters.[7, 8] Typically, the amount of inactive templating agents in the product must be 50% or more to direct the assembly. Recently, sub-100 nm nanoclusters of ~5 nm Au primary charged nanoparticles with controlled size were assembled by adding small amounts of stabilizing polymers.[4, 5] Additionally, the "self-limiting" assembly of citrate-stabilized cadmium selenide (CdSe) nanoparticles into clusters was observed upon the addition of cadmium perchlorate and sodium selenosulfate precursors in water, as characterized by computer simulation.[6] Furthermore, "kinetically trapped" clusters of controlled size comprising poly(ethylene glycol) (PEG)-stabilized Au nanoparticles have been reported by balancing van der Waals attractive forces with the steric repulsion provided by the PEG layer, which is modulated by the addition of an alkanethiol to the Au nanoparticle surface.[9]

Although aggregates of nanoparticles may be formed by kinetic assembly, the growth often produces large, uncontrolled microparticle aggregates and/or gels upon varying colloidal interactions through pH, salinity,[10] and the addition of polymers to induce depletion attraction.[11] Given the uncertainty in control of the cluster size morphology *via* kinetic assembly, it would be desirable to devise a fundamental strategy to tune cluster architecture and size by equilibrium assembly. If this equilibrium assembly were fully reversible, the clusters may dissociate all the way to monomer upon changes in the solvent conditions.

The equilibrium assembly of nanoparticles into nanoclusters has been reported in organic solvents[12, 13] and more recently in aqueous environments.[6, 14] The size of clusters of poly(methylmethacrylate) (PMMA) spheres (~4-10 μm)[12] and Boehmite rods (~350-450 nm)[13] in organic solvents with low dielectric constants is governed by a balance of strong, short-ranged attraction and weak, longer-ranged electrostatic repulsion, as described with a free energy equilibrium model.[15] In aqueous solvents, nanoclusters of primary protein nanocolloids were found to be extremely small[16] and short-lived[17] given strong electrostatic repulsion between primary particles.[15] However, for slightly charged proteins near the isoelectric point, large (~100 nm), long-lived equilibrium clusters of ~10 nm protein molecules were formed.[14] Here, crowder molecules (depletants) were added to balance short-ranged depletion attraction between the protein particles against the long ranged electrostatic repulsion and thereby tune the cluster size.[14, 15] Upon dilution, these clusters reversibly dissociated to stable protein monomers.

To date, it is unknown whether equilibrium nanoclusters may be assembled from inorganic nanoparticles in aqueous media and whether they would reversibly dissociate back to individual nanoparticles. Partially dissociable Au nanoclusters, with sizes < 100 nm in diameter, were formed by mixing Au nanoparticle dispersions with small amounts (~20%) of solid polylactic acid (PLA) and PEG copolymer, PLA(1k)-*b*-PEG(10k)-*b*-PLA(1k). The shift in the surface plasmon resonance (SPR) to the near-infrared (NIR) indicated very close spacings between the Au nanoparticles, consistent with the low polymer loadings.[4, 5] The cluster formation was attributed to kinetic assembly upon screening the electrostatic repulsion between the primary particles by the weakly adsorbed polymer. Upon biodegradation of the polymer, the clusters underwent significant, but not full dissociation into ~5.5 nm Au primary particles, according to the measured change in the SPR.

Herein, we demonstrate the assembly of Au nanoclusters with tunable equilibrium sizes from ~20 nm to ~40 nm, whereby the equilibrium state is quenched by weak adsorption of a triblock copolymer, PLA(1k)-*b*-PEG(10k)-*b*-PLA(1k) stabilizer on the nanocluster surface. Furthermore, the nanoclusters reversibly dissociate completely to ~5 nm Au nanospheres upon biodegradation of the polymeric quencher, as shown in Figure 4.1. The magnitude of the charge of the mixed ligand monolayer on the Au surfaces was designed to be small enough to enable formation of nanoclusters in the presence of the copolymer, yet sufficiently large for nanocluster dissociation upon dilution after polymer biodegradation. The polymer is shown to induce depletion attraction between the Au spheres to supplement van der Waals attraction to drive assembly of the charged Au nanoparticles into nanoclusters. The equilibrium cluster size is predicted semi-quantitatively with a free energy model that balances short-ranged attraction with long-ranged electrostatic repulsion, as a function of the experimentally measured charges on both the primary Au particles and the nanoclusters. Remarkably, the same model describes both Au and protein[14] nanoclusters. The cluster size is tuned with the Au and polymer concentrations in a new process that utilized well-controlled mixing and partial solvent evaporation, as shown in Figure 4.1. Additionally, polymer adsorption to the Au nanocluster surface quenches the nanoclusters such that their size does not change upon dilution in deionized water. The close spacings of the Au nanoparticles in the clusters produce strong NIR extinction over a broad range in wavelength from 650 nm to 900 nm. This wavelength range, where blood is weakly absorbing,[18] is of interest in biomedical imaging including photoacoustic imaging,[19-21] photothermal therapy[22, 23] and combined imaging and therapy.[24-26] Furthermore, the nanoclusters are shown to dissociate completely to 5.5 nm Au nanoparticles, which would be small enough for kidney clearance.[27]

4.2 EXPERIMENTAL

4.2.1 Materials

$HAuCl_4 \cdot 3H_2O$ was obtained from MP Biomedicals LLC (Solon, OH) and $Na_3C_3H_5O(COO)_3 \cdot 2H_2O$ was acquired from Fisher Scientific (Fair Lawn, NJ). $NaBH_4$ was also obtained from Fisher Scientific. L-(+)-lysine was purchased from Acros Chemicals (Morris Plains, NJ), and PLA(1k)-*b*-PEG(10k)-*b*-PLA(1k) was obtained from Sigma-Aldrich (St. Louis, MO).

4.2.2 Synthesis of citrate-capped Au nanospheres and lysine ligand exchange

~ 4 nm citrate-capped Au nanospheres were formed by reduction of $HAuCl_4$ with $NaBH_4$ by scaling up an earlier method and purifying synthesized particles with tangential flow filtration, as described in Appendix C.[5] The synthesis resulted in ~25 mL of 3 mg/ml Au.

Lysine place exchange was conducted by adding 20 µl of freshly prepared aqueous solution of 5% w/v (50 mg/ml) lysine to 1.2 mL of the 3 mg/ml citrate-capped Au nanosphere dispersion. Here the pH of the solution increased from pH ~6 to pH ~8.8 upon addition of the basic lysine ligand. At pH 8.8, lysine has two positive charges and one negative charge.[58] After lysine addition, the mixture was stirred for 15 min at room temperature to enable place exchange. Immediately after this reaction, nanosphere samples were either ultracentrifuged for X-ray photoelectron spectroscopy (XPS) or thermogravimetric analysis (TGA), diluted for dynamic light scattering (DLS), UV-

Visible-NIR (UV-Vis-NIR) spectroscopy, or zeta potential (ζ) analysis, or used to form nanoclusters.

4.2.3 Nanocluster Formation

Immediately after 15 min of lysine place exchange, Au nanospheres were used to form nanoclusters. An aqueous, 120 mg/ml solution of PLA(1k)-*b*-PEG(10k)-*b*-PLA(1k) was freshly prepared. In the base case, the lysine/citrate capped Au dispersion was diluted to 1 mg/ml from 3 mg/ml. 500 µl of the PLA(1k)-*b*-PEG(10k)-*b*-PLA(1k) solution was then added to 3 ml of 1 mg/ml lysine/citrate capped Au nanospheres in 5 iterations of 100 µl each over 10 min. The addition of polymer solution was done under vigorous stirring. After addition of the polymer solution, the resulting Au concentration was 0.9 mg/ml, and the polymer concentration was 17 mg/ml. This mixture was placed in a 19 x 48 mm glass vial, and the vial was placed in a 40 °C water bath and stirred using a magnetic stirrer. Dried air was blown gently over the sample *via* a small tube that was inserted a few cm into the vial. The combination of water bath and airflow kept the sample temperature at 25 ± 3 °C as the sample was evaporated to 50% of its original volume over ~40 min, resulting in final Au and polymer concentrations of 1.7 mg/ml and 36 mg/ml, respectively. These base-case samples were denoted 20-1.7 particles, designating to a polymer/Au ratio of 20/1 and a final Au concentration of 1.7 mg/ml (nomenclature adopted throughout). After sample evaporation, the cluster formation was terminated by adding 30 mL of DI water to dilute the Au. The solution was then centrifuged at 10000 rpm for 10 min in order to separate unclustered and loosely-bound particles from the ~30% (by mass) dense Au nanoclusters.

The nanocluster formation process described above was carried out at initial Au concentrations (after addition of polymer solution) from 0.5 to 2.0 mg/ml, and initial polymer concentrations of 9 mg/ml, 40 mg/ml, 8.5 mg/ml, and 42.5 mg/ml (after polymer solution addition). Evaporation, centrifugation, and redispersion were carried out in a manner identical to 20-1.7 particles.

4.2.4 Characterization of primary Au nanospheres

After lysine place exchange, samples were diluted to ~0.04 mg/ml in DI water for DLS measurements, measurement of ζ potential, and UV-Vis-NIR spectroscopy measurements, without purification. DLS measurements were taken using a custom-built apparatus at a scattering angle of 45° using an avalanche photodiode at ~ 25°C.[59] Data were analyzed using a digital autocorrelator (Brookhaven BI-9000AT) and the CONTIN method. The Stokes-Einstein equation was used to obtain a volume-weighted distribution of hydrodynamic diameters (D_H). UV-Vis-NIR spectroscopy was performed using a Varian Cary 3E spectrophotometer with a 1 cm path length. UV-Vis-NIR extinction measurements were all conducted at a Au concentration of ~90 μg/ml. Extinction values at 800 nm were used to calculate extinction coefficients (ε_{800}) for nanospheres, as described in Appendix C. ζ analysis was conducted using a Brookhaven ZetaPlus zeta potential analyzer. Samples were diluted to ~0.02-0.04 mg/ml in 1 mM KCl at pH 7, and the average and standard deviations for 30 single-cycle measurements are reported. Due to the small size of the nanospheres (see Results), the Huckel model was used to relate the measured electrophoretic mobility to a ζ potential.[60]

For TGA and XPS analysis, nanosphere samples were ultracentrifuged for 45 min at 40000 rpm in order to remove excess citrate and lysine ligands, and the resulting pellet was dried. TGA was performed using a Mettler Toledo TGA/DSC 1 STAR^e system with a gas controller (GC 200) and a temperature set at 22°C (Julabo). TGA samples were initially heated to 100 °C and held at that temperature for 10 min to eliminate any residual moisture remaining in the samples. The samples were subsequently heated to 900 °C at a heating rate of 20 °C/min, and the mass loss of organic content of the samples was determined.

XPS analysis was performed using a Kratos AXIS Ultra DLD spectrometer equipped with a monochromatic Al X-ray source (Al α, 1.4866 keV). High-resolution elemental analysis was performed on the Au 4f, C 1s, N 1s and O 1s regions with pass energies of 30 eV, 20 eV, 40 eV, and 20 eV, respectively. A 0.1 eV step and a 4 s dwell time was used in all cases. Charge compensation was not used because of the conductivity of each sample. Peak positions and areas were calculated using a Gaussian + Lorentzian fit and a Shirley background correction.

Au concentrations in nanosphere samples were determined using flame atomic absorption spectroscopy (FAAS) using a GBC FAAS analyzer (GBC Scientific Equipment Pty Ltd., GBC 908AA) with an air-acetylene flame and at a wavelength of 242.8 nm. Samples were diluted, without purification, in aqua regia to between 1 ppm and 5 ppm before analysis.

4.2.5 Nanocluster Characterization

Nanocluster morphologies were observed by transmission electron microscopy (TEM) performed on an FEI TECNAI G2 F20 X-TWIN TEM using a high-angle annular dark-field detector. Samples were prepared by dipping 200 mesh copper-coated carbon TEM grids (Electron Microscopy Sciences, Hatfield, PA) into liquid nitrogen and then pipetting 5 µl of a dilute nanocluster dispersion onto the grid. The grid was then dried using a VirTis AdVantage tray lyophilizer (VirTis, Gardiner, NY). Unless otherwise noted, DLS, UV-Vis-NIR spectroscopy, ζ analysis, and FAAS were performed identically to nanosphere characterization. DLS was conducted on a Brookhaven ZetaPALS analyzer with a scattering angle of 90°. Due to nanocluster size (see Results), the Huckel model was also used to fit measured electrophoretic mobilities in ζ analysis.[60] TGA was conducted on nanoclusters after centrifugation without the ultracentrifugation necessary for nanospheres, using a Mettler-Toledo TGA/SDTA851e instrument.

4.2.6 Nanocluster Dissociation

Dissociation of 20-4.0 and 20-1.7 particles was performed *via* dilution in pH 5 HCl. Dissociation of 20-4.0 particles was monitored by adding ~200 µl of ~1.6 mg/ml nanocluster dispersion to 2 ml of pH 5 HCl, such that the Au concentration was ~160 µg/ml. For 20-1.7 particles, ~200 µl of a ~0.4 mg/ml nanocluster dispersion was added to 2 ml of pH 5 HCl, such that the Au concentration was ~60 µg/ml. Addition of the pH 7 nanocluster dispersion did not change the mixture pH from pH 5 in either case. Nanoclusters were analyzed *via* UV-Vis-NIR spectroscopy and DLS without further

dilution at 6 h, 12 h, 24 h, and 48 h time points for 20-4.0 particles, and after 24 h for 20-1.7 particles. DLS was performed at a scattering angle of 45°, similar to the case for nanospheres.

4.3 RESULTS

4.3.1 Place Exchange of Citrate Ligands with Lysine to Design the Surface Charge

The properties of primary Au nanospheres before and after lysine ligand exchange are given in Table 4.1. The hydrodynamic diameter (DH) of nanospheres before ligand exchange was 4.3 ± 0.7 nm (Table 4.1, Table C.1a), and the extinction at 800 nm, with a Au concentration of 90 μg/ml, was 0.04. As a result, the extinction coefficient at 800 nm (ε_{800}) was 0.44 cm^2/mg. (Table 4.1, Table C.1b). The ζ potential was -58.4 ± 5.3 mV (Table 4.1). The ligand coverage was determined to be 4% w/w by thermogravimetric analysis (TGA) (Table 4.1), which is similar to the theoretical weight percent of a citrate monolayer on a 4 nm Au nanoparticle (see Appendix C). The concentration of the citrate-capped Au particle dispersion was determined to be 3.0 ± 0.1 mg Au/ml by flame atomic absorption spectroscopy (FAAS).

After place exchange, the D_H of the lysine/citrate capped Au nanoparticles was 4.7 ± 0.8 nm (Table 4.1, Figure C.1a), relatively close to the initial value, indicating that the nanospheres did not aggregate. In addition, the extinction was 0.06 at 800 nm, and the ε_{800} value was similar to that of citrate-capped nanospheres at 0.67 cm^2/mg (Table 4.1, Figure C.1b). The slight red-shift of the peak of the extinction spectra on lysine/citrate nanospheres from 512 nm to 520 nm (Figure C.1b) may be attributed to the change in

surface properties and thus local dielectric constants of the nanoparticles upon lysine displacement of citrate.[28] After place exchange, the magnitude of the ζ potential dropped significantly to -16.0 ± 6.6 mV (Table 4.1), indicating a substantial degree of replacement of negatively-charged citrate ligands with positively-charged lysine. The ligand weight percentage did not increase from 4% w/w, as may be expected given the similar molecular weights of lysine and citrate of 146 g/mol and 192 g/mol, respectively. The XPS spectrum revealed characteristics peaks at ~532 eV for O 1s, ~400 eV for N 1s, ~285 eV for C 1s, and peaks at 88 eV and 84 eV for Au 4f (Figure C.2a). The atomic ratio of nitrogen to oxygen was determined by integration of the O 1s peak (Figure C.2b) and the N 1s peak (Figure C.2c). Integration of the N 1s peak yielded a peak area of 2387, while integration of the O 1s peak yielded an area of 8574. Based on these peak integrations, the nitrogen/oxygen atomic ratio was 0.28. From this value, the lysine/citrate ratio was calculated to be 1.4 (Table 4.1), as discussed in Appendix C.

The reduction in nanosphere surface charge after ligand exchange can be correlated to the XPS results of the composition of the mixed surface layer. TGA results on citrate-capped nanospheres (Table 4.1) indicate that approximately 196 citrate ligands are present per particles (Appendix C), which corresponds to 196 × 3 = 588 negative charges. Ligand exchange with lysine replaces 3 negative charges with 1 positive charge, such that the 114 lysine ligands and 82 citrate ligands present after ligand exchange (Appendix C), which corresponds to an equivalent of (82 × 3) – (114 × 1) = 132 negative charges. Thus, the surface charge magnitude after ligand exchange would be expected to be 132/588 = 22% of the original surface charge, which is in good agreement with the zeta potential values, which dropped to 28% of its original value after lysine ligand exchange. While the actual number of negative charges on the surface cannot be directly

captured by ζ potential measurements, the amount of *relative* charge can be compared, as is done here.

4.3.2 Nanocluster Formation by Equilibrium Assembly of the Primary Au Nanoparticles

After ligand exchange, citrate/lysine capped primary nanoparticles were assembled into nanoclusters, as shown schematically in Figure 4.1. The morphologies of equilibrium nanoclusters formed *via* the pathways depicted in Figure 4.1 are shown in Figure 4.2, based on transmission electron microscopy (TEM), for the Au and polymer concentrations given in Table 4.2. Images of several 20-4.0 and 20-0.9 particles are shown in Figure C.5. These images show densely-packed primary Au nanoparticles within each nanocluster. Due to this dense Au packing and the polymer, it can be difficult to discern the boundaries of individual nanospheres. These nanoclusters were purified by centrifugation and redispersed in DI water. Centrifugation removed unclustered primary nanospheres, excess polymer and ligands, and smaller and/or less closely-packed nanoclusters, yielding a substantial population of densely-packed nanoclusters (as seen by TEM). Nanocluster yields increased with Au concentration and polymer/Au ratio, reaching 61%, as both of these factors will be shown to drive equilibrium nanocluster formation.

The effects of increasing final Au concentration on the Au nanocluster hydrodynamic diameter and optical properties are shown in Figure 4.3 and Table 4.2. In the first set of experiments, the polymer/Au ratio was fixed at 20/1. As the final Au concentration is increased from 0.9 mg/ml to 1.7 mg/ml, the nanocluster D_H increased

from 21.4 ± 4.4 nm to 29.4 ± 3.2 nm (Figure 4.3a, Table 4.2). The D_H increased to 40.1 ± 4.3 nm (Figure 4.3a, Table 4.2) as the final Au concentration was increased from 1.7 mg/ml to 4.0 mg/ml. Secondary populations of large aggregates were not observed in either volume-weighted D_H distributions or intensity-weighted D_H distributions, which are more sensitive to large aggregates (Figure C.8a). Nanocluster D_H distributions were highly reproducible, as shown for 20-0.9 and 20-4.0 particles in Figure C.10. Furthermore, analysis of TEM images of the nanoclusters (at least 20 clusters in several images analyzed) indicated reasonable agreement between the measured D_H and the nanocluster size measured with TEM (Table 4.2). For TEM analysis, it is somewhat challenging to discern the boundaries between individual nanoclusters at high surface coverages in the images, relative to simpler geometries such as spheres or rods.[4, 5] Thus, we intentionally used low surface coverage on the grids, and acquired multiple images of nanoclusters to conduct a sizing analysis. Histograms which present a detailed analysis of the TEM images for 20-0.9, 20-1.7, and 20-4.0 particles are shown in Figure C.6. An increase in the final Au concentration from 0.9 mg/ml to 1.7 mg/ml also increased the extinction at 800 nm from 0.95 to 1.05, thus increasing the extinction coefficient ε_{800} from 10.6 cm^2/mg to 11.7 cm^2/mg (Figure 4.3b, Table 4.2). Further increase of the final Au concentration from 1.7 mg/ml to 4.0 mg/ml increased the nanocluster extinction at 800 nm and ε_{800} to 1.16 and 12.9 cm^2/mg (Figure 4.3b, Table 4.2), respectively. The nanocluster ζ potential increased in magnitude slightly from -12.3 ± 1.1 mV for 20-0.9 particles to -16.4 ± 3.6 mV for 20-1.7 particles (Table 4.2). For 20-4.0 particles, the nanocluster ζ potential decreased very slightly in magnitude to -13.2 ± 0.6 mV (Table 4.2).

For a final Au concentration of 1.7 mg/ml, the morphologies from TEM with increasing polymer/Au concentration, for samples 10-1.7, 20-1.7, and 50-1.7 particles are

shown in Figure 4.4. In each case, densely packed Au nanoclusters are observed. The Au yields for 10-1.7, 20-1.7, and 50-1.7 particles were 26 ± 13%, 31 ± 12%, and 57 ± 18% by mass of Au, respectively, indicating that the increase in polymer concentration facilitated nanocluster formation.

The effect of polymer/Au ratio on nanocluster size and extinction are shown in Figure 4.5 and Table 4.2. As the polymer/Au ratio is increased from 10/1 to 20/1, the nanocluster D_H increases modestly from 24.0 ± 5.6 nm to 29.4 ± 3.2 nm (Figure 4.5a, Table 4.2), and increasing the polymer/Au ratio further to 50/1 increased the D_H to 38.4 ± 7.3 nm (Figure 4.5a, Table 4.2). Size analysis of TEM images of 10-1.7 and 50-1.7 particles (at least 20 particles in several images analyzed) revealed agreement between D_H distributions measured by dynamic light scattering (DLS) and the size measured by TEM analysis (Table 4.2). TEM histograms for 10-1.7 and 50-1.7 particles are shown in Figure C.7. NIR extinction increased with nanocluster D_H, as the extinction at 800 nm increased slightly from 1.01 to 1.05 as polymer/Au ratio was increased from 10/1 to 20/1 (Figure 4.5b). As a result, the ε_{800} increased from 11.2 cm^2/mg to 11.7 cm^2/mg (Figure 4.5b, Table 4.2). A further increase in polymer/Au ratio to 50/1 increased the extinction at 800 nm to 1.17 (Figure 4.5b) and increased ε_{800} to 13.0 cm^2/mg (Figure 4.5b, Table 4.2). The nanocluster ζ potential did not change significantly as the polymer/Au ratio was increased from 10/1 to 20/1, while the ζ potential decreased slightly in magnitude to -12.5 ± 1.2 mV for a polymer/Au ratio of 50/1 (Table 4.2). Large aggregates were not observed in any of these nanocluster samples, even in intensity-weighted D_H distributions (Figure C.8). TGA was conducted on 20-0.9, 20-1.7, and 20-4.0 particles. The organic content in the nanoclusters remained fairly constant (Table C.1) for 20-0.9 and 20-1.7 particles, but a decrease in organic content from 50% w/w to 31.8% w/w was observed as the nanocluster size increased.

In order to provide further evidence for equilibrium formation of nanoclusters, a control experiment was performed, in which 20-0.9 particles were synthesized with solvent evaporation over approximately 4.5 h, in contrast to only ~40 min for particles shown in Figures 3-4. Here, the extinction spectrum and D_H did not change with evaporation rate (Table C.9), supporting the concept of equilibrium rather than kinetically-controlled assembly.

4.3.3 Nanocluster Dissociation

Dissociation of 20-4.0 particles was monitored over 48 h in pH 5 HCl by DLS and UV-Vis-NIR spectroscopy. As the incubation time increased from 6 h to 48 h, the D_H decreased monotonically from 40.1 ± 4.3 nm to 5.0 ± 4.3 nm (Figure 4.6a, Table 4.3), and the extinction at 800 nm (for a Au concentration of 160 μg/ml) decreased from 1.85 to 1.00. As a result, ε_{800} decreased from 12.9 cm^2/mg to 6.3 cm^2/mg (Figure 4.6b, Table 4.3). After 48 h in pH 5 HCl, 20-4.0 nanoclusters dissociated nearly completely to monomer. The high standard deviation of the D_H distribution of dissociated nanoclusters indicates very small oligomers are still present, which is supported by the small (~3% by volume) peak in the size distribution centered around 20 nm as well as the difference between the dissociated nanocluster ε_{800} and the primary particle ε_{800} value of 0.67 cm^2/mg (Table 4.1). These differences are attributed to dimers, trimers, and undissociated nanoclusters that might still be present in solution and which contribute to the NIR extinction and scattering for DLS.[4] The variation of the natural logarithm of the number of particles per nanocluster *versus* time is shown in Figure 4.6c. The number of particles in a cluster n_c is determined by Equation C.6. The plot is quite linear with an R^2 value of ~0.98 (Figure 4.6c) indicating approximately first-order kinetics. The dissociation of 20-

4.0 particles was also highly reproducible for two separate samples, as shown in the kinetics plots in Figure C.11. TEM analysis of dissociated 20-4.0 particles after 48 h incubation in pH 5 HCl showed similar results as those given by DLS, as the image showed small primary ~5 nm Au nanospheres (Figure C.12a).

The nanocluster dissociation was further investigated by also placing 20-1.7 particles into pH 5 HCl. Interestingly, after only 24 h of exposure to HCl, the D_H of 20-1.7 particles decreased all the way from 30.0 ± 3.3 nm to 4.0 ± 3.1 nm (Figure 4.7a), and the extinction at 800 nm (for an Au concentration of 60 ug/ml) dropped from 0.71 to 0.06 (Figure 4.7b). As a result, the ε_{800} dropped from 11.8 cm^2/mg to 1.0 cm^2/mg, which is reasonably close to the primary particle ε_{800} value of 0.67 cm^2/mg (Table 4.1). Here, only 0.4% of the particles by volume show a D_H above 5.5 nm, thus leading to the lower standard deviation in the DLS distribution as well as the lower ε_{800} relative to dissociated 20-4.0 particles. TEM analysis of dissociated 20-1.7 particles after 24 h in pH 5 HCl showed ~5 nm primary Au nanospheres, as shown in Figure C.12b.

4.4 DISCUSSION

4.4.1 Equilibrium Cluster Size Model

The equilibrium formation of nanoclusters of primary nanoparticles may be shown to be governed by a balance of short-ranged attractive forces with longer-ranged electrostatic repulsion[29, 30] as described with a free energy model.[12, 14-16, 31] An equilibrium nanocluster with a diameter D_c is depicted in Figure 4.8, along with primary nanoparticles with charge of magnitude q. A fraction of the counter-ions within the

nanocluster dissociate and leave the cluster. As the total nanocluster charge grows with added monomer, eventually, the cluster reaches an equilibrium size when the electric field from the nanocluster repels addition of further monomer. Here, short-ranged attractive forces between individual nanoparticle monomers which favor cluster growth are mediated by longer-ranged electrostatic repulsion at the monomer-cluster levels.

The free energy model describes the assembly of nc primary particles into a cluster of radius R_c. [14, 15] Here, the magnitude of attractive interaction between two primary particles with C nearest neighbors is represented by a. The surface energy of the cluster is $4\pi R_c^2\gamma$, where the surface tension γ is approximated as $a/4\pi R^2$, where R is the radius of the primary particle. The attractive component of the free energy is then

$$F_A = -\frac{aCn_c}{2} + a\left(\frac{R_c}{R}\right)^2 \qquad (4.1)$$

The repulsive component to cluster free energy is approximated by the expression for a uniform distribution of point charges within a sphere

$$F_R = \frac{3\lambda_b k_B T n_c^2 q^2}{5R_c} \qquad (4.2)$$

where λ_b is the Bjerrum length

$$\lambda_b = \frac{e^2}{4\pi\epsilon_r\epsilon_0 k_B T} \qquad (4.3)$$

Here, e is the elementary unit of charge, ϵr is the dielectric constant within the nanocluster, and ϵ_0 is the relative permittivity of free space.

The minimization of the free energy with respect to the cluster radius R_c yields the following expression for equilibrium cluster size:

$$n^* = \frac{5aR}{6\lambda_b k_B T q^2} \qquad (4.4)$$

where n* is the equilibrium number of monomers per cluster. From Equation 4.4, the cluster size increases with the magnitude of attraction a between primary particles and decreases with the magnitude of charge q. More recently, this theory was extended to include the effect of the fractal dimension of the cluster, and was shown to capture the

trends in the size of protein nanoclusters, by fitting ϵ_r and the number of dissociable ion sites per primary particle, σ_s (Appendix C), as adjustable parameters.[14]

The experimentally observed correlation between polymer concentration and nanocluster size led us to postulate that polymer-induced depletion attraction plays an important role in nanocluster formation. Upon addition of the weakly adsorbing triblock copolymer, an osmotic pressure gradient is produced from the exclusion of the polymer from the gap between Au particles. This pressure gradient creates an attractive force ("depletion attraction") between the Au nanoparticles. Depletion interactions, which have been carefully characterized in other related systems (see, e.g., Edwards and Bevan,[32] Piech and Walz,[33] and Kulkarni et al.[34]), are strongly dependent on polymer concentration and the distance between Au particles.[35] We estimate the depletion potential using the Asakura-Oosawa potential,[36, 37] which can be written as:[35]

$$\frac{V_{dep}}{kT} = -\left(\frac{R_g}{R}\right)^{-3}\left(\frac{c_p}{c^*}\right)\left(\frac{R_g}{R}-\frac{H}{2R}\right)^2\left(\frac{3}{2}+\frac{R_g}{R}+\frac{H}{4R}\right) \qquad (3.5)$$

where R_g is the radius of gyration of the polymer depletant, c_p is the polymer concentration, and c* is the overlap concentration where polymer chains begin to overlap, which is defined as:[35]

$$c^* = \frac{3M}{4\pi R_g^3 N_{av}} \qquad (3.6)$$

where M is the molecular weight of the polymer, and N_{av} is Avogadro's number. Here, we assume that the polymer micelles may be approximated by a PEG chain with a hydrodynamic radius (R_h) equivalent to the radius of the micelle, which was measured to be 7 nm.[5] This assumption is reasonable since the triblock copolymer is mostly composed

of PEG. The calculation of the molecular weight of the micelle from the hydrodynamic diameter is given in Appendix C.

4.4.2 Equilibrium Assembly of Au Nanoclusters

The assembly of ~5 nm Au nanoparticles into nanoclusters will now be described in terms of the colloidal forces shown schematically to Figure 4.8. The magnitude of the charge on primary particles was initially reduced by replacing some of the citrate ligands (charge of -3) with cationic lysine ligands (charge of +1) to create a mixed charge monolayer.[38] The resulting reduction in the zeta potential magnitude from -58 mV to -16 mV will be shown to favor nanocluster formation below.

Equilibrium nanocluster diameters (D_c) predicted by the free energy model are shown to increase over a selected range of 20 to 40 nm with increasing c_{Au} and/or c_p in Figure 4.9.[14, 15] The theoretical model, despite its simplicity, semi-quantitatively predicts the experimental data. The parameters in the model, shown in Table C.2, are discussed in detail in the Appendix C. The total number of charges on the primary nanoparticles in water, 2.78, was determined from zeta potential measurements on lysine/citrate capped primary particles (Table 4.1) using Equation C.6. The charge on a Au nanoparticle within the nanoclusters q was determined by calculating the total number of charges per nanocluster from the measured zeta potentials using Equation C.6, as shown in Appendix C and the number of nanoparticles in a cluster from Equation C.7. We chose a local dielectric constant in the dense nanoclusters of 25, approximately capturing the expected loss with respect to bulk water, as described further in Appendix C. This value is the only adjustable parameter in the model. The interparticle distance in the model was assumed to

be 1 nm, which is reasonable because of the high NIR extinction and dense morphologies observed within the nanoclusters. Additionally, the equilibrium model is not very sensitive to interparticle distance, as further discussed in Appendix C.

The rate of depletion-attraction-induced cluster assembly is assumed to be much faster than the rate of polymer adsorption on Au. This is a reasonable assumption given the very low affinity of the dominant PEG block for Au. While depletion attraction is the first effect of the polymer during nanocluster formation, the slower polymer adsorption quenches the final nanocluster size. Thus, we treat the nanocluster formation process, prior to polymer adsorption, as a pseudo-equilibrium process.

As the polymer concentration c_p increases, depletion attraction raises the overall attraction a in Eq. 4.4, consequently increasing the nanocluster size. This trend is shown in Table 4.2 and Figure 4.9 for a final Au concentration of 1.7 mg/ml. Note that the theory mildly underpredicts D_H for the highest polymer concentration (50-1.7). As the number of monomers in the cluster increases, the charge per cluster determined from the zeta potential increases. This experimental charge in the nanocluster, relative to the total charge expected based on the initial charge on each primary particle, was only 11.0% for the 10-1.7 cluster, indicating significant ion pairing. Furthermore, this ratio decreased monotonically from 11.0% to 4.3% (Table 4.4) as the cluster size increased with c_p. Additionally, an increase in final c_{Au} leads to a decrease in the charge per particle q, since fewer counterions are required to dissociate per volume to provide the same entropic gain, as shown in Equation C.11. As the charge decreases, the equilibrium nanocluster size increases, according to Equation 4.4. Thus, as the final c_{Au} is increased, D_c increases.

The combined effect of increased depletion attraction and reduction in charge is seen experimentally through the variance in final Au concentration while maintaining a constant polymer/Au ratio. As c_{Au} is increased from 0.9 mg/ml (20-0.9 particles) to 4.0 mg/ml (20-4.0 particles), the enhanced depletion attraction as well as the reduced Coulombic repulsion increase the D_c of the cluster. The decrease in q is shown in Table 4.4, as the charge retained in a nanocluster decreases monotonically from 10.0% to 4.3% (Table 4.4), due to entropic effects. Thus, the experimental nanocluster sizes are predicted semi-quantitatively by the theoretical model.

Nanocluster formation pathways are illustrated schematically in Figure 4.10. Here, open symbols represent the Au and polymer concentrations resulting from the mixing of polymer and Au nanoparticle solutions. Evaporation of water from these mixed solutions is shown by the solid lines with arrows, resulting in the final Au and c_p represented by the solid symbols (Figure 4.10). During solvent evaporation, the increase in c_p increases the magnitude of polymer- induced depletion attraction between particles, as is shown by Equation 4.5. In addition, the increase in c_{Au} decreases the charge, as shown in Equation C.11. Both of these factors increase the cluster size.

4.4.3 Quenching of Nanocluster Size

After assembly of the Au nanospheres into nanoclusters, this quasi-equilibrium state is quenched by irreversible polymer adsorption. The hydrophobic nature of the PLA groups in the PLA-PEG-PLA triblock copolymer drives the polymer adsorption on the hydrophobic Au surface.[39] The rate of this polymer adsorption, however, is expected to be much slower than the rate of depletion attraction-induced equilibrium particle

assembly. The weak driving force for adsorption reflects the large amount of hydrophilic PEG in the polymer which interacts only weakly with the hydrophobic Au surface.[39] If polymer adsorbed on individual Au spheres, which then formed clusters, the Au primary particle spacings would be too large for the intense NIR extinction observed in Figures 3b and 5b. Instead, the slow kinetics of polymer adsorption relative to rapid nanocluster formation, led to very closely spaced Au particles. Additionally, the adsorbed polymer provided steric stabilization on the nanoclusters surface. To harvest the nanoclusters, they were rapidly diluted in deionized water, as shown by the dashed lines in Figure 4.10. Here, the cluster size did not change. The high degree of dilution would lead to Au monomer particles according the equilibrium model (Figure 4.10). Instead, the irreversible polymer adsorption on the nanocluster surface maintained a "quenched" equilibrium cluster size. Furthermore, attraction between the highly ion paired Au primary particles within the cluster with low charge prevented nanocluster dissociation. The polymer played a multifunctional role in: (1) driving the depletion attraction to assemble the primary Au particles into clusters, (2) providing steric stabilization of the clusters, and (3) quenching the nanoclusters with an equilibrium size. The clusters were fairly dilute and colloidally stable over weeks, so we did not calculate the interaction potential between the clusters.

The concept of quenched equilibrium Au nanoclusters presented in this work is substantially different from our previous Au nanocluster studies, which attributed nanocluster formation to a kinetic assembly mechanism.[5] In our previous work, a kinetic stability ratio was estimated based on the time required for a qualitative color change in the nanocluster dispersion by eye during formation.[5] This approach was not applicable to nanoclusters smaller than 50 nm where the color change was very rapid and heavily dependent upon the evaporation rate of the solvent. The previous work did not recognize

the depletion force was sufficiently strong to produce equilibrium assembly (given the micelle concentration was unknown), and thus equilibrium assembly was not thought to be present.[5] Furthermore, the composition of the ligands on the surface was not measured, and the charge on the Au surface was not well-characterized, which limited the analysis of the formation mechanism.[4, 5] In most cases, all of the water was evaporated for form Au-polymer films which were later diluted to harvest the clusters. This two-step approach may involve complex cluster formation mechanisms. As a result, the present study represents a major and novel advance over previous work by demonstrating equilibrium nanocluster assembly and control over nanocluster size.

In an insightful related study, "self-limiting" clusters of CdSe primary particles have been observed in water, where cluster growth stopped upon reaching a balance between charge in the cluster and van der Waals attraction between particles.[6] Both nanocluster size and zeta potential measurements showed cluster growth followed by a plateau as the self-limited cluster state was reached.[6] Building upon this "self-limiting" nanocluster concept, a novel aspect of the present work is that degradation of the polymer quencher allows for reversible cluster dissociation to recover ~5 nm monomers, which is critical for effective renal clearance. Moreover, the present study demonstrates the ability to tune nanocluster size by balancing effective colloidal interactions as well as the ability to semi-quantitatively predict this cluster size.

In the current study, we chose to form nanoclusters at a desired evaporation extent of only 50% and from primary Au nanospheres with a zeta potential of only -16 mV. If the zeta potential of the primary nanospheres were more negative, electrostatic repulsion would be too dominant, and the size would be too small, as shown in Equation 4.4. For example, for highly charged Au particles with only citrate ligands, the required evaporation extent was 85% to form nanoclusters, as would be evident in Figure 4.10.

However at such high evaporation amounts, the particles form a viscous gel and it may become difficult to redisperse the clusters with the desired size and with low polydispersity.

For particular experimental pathways, other than those in Table 4.1 and Figure 4.10, we observed kinetic traps that prevented attainment of the sizes predicted by the equilibrium model. For example, adding polymer solution in one step, instead of iteratively, to the Au solution led to large nanoclusters with weak NIR extinction. Immediately after mixing the Au dispersion with the polymer solution, we observed a large increase in viscosity, which may have limited access to equilibrium configurations, leading to relatively large ~120 nm aggregates with weak NIR extinction (Table C.4). In addition, initial Au concentrations in excess of 6 mg/ml led to irreversible aggregation of nanoparticles even without adding any polymer, indicating insufficient electrostatic stabilization.

These quenched equilibrium Au nanoclusters are quite different from other clusters which are affected by dilution, such as protein nanoclusters[14] as well as clusters of cerium oxide[40] and iron oxide[41] nanoparticles and oppositely-charged diblock polymers. The size of kinetically "frozen" clusters of cerium oxide, from 100 nm to 500 nm in diameter, has been shown to change with dilution rate, with smaller clusters formed at faster dilution rates.[40] Equilibrium Au nanoclusters, if quenched by irreversible polymer adsorption, in contrast, do not change size after dilution.

4.4.4 Nanocluster Dissociation

For a Au dispersion without polymer present, depletion attraction between Au nanoparticles is not present and the equilibrium state was found to be individual charged

primary particles (Figure 4.10). For polymer coated Au nanoclusters, dissociation was initiated by exposure to a pH 5 HCl environment, which accelerates the degradation rate of the PLA segments, relative to pH7.[42] As the polymeric quencher was gradually removed upon hydrolysis, the cluster size decreased continuously as charged Au primary particles left the nanocluster surface. After 48 h, enough polymer had degraded for the 20-4.0 nanoclusters to dissociate almost completely to monomer.

The plot of ln(n_c) *versus* time shown in Figure 4.6c indicates approximately first-order kinetics, as demonstrated in Equation 4.6:

$$\frac{dn_c}{dt} = -kn_c \tag{4.6}$$

Here, n_c is the number of particles in a cluster, given by Equation C.7, and k is the first-order rate constant. The linear fit to the data shown in Figure 4.6c reveals a k of ~0.12 hr^{-1}.

The dissociation of the smaller 20-1.7 nanoclusters was faster and more complete (Figure 4.7) relative to the larger 20-4.0 ones. For the smaller nanocluter size, less time is needed to degrade the smaller amount of polymeric quencher, for a fixed polymer/Au ratio. Additionally, there are fewer chances for dissociating nanoclusters to become trapped in metastable irreversible states involving even a small number dimers, trimers, and higher-order assemblies. The NIR extinction is significant for dimers and trimers at close spacing,[5] as seen in Figure 4.6 with 20-4.0 particles. The complete dissociation to charged Au monomer nanospheres supports the quenched equilibrium concept, whereby the polymer no longer influences the Au particles size after it is degraded. After PLA hydrolysis, the PEG central block did not have a tendency to adsorb strongly on Au,[39]

and during dissociation the polymer concentration was too low to produce depletion attraction.

4.4.5 Nanocluster Spectral Properties

The surface plasmon resonance for Au nanoparticles is well known to shift to the NIR for various morphologies including nanoshells,[23, 24, 43, 44] nanocages,[45, 46] high aspect ratio nanorods,[47, 48] nanoflowers[49, 50] or nanostars.[51, 52] These particles with NIR extinction, however, often have diameters greater than 5.5 nm in diameter, which would be too large for efficient kidney clearance from the body.[27] Alternatively, the SPR has been experimentally demonstrated to shift towards the NIR for dimers and trimers of Au nanospheres,[43] and broad NIR extinction has been observed in larger clusters of Au nanospheres.[4, 5] The amount of extinction broadening has been shown to be dependent on the interparticle spacing between constituent particles.[43] In the present work, intense NIR extinction is achieved *via* extremely close (less than a particle diameter[8, 53]) interparticle spacings within Au nanoclusters. As the polymer/Au ratio is increased, the corresponding increase in depletion attraction can potentially decrease the interparticle spacing, while simultaneously increasing nanocluster size. As a result, the amount of NIR extinction increases, as is shown in Figure 4.5b. In addition, as the final Au concentration was increased (along with the final polymer concentration), the charge per primary particle in a cluster was decreased, potentially decreasing the interparticle spacing and increasing nanocluster size. The resultant increase in cluster size and decrease in interparticle spacings creates broader extinction spectra and greater NIR extinction (Figure 4.3b).

The Au nanoclusters exhibited intense NIR extinction which is of interest in applications such as photoacoustic imaging[20] and photothermal therapy.[22, 23, 44] The fine control over nanocluster size demonstrated in this study from ~20 nm to ~40 nm is in an optimal range for cell uptake[54] and blood circulation.[55] In addition, the biodegradability of these nanoclusters into ~5 nm primary particles offers the possibility of clearance *via* the kidneys.[27] In future applications, the nanoclusters would potentially be targeted to cancer cells *via* biomarkers such as epidermal growth factor receptor (EGFR) and consequently undergo endosomal uptake.[56] Multiple studies have demonstrated that after intravascular (IV) administration in tumor animal models, injected nanoparticles accumulate mostly in the liver, spleen, and tumor.[57] Since nanoclusters have been shown to dissociate within acidic endosomal and lysosomal compartments,[4] we hypothesize that the nanoclusters in this work will dissociate completely to primary particles in the acidic endosomal/lysosomal cellular compartments, and that these particles will then be cleared from the body.

4.5 CONCLUSIONS

Equilibrium phenomena play a major role in governing the size of Au nanoclusters, which are quenched by irreversibly adsorbed polymer on the surface. Upon biodegradation of various amounts of the quencher, PLA(1k)-b-PEG(10k)-b-PLA(1k), the clusters reversibly become smaller and eventually dissociate completely to ~5 nm Au monomer nanospheres. Nanocluster size was tuned from ~20 nm to ~40 nm by varying the ratio of polymer/Au from 10/1 to 50/1 w/w, to vary the depletion attraction induced by the polymer, and also by varying the Au nanoparticle concentrations from 0.9 mg/ml to 4 mg/ml. The surface charge on primary Au nanospheres was modified by the addition

of positively charged lysine to originally citrate-capped nanospheres to create a mixed charge monolayer on the Au nanosphere surface. The incremental mixing of the polymer solution with the initial Au dispersion, along with solvent evaporation to raise Au and polymer concentrations, provided exquisite regulation of the nanocluster size. The size was predicted semi-quantitatively with an equilibrium free energy model as a function of the Au concentration and the polymer/Au ratio. The free energy model describes the balance between long-ranged electrostatic repulsion between primary Au nanospheres with short-ranged van der Waals and depletion attractive interactions. The equilibrium size is quenched by an irreversibly adsorbed polymer layer on the nanocluster surface, and remains constant even after removal of excess polymer. The close spacings of primary nanospheres within the nanoclusters resulted in high NIR extinction for all sizes of nanoclusters explored in this work. Thus, a general concept has been demonstrated for forming quenched equilibrium nanoclusters with tunable sizes (and in this case NIR extinction), which reversibly dissociate upon biodegradation of the polymer quencher.

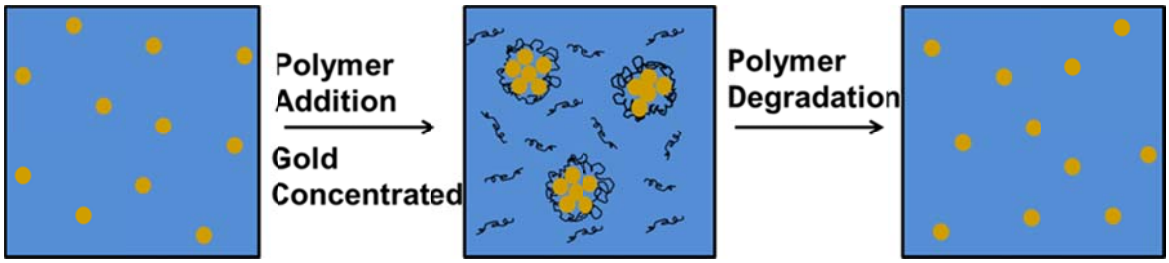

Figure 4.1: Schematic of quenched equilibrium nanocluster formation and dissociation process. A polymer solution is added to a Au nanoparticle dispersion, and the mixture is then concentrated through partial water evaporation in order to form Au nanoclusters. Polymer degradation upon hydrolysis results in the dissociation of nanoclusters back to primary charged Au nanospheres.

Table 4.1: Properties of nanospheres before and after place exchange

Sample	**D_H (nm)**	**ε_{800} (cm^2/mg)**	**Zeta Potential (mV)**	**Ligand % by weight (TGA)**	**Lysine/Citrate ratio (XPS)**
Citrate	4.3 ± 0.7	0.44	-58.4 ± 5.3	4%	n/a
Citrate/lysine	4.7 ± 0.8	0.67	-16.0 ± 6.6	4%	1.4

Table 4.2: Properties of nanoclusters. The final Au and polymer concentrations are after solvent evaporation but prior to dilution to harvest the nanoclusters. Sample names contain two numbers separated by a dash: final polymer/Au mass ratio and final Au concentration in mg/ml.

Sample	**Final Au Conc (mg/ml)**	**Final Polymer Conc (mg/ml)**	**D_H (nm)**	**TEM Diameter (nm)**	**ε_{800} (cm^2/mg)**	**Zeta Potential (mV)**	**Au Yield By Mass (%)**
20-0.9	0.9	18	21.4 ± 4.4	24.0 ± 6.2	10.6	-12.3 ± 1.1	17 ± 6
20-1.7	1.7	34	29.4 ± 3.2	31.1 ± 6.9	11.7	-16.4 ± 3.6	31 ± 12
20-4.0	4.0	80	40.1 ± 4.3	42.7 ± 9.4	12.9	-13.2 ± 0.6	61 ± 15
10-1.7	1.7	17	24.0 ± 5.6	21.0 ± 4.3	11.2	-16.7 ± 3.6	26 ± 13
50-1.7	1.7	85	38.4 ± 7.3	36.3 ± 5.6	13.0	-12.5 ± 1.2	57 ± 18

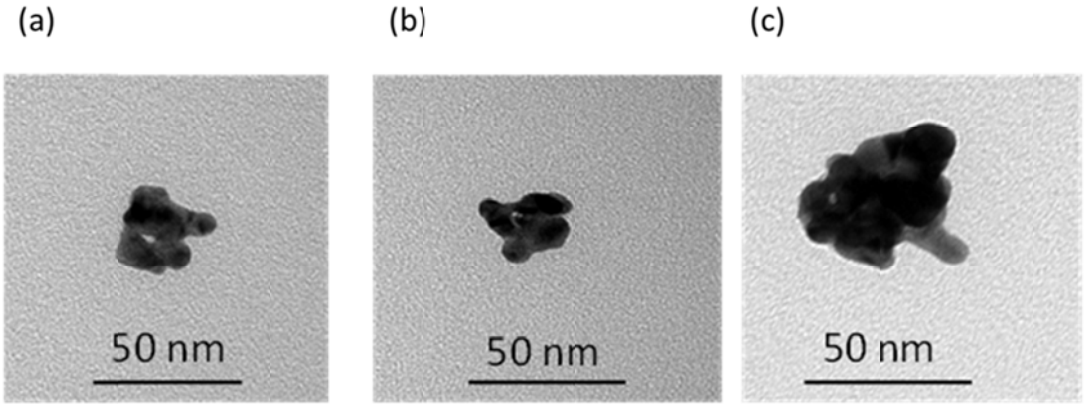

Figure 4.2: Representative TEM images of nanoclusters formed with a final Au concentration of (a) 0.9 mg/ml (20-0.9), (b) 1.7 mg/ml (20-1.7), and (c) 4.0 mg/ml (20-4.0). All samples had a final polymer/Au ratio of 20/1.

(a)

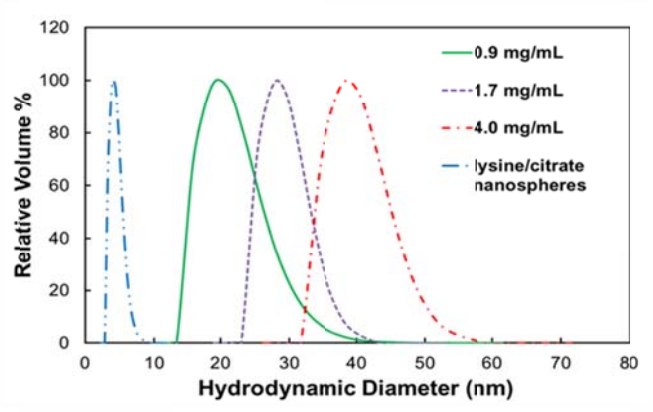

(b)

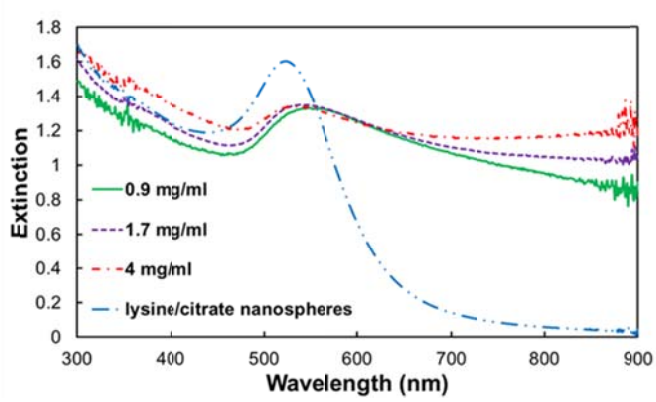

Figure 4.3: (a) DLS D_H distributions, and (b) UV-Vis-NIR extinction spectra of nanoclusters formed with 0.9 mg/ml (20-0.9), 1.7 mg/ml (20-1.7), and 4 mg/ml (20-4.0) final Au concentrations. UV-Vis-NIR spectra were taken at a Au concentration of ~90 µg/ml. All samples had a polymer/Au ratio of 20/1.

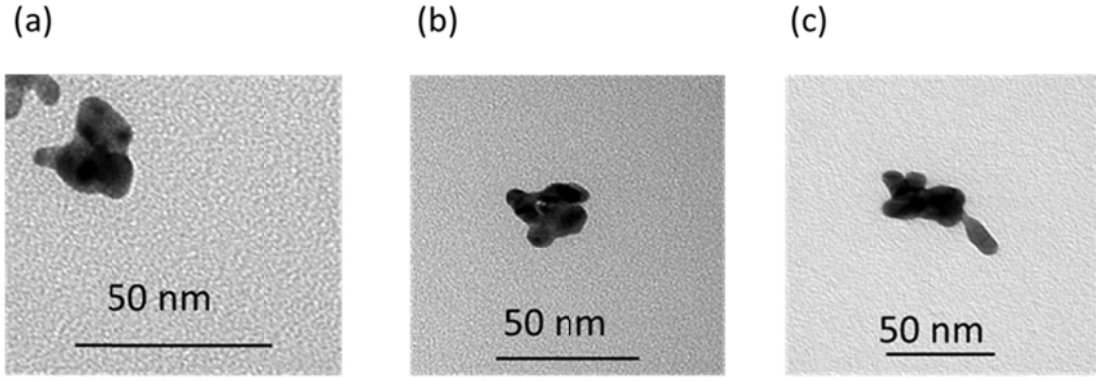

Figure 4.4: Representative TEM images of nanoclusters formed with a final Au concentration of 1.7 mg/ml and polymer/Au ratio of (a) 10/1 (10-1.7), (b) 20/1 (20-1.7), and (c) 50/1 (50-1.7).

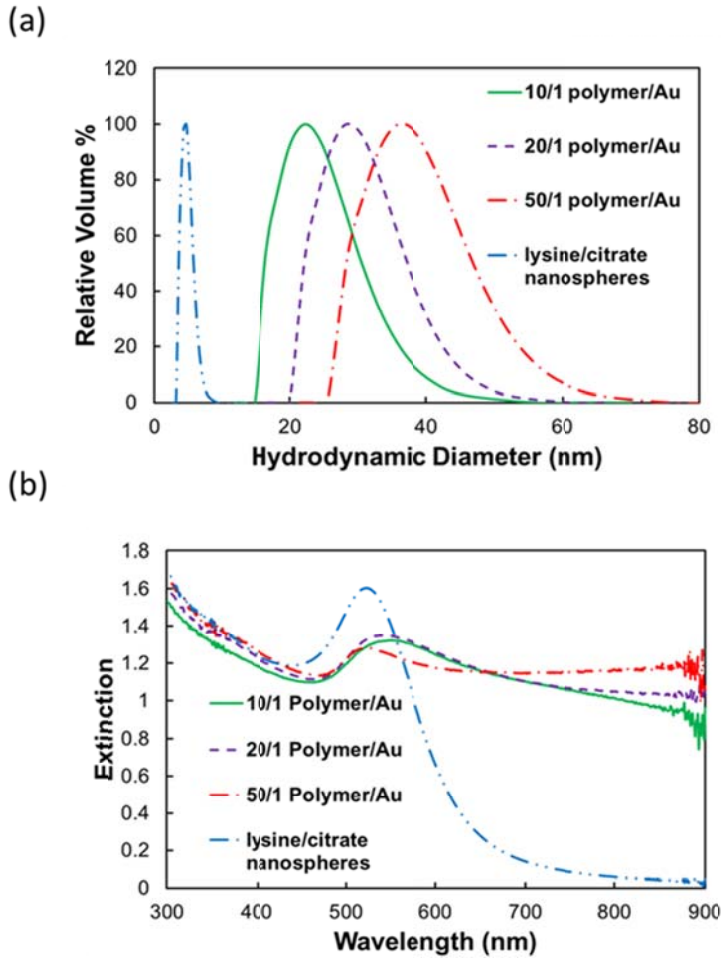

Figure 4.5: (a) DLS D_H distributions, and (b) UV-Vis-NIR extinction spectra of nanoclusters formed with polymer/Au ratios of 10/1 (10-1.7), 20/1 (20-1.7) and 50/1 (50-1.7). UV-Vis-NIR spectra were taken at a Au concentration of ~90 µg/ml. All samples had final Au concentrations of 1.7 mg/ml.

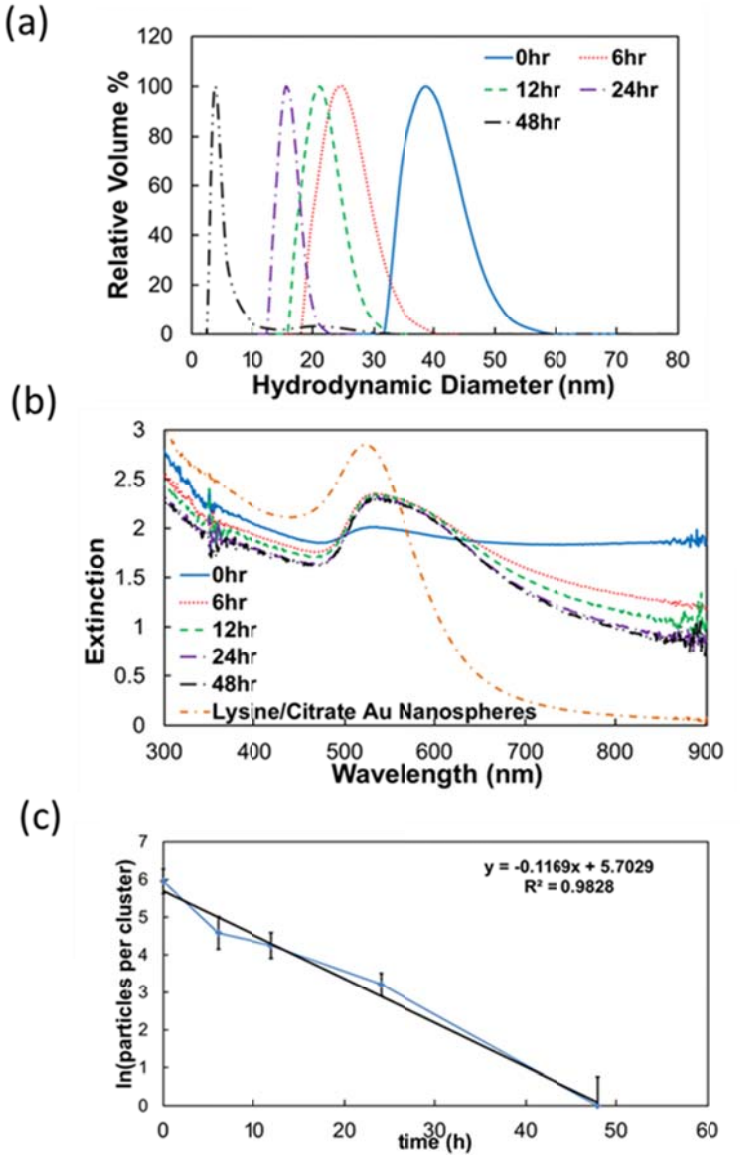

Figure 4.6: (a) DLS D_H distributions (b) UV-Vis-NIR extinction spectra, and (c) kinetics of dissociation of nanoclusters with a polymer/Au ratio of 20/1 and Au concentration of 4.0 mg/ml (20-4.0 particles) at various times after being exposed to a pH 5 HCl environment. UV-Vis-NIR spectra were taken at a Au concentration of ~160 μg/ml. Error bars in (c) correspond to the calculated standard deviation taken from D_H distributions measured by DLS.

Table 4.3: DLS sizes and extinction coefficients of nanoclusters at various dissociation time points.

Incubation Time (h)	**D_H (nm)**	**ε_{800} (cm^2/mg)**
0	40.1 ± 4.3	12.9
6	25.2 ± 3.6	8.4
12	22.7 ± 2.6	7.4
24	16.1 ± 1.6	6.4
48	5.0 ± 4.3	6.3

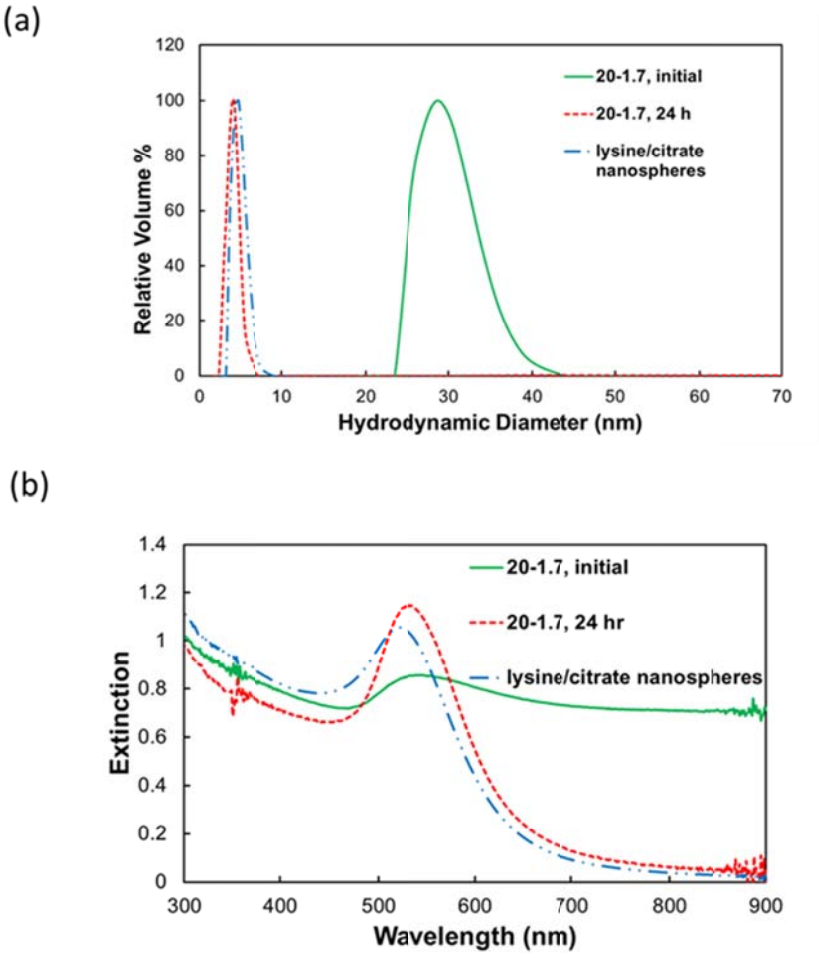

Figure 4.7: (a) DLS D_H distributions and (b) UV-Vis-NIR extinction spectra for nanoclusters with a polymer/Au ratio of 20/1 and a final Au concentration of 1.7 mg/ml (20-1.7 particles) before and after being exposed to a pH 5 HCl environment for 24 h. D_H distributions and UV-Vis-NIR spectra of lysine/citrate capped nanospheres are also included for reference. UV-Vis-NIR spectra were taken at a Au concentration of ~60 μg/ml.

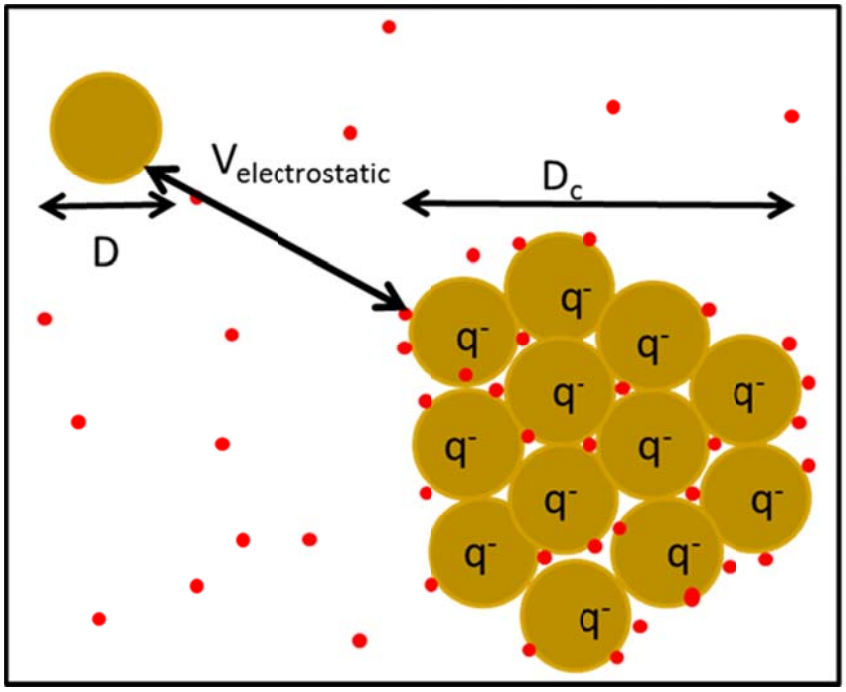

Figure 4.8: Equilibrium nanocluster with diameter D_c composed of primary particles (of diameter D) each with ion pairs and a negative charge of magnitude q. The highly charged monomer coated with ligands (negligible ion pairing) on the top left is repelled by the charged nanocluster ($V_{electrostatic}$). Bound and free counterions are represented by red dots.

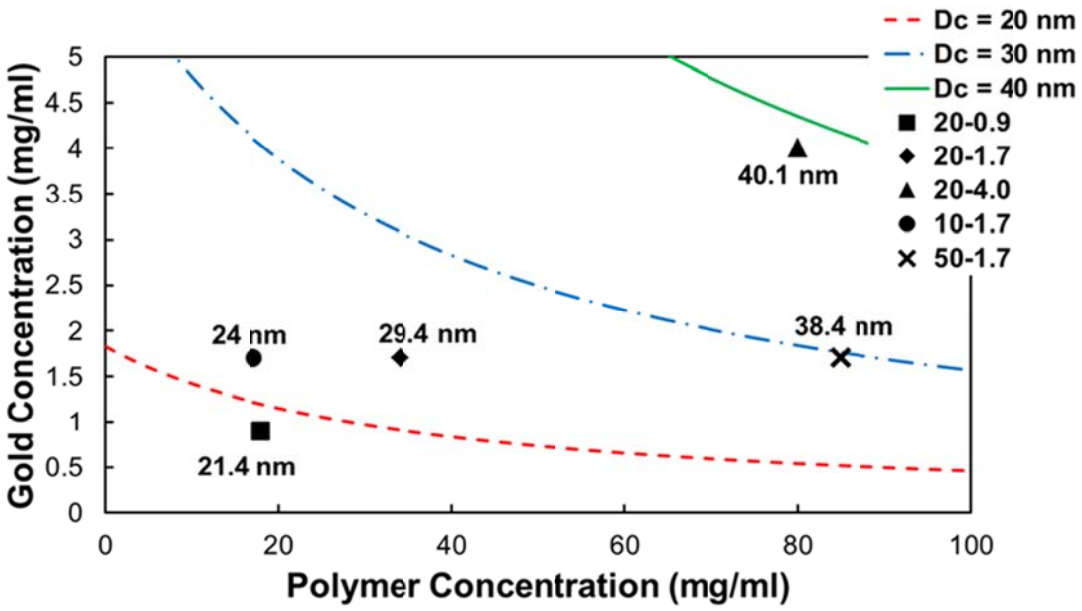

Figure 4.9: Cluster-size contours for various values of polymer and Au concentration, based on the equilibrium free energy model discussed in the text. Hydrodynamic diameters (DLS) shown by points are in reasonable agreement with the model.

Table 4.4: Zeta potentials and charges per cluster (experimental, based on zeta potential and aggregation number) compared with calculated charge if all monomers stayed fully charged upon cluster formation

Sample	**Zeta Potential (mV)**	**Negative Charges per Cluster**	**Negative Charges per Cluster Calc.**	**% Charge Retained**
20-0.9	-12.3 ± 1.1	15.1	157	10.0%
20-1.7	-16.4 ± 3.6	33.0	407	8.1%
20-4.0	-13.2 ± 0.6	44.2	1033	4.3%
10-1.7	-16.7 ± 3.6	24.4	221	11.0%
50-1.7	-12.5 ± 1.2	38.8	907	4.3%

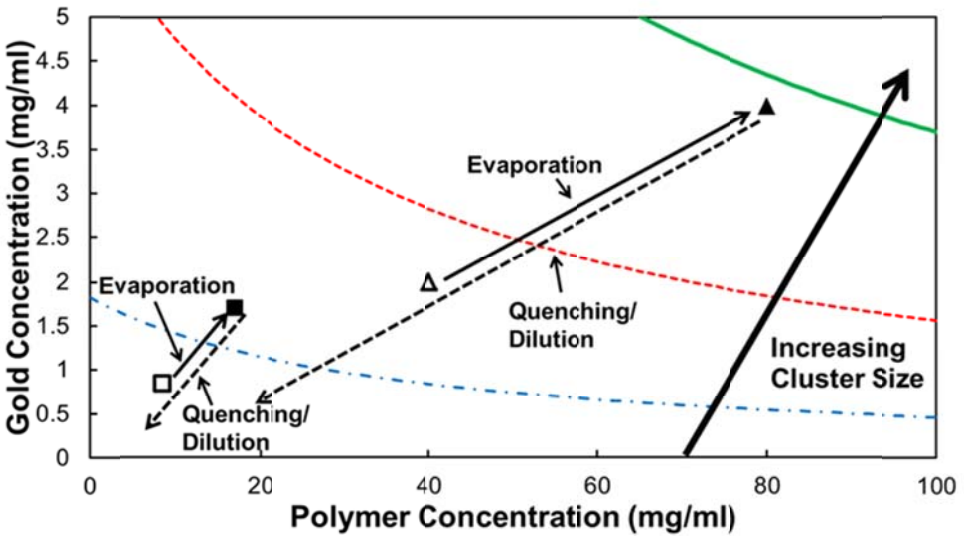

Figure 4.10: Schematic of equilibrium nanocluster formation process followed by polymer quenching. Curves of constant cluster diameter (D_c) as a function of polymer and Au concentrations are shown as countours predicted from the equilibrium free energy model discussed in the text and parameters in Table C.2. Open symbols represent concentrations upon mixing of polymer and Au nanoparticle solutions, and filled symbols represent Au and polymer concentrations after evaporation of 50% of the solvent. Solid lines represent the evaporation process, and dashed lines represent the dilution of the quenched clusters, during which nanocluster size is constant (*i.e.*, quenched due to polymer adsorption). Process lines are presented for 20-4.0 (triangles) and 10-1.7 particles (squares).

4.6 REFERENCES

1. Boal, A. K.; Ilhan, F.; DeRouchey, J. E.; Thurn-Albrecht, T.; Russell, T. P.; Rotello, V. M. Self-Assembly of Nanoparticles into Structured Spherical and Network Aggregates. *Nature* **2000**, *404*, 746-748.
2. Shenhar, R.; Norsten, T. B.; Rotello, V. M. Polymer-Mediated Nanoparticle Assembly: Structural Control and Applications. *Adv. Mater.* **2005**, *17*, 657-669.
3. Ma, L. L.; Feldman, M. D.; Tam, J. M.; Paranjape, A. S.; Cheruki, K. K.; Larson, T. A.; Tam, J. O.; Ingram, D. R.; Paramita, V.; Villard, J. W.*, et al.* Small Multifunctional Nanoclusters (Nanoroses) for Targeted Cellular Imaging and Therapy. *ACS Nano* **2009**, *3*, 2686-2696.
4. Tam, J. M.; Tam, J. O.; Murthy, A.; Ingram, D. R.; Ma, L. L.; Travis, K.; Johnston, K. P.; Sokolov, K. V. Controlled Assembly of Biodegradable Plasmonic Nanoclusters for Near-Infrared Imaging and Therapeutic Applications. *ACS Nano* **2010**, *4*, 2178-2184.
5. Tam, J. M.; Murthy, A. K.; Ingram, D. R.; Nguyen, R.; Sokolov, K. V.; Johnston, K. P. Kinetic Assembly of Near-IR Active Gold Nanoclusters Using Weakly Adsorbing Polymers to Control the Size. *Langmuir* **2010**, *26*, 8988-8999.
6. Xia, Y. S.; Nguyen, T. D.; Yang, M.; Lee, B.; Santos, A.; Podsiadlo, P.; Tang, Z. Y.; Glotzer, S. C.; Kotov, N. A. Self-Assembly of Self-Limiting Monodisperse Supraparticles from Polydisperse Nanoparticles. *Nat. Nanotechnol.* **2011**, *6*, 580-587.
7. Ofir, Y.; Samanta, B.; Rotello, V. M. Polymer and Biopolymer Mediated Self-Assembly of Gold Nanoparticles. *Chem. Soc. Rev.* **2008**, *37*, 1814-1825.
8. Srivastava, S.; Frankamp, B. L.; Rotello, V. M. Controlled Plasmon Resonance of Gold Nanoparticles Self-Assembled with PAMAM Dendrimers. *Chem. Mater.* **2005**, *17*, 487-490.
9. Larson-Smith, K.; Pozzo, D. C. Scalable Synthesis of Self-Assembling Nanoparticle Clusters Based on Controlled Steric Interactions. *Soft Matter* **2011**, *7*, 5339-5347.
10. Wilcoxon, J. P.; Martin, J. E.; Schaefer, D. W. Aggregation in Colloidal Gold. *Phys. Rev. A* **1989**, *39*, 2675-2688.
11. Lu, P. J.; Zaccarelli, E.; Ciulla, F.; Scholfield, A. B.; Sciortino, F.; Weitz, D. A. Gelation of Particles with Short-Range Attraction. *Nature* **2008**, *453*, 499-504.
12. Sedgwick, H.; Egelhaaf, S. U.; Poon, W. C. K. Clusters and Gels in Systems of Sticky Particles. *J. Phys.-Condes. Matter* **2004**, *16*, S4913-S4922.

13. Buitenhuis, J.; Dhont, J. K. G.; Lekkerkerker, H. N. W. Static and Dynamic Light Scattering by Concentrated Colloidal Suspensions of Polydisperse Sterically Stabilized Boehmite Rods. *Macromolecules* **1994**, *27*, 7267-7277.

14. Johnston, K. P.; Maynard, J. A.; Truskett, T. M.; Borwankar, A. U.; Miller, M. A.; Wilson, B. K.; Dinin, A. K.; Khan, T. A.; Kaczorowski, K. J. Concentrated Dispersion of Equilibrium Protein Nanoclusters That Reversibly Dissociate into Active Monomers. *ACS Nano* **2012**, *6*, 1357-1369.

15. Groenewold, J.; Kegel, W. K. Anomalously Large Equilibrium Clusters of Colloids. *J. Phys. Chem. B* **2001**, *105*, 11702-11709.

16. Stradner, A.; Sedgwick, H.; Cardinaux, F.; Poon, W. C. K.; Egelhaaf, S. U.; Schurtenberger, P. Equilibrium Cluster Formation in Concentrated Protein Solutions and Colloids. *Nature* **2004**, *432*, 492-495.

17. Porcar, L.; Falus, P.; Chen, W.-R.; Faraone, A.; Fratini, E.; Hong, K.; Baglioni, P.; Liu, Y. Formation of the Dynamic Clusters in Concentrated Lysozyme Protein Solutions. *J. Phys. Chem. Lett.* **2010**, *1*, 126-129.

18. Weissleder, R. A Clearer Vision for *in Vivo* Imaging. *Nat. Biotechnol.* **2001**, *19*, 316-317.

19. Mallidi, S.; Larson, T.; Aaron, J.; Sokolov, K.; Emelianov, S. Molecular Specific Optoacoustic Imaging with Plasmonic Nanoparticles. *Opt. Express* **2007**, *15*, 6583-6588.

20. Mallidi, S.; Larson, T.; Tam, J.; Joshi, P. P.; Karplouk, A.; Sokolov, K.; Emelianov, S. Multiwavelength Photoacoustic Imaging and Plasmon Resonance Coupling of Gold Nanoparticles for Selective Detection of Cancer. *Nano Lett.* **2009**, *9*, 2825-2831.

21. Agarwal, A.; Huang, S. W.; O'Donnell, M.; Day, K. C.; Day, M.; Ashkenazi, S. Targeted Gold Nanorod Contrast Agent for Prostate Cancer Detection by Photoacoustic Imaging. *J. Appl. Phys.* **2007**, *102*, 0647011-0647014.

22. Khlebtsov, B.; Zharov, V.; Melnikov, A.; Tuchin, V.; Khlebtsov, N. Optical Amplification of Photothermal Therapy with Gold Nanoparticles and Nanoclusters. *Nanotechnology* **2006**, *17*, 5167-5179.

23. Hirsch, L. R.; Stafford, R. J.; Bankson, J. A.; Sershen, S. R.; Rivera, B.; Price, R. E.; Hazle, J. D.; Halas, N. J.; West, J. L. Nanoshell-Mediated Near-Infrared Thermal Therapy of Tumors under Magnetic Resonance Guidance. *Proc. Natl. Acad. Sci.* **2003**, *100*, 13549-13554.

24. Loo, C.; Lowery, A.; Halas, N.; West, J.; Drezek, R. Immunotargeted Nanoshells for Integrated Cancer Imaging and Therapy. *Nano Lett.* **2005**, *5*, 709-711.

25. Larson, T. A.; Bankson, J.; Aaron, J.; Sokolov, K. Hybrid Plasmonic Magnetic Nanoparticles as Molecular Specific Agents for MRI/Optical Imaging and Photothermal Therapy of Cancer Cells. *Nanotechnology* **2007**, *18*.

26. von Maltzahn, G.; Park, J.-H.; Agrawal, A.; Bandaru, N. K.; Das, S. K.; Sailor, M. J.; Bhatia, S. N. Computationally Guided Photothermal Tumor Therapy Using Long-Circulating Gold Nanorod Antennas. *Cancer Res.* **2009**, *69*, 3892-3900.

27. Choi, H. S.; Liu, W.; Misra, P.; Tanaka, E.; Zimmer, J. P.; Ipe, B. I.; Bawendi, M. G.; Frangioni, J. V. Renal Clearance of Quantum Dots. *Nat. Biotechnol.* **2007**, *25*, 1165-1170.

28. Gavrilenko, V. I., *Optics of Nanomaterials*. Pan Stanford Publishing: Singapore, 2011; p 63-66.

29. Zhang, C.; Pansare, V. J.; Prud'homme, R. K.; Priestley, R. D. Flash Nanoprecipitation of Polystyrene Nanoparticles. *Soft Matter* **2012**, *8*, 86-93.

30. Cheng, C.; Wen, Y.; Xu, X.; Gu, H. Tunable Synthesis of Carboxyl-Functionalized Magnetite Nanocrystal Clusters with Uniform Size. *J. Mater. Chem.* **2009**, *19*, 8782-8788.

31. Zaccarelli, E. Colloidal Gels: Equilibrium and Non-Equilibrium Routes. *J. Phys.-Condes. Matter* **2007**, *19*, 1-50.

32. Edwards, T. D.; Bevan, M. A. Polymer Mediated Depletion Attraction and Interfacial Colloidal Phase Behavior. *Macromolecules* **2012**, *45*, 585-594.

33. Piech, M.; Walz, J. Y. Direct Measurement of Depletion and Structural Forces in Polydisperse, Charged Systems. *J. Colloid Interface Sci.* **2002**, *253*, 117-129.

34. Kulkarni, A. M.; Chatterjee, A. P.; Schweizer, K. S.; Zukoski, C. F. Depletion Interactions in the Protein Limit: Effects of Polymer Density Fluctuations. *Phys. Rev. Lett.* **1999**, *83*, 4554-4557.

35. Lekkerkerker, H. N. W.; Tuinier, R., *Colloids and the Depletion Interaction*. Springer: New York, 2011; Vol. 833, p 12-15.

36. Asakura, S.; Oosawa, F. On Interaction between 2 Bodies Immersed in a Solution of Macromolecules. *J. Chem. Phys.* **1954**, *22*, 1255-1256.

37. Asakura, S.; Oosawa, F. Interaction between Particles Suspended in Solutions of Macromolecules. *J. Polym. Sci.* **1958**, *33*, 183-192.

38. Chen, S.; Yu, F.; Yu, Q.; He, Y.; Jiang, S. Strong Resistance of a Thin Crystalline Layer of Balanced Charged Groups to Protein Adsorption. *Langmuir* **2006**, *22*, 8186-8191.

39. Sakai, T.; Alexandridis, P. Mechanism of Gold Metal Ion Reduction, Nanoparticle Growth and Size Control in Aqueous Amphiphilic Block Copolymer Solutions at Ambient Conditions. *J. Phys. Chem. B* **2005**, *109*, 7766-7777.

40. Fresnais, J.; Lavelle, C.; Berret, J.-F. Nanoparticle Aggregation Controlled by Desalting Kinetics. *J. Phys. Chem. C* **2009**, *113*, 16371-16379.

41. Berret, J.-F. Stoichiometry of Electrostatic Complexes Determined by Light Scattering. *Macromolecules* **2007**, *40*, 4260-4266.

42. Ivanova, T.; Panaiotov, I.; Proust, J. E.; Benoit, J. P.; Verger, R. Hydrolysis Kinetics of Poly(D,L-Lactide) Monolayers Spread on Basic or Acidic Aqueous Subphases. *Colloids and Surfaces B: Biointerfaces* **1997**, *8*, 217-225.

43. Halas, N. J.; Lal, S.; Chang, W.-S.; Link, S.; Nordlander, P. Plasmons in Strongly Coupled Metallic Nanostructures. *Chem. Rev.* **2011**, *111*, 3913-3961.

44. Gobin, A. M.; Lee, M. H.; Halas, N. J.; James, W. D.; Drezek, R. A.; West, J. L. Near-Infrared Resonant Nanoshells for Combined Optical Imaging and Photothermal Cancer Therapy. *Nano Lett.* **2007**, *7*, 1929-1934.

45. Chen, J.; Saeki, F.; Wiley, B. J.; Cang, H.; Cobb, M. J.; Li, Z. Y.; Au, L.; Zhang, H.; Kimmey, M. B.; Li, X.*, et al.* Gold Nanocages: Bioconjugation and Their Potential Use as Optical Imaging Contrast Agents. *Nano Lett.* **2005**, *5*, 473-477.

46. Song, K. H.; Kim, C.; Cobley, C. M.; Xia, Y.; Wang, L. V. Near-Infrared Gold Nanocages as a New Class of Tracers for Photoacoustic Sentinel Lymph Node Mapping on a Rat Model. *Nano Lett.* **2009**, *9*, 183-188.

47. Huang, X.; El-Sayed, I. H.; Qian, W.; El-Sayed, M. A. Cancer Cell Imaging and Photothermal Therapy in the Near-Infrared Region by Using Gold Nanorods. *J. Am. Chem. Soc.* **2006**, *128*, 2115-2120.

48. Link, S.; Mohamed, M. B.; El-Sayed, M. A. Simulation of the Optical Absorption Spectra of Gold Nanorods as a Function of Their Aspect Ratio and the Effect of the Medium Dielectric Constant. *J. Phys. Chem. B* **1999**, *103*, 3073-3077.

49. Wang, W.; Yang, X.; Cui, H. Growth Mechanism of Flowerlike Gold Nanostructures: Surface Plasmon Resonance (SPR) and Resonance Rayleigh Scattering (RRS) Approaches to Growth Monitoring. *J. Phys. Chem. C* **2008**, *112*, 16348-16353.

50. Wang, Z.; Zhang, J.; Ekman, J. M.; Kenis, P. J. A.; Lu, Y. DNA-Mediated Control of Metal Nanoparticle Shape: One-Pot Synthesis and Cellular Uptake of Highly Stable and Functional Gold Nanoflowers. *Nano Lett.* **2010**, *10*, 1886-1891.

51. Nehl, C. L.; Liao, H.; Hafner, J. H. Optical Properties of Star-Shaped Gold Nanoparticles. *Nano Letters* **2006**, *6*, 683-688.

52. Trigari, S.; Rindi, A.; Margheri, G.; Sottini, S.; Dellepiane, G.; Giorgetti, E. Synthesis and Modelling of Gold Nanostars with Tunable Morphology and Extinction Spectrum. *J. Mater. Chem.* **2011**, *21*, 6531-6540.

53. Rechberger, W.; Hohenau, A.; Leitner, A.; Krenn, J. R.; Lamprecht, B.; Aussenegg, F. R. Optical Properties of Two Interacting Gold Nanoparticles. *Opt. Commun.* **2003**, *220*, 137-141.

54. Chithrani, B. D.; Ghazani, A. A.; Chan, W. C. W. Determining the Size and Shape Dependence of Gold Nanoparticle Uptake into Mammalian Cells. *Nano Lett.* **2006**, *6*, 662-668.

55. Kooi, M. E.; Cappendijk, V. C.; Cleutjens, K. B. J. M.; Kessels, A. G. H.; Kitslaar, P. J. E. H. M.; Borgers, M.; Frederik, P. M.; Daemen, M. J. A. P.; van Engelshoven, J. M. A. Accumulation of Ultrasmall Superparamagnetic Particles of Iron Oxide in Human Atherosclerotic Plaques Can Be Detected by *in Vivo* Magnetic Resonance Imaging. *Circulation* **2003**, *107*, 2453-2458.

56. Aaron, J.; Travis, K.; Harrison, N.; Sokolov, K. Dynamic Imaging of Molecular Assemblies in Live Cells Based on Nanoparticle Plasmon Resonance Coupling. *Nano Lett.* **2009**, *9*, 3612-3618.

57. Khlebtsov, N.; Dykman, L. Biodistribution and Toxicity of Engineered Gold Nanoparticles: A Review of *in Vitro* and *in Vivo* Studies. *Chem. Soc. Rev.* **2011**, *40*, 1647-1671.

58. Xu, L.; Guo, Y.; Xie, R.; Zhuang, J.; Yang, W.; Li, T. Three-Dimensional Assembly of Au Nanoparticles Using Dipeptides. *Nanotechnology* **2002**, *13*, 725-728.

59. Ryoo, W.; Webber, S. E.; Johnston, K. P. Water-in-Carbon Dioxide Microemulsions with Methylated Branched Hydrocarbon Surfactants. *Ind. Eng. Chem. Res.* **2003**, *42*, 6348-6358.

60. Hiemenz, P. C.; Rajagopalan, R., *Principles of Colloid and Surface Chemistry*. 3 ed.; Taylor & Francis: New York, 1997; p 546-556.

Chapter 5: Effect of Salt Addition on the Formation of Biodegradable Gold Nanoclusters of Controlled Size with Intense NIR Extinction

The properties of nanoclusters formed from Au nanospheres capped with a binary monolayer of anionic citrate and cationic lysine are systematically tuned using a novel method whereby NaCl is added to the nanocluster formation process, along with the biodegradable triblock copolymer PLA(1k)-*b*-PEG(10k)-*b*-PLA(1k). Nanocluster size is tuned from ~20 nm to ~200 nm by experimentally varying Au nanoparticle, polymer, and salt concentrations during formation in order to appropriately balance van der Waals, depletion, and polymer-induced bridging attractions as well as electrostatic repulsions. Moreover, the addition of salt decreases polymer adsorption on the growing nanoclusters and the potentially decreases potential polymer bridging between individual nanospheres, cluster sub-units, and nanoclusters which would otherwise increase nanocluster diameter. The addition of NaCl furthermore screens electrostatic repulsions between constituent Au nanospheres, forming dense nanoclusters with close interparticle spacings. The close spacings of constituent nanoparticles within nanoclusters as small as ~20 nm allow for intense NIR extinction in these nanoclusters. A general paradigm is furthermore presented to evaluate the effects of the aforementioned experimental parameters on the colloidal interactions and the resulting effects on nanocluster size and NIR extinction. Complete, reversible dissociation to monomer of these nanoclusters is demonstrated upon hydrolysis of the polymer quencher over the course of 24 h. These nanoclusters are therefore promising candidates for biomedical imaging applications, as they simultaneously: (1) exhibit intense NIR extinction, (2) are of tunable size necessary for rapid cellular uptake and long circulation times in the body, and (3) completely dissociate

to sub-5.5 nm nanospheres which do not adsorb serum proteins and thus can efficiently clear from the body through the renal system.

5.1 INTRODUCTION

Gold nanoparticles which exhibit strong extinction in the near infrared (NIR) wavelength range from 650 nm to 900 nm, where tissue absorbs weakly,[1] are of great interest in biomedical imaging applications such as photoacoustic imaging. [2, 3] As two or more Au nanoparticles become closely spaced to form clusters, the surface plasmon resonance (SPR) is shifted to the NIR region, as a consequence of hybridized plasmon modes including dipoles, quadropoles, and higher-order multipoles.[4] These close spacings have been produced NIR extinction upon aggregation of Au nanoparticles within cells[5, 6] as well as *in vitro* by tunable assembly of nanoclusters with controlled size and morphology[7-10] In addition to exhibiting substantial NIR extinction, biomedical contrast agents must also clear efficiently from the body; kidney clearance requires diameters of less than ~5.5 nm.[11, 12] Even the adsorption of a single protein molecule from the bloodstream on a Au nanoparticle increase the size enough to preclude renal clearance.[10, 11, 13-15] Thus, a major challenge is to design NIR active nanoclusters which dissociate back to their primary constituents as well as avoid any protein adsorption to allow the possibility of kidney clearance.

Aggregates of Au nanospheres formed by manipulating the ionic strength or pH of a nanoparticle dispersion are often large and irreversible.[16, 17] Greater control of the size of nanoparticle clusters may be achieved by judiciously balancing the relevant repulsive and attractive colloidal forces.[7, 10, 18, 19] For example, ~6 nm oleic acid functionalized iron oxide nanoparticles may be assembled into clusters of ~100 nm to

~500 nm in diameter by tuning solvophobic interactions between the oleic acid ligands and the ethylene glycol solvent.[18] Moreover, clusters of ~12 nm primary Au nanoparticles may be assembled into clusters by balancing steric and van der Waals forces.[19] Here, the addition of alkane thiol molecules to the surface of poly(ethylene glycol) (PEG)-stabilized nanoparticles resulted in stable clusters in which size was tuned via altering the PEG concentration on the particle surface.[19] Our group has developed a method for the "quenched equilibrium" assembly of gold nanoparticles into nanoclusters of controlled size which also dissociate fully to their primary ~5 nm constituents upon degradation of a polymer quencher as shown in Figure 5.1.[7-10] Here, the sizes of NIR-active gold nanoclusters were tuned from ~20 nm to ~40 nm by balancing short-ranged van der Waals and depletion attractions with longer-ranged electrostatic repulsions provided by charged ligands.[7, 10] A biodegradable triblock copolymer, PLA(1k)-*b*-PEG(10k)-*b*-PLA(1k) was used to "quench" the nanoclusters at an equilibrium size during formation via adsorption of the hydrophobic poly(lactic acid) (PLA) blocks to the gold surface. Additionally, a free-energy model was applied to semi-quantitatively predict cluster size from gold and polymer concentrations.[7]

The reversible, quenched equilibrium nanoclusters described above were formed from nanospheres coated with a combination of anionic citrate and cationic lysine ligands.[7, 10] Here, the interaction of the highly-charged citrate-capped gold nanospheres with positively charged lysine ligands decreases the surface charge and electrostatic repulsion, and allows for cluster formation.[7, 20, 21] Lysine, which has two positive charges and one negative charge at pH 7, is known to bind weakly to gold while in a protonated state.[22] Due to this weak binding to Au, it can be assumed that lysine binds electrostatically to the negatively-charged citrate to a greater extent than to the Au surface,[7, 10] although the exact conformation of lysine on the Au surface is not fully

understood. Moreover, the lysine/citrate mixed monolayers on the Au nanosphere surfaces have been shown to completely prevent the adsorption of serum proteins in undiluted fetal bovine serum (FBS), which was attributed to the the charges being buried below the zwitterionic tips of the lysine ligand.[10] While nanoclusters of controlled size have been formed from lysine/citrate capped Au nanospheres, it would be desirable to further manipulate the colloidal forces to further control the spacing between the primary particles, the cluster size and the reversibility. For example, it is highly challenging to achieve strong NIR extinction as the cluster size decreases below 50 nm, particularly at wavelengths of interest for imaging out to 1300 nm. One way to achieve these properties would be to minimize polymer adsorption on the Au surfaces which increases the separation between particles, and bridging of polymer between nanoclusters.

Herein, we systematically tune the properties of quenched nanoclusters formed from Au nanospheres capped with a mixture of anionic citrate and cationic lysine by introducing a monovalent salt, NaCl, to vary the ionic strength. The clusters are formed from primary ~4 nm Au nanopspheres with binary ligand surfaces with a lysine/citrate ratio of 1.4/1 formed by place exchange, which has been shown to completely prevent serum protein adsorption.[10] As done previously,[7, 10] the lysine/citrate-capped nanospheres are assembled into nanoclusters by mixing a nanosphere dispersion with the biodegradable triblock copolymer PLA(1k)-*b*-PEG(10k)-*b*-PLA(1k) and subsequently controllably evaporating the aqueous solvent, as shown in Figure 5.1. The objective is to control nanocluster size and morphology by varying Au nanoparticle, polymer, and NaCl concentrations in order to systematically tune van der Waals, depletion, polymer bridging, and electrostatic interactions between primary particles. A broad framework is presented to consider the influence of each of these concentrations on the relevant colloidal interactions and how they influence the nanocluster size and morphology. The

NIR extinction provides a qualitative measure of the spacing of the primary Au nanoparticles within the clusters. The manipulation of the colloidal forces by varying the ionic strength is shown for the first time to to have a profound effect on the nanocluster morphology and spectra, as has also been reported in a companion study with cysteine/citrate capped nanospheres.[23] In both studies, the addition of salt is shown to reduce polymer adsorption on the nanoclusters, and minimize the potential for polymer bridging, resulting in closely spaced primary particles for strong NIR extinction even for nanocluster sizes as small as 24 nm. Finally, nanoclusters formed with added salt are shown to dissociate fully to sub-5.5 nm monomer upon degradation of the polymeric quencher, which is ideal for potential renal clearance from the body.

5.2 EXPERIMENTAL

5.2.1 Materials

$HAuCl_4 \cdot 3H_2O$ was acquired from MP Biomedicals LLC (Solon, OH). $NaBH_4$ and $Na_3C_3H_5O(COO)_3 \cdot 2H_2O$, and NaCl were purchased from Fisher Scientific (Fair Lawn, NJ), with L-(+)-Lysine obtained from Acros Chemicals (Morris Plains, NJ). Sigma Aldrich (St. Louis, MO) supplied PLA(1k)-*b*-PEG(10k)-*b*-PLA(1k).

5.2.2 Synthesis of Citrate-Capped Au Nanospheres and Lysine Reaction

The synthesis of the primary citrate-capped nanoparticles and the place exchange reaction to add lysine ligands in a final lysine/citrate ratio of 1.4/1 followed an earlier procedure.[7, 10]

5.2.3 Nanosphere Characterization

The following procedures are described in greater detail elsewhere.[7, 10, 23] Briefly, immediately after completion of the lysine reaction with citrate-capped Au nanospheres, the lysine/citrate Au nanospheres were diluted to ~0.04-0.08 mg/mL in DI water for dynamic light scattering (DLS) or UV-Visible-NIR (UV-Vis-NIR) analysis or diluted to the same concentration in 1 mM KCl for zeta potential measurements. DLS measurements were taken on a Brookhaven ZetaPALS analyzer with a detector angle of 90°.[10] The CONTIN method and Stokes-Einstein equation were used to analyze the data and obtain a volume-weighted distribution of hydrodynamic diameters. UV-Vis-NIR spectroscopy was also conducted on the diluted nanospheres using a Varian Cary 3E spectrophotometer with a path length of 1 cm. In order to quantify the amount of NIR extinction in each sample, we calculate the ratio of the measured absorbance at 800 nm to the measured absorbance at 525 nm (A_{800}/A_{525}). Zeta potential measurements were taken using a Brookhaven ZetaPlus analyzer. Here, zeta potential of the diluted nanosphere dispersion was determined from the average values of 30 single-cycle measurements in high-precision mode. Due to the ~4 nm nanosphere size, the Huckel model was used to relate electrophoretic mobility to zeta potential.[24]

5.2.4 Nanocluster Formation

Nanocluster formation was performed by modifying previous methods.[7, 10] An initial polymer solution concentration of 30 mg/ml was used in this work, instead of the 120 mg/ml concentration used previously. Various solutions of PLA(1k)-*b*-PEG(10k)-*b*-PLA(1k) were prepared, with NaCl concentrations between 0-200 mM, as shown in Table D.1. Nanocluster formation conditions, including initial Au and NaCl

concentrations, the polymer/Au ratio, and the evaporation extent are given in Table D.1. The quenching and purification of the nanoclusters were performed in an identical manner to previous reports.[7, 10, 23]

5.2.5 Nanocluster Characterization

DLS and UV-Vis-NIR measurements were conducted on nanoclusters in an identical manner to the analysis of nanospheres described above. Furthermore, nanocluster structure and morphology was determined via transmission electron microscopy (TEM), performed on an FEI TECNAI G2 F20 X-TWIN TEM using a high-angle annular dark-field detector. TEM samples were prepared using a VirTis AdVantage tray lyophilizer (VirTis, Gardiner, NY) after first dipping a 200 mesh Formvar coated copper TEM grid (Electron Microscopy Sciences, Hatfield, PA) into liquid nitrogen after which 5 μL of a dilute nanoclusters dispersion was pipetted onto the grid.

Thermogravimetric analysis (TGA) was conducted on the dried pellets of the 2-40-0 and 2-40-67 samples. Here, the samples were heated to 110 °C for 10 min to remove residual moisture, and then heated to 900 °C at 20 °C/min.

5.2.6 Nanocluster Dissociation

Dissociation of 20-40-67 nanoclusters was carried out *via* dilution to ~0.2 mg/ml Au in pH 5 HCl. 200 uL of a ~2 mg/mL nanocluster dispersion was added to 2.4 mL of the acid solution and the mixture was placed in a 37 °C water bath for the duration of the study (24 hours). Periodically over the 24 hours, the sample was tested for changes in extinction and hydrodynamic diameter via UV-Vis-NIR and DLS analysis without further

dilution. DLS measurements were conducted at a scattering angle of 90°, similar to the previously described characterization of Au nanospheres.

5.3 RESULTS

5.3.1 Lysine/Citrate Nanosphere Formation

The lysine/citrate-capped primary nanospheres in this study were synthesized by place exchange of lysine on citrated capped Au nanospheres in an identical manner as reported previously[7, 10] and thus exhibited very similar UV-Vis-NIR spectra and DLS size distributions, as shown in Figure D.1. Moreover, the measured zeta potential was -14.0 ± 2.8 mV, similar to the previously determined zeta potential of -16.6 ± 6.0 mV.[7, 10] These nanospheres were subsequently used to form nanoclusters.

5.3.2 Nanocluster Formation with varied Au concentration

The effects of polymer, Au, and NaCl concentrations on the diameter of Au nanoclusters are given in Table 5.1 both with and without added salt. For nanoclusters formed without added NaCl in Figure 5.2, the D_h of the smallest peak was in most cases smaller than 40 nm with small standard deviations over the mean in some cases of about 10%. However, the size distribution also included second much larger aggregate peaks often well above 100 nm (Table 5.1, Figure 5.2a). In Table 5.1, we report the average and standard deviations for both primary and secondary peaks, as well as the cumulative volume percentages of each peak. . At a constant final polymer concentration of 40 mg/ml, the increase in Au concentration to 4 mg/ml from 2 mg/ml significantly increased the D_h (Table 5.1, Figure 5.2a) for both the primary and secondary peaks in the D_h

distribution. At 8 mg/ml Au (8-40-0) the D_h increased to 223.5 ± 190.6 nm (Table 5.1, Figure 5.2a). In this case the distribution no longer appeared to be bimodal and the polydispersity was very high (Table 5.1, Figure 5.2a). For nanoclusters formed without salt, the NIR extinction is not reported, as it is unknown whether the extinction results from the primary nanocluster peak or from the secondary peak of large aggregates.

With the addition of salt at a concentration of 67 mM, the D_h distributions were relatively monodisperse without the large secondary peaks seen without salt (Table 5.1, Figure 5.2b). At the Au concentration increased from 2 mg/ml (2-40-67 particles) to 4 mg/ml (4-40-67 particles), the nanocluster D_h increased from 23.7 ± 5.2 nm to 52.0 ± 5.6 nm (Table 5.1, Figure 5.2b). Each of these values was similar to that of the smaller of the two peaks in the size distribution for nanoclusters formed without salt (Table 5.1, Figure 5.2b). For the high Au concentration of 8 mg/ml (8-40-67), the added salt reduced the nanocluster D_h markedly down to 77.6 ± 10.2 nm (Table 5.1, Figure 5.2b). At this salt concentration of 67 mM, the NIR extinction was still substantial for nanoclusters for diameters as small as ~24 nm (Table 5.2, Figure 5.3a), a remarkable result that was not possible without salt for the conditions studied. Here, for 2-40-67 samples, the yield by mass of Au, as measured by FAAS, was 20 ± 9%, similar to previously reported ~20 nm nanoclusters made with the same ligand ratio and evaporation extent (50%) used in the current study, although the mixing pathway used in this work was substantially different than in our previous work (see Discussion section).[7] Moreover, the addition of NaCl decreased the amount of polymer adsorbed on the nanoclusters, as the organic mass content, as determined by TGA, decreased from 74.2% for 2-40-0 nanoclusters to 44.1% for 2-40-67 nanoclusters (Figure 5.4).

As the salinity was increased further from 67 to 133 mM, the nanocluster diameters increased modestly at 2 mg/ml and 8 mg/ml Au, and decreased modestly for an

Au concentration of 4 mg/ml (Figure 5.2c). The changes were not far beyond experimental uncertainty in both the synthesis and characterization steps. In the discussion section we illustrate several changes in colloidal forces with added salt that may lead to either an increase or reduction in nanocluster size. The nanocluster diameter was observed to increase with increasing Au concentration in all cases, as shown in Table 5.1 and Figure 5.2c. Here, as with the 67 mM salt concentration, the large aggregates seen without salt were not present (Table 5.1, Figure 5.2c). For a salt concentration of 133 mM, the NIR extinction was quite high with an A_{800}/A_{525} above 0.6 at two of the conditions even with small D_h values from 35 to 40 nm (Table 5.2, Figure 5.3b).

5.3.3 Nanocluster Formation versus Polymer Concentration

The effect of final polymer concentration was studied for a constant final Au concentration of 2 mg/ml, without added salt and for two salinities of 67 mM, and 133 mM. Without salt, as the polymer concentration was increased from 20 mg/ml (2-20-0) to 40 mg/ml (2-40-0), the sizes of both the primary and secondary D_h peaks increased negligibly (Table 5.1, Figure 5.5a), although the volume percentage of the secondary peak increased from 8% to 15% (Table 5.1, Figure 5.5a). As with the previous set of experiments with varying Au concentration, the NIR extinction was not determined here for the polydisperse nanocluster samples formed without NaCl.

The addition of NaCl at 67 mM reduced D_h to the same value of ~24 nm for both of the lower polymer concentrations of 20 mg/ml and 40 mg/ml (Table 5.1, Figure 5.5b). This modest size decrease with salt addition is furthermore observed in TEM images for 2-20-0 and 2-20-67 particles (Figure D.2). Additionally, the NIR extinction was essentially the same in each case (Table 5.2, Figure 5.6a). At the highest salinity of 133

mM, the nanocluster D_h was about the same at both 20 mg/ml and 40 mg/ml polymer concentrations, essentially within experimental error (Table 5.1, Figure 5.5c). For both salinities, the D_h values were quite similar to the values without added salt, but without the secondary aggregate peaks above 100 nm (Table 5.1, Figure 5.5). At a salt concentration of 133 mM, the NIR extinction increases substantially from 0.330 to 0.618 with an increase in polymer concentration from 20 mg/ml to 40 mg/ml (Table 5.2, Figure 5.6b).

5.3.4 Nanocluster Dissociation

The dissociation of the 2-40-67 nanocluster sample was analyzed over a period of 24 h in pH 5 HCl by monitoring the D_h and UV-Vis-NIR spectra. Over the entire time range 24 h, the D_h decreased monotonically from 22.0 ± 5.1 nm to 4.4 ± 2.8 nm (Figure 5.7a), and the NIR extinction correspondingly decreased. The NIR extinction ratio (A_{800}/A_{525}) decreased montonically from 0.677 to 0.101 over 24 h (Figure 5.7b). The dissociation as a function of time is shown as the natural logarithm of the estimated number of particles per cluster (see Appendix D) versus time in Figure 5.7c. Here, the behavior starts out as first order kinetics and then for the last time point the magnitude of the slope of the curve decreases. After 24 hr, the nanoclusters had dissociated completely to monomer, as shown by both DLS and UV-Vis-NIR measurements (Figure 5.7).

5.4 DISCUSSION

5.4.1 Theory: Quenched Equilibrium Nanocluster Formation

We begin by summarizing the concept of the quenched equilibrium formation of Au nanoclusters, whereby nanoclusters of controlled size can be formed by balancing strong, short-ranged attractive van der Waals and depletion interactions with relatively weak, longer-ranged electrostatic interactions.[7] The nanocluster size can be predicted semi-quantitatively using a model which minimizes the nanocluster free energy to predict the equilibrium nanocluster size, n^*:[7, 20, 21]

$$n^* = \frac{5aR}{6\lambda_b kTq^2} \tag{5.1}$$

where the equilibrium size increases with the magnitude of the attraction, a, and decreases with repulsion provided by the particle charge q. Here, R is the monomer radius, and λ_b is the Bjerrum length.[7] In this way, the equilibrium cluster size is observed to increase upon an increase in attractive interactions and decrease with an increase in charge repulsion. If the surface charge on the primary nanospheres is too large, electrostatic repulsion between primary nanospheres prevents the formation of nanoclusters. As a result, equilibrium nanoclusters are often formed in organic solvents with low dielectric constants where the charge is reduced due to significant ion pairing.[25, 26] Recently, nanoclusters in water have been assembled by reducing the charge on the monomers by either moving close to the pI for protein colloids[20] or by manipulating the ligands on the surface of Au nanoparticles.[7] For Au nanoclusters, the addition of cationic lysine to citrate-capped Au nanospheres, reduces the nanosphere surface charge to the proper level.[7] At neutral pH values, the interaction between cationic lysine and the Au

nanosphere surface is extremely weak.[22] As a result, the cationic amine group on the lysine is thought to interact electrostatically with the negatively charged carboxylate groups on the citrate ligand. The interaction of lysine with a citrate-capped Au nanosphere dispersion has been shown to lower the nanosphere surface charge magnitude almost 4-fold,[7, 10] enabling nanocluster assembly.

Upon the assembly of Au nanoclusters of a controlled equilibrium size, the nanoclusters are quenched at this quasi-equilibrium state via adsorption of a polymeric stabilizer on the nanocluster surface. Adsorption of the biodegradable triblock copolymer PLA(1k)-*b*-PEG(10k)-*b*-PLA(1k), for example, quenches Au nanoclusters at an equilibrium size such that the size does not change upon dilution of the nanoclusters, which would otherwise lead to nanocluster dissociation upon the drop in Au and polymer concentrations.[7, 20, 21] It was assumed that the rate of polymer adsorption is assumed to be much slower than that rate of nanocluster assembly, such that an equilibrium size is reached prior to polymer quenching.[7] Moreover, since the polymer is biodegradable, nanocluster dissociation occurs upon polymer degradation, whereby the charged ligands on the constituent particles in the cluster reversibly force the nanoclusters apart. In the previous work, however, the effect of reducing the polymer adsorption strength on the nanoclusters and polymer bridging were not investigated. Below we show that by reducing the polymer adsorption with added salt, the potential for bridging between individual nanospheres, nanocluster sub-units, or nanoclusters is reduced as shown experimentally by the removal of the large aggregates in Figure 5.2.

5.4.2 Effect of Salt on Primary Nanoparticle Pair Potentials

The addition of salt to a nanoparticle dispersion screens the charged ligands on the nanosphere surfaces and thus reduces electrostatic repulsions between primary nanospheres. Here, the total interaction potential between two nanospheres, V_{total}, can be expressed as the sum of van der Waals, electrostatic, and depletion potentials:

$$V_{total} = V_{vdW} + V_{electrostatic} + V_{depletion} \tag{5.2}$$

Expressions for the van der Waals and depletion potentials are given in the supplemental section,[7, 24, 27] and the electrostatic potential is given by:

$$V_{electrostatic} = \frac{64\pi R\Gamma_0^2 n_\infty}{\kappa^2} e^{-\kappa H} \tag{5.3}$$

where H is the surface-surface separation distance between two spherical nanoparticles of radius R, n_∞ is the bulk ion concentration, and Γ_0 is a function of the nanoparticle surface potential ψ_0:[24]

$$\Gamma_0 = \frac{exp\left(\frac{e\psi_0}{2kT}\right)-1}{exp\left(\frac{e\psi_0}{2kT}\right)+1} \tag{5.4}$$

where e is the elementary unit of charge. ψ_0 can be derived from the experimental value of nanosphere zeta potential (see Appendix D). The inverse Debye length κ is given by:

$$\kappa = \sqrt{\frac{1000e^2 N_A}{\epsilon_r \epsilon_0 k_b T} \sum_i z_i M_i} \tag{5.5}$$

where N_A is Avogadro's number, ϵ_r is the dielectric constant of the medium, ϵ_0 is the permittivity of free space, k_b is Boltzmann's constant, T is the temperature, z_i and M_i are the valence and molarities of species *i*. From Eq. 5.5, we can deduce that the electrostatic repulsion between primary particles is affected by the salt concentration through the ionic strength dependence of the Debye parameter.

A framework for the effects of concentrations of the various species on the colloidal interactions and morphology of the nanoclusters is given in Table 5.3. The electrostatic and total interaction potentials for two primary lysine/citrate-capped nanospheres are shown in Figure 5.8 for the polymer and NaCl concentrations used to form selected nanoclusters. The vdW and depletion potentials for these conditions are shown in Figure D.3. In Figure 5.8, as the NaCl concentration is increased, the electrostatic potential decays more sharply (Figure 5.8a), resulting in a decrease in the total interaction potential (Figure 5.8b). Moreover, as polymer is added, the increase in depletion attraction changes the total interaction potential from slightly repulsive to strongly attractive, indicating the potential formation of nanoclusters (Figure 5.8b). Here, the experimentally observed increase in D_h as the salt concentration is increased from 67 mM to 133 mM is expected, as the total interaction potential becomes more attractive. However, the decrease in size and polydispersity as salt is added is not predicted by the pair potentials, as the size is expected to increase with added salt. In order to explain the observed decrease in nanocluster diameter upon NaCl addition, it is necessary to take into account the effect of salt on polymer adsorption and bridging, as is discussed in the following section.

5.4.3 Effect of Salt on Polymer Adsorption and Bridging

In this study, we show that the addition of NaCl reduces the polymer adsorption on the nanoclusters, as shown by the TGA results in Figure 5.4. The triblock copolymer PLA(1k)-b-PEG(10k)-b-PLA(1k) adsorbs weakly to the ligand capped Au surfaces through both the hydrophobic PLA groups and the PEO.[7, 8, 28] The addition of electrolytes such as NaCl has been shown to raise the chemical potential of the polymer in the aqueous phase, which would contribute an increase polymer adsorption.[29-34] This effect, however, is opposed by double layer screening of nanosphere surface charge induced by NaCl, which weakens charge-dipole and hydrogen bonding interactions between the charged ligands and polar sites on the polymer. Given the experimentally observed reduction polymer adsorption upon salt addition, it appears that the weakening of Au polymer interactions is dominant over the increase of the chemical potential of the polymer in the aqueous phase.

A short-ranged "bridging attraction" interaction is often induced by adsorbed polymers on nanoparticles, wherein the polymer is adsorbed on the surfaces of more than one entity, and thus exerts an attractive force on the two entities.[24, 35-37] This interaction has been observed both experimentally and computationally to form both aggregates of nanoparticles[35, 37-39] and nanoparticle gels.[36] For example, the aggregation of iron oxide nanoparticles has been observed to occur due to the adsorption of poly(acrylic acid) (PAA),[38, 39] whereby bridging of PAA segments complemented depletion attraction to form nanoparticle aggregates.[39] Moreover, shear-induced bridging of silica nanoparticles has been observed upon the weak adsorption of poly(ethylene oxide) (PEO).[40] We will show below that polymer adsorption and bridging have a large effect on the nanocluster morphology.

5.4.4 Nanocluster Assembly

In this section we summarize Table 5.3 to explain how changes in the composition of the Au, polymer and salt influence various colloidal interactions that effect the nanocluster diameter and interparticle spacings. An increase in Au concentration increases vdW attractions due to decreased distances between the individual Au nanospheres. The increase in vdW attraction decreases interparticle spacings within nanoclusters and increases the nanocluster diameter. With an increase in polymer concentration, both depletion attraction and bridging attraction are increased. The increase in depletion attraction both decreases interparticle spacings and increases nanocluster diameter. As explained for the influence of Au and polymer concentrations, increasing salinity also affects multiple colloidal interactions. It weakens electrostatic repulsion, which decreases the interparticle spacings within nanoclusters and allows attraction to increase the nanocluster diameter. The decrease in polymer adsorption induced by increased salinity, however, decreases bridging and thus decreases both interparticle spacings (polymer adsorption between Au primary particles) as well as nanocluster diameter. The complex balance between the relevant colloidal forces illustrated in Table 5.3 at various nanocluster conditions is now elucidated for the key conditions in this study.

5.4.4.1 Nanocluster Assembly without Salt

Without added NaCl, polymer adsorption is high relative to clusters formed with added salt. Here, an increase in Au concentration increases van der Waals attractions (Table 5.3). These increased attractive interactions result in both an increase in the nanocluster diameter for the primary nanocluster population, as shown in Figure 5.2a, as well as an increase in the size and relative amount of larger aggregates, as shown by

secondary peaks in the D_h distributions in Figure 5.2a. The large aggregates indicate the potential effects of bridging.

For nanoclusters formed without added salt, as the polymer concentration was systematically increased with a constant Au concentration, depletion attraction, and polymer bridging attractive interactions are increased (Table 5.3). As the polymer concentration is increased from 20 to 40 mg/ml, the increase in depletion attractions and bridging between nanoclusters and leads to an increase in the amount of large aggregates, as seen in Figure 5.5a. Here, the increase in these attractive interactions appeared to have a negligible effect on the size of the primary peak in the size distribution.

5.4.4.2 Effect of Salt Addition

The addition of salt to the nanocluster formation process decreases both electrostatic repulsions and polymer bridging interactions, as summarized in Table 5.3, resulting in the observed decrease in large aggregates at each salinity (Table 5.1, Figure 5.2). At the lowest Au concentration of 2 mg/ml, the opposite effects of added salt on electrostatic repulsion and bridging on nanocluster size appear to compensate each other, with a slight dominance of the effect of reduced bridging at the intermediate salinity (Figure 5.2). At the intermediate Au concentration of 4 mg/ml, the slight dominance of reduced bridging is observed at the high 133 mM salinity, as shown in Figure 5.2. For the high Au concentration of 8 mg/ml, however, the effect of bridging is apparently more substantial, and the weakened bridging may produce the significant decrease in nanocluster diameter shown in Figure 5.2. At all salinities, the nanocluster size increases monotonically with Au concentration, reflecting the increase in vdW attractions. A clear trend is not observed for either the effect of salinity or Au concentration on the

nanocluster NIR extinction, as shown in Figure 5.3. Thus, the relationship between interparticle spacing within the cluster and the colloidal interactions is complex; furthermore the NIR extinction ratio may increase with cluster size, and is therefore not only a function of the interparticle spacings within the nanoclusters.

While the addition of salt prevents the formation of large aggregates at all polymer concentrations, the peak size is similar to that of the primary DLS peak without added salt. Here, increasing the salinity from 0 mM to 67 mM slightly decreases the nanocluster diameter, as the effect of reducing bridging dominates the decrease in electrostatic repulsions and decreases size, as shown in Table 5.3. This effect is reversed at higher salinity, however, as the sizes increase at both polymer concentrations. At all salinities, the effect of increasing polymer concentration is negligible, indicating that the increases in depletion attraction and bridging are not significant enough to increase the nanocluster diameter. The effect of salinity on NIR extinction is complex, and thus a clear trend is not observed. At each salinity, an increase in NIR extinction is observed with increasing polymer concentration, particularly at the highest salinity, indicating that depletion attraction overcomes any bridging effects which would increase interparticle spacings, as shown in Table 5.3.

5.4.5 Nanocluster Dissociation

For the nanoclusters quenched with the biodegradable polymer PLA(1k)-*b*-PEG(10k)-*b*-PLA(1k), the acid catalyzed hydrolysis of the polymer quencher would result in nanocluster dissociation to charged primary Au nanoparticles.[7] As the pH is lowered to pH 5, the rate of PLA hydrolysis accelerates significantly.[41] In previous work, complete nanocluster dissociation was observed for ~30 nm nanoclusters over the course

of 24 h.[7] Here, even though the nanoclusters are formed with salt and with a different mixing pathway, the slightly smaller ~24 nm nanoclusters again dissociate completely to monomer by both UV-Vis-NIR and DLS measurements, as shown in Figure 5.7.

5.4.6 Comparison to previous lysine/citrate nanoclusters

In the current work, large aggregate peaks are observed in the D_h distributions of clusters synthesized without salt, which were not formed in our earlier study at similar conditions.[7] In the earlier study, the polymer concentration in the initial polymer solution (prior to mixing with Au nanoparticles) was high as 120 mg/ml and later found to be near a phase boundary for polymer gelation.[7] The current study uses a much lower polymer solution concentration of 30 mg/ml to avoid this gelation boundary. As a result, the initial Au concentrations, prior to mixing, were generally higher in the current work. As the polymer solution was added, bridging of this more concentrated Au dispersion may have produced the large aggregates. Fortunately, these large aggregates were not formed with the added NaCl.

5.4.7 Lysine on Au Nanoparticle Surfaces to Control the Charge

In addition to enabling nanocluster formation, the lysine/citrate nanospheres utilized in this study have been shown to completely resist the adsorption of serum proteins in undiluted fetal bovine serum (FBS).[10] Here, the lysine/citrate ratio of 1.4/1 was utilized to prevent protein adsorption, whereby the zwitterionic tips present on the lysine ligands minimize the interaction of the nanosphere surface with the proteins,[10, 13-15] and the D_h of the nanospheres does not increase from ~5 nm after incubation in 100% FBS.[10] Since these nanospheres could potentially maintain a diameter of ~5 nm even after

exposure to proteins in the bloodstream, they are good candidates for efficient renal clearance.[11, 12]

5.4.8 Applications to Biomedical Imaging and Therapy

In order for nanoparticles to be effective contrast agents in biomedical imaging, they must exhibit sufficient extinction in the NIR region.[1] Au nanoparticles such as high aspect-ratio nanorods,[42-44] nanocages,[45, 46] nanoshells,[4, 47-49] and nanostars[50, 51] have been synthesized which provide intense extinction in the NIR for biomedical imaging modalities such as photoacoustic imaging.[2, 3] The nanoclusters presented in this study are of interest for biomedical imaging due to their strong NIR extinction even for nanoclusters as small as 24 nm. The ability of these nanoclusters to biodegrade to sub-5.5 nm nanospheres which do not adsorb serum proteins, furthermore, enables these particles to clear efficiently through the kidneys.[11, 12] As a result, the nanoclusters presented in this study show enormous potential promise as biomedical contrast agents which can avoid potential toxic accumulation in the body through efficient kidney clearance.

5.5 CONCLUSIONS

The concept of quenched assembly of lysine/citrate capped Au nanospheres has been extended by the controlling the ionic strength during nanocluster formation. The addition of salt provides an enormous new degree of freedom whereby the sizes and morphologies of biodegradable nanoclusters can be tuned by controlling the amount of polymer adsorption to the Au nanocluster surface. Au nanoparticle, polymer, and NaCl concentrations have been manipulated in order to systematically balance van der Waals, depletion, electrostatic, and polymer bridging interactions in order to control nanocluster

diameter and interparticle spacings. Nanoclusters are furthermore quenched by polymer adsorption to the Au surface, such that they do not dissociate upon dilution in deionized water. The addition of salt during the nanocluster formation process minimizes the potential for polymer bridging between individual nanoclusters, nanocluster sub-units, and fully formed nanoclusters, thus quenching smaller clusters. Moreover, salt addition has been shown to reduce electrostatic repulsions between primary particles within a nanocluster and thus produce intense NIR extinction from closely-spaced constituent nanospheres within small nanoclusters, which is ideal for biomedical imaging modalities such as photoacoustic imaging.[2, 3] A general platform has been presented in which the effects of Au nanoparticle, polymer, and salt concentrations on van der Waals, depletion, polymer bridging, and electrostatic interactions has been evaluated. Moreover, the effects of the modulation of these colloidal interactions on nanocluster diameter and NIR extinction have been investigated. Furthermore, the nanoclusters are demonstrated to completely dissociate to sub-5.5 nm primary lysine/citrate capped Au nanospheres upon degradation of the polymer quencher, thus enabling them to potentially clear from body through the kidneys.

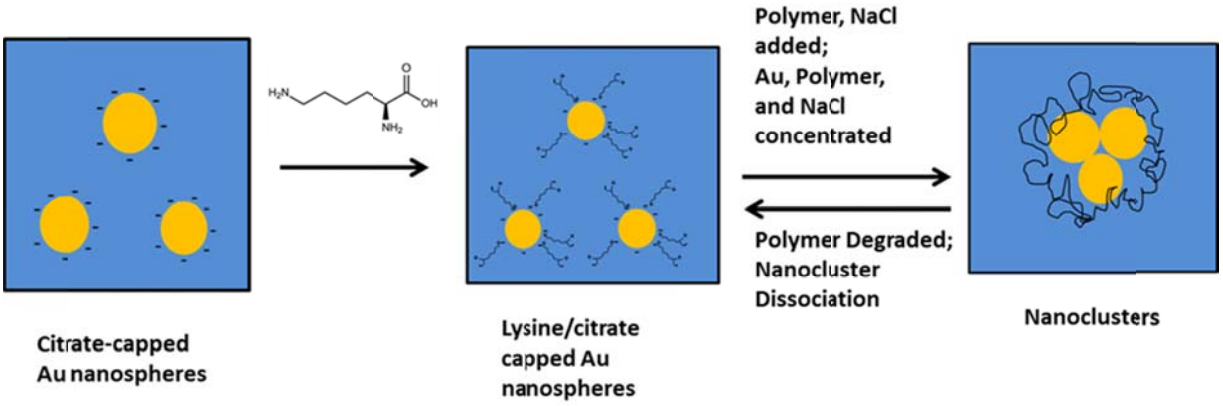

Figure 5.1: Schematic of lysine ligand exchange, nanocluster formation, and nanocluster dissociation.

Table 5.1: Nanocluster D_h values for samples synthesized at various polymer, Au, and NaCl concentrations

Sample	**Final Polymer Conc (mg/ml)**	**Final Au Conc (mg/ml)**	**Final NaCl Conc (mM)**	**Evaporation Extent (%)**	**D_h (nm) (volume percent)**
2-40-0	40	2	0	50	32.2 ± 4.4 (85%); 155.7 ± 21.1 (15%)
4-40-0	40	4	0	75	56.9 ± 8.5 (77%); 329.6 ± 49.9 (23%)
8-40-0	40	8	0	75	223.5 ± 190.6
2-20-0	20	2	0	50	34.6 ± 6.0 (92%); 163.0 ± 36.6 (8%)
2-40-67	40	2	67	50	23.7± 5.2
4-40-67	40	4	67	75	52.0 ± 5.6
8-40-67	40	8	67	75	77.6 ± 10.2
2-20-67	20	2	67	50	23.8 ± 5.2
2-40-133	40	2	133	50	35.6 ± 3.9
4-40-133	40	4	133	75	40.3 ± 4.6
8-40-133	40	8	133	75	63.3 ± 7.0
2-20-133	20	2	133	50	31.7 ± 6.5

Table 5.2: A_{800}/A_{525} values for nanoclusters formed with NaCl addition

Sample	**Final Polymer Conc (mg/ml)**	**Final Au Conc (mg/ml)**	**Final NaCl Conc (mM)**	**Evaporation Extent (%)**	**UV-Vis-NIR Extinction Ratio (A_{800}/A_{525})**
2-40-67	40	2	67	50	0.623
4-40-67	40	4	67	75	0.482
8-40-67	40	8	67	75	0.525
2-20-67	20	2	67	50	0.610
2-40-133	40	2	133	50	0.618
4-40-133	40	4	133	75	0.631
8-40-133	40	8	133	75	0.463
2-20-133	20	2	133	50	0.330

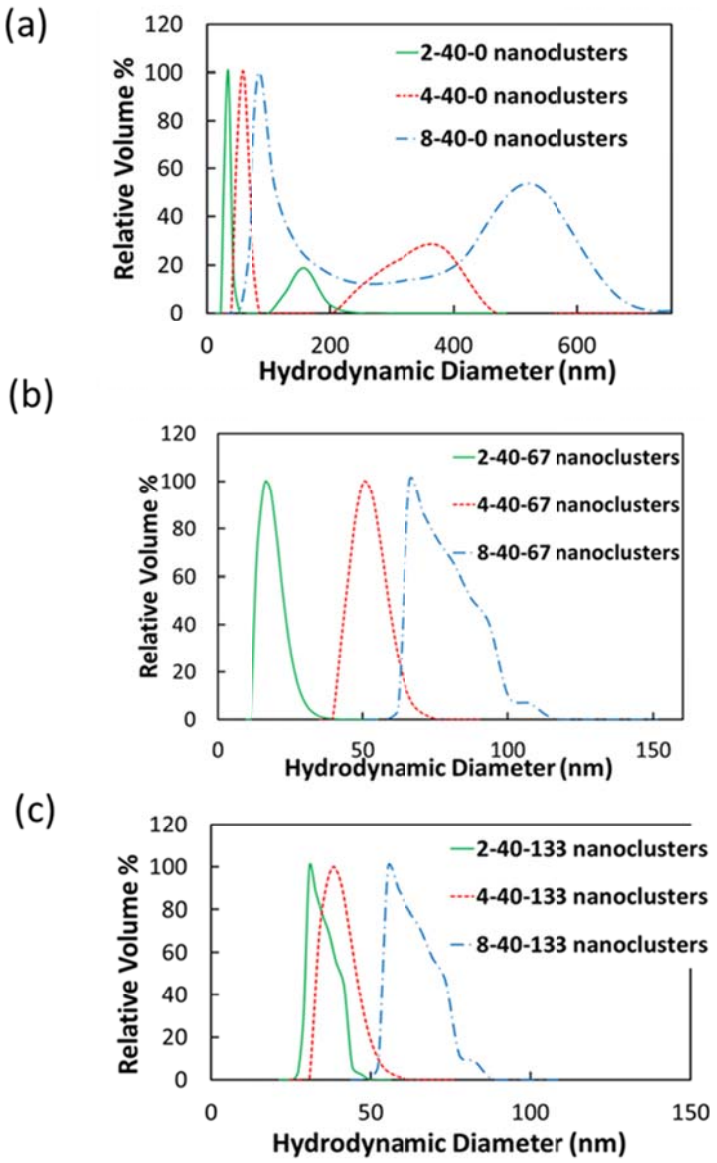

Figure 5.2: Nanocluster D_h distributions for nanoclusters formed at salinities of (a) 0 mM, (b) 67 mM, and (c) 133 mM and final Au concentrations of 2 mg/ml (green solid curves), 4 mg/ml (red dashed curves), and 8 mg/ml (blue dash-dot curves). Here the polymer concentration was kept constant at 40 mg/ml.

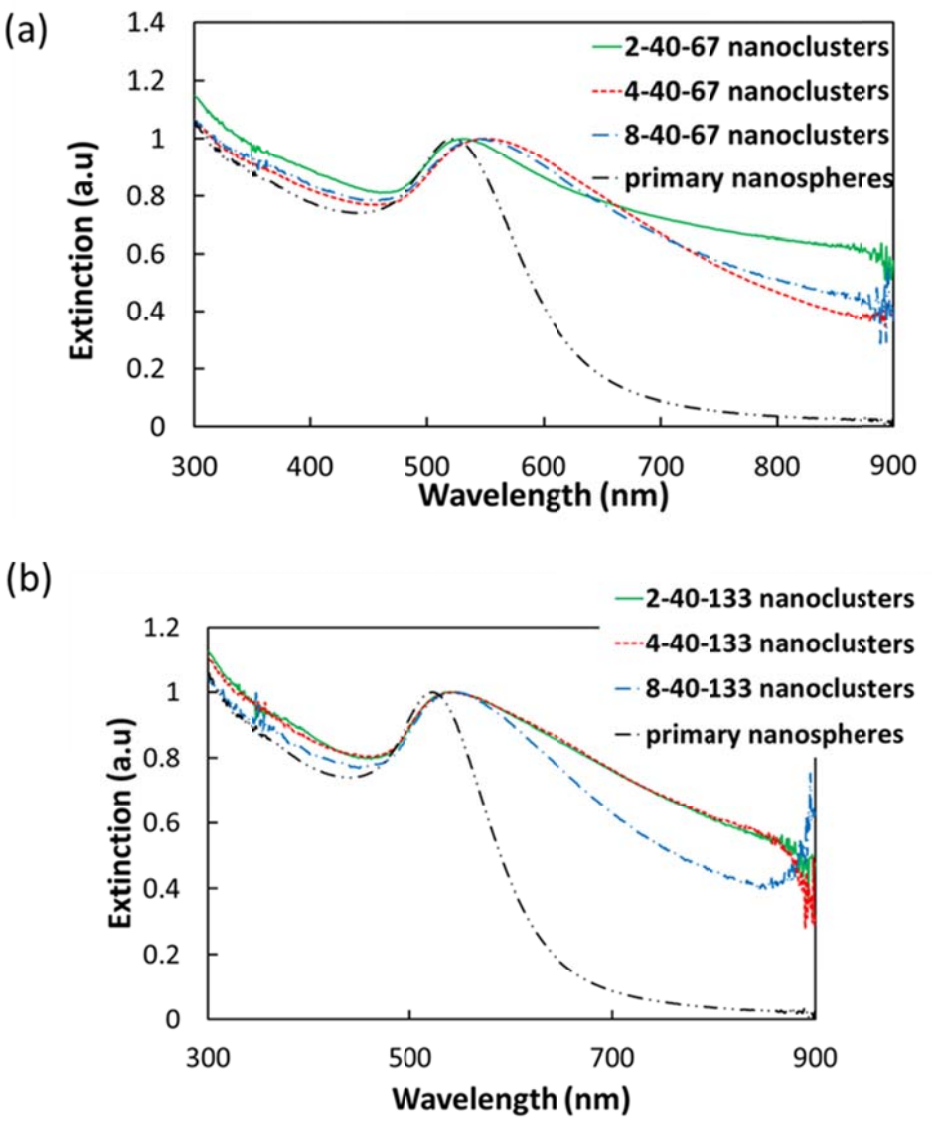

Figure 5.3: UV-Vis-NIR extinction spectra for nanoclusters formed at salinities of (a) 67 mM and (b) 133 mM. Here, the Au concentration was varied from 2 mg/ml to 8 mg/ml, while the polymer concentration was held constant at 40 mg/ml.

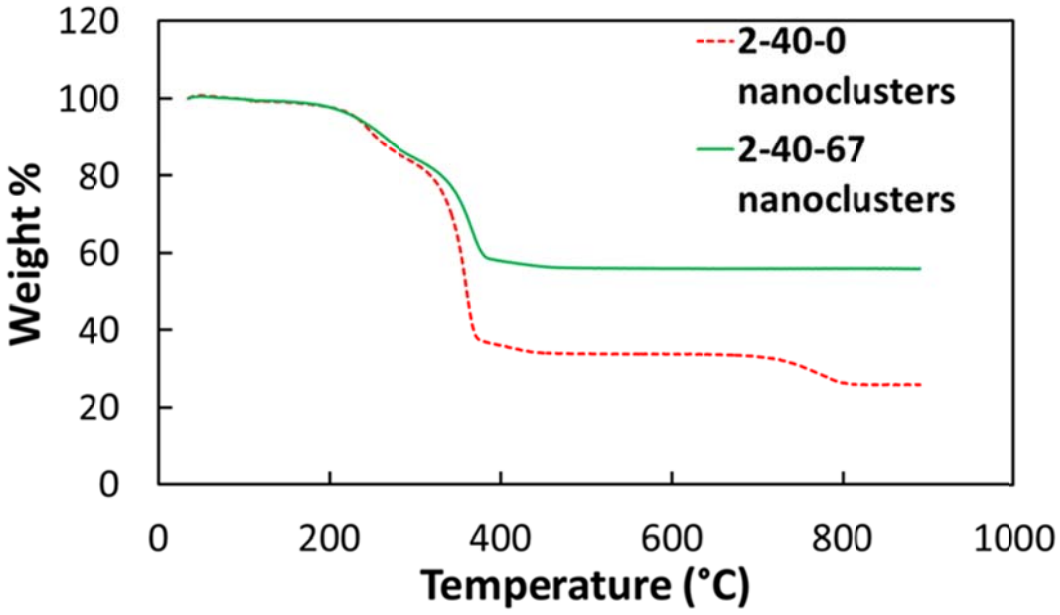

Figure 5.4: TGA results indicating the relative weight loss of 2-40-0 (dashed red curve) and 2-40-67 (solid green curve) nanoclusters as the samples are heated to 900 °C.

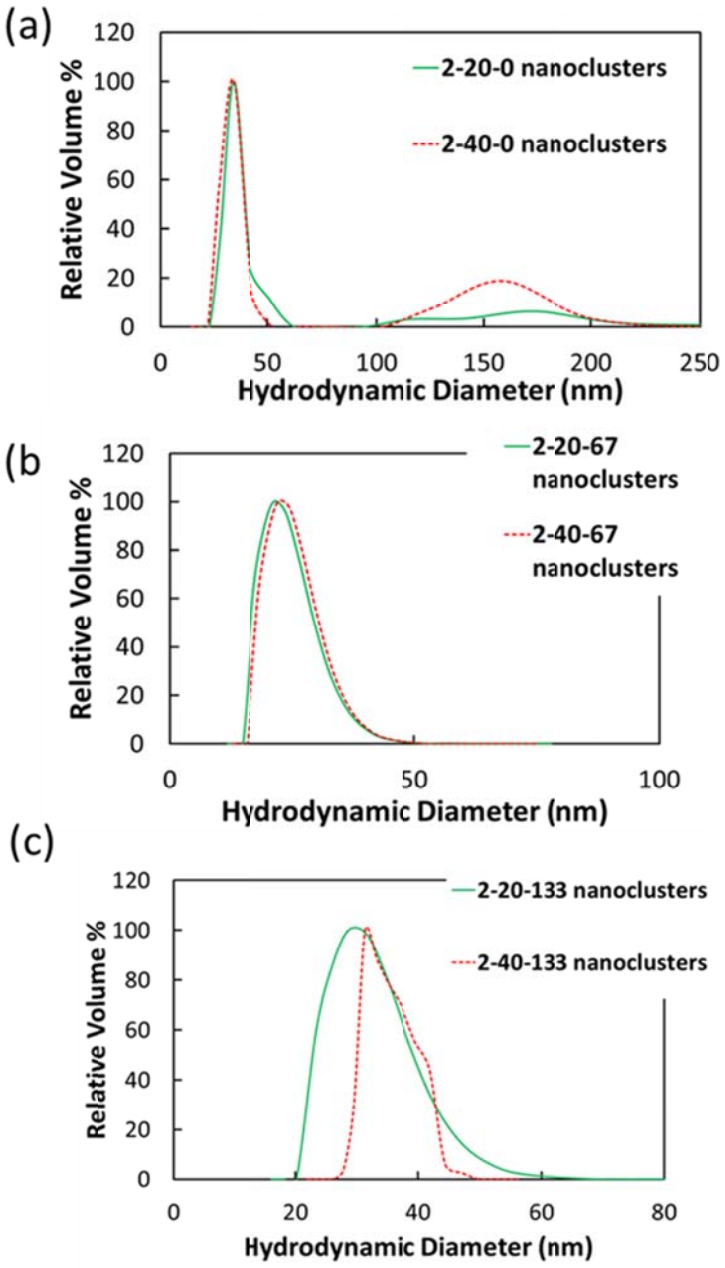

Figure 5.5: Nanocluster D_h distributions for nanoclusters formed at salinities of (a) 0 mM, (b) 67 mM, and (c) 133 mM and final polymer concentrations of 20 mg/ml (green solid curves) and 40 mg/ml (red dashed curves). Here the final Au concentration was kept constant at 2 mg/ml.

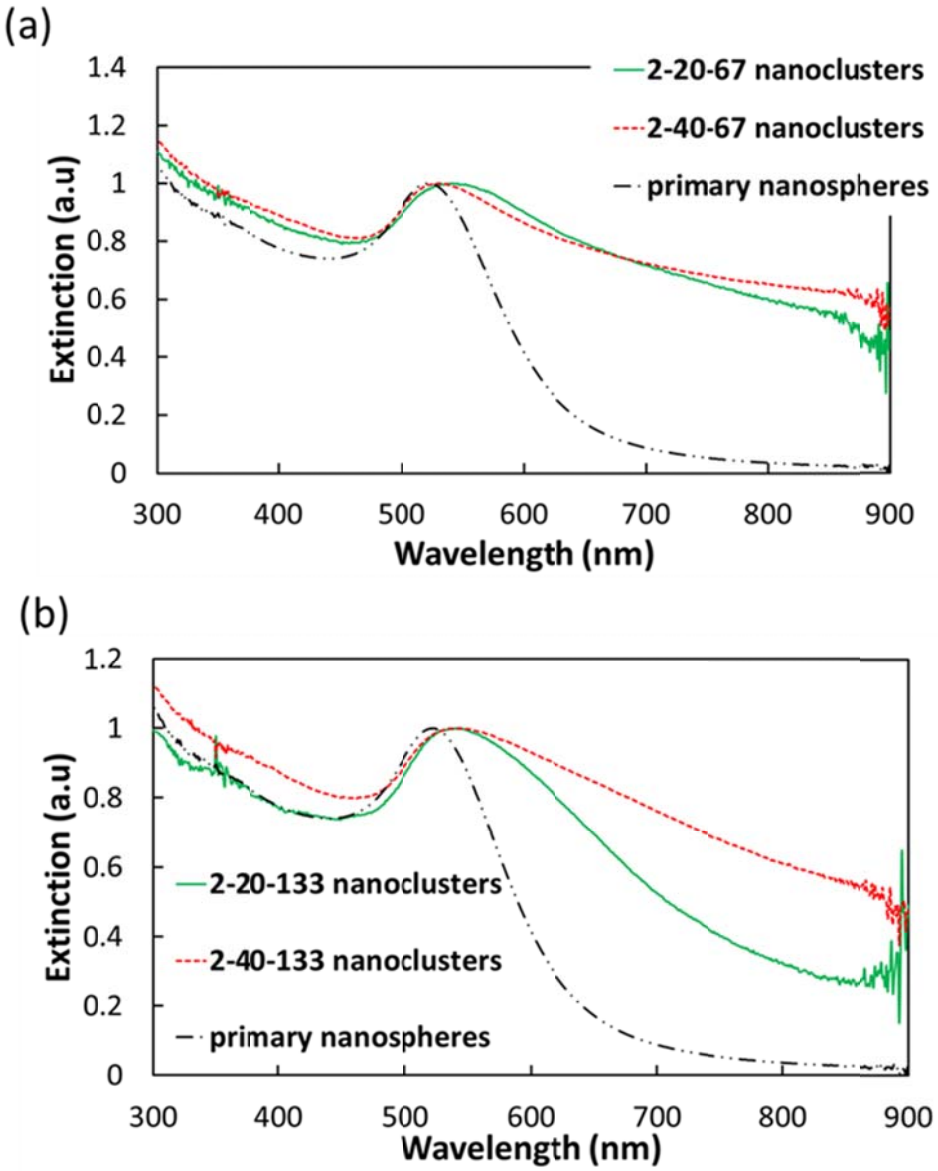

Figure 5.6: UV-Vis-NIR extinction spectra for nanoclusters formed at 20 mg/ml and 40 mg/ml polymer concentrations and salinities of (a) 67 mM and (b) 133 mM. Here the Au concentration was maintained at 2 mg/ml.

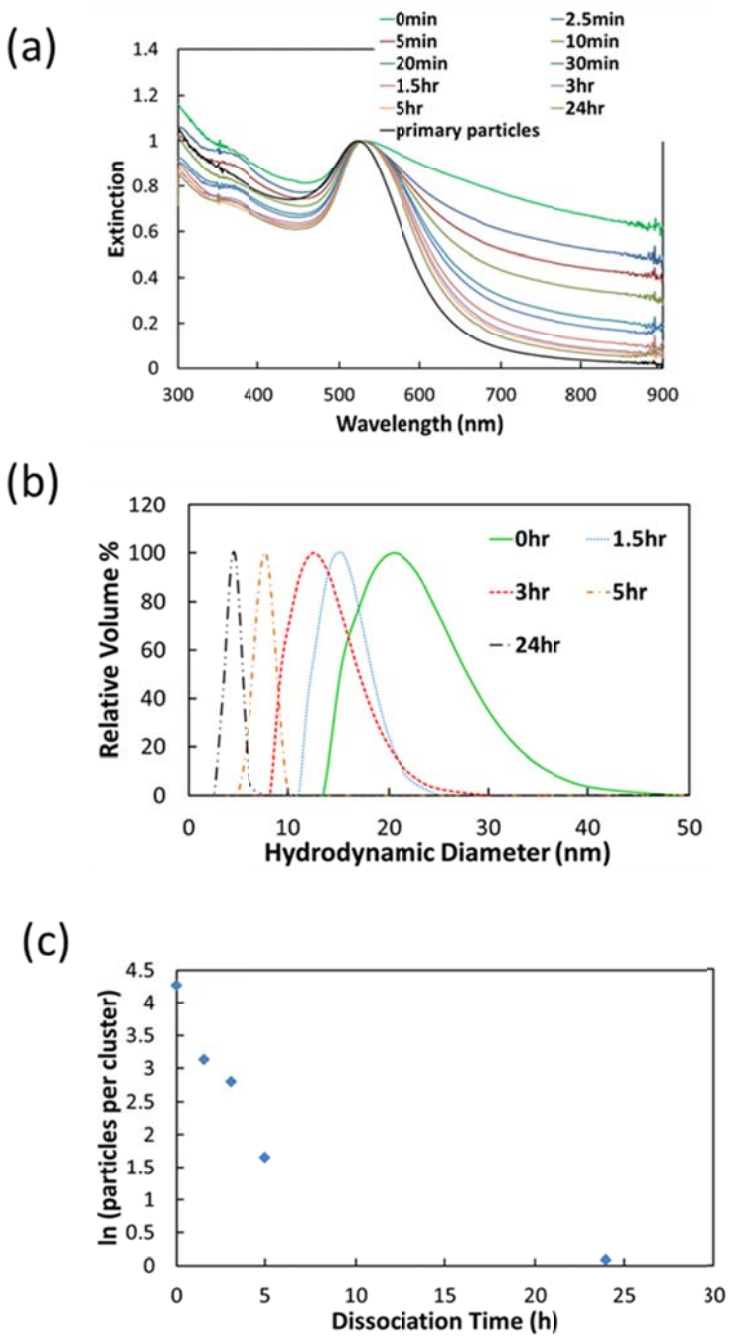

Figure 5.7: (a) UV-Vis-NIR extinction spectra, (b) DLS D_h distributions, and (c) dissociation kinetics for the in vitro dissocation of 2-40-67 nanoclusters over time. Clusters were immersed in pH 5 HCl throughout dissociation.

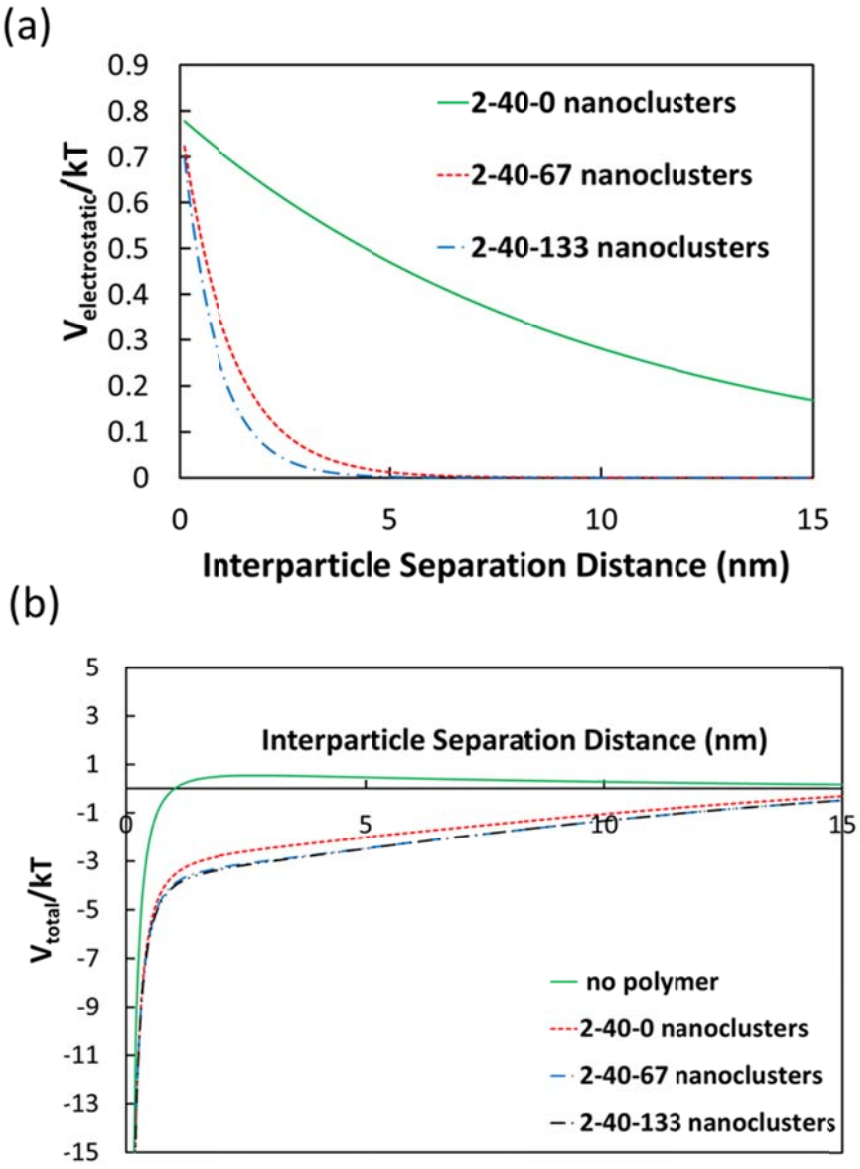

Figure 5.8: (a) Electrostatic pair potentials and (b) Total interaction pair potentials for two lysine/citrate-capped nanospheres at conditions at which 2-40-0, 2-40-67, and 2-40-133 nanoclusters are formed.

Table 5.3: Summary of tunable parameters and their effect on colloidal interactions, interparticle spacings within nanoclusters, and nanocluster diameter.

Parameter	**Interaction**	**Spacing**	**Diameter**
Increase Au Concentration	Increase vdW attraction	Decrease	Increase
Increase Polymer Concentration	Increase depletion attraction	Decrease	Increase
	Increase polymer bridging	**Increase**	**Increase**
Increase Salinity	**Decrease electrostatic repulsion**	**Decrease**	**Increase**
	Decrease polymer adsorption and bridging	**Decrease**	**Decrease**

5.6 REFERENCES

1. Weissleder, R. A Clearer Vision for in Vivo Imaging. *Nature Biotechnology* **2001**, *19*.
2. Mallidi, S.; Larson, T.; Tam, J.; Joshi, P. P.; Karplouk, A.; Sokolov, K.; Emelianov, S. Multiwavelength Photoacoustic Imaging and Plasmon Resonance Coupling of Gold Nanoparticles for Selective Detection of Cancer. *Nano Letters* **2009**, *9*, 2825-2831.
3. Yoon, S. J.; Mallidi, S.; Tam, J. M.; Tam, J. O.; Murthy, A.; Johnston, K. P.; Sokolov, K. V.; Emelianov, S. Y. Utility of Biodegradable Plasmonic Nanoclusters in Photoacoustic Imaging. *Optics Letters* **2010**, *35*, 3751-3753.
4. Halas, N. J.; Lal, S.; Chang, W.-S.; Link, S.; Nordlander, P. Plasmons in Strongly Coupled Metallic Nanostructures. *Chemical Reviews* **2011**, *111*, 3913-3961.
5. Aaron, J.; Nitin, N.; Travis, K.; Kumar, S.; Collier, T.; Park, S. Y.; Jose-Yacaman, M.; Coghlan, L.; Follen, M.; Richards-Kortum, R.*, et al.* Plasmon Resonance Coupling of Metal Nanoparticles for Molecular Imaging of Carcinogenesis in Vivo. *Journal of Biomedical Optics* **2007**, *12*.
6. Aaron, J.; Travis, K.; Harrison, N.; Sokolov, K. Dynamic Imaging of Molecular Assemblies in Live Cells Based on Nanoparticle Plasmon Resonance Coupling. *Nano Letters* **2009**, *9*, 3612-3618.
7. Murthy, A. K.; Stover, R. J.; Borwankar, A. U.; Nie, G. D.; Gourisankar, S.; Truskett, T. M.; Sokolov, K. V.; Johnston, K. P. Equilibrium Gold Nanoclusters Quenched with Biodegradable Polymers. *ACS Nano* **2013**, *7*, 239-251.
8. Tam, J. M.; Murthy, A. K.; Ingram, D. R.; Nguyen, R.; Sokolov, K. V.; Johnston, K. P. Kinetic Assembly of near-Ir Active Gold Nanoclusters Using Weakly Adsorbing Polymers to Control the Size. *Langmuir* **2010**, *26*, 8988-8999.
9. Tam, J. M.; Tam, J. O.; Murthy, A.; Ingram, D. R.; Ma, L. L.; Travis, K.; Johnston, K. P.; Sokolov, K. V. Controlled Assembly of Biodegradable Plasmonic Nanoclusters for near-Infrared Imaging and Therapeutic Applications. *ACS Nano* **2010**, *4*, 2178-2184.
10. Murthy, A. K.; Stover, R. J.; Hardin, W. G.; Schramm, R.; Nie, G. D.; Gourisankar, S.; Truskett, T. M.; Sokolov, K. V.; Johnston, K. P. Charged Gold Nanoparticles with Essentially Zero Serum Protein Adsorption in Undiluted Fetal Bovine Serum. *Journal of the American Chemical Society* **2013**, *Just Accepted Manuscript*.

11. Choi, H. S.; Liu, W.; Misra, P.; Tanaka, E.; Zimmer, J. P.; Ipe, B. I.; Bawendi, M. G.; Frangioni, J. V. Renal Clearance of Quantum Dots. *Nature Biotechnology* **2007**, *25*, 1165-1170.

12. Zhou, C.; Long, M.; Qin, Y.; Sun, X.; Zheng, J. Luminescent Gold Nanoparticles with Efficient Renal Clearance. *Angewandte Chemie International Edition* **2011**, *50*, 3168-3172.

13. Ladd, J.; Zhang, Z.; Chen, S.; Hower, J. C.; Jiang, S. Zwitterionic Polymers Exhibiting High Resistance to Nonspecific Protein Adsorption from Human Serum and Plasma. *Biomacromolecules* **2008**, *9*, 1357-1361.

14. Yang, W.; Xue, H.; Li, W.; Zhang, J.; Jiang, S. Pursuing "Zero" Protein Adsorption of Poly(Carboxybetaine) from Undiluted Blood Serum and Plasma. *Langmuir* **2009**, *25*, 11911-11916.

15. Yang, W.; Zhang, L.; Wang, S.; White, A. D.; Jiang, S. Functionalizable and Ultra Stable Nanoparticles Coated with Zwitterionic Poly(Carboxybetaine) in Undiluted Blood Serum. *Biomaterials* **2009**, *30*, 5617-5621.

16. Wilcoxon, J. P. M., J.E; Schaefer, D.W. Aggregation in Colloidal Gold. *Physical Review A* **1989**, *39*.

17. Chow, M. K.; Zukoski, C. F. Gold Sol Formation Mechanisms: Role of Colloidal Stability. *Journal of Colloid and Interface Science* **1994**, *165*, 97-109.

18. Zhuang, J.; Wu, H.; Yang, Y.; Cao, Y. C. Controlling Colloidal Superparticle Growth through Solvophobic Interactions. *Angewandte Chemie International Edition* **2008**, *47*, 2208-2212.

19. Larson-Smith, K.; Pozzo, D. C. Scalable Synthesis of Self-Assembling Nanoparticle Clusters Based on Controlled Steric Interactions. *Soft Matter* **2011**, *7*, 5339-5347.

20. Johnston, K. P.; Maynard, J. A.; Truskett, T. M.; Borwankar, A. U.; Miller, M. A.; Wilson, B. K.; Dinin, A. K.; Khan, T. A.; Kaczorowski, K. J. Concentrated Dispersion of Equilibrium Protein Nanoclusters That Reversibly Dissociate into Active Monomers. *ACS Nano* **2012**, *6*, 1357-1369.

21. Groenewold, J.; Kegel, W. K. Anomalously Large Equilibrium Clusters of Colloids. *Journal of Physical Chemistry B* **2001**, *105*, 11702-11709.

22. Joshi, H.; Shirude, P. S.; Bansal, V.; Ganesh, K. N.; Sastry, M. Isothermal Titration Calorimetry Studies on the Binding of Amino Acids to Gold Nanoparticles. *Journal of Physical Chemistry B* **2004**, *108*, 11535-11540.

23. Murthy, A. K.; Stover, R. J.; Nie, G. D.; Gourisankar, S.; Martinez, M.; Truskett, T. M.; Sokolov, K. V.; Johnston, K. P. Nanoclusters of Gold Nanospheres with Binary Monolayers of Cysteine and Citrate Formed by Quenched Assembly. *Langmuir* **2013**, *in prep*.

24. Hiemenz, P. C.; Rajagopalan, R., *Principles of Colloid and Surface Chemistry*. 3 ed.; Taylor & Francis: New York, 1997; p 546-556.

25. Sedgwick, H.; Egelhaaf, S. U.; Poon, W. C. K. Clusters and Gels in Systems of Sticky Particles. *J. Phys.-Condes. Matter* **2004**, *16*, S4913-S4922.

26. Buitenhuis, J.; Dhont, J. K. G.; Lekkerkerker, H. N. W. Static and Dynamic Light Scattering by Concentrated Colloidal Suspensions of Polydisperse Sterically Stabilized Boehmite Rods. *Macromolecules* **1994**, *27*, 7267-7277.

27. Lekkerkerker, H. N. W.; Tuinier, R., *Colloids and the Depletion Interaction*. Springer: New York, 2011; Vol. 833, p 12-15.

28. Sakai, T. A., P. Mechanism of Gold Metal Ion Reduction, Nanoparticle Growth and Size Control in Aqueous Amphiphilic Block Copolymer Solutions at Ambient Conditions. *Journal of Physical Chemistry B* **2005**, *109*, 7766-7777.

29. Tadros, T. F.; Vincent, B. Influence of Temperature and Electrolytes on the Adsorption of Poly(Ethylene Oxide)-Poly(Propylene Oxide) Block Copolymer on Polystyrene Latex and on the Stability of the Polymer-Coated Particles. *Journal of Physical Chemistry* **1980**, *84*, 1575-1580.

30. Alexandridis, P.; Holzwarth, J. F. Differential Scanning Calorimetry Investigation of the Effect of Salts on Aqueous Solution Properties of an Amphiphilic Block Copolymer (Poloxamer). *Langmuir* **1997**, *13*, 6074-6082.

31. Armstrong, J. K.; Chowdhry, B. Z.; Snowden, M. J.; Leharne, S. A. Effect of Sodium Chloride Upon Micellization and Phase Separation Transitions in Aqueous Solutions of Triblock Copolymers: A High-Sensitivity Differential Scanning Calorimetry Study. *Langmuir* **1998**, *14*, 2004-2010.

32. Su, Y.-L.; Wei, X.-F.; Liu, H.-Z. Effect of Sodium Chloride on Association Behavior of Poly(Ethylene Oxide)-Poly(Propylene Oxide)-Poly(Ethylene Oxide) Block Copolymer in Aqueous Solutions. *Journal of Colloid and Interface Science* **2003**, *264*, 526-531.

33. Jain, N. J.; George, A.; Bahadur, P. Effect of Salt on the Micellization of Pluronic P65 in Aqueous Solution. *Colloids and Surfaces A* **1999**, *157*, 275-283.

34. Mata, J. P.; Majhi, P. R.; Guo, C.; Liu, H. Z.; Bahadur, P. Concentration, Temperature, and Salt-Induced Micellization of a Triblock Copolymer Pluronic L64 in Aqueous Media. *Journal of Colloid and Interface Science* **2005**, *292*, 548-556.

35. Ganesan, V.; Ellison, C. J.; Pryamitsyn, V. Mean-Field Models of Structure and Dispersion of Polymer-Nanoparticle Mixtures. *Soft Matter* **2010**, *6*, 4010-4025.

36. Surve, M.; Pryamitsyn, V.; Ganesan, V. Polymer-Bridged Gels of Nanoparticles in Solutions of Adsorbing Polymers. *Journal of Chemical Physics* **2006**, *125*.

37. Hooper, J. B.; Schweizer, K. S. Contact Aggregation, Bridging, and Steric Stabilization in Dense Polymer-Particle Mixtures. *Macromolecules* **2005**, *38*, 8858-8869.

38. Cohen-Tannoudji, L.; Bertrand, E.; Bressy, L.; Goubault, C.; Baudry, J.; Klein, J.; Joanny, J.-F.; Bibette, J. Polymer Bridging Probed by Magnetic Colloids. *Physical Review Letters* **2005**, *94*.

39. Goubault, C.; Leal-Calderon, F.; Viovy, J.-L.; Bibette, J. Self-Assembled Magnetic Nanowires Made Irreversible by Polymer Bridging. *Langmuir* **2005**, *21*, 3725-3729.

40. Kamiayashi, M.; Ogura, H.; Otsubo, Y. Shear-Thickening Flow of Nanoparticle Suspensions Flocculated by Polymer Bridging. *Journal of Colloid and Interface Science* **2008**, *321*, 294-301.

41. Ivanova, T.; Panaiotov, I.; Proust, J. E.; Benoit, J. P.; Verger, R. Hydrolysis Kinetics of Poly(D,L-Lactide) Monolayers Spread on Basic or Acidic Aqueous Subphases. *Colloids and Surfaces B: Biointerfaces* **1997**, *8*, 217-225.

42. Huang, X.; Peng, X.; Wang, Y.; Wang, Y.; Shin, D. M.; El-Sayed, M. A.; Nie, S. A Reexamination of Active and Passive Tumor Targeting by Using Rod-Shaped Gold Nanocrystals and Covalently Conjugated Peptide Ligands. *ACS Nano* **2010**, *4*, 5887-5896.

43. Huang, X.; El-Sayed, I. H.; Qian, W.; El-Sayed, M. A. Cancer Cell Imaging and Photothermal Therapy in the near-Infrared Region by Using Gold Nanorods. *Journal of the American Chemical Society* **2006**, *128*, 2115-2120.

44. Link, S.; Mohamed, M. B.; El-Sayed, M. A. Simulation of the Optical Absorption Spectra of Gold Nanorods as a Function of Their Aspect Ratio and the Effect of the Medium Dielectric Constant. *Journal of Physical Chemistry B* **1999**, *103*, 3073-3077.

45. Chen, J.; Saeki, F.; Wiley, B. J.; Cang, H.; Cobb, M. J.; Li, Z. Y.; Au, L.; Zhang, H.; Kimmey, M. B.; Li, X.*, et al.* Gold Nanocages: Bioconjugation and Their Potential Use as Optical Imaging Contrast Agents. *Nano Letters* **2005**, *5*, 473-477.

46. Song, K. H.; Kim, C.; Cobley, C. M.; Xia, Y.; Wang, L. V. Near-Infrared Gold Nanocages as a New Class of Tracers for Photoacoustic Sentinel Lymph Node Mapping on a Rat Model. *Nano Letters* **2009**, *9*, 183-188.

47. Gobin, A. M.; Lee, M. H.; Halas, N. J.; James, W. D.; Drezek, R. A.; West, J. L. Near-Infrared Resonant Nanoshells for Combined Optical Imaging and Photothermal Cancer Therapy. *Nano Letters* **2007**, *7*, 1929-1934.

48. Hirsch, L. R.; Stafford, R. J.; Bankson, J. A.; Sershen, S. R.; Rivera, B.; Price, R. E.; Hazle, J. D.; Halas, N. J.; West, J. L. Nanoshell-Mediated near-Infrared

Thermal Therapy of Tumors under Magnetic Resonance Guidance. *Proceedings of the National Academy of Sciences* **2003**, *100*, 13549-13554.

49. Loo, C.; Lowery, A.; Halas, N.; West, J.; Drezek, R. Immunotargeted Nanoshells for Integrated Cancer Imaging and Therapy. *Nano Letters* **2005**, *5*, 709-711.

50. Khoury, C. G.; Vo-Dinh, T. Gold Nanostars for Surface-Enhanced Raman Scattering: Synthesis, Characterization and Optimization. *J. Phys. Chem. C* **2008**, *112*, 18849-18859.

51. Trigari, S.; Rindi, A.; Margheri, G.; Sottini, S.; Dellepiane, G.; Giorgetti, E. Synthesis and Modelling of Gold Nanostars with Tunable Morphology and Extinction Spectrum. *Journal of Materials Chemistry* **2011**, *21*, 6531-6540.

Chapter 6: Nanoclusters of Gold Nanospheres with Binary Monolayers of Cysteine and Citrate Formed by Quenched Assembly with Strong NIR Extinction

Gold nanospheres coated with a binary monolayer of strongly bound citrate and cysteine ligands were assembled into nanoclusters with controlled diameters from ~20 nm to ~110 nm. The short ranged depletion and van der Waals attractive forces were balanced against the long ranged electrostatic repulsion, to control the nanocluster diameter. These forces were manipulated by varying the concentrations of the nanospheres and a stabilizing polymer, PLA(1k)-*b*-PEG(10k)-*b*-PLA(1k), and in some cases of added salt. Upon reducing the charge on the Au surfaces with added salt, the polymer adsorption decreased, as determined by thermogravimetric analysis, which lowered polymer bridging of primary particle, sub-cluster, and nanocluster populations, and thus the nanocluster size. Even for clusters smaller than ~30 nm, the screening of electrostatic repulsion between the charged primary particles with added salt produced more densely packed clusters as characterized by UV-Vis-NIR spectroscopy. With the close spacings between Au primary nanospheres as small as 27 nm, the NIR extinction was strong out to 900 nm and significant even at 1300 nm. For applications in biomedical optical imaging, these small nanoclusters satisfied several key practical requirements: small ~4 nm primary particles (enabling the possibility of kidney clearance), lack of protein adsorption on the primary nanospheres, tunability of nanocluster size (beneficial for rapid cellular uptake and reducing uptake by the reticuloendothelial system), and finally close spacing of the Au nanospheres for strong NIR extinction.

6.1 INTRODUCTION

Gold nanoparticles which absorb light strongly in the near-infrared (NIR) wavelength region from 650-900 nm, where blood and tissue absorb weakly,[1] are of great utility in biomedical imaging modalities such as photoacoustic imaging.[2-5] Strong NIR extinction is often produced from nanoclusters of closely-spaced individual gold spheres, which can be assembled *in vivo*[6, 7] or *in vitro*.[8-10] Gold nanoparticles have been assembled with organic templates such as polymers, proteins, and DNA.[11] The interparticle spacing may be controlled in order to tune the NIR extinction properties of the assemblies.[12] In most cases, substantial amounts of inactive templating agent were required which may limit the spectral properties or functionality of the active material, for example, the spacing between gold plasmonic nanoparticles. Primary nanoparticles may be assembled into clusters of controlled sizes with small amounts of structure-directing agents by properly balancing the relevant colloidal forces.[8-10, 13-16] Clusters of nanoparticles have also been formed during synthesis of primary particles from precursors in both organic[17] and aqueous solvents in the presence of various stabilizers.[18-20] In these cases, the kinetics of primary particle formation must be synchronized properly relative to the kinetics of nucleation and growth of the primary particles into clusters to control to prevent excessive growth and precipitation. The reversibility of nanoclusters to dissociate back into individual primary particles has received relatively little attention. In many cases, bridges between particles formed from soluble precursors will fuse the clusters together permanently.[19]

A highly versatile synthetic concept has been presented to assemble pre-synthesized primary particles into clusters by tuning equilibrium and non-equilibrium colloidal interactions, even for small amounts of stabilizers.[8-10, 13-15] For example, primary iron oxide particles (~ 6 nm in diameter) have been assembled in ethylene glycol into

clusters of ~100 nm to ~500 nm by controlling solvophobic interactions between oleic acid ligands on the primary particles and the glycol solvent.[13] Additionally, the poly(ethylene glycol) (PEG)-capped gold nanoparticles, have been assembled into clusters by modulating interparticle steric repulsions via an alkanethiol addition in water.[14] Recently, our group has developed a "quenched equilibrium" assembly protocol to assemble small (~4 nm) gold nanoparticles into clusters of controlled size and intense NIR extinction which reversibly dissociated to monomer.[8-10] the nanocluster diameter was predicted semi-quantitatively with a free-energy equilibrium model whereby attractive, short-ranged van der Waals and depletion interactions were balanced against repulsive, longer-ranged electrostatic interactions. Nanoclusters were "quenched" at a metastable equilibrium size by the adsorption of a biodegradable triblock copolymer, PLA(1k)-*b*-PEG(10k)-*b*-PLA(1k), to the gold surface, which was assumed to occur at a much slower rate than equilibrium nanocluster assembly. However, the adsorbed polymer may also modify the equilibrium colloidal interactions and perturb the cluster size through bridging of sub-clusters and clusters, which was not considered in this previous study. These equilibrium clusters, moreover, reversibly dissociated to monomer upon degradation of the polymeric quencher.[8-10] While these studies demonstrated equilibrium behavior and reversible gold nanoclusters with high NIR extinction, the stabilities of the mixed monolayers of citrate and cationic lysine ligands on the Au surfaces were not fully known. In the protonated form, the amine group in lysine is known to bind very weakly to Au,[21] although it forms ion pair with citrate ligands on Au surfaces.[22] If the binding of a ligand on Au becomes too weak it may be displaced *in vivo* or in cells by free thiols such as glutathione (GSH), as has been observed in related systems.[23, 24] Although nanoclusters have been formed with PEG-SH, the tunability of their size has received

little attention.[8] Thus, studies of Au nanoparticles with more permanently bound thiolated ligands would be warranted, in contrast with weakly bound ligands such as lysine.

It would be desirable to further understand the mechanism of formation of quenched nanoclusters and their properties as a function of the structure and interactions of the ligands on the primary nanosphere surfaces. To date, however, quenched colloidal assembly of nanoclusters of nanospheres has not been reported for either thiolated or zwitterionic ligands. Recently, we reported ~4 nm Au primary particles capped with a binary monolayer of cysteine and citrate ligands at a ratio of 1.6/1 that do not adsorb any protein when incubated in fetal bovine serum, despite a moderate surface charge (zeta potential of -22 mV).[16] We hypothesize that the zwitterionic tips on the cysteine facilitate the weak protein adsorption by shielding the protein from the buried carboxylate charged groups of citrate. However, it remains unknown whether nanoclusters could be formed from these primary particles or others coated with thiols or zwitterionic ligands.

Herein, we extend the concept of colloidal assembly of quenched nanoclusters to primary Au nanospheres capped with a mixed monolayer containing a zwitterionic strongly bound thiol ligand, cysteine, along with citrate. The nanocluster size is shown to be tunable while achieving strong NIR extinction, indicating very closely spaced primary particles, for nanocluster diameters from ~20 nm to ~110 nm. The compositions of the mixed ligand monolayers on the surface of primary gold nanoparticles are controlled *via* a place exchange reaction of anionic citrate ligands with zwitterionic cysteine ligands, as shown in Figure 6.1. A dispersion of cysteine/citrate-capped Au nanospheres was assembled into nanoclusters upon mixing with an aqueous solution of the triblock copolymer PLA(1k)-*b*-PEG(10k)-*b*-PLA(1k) and subsequent partial evaporation of the solvent.[10] The nanoclusters were quenched at an particular diameter by polymer adsorption to the nanocluster surface, as shown in Figure 6.1. A new concept is presented

to further control nanocluster size and spectra by addition of sodium chloride to the polymer solution. The NaCl lowers the charge on the Au surface, which may be expected to weaken the polymer adsorption and thus minimizes polymer bridging attraction between constituent nanospheres, cluster sub-units, and nanoclusters. The low levels of bridging results in smaller nanoclusters, as small as 20 nm in diameter. Additionally, salt addition weakens electrostatic repulsion between primary particles and may potentially create closer particle spacings within the nanoclusters, resulting in intense and broad NIR extinction, even for ~27 nm nanoclusters. The strong thiol-Au bond for cysteine decreases the likelihood of cysteine ligands being replaced by free thiols *in vivo*.

6.2 EXPERIMENTAL

6.2.1 Materials

$HAuCl_4 \cdot 3H_2O$ was purchased from MP Biomedicals LLC (Solon, OH). $Na_3C_3H_5O(COO)_3 \cdot 2H_2O$, $NaBH_4$ from Fisher Scientific (Fair Lawn, NJ), and L-cysteine from Acros Chemicals (Morris Plains, NJ). PLA(1k)-*b*-PEG(10k)-*b*-PLA(1k) was acquired from Sigma-Aldrich (St. Louis, MO). Phosphate-buffered saline (PBS) was purchased from Gibco (Grand Island, NY).

6.2.2 Synthesis of citrate-capped Au nanospheres and cysteine ligand exchange

The ~4 nm citrate-capped Au nanospheres were synthesized by the $NaBH_4$ reduction of $HAuCl_4$ and purified by tangential flow filtration, as described previously.[10] Cysteine place exchange was conducted according to a previously described method.[16] Briefly, a solution of 1% (w/v) cysteine in deionized water was freshly prepared. In a

typical experiment, 3.2 µl of this solution was added to 0.6 ml of a 3 mg/ml citrate-capped Au nanosphere dispersion, and the mixture was stirred at room temperature for 15 min. Immediately after this reaction, nanospheres were either used for nanocluster formation or diluted for characterization.

6.2.3 Nanosphere Characterization

Immediately after cysteine ligand exchange, nanospheres samples were either diluted to a concentration of ~0.04 mg/ml Au in DI water for dynamic light scattering (DLS) or UV-Visible-NIR (UV-Vis-NIR) analysis, or diluted to ~0.04 mg/ml Au in 1 mM KCl for zeta potential analysis. DLS measurements were taken on these diluted samples using a Brookhaven ZetaPALS analyzer with a scattering angle of 90° as reported previously.[10, 16] The data were analyzed using the CONTIN method, and the Stokes-Einstein equation was used to obtain a volume-weighted distribution of hydrodynamic diameters. UV-Vis-NIR spectroscopy was also conducted on the diluted nanocluster samples using a Varian Cary 3E spectrophotometer with a path length of 1 cm. Unless otherwise noted, the extinction was normalized as unity at the peak wavelength longer than 500 nm. Zeta potential measurments were performed using a Brookhaven ZetaPlus analyzer in high-precision mode with an applied electric field of ~15 V/cm, in which 30 single-cycle measurements were taken. The average and standard deviations of these measurements are reported. Due to the nanocluster size (see Results), the Huckel model was used to relate the measured electrophoretic mobility to a zeta potential.[25] Au dispersion concentrations were determined by flame atomic absorption spectroscopy (FAAS), utilizing a GBC 908AA analyzer (GBC Scientific Equipment Pty Ltd.) with an air/acetylene flame at a wavelength of 242.8 nm. Long-range UV-Vis-NIR

measurements were performed on a Cary 5000UV-Vis NIR spectrometer using a quartz cuvette with a path length of 1 cm.

6.2.4 Nanocluster Formation

Immediately after the completion of the cysteine place exchange reaction, cysteine/citrate-capped Au nanospheres were used to synthesize nanoclusters in a manner adapted from a previously reported method.[10] In most cases, a 30 mg/ml solution of PLA(1k)-*b*-PEG(10k)-*b*-PLA(1k) was freshly prepared with a NaCl concentration of 100 mM. For the base case with a 5/1 polymer/Au ratio, 300 µl of 30 mg/ml polymer solution was added to 0.6 ml of 3 mg/ml cysteine/citrate capped nanospheres in 5 iterations of 60 µl each over a time period of 10 min, under vigorous stirring. After the polymer solution was added, the mixture was placed in a 13 mm x 44 mm glass vial, which was placed in a 40 °C water bath and stirred vigorously. Dried air was subsequently blown over the sample by a small tube inserted into the vial at a rate of approximately 26 L/min. The sample was then evaporated to the desired amount, which was determined volumetrically by a pre-marked line drawn on the sample vial to indicate the desired evaporation extent, wherein the drop in height of the solvent meniscus was monitored to determine the evaporation extent to within ~5%. Typically, 50% solvent evaporation required ~20 min. and 100% ~35 min. After solvent evaporation, nanocluster formation was stopped by adding 30 ml of deionized water to the sample. The resulting solution was then centrifuged in a 50 ml polystyrene centrifuge tube at 9700 rpm for 10 min, resulting in ~500 ul of a lower colloidal phase of densely-packed nanoclusters, which was collected, and an upper colloidal phase (~ 25.5 ml) of monomer Au and highly fractal smaller aggregates was discarded. A light meniscus was observed between the dense lower phase

and the upper phase. A representative photograph of these colloidal phases for 3-5-95 nanoclusters is shown in Figure E.2.

Nanocluster formation was carried out at polymer/Au ratios ranging from 5/1 to 20/1, and with initial Au concentrations ranging from 0.5 mg/ml to 3 mg/ml. The extent of evaporation was varied from 50% to 95%, and the salt concentration in the polymer solution was varied from 0 mM to 100 mM.

6.2.5 Nanocluster Characterization

Nanocluster morphology was assessed by transmission electron microscopy (TEM), which was performed on an FEI TECNAI G2 F20 X-TWIN TEM using a high-angle annular dark-field detector. Samples were prepared by first dipping a 200 mesh copper-coated carbon TEM grid (Electron Microscopy Sciences, Hatfield, PA) into liquid nitrogen. 5 ul of a dilute nanocluster dispersion was then pipetted on the grid, which was subsequently dried using a VirTis AdVantage tray lyophilizer (VirTis, Gardiner, NY). DLS, UV-Vis-NIR, long-range UV-Vis-NIR, and zeta potential measurements were performed on nanoclusters in an identical manner to nanospheres.

Thermogravimetric analysis (TGA) was conducted on dried 3-5-95 and NS-95 samples using a Mettler-Toledo TGA/SDTA851e instrument. TGA samples were initially heated to 110 °C and held at that temperature for 10 min in order to remove any water that may have remained in the samples. These samples were subsequently heated to 900 °C at a rate of 20 °C/min.

6.3 RESULTS

6.3.1 Synthesis of Cysteine/Citrate Capped Nanospheres

The cysteine/citrate-capped nanospheres used in this study were synthesized identically to nanospheres reported in a previous study.[16] The UV-Vis-NIR spectra and DLS D_h distribution of these nanospheres were determined to be essentially the same as those in the previous study, as shown in Figure E.1. Moreover, the measured zeta potential of the nanospheres was -20.5 ± 1.3 mV, similar to the previously reported value of -21.6 ± 1.7 mV.[16]

6.3.2 Effect of Evaporation Extent on Nanocluster Formation without Salt Addition

In order to investigate the effect of NaCl addition on nanocluster formation, we first synthesized nanoclusters without any added salt at an initial Au concentration of 3.0 mg/ml, a polymer/Au ratio of 5/1 (w/w) as shown in Table 6.1 and Figures 6.3a and 6.3b. The sample name consists of three numbers, the initial Au concentration in mg/ml, the polymer/Au ratio by mass, and the extent of evaporation. As shown in TEM images in Figure 6.2, substantial nanocluster growth is as the evaporation extent is increased from 50% to 95% (Figure 6.2a-c). For the NS samples, as the extent of evaporation is increased from 50% to 75%, the Au and polymer concentrations are increased from 4 mg/ml and 20 mg/ml, respectively, to 8 mg/ml and 40 mg/ml, and the nanocluster D_h increased only modestly from 27.9 ± 3.1 nm to 38.5 ± 4.9 nm (Figure 6.3a, Table 6.1). Interestingly, the NIR extinction ratio at 800 nm (defined as the ratio of the measured absorbance at 800 nm to the measured absorbance at 525 nm, or A_{800}/A_{525}) decreased slightly with increasing evaporation extent, from 0.376 to 0.321 (Figure 6.3b, Table 6.1). As the evaporation extent was further increased to 95%, the Au and polymer

concentrations were increased to 40 mg/ml and 200 mg/ml, respectively, and the nanocluster D_h increased markedly to 109.3 ± 9.8 nm (Figure 6.3a, Table 6.1). For the much larger clusters, the NIR extinction ratio increased to 0.673 (Figure 6.3b, Table 6.1) as has been seen for lysine/citrate clusters.[8]

6.3.3 Effect of Salt Addition on Nanocluster Formation

With 100 mM added salt in the polymer solution, a series of three experiments was performed with increasing evaporation extents at otherwise the same conditions as for the no salt experiments, as shown in Table 6.1 and Figure 6.3c and d. For these experiments, the final NaCl concentrations were 66.7 mM, 133 mM, and 668 mM for evaporation extents of 50%, 75%, and 95%, respectively (Table 6.1). As the extent of evaporation was increased from 50% to 75%, the Au and polymer concentrations increased from 4 mg/ml to 8 mg/ml and from 20 mg/ml to 40 mg/ml, respectively.(Table 6.1). Here, the nanocluster D_h changed negligibly, from 24.9 ± 4.9 nm to 25.9 ± 4.6 nm (Figure 6.3c, Table 6.1), and the NIR extinction ratio increased modestly from 0.381 to 0.421 (Figure 6.3d, Table 6.1). When the evaporation extent was increased to 95%, the nanocluster D_h increased only slightly, to 27.2 ± 4.2 nm (Figure 6.3c, Table 6.1). The corresponding NIR extinction ratio, however, increased substantially to 0.676 (Figure 6.3d, Table 6.1). The nanocluster yield for 3-5-95 nanoclusters was 30 ± 2% by mass of Au, as determined by FAAS. At a concentration of 70 μg/ml, the extinction for 3-5-95 nanoclusters was 0.731, resulting in a nanocluster extinction coefficient at 800 nm (ε_{800}) of 0.010 $cm^2/\mu g$ (see Appendix E for calculation), which is similar to previously reported nanoclusters.[10] Moreover, substantial NIR extinction was observed for 3-5-95

nanoclusters at wavelengths as high as 1300 nm, where the ε_{800} was 0.004 $cm^2/\mu g$ (Figure 6.4).

These results indicate a profound effect of salt on the nanocluster properties, particularly at higher salinities. At an evaporation extent of 50% with a salinity of only 66.7 mM, nanocluster D_h changes negligibly, from 27.9 ± 3.1 nm at 0 mM to 24.9 ± 4.9 nm at (Figure 6.3 and Table 6.1). Similarly, the NIR spectra and extinction ratio stays relatively constant, As the extent of evaporation is increased to 75%, however, where [NaCl] increases to 133 mM (Table 6.1), the D_h decreases significantly from 38.5 ± 4.9 nm without NaCl to 25.9 ± 4.6 nm. Remarkably, despite the decrease in size, the NIR extinction ratio, acutally increases from 0.321 to 0.421 with added salt (Figure 6.3b, Figure 6.3d, Table 6.1). In previous studies that did not use salt, the NIR extinction ratio nearly always increased with nanocluster size.[8, 10] At the highest salinity of 668 mM for 95% evaporation (Table 6.1) the effect of salt was even more dramatic, as D_h, decreased from 109.3 ± 9.8 nm without salt to 27.2 ± 4.2 nm with added salt. Here, the NIR extinction ratio changed negligibly, from 0.673 for 0 mM NaCl to 0.676 for 668 mM NaCl (Figure 6.3b, Figure 6.3d, Table 6.1), as the NIR extinction was already high for the large nanocluster without added salt. Thermogravimetric analysis (TGA) was also performed on 3-5-95 and NS-95 nanoclusters in order to determine organic content in the nanoclusters. Here, a marked decrease in the percent of organic content was observed from 31.4% for NS-95 particles without salt to 14.4% for 3-5-95 particles with salt (Figure 6.5). In the cases of particles made both with salt and without salt, the zeta potentials of the nanoclusters did not change substantially with the extent of evaporation nor with the salt concentration (Table 6.1).

6.3.4 Effect of Starting Gold Concentration on Nanocluster Formation

The starting Au concentration was varied from 0.5 mg/ml to 3 mg/ml to attempt to manipulate the nanocluster sizes and spectra, in each case with salt present. These nanocluster samples were synthesized with a 5/1 (w/w) polymer/Au ratio and 95% evaporation, such that the final Au concentrations were 9.2 mg/ml (0.5-5-95) and 40 mg/ml (3-5-95), respectively, and the final polymer concentrations were 46.2 mg/ml and 200 mg/ml (Table 6.2). A slight increase in size of nanoclusters formed with initial Au concentrations of 0.5 mg/ml (0.5-5-95) and 3 mg/ml (3-5-95) shown in the TEM images in Figure 6.6 was consistent with the D_h values given in Table 6.2 and Figure 6.7, which increased from 22.5 ± 4.4 nm to 27.2 ± 4.2 nm (Figure 6.7a, Table 6.2). The NIR extinction ratio, however, decreased slightly from 0.718 to 0.676. The nanocluster zeta potentials also decreased in magnitude slightly from -24.1 ± 0.7 mV to -19.1 ± 0.7 mV. The sample hydrodynamic diameters and extinction spectra were highly reproducible, as shown in Figures E.4 and E.5.

6.3.5 Effect of Polymer/Au Ratio on Nanocluster Formation

Nanocluster formation was also investigated by varying the polymer/Au ratio. Here, the initial Au concentration and evaporation extent were held constant at 3.0 mg/ml and 95%, respectively. The salt concentration in all of these samples in the feed polymer solution was 100 mM, and the polymer/Au ratio was varied from 5/1 (3-5-95) to 20/1 (3-20-95) whereby the final polymer concentration increased from 200 to 400 mg/ml. With the increase in polymer concentration, the final Au concentration decreased from 40 mg/ml (3-5-95) to 20 mg/ml (3-20-95), whereas the final NaCl concentration increased from 668 mM to 1333 mM (Table 6.2). The morphologies of nanoclusters are shown in the TEM images in Figure 6.8. As the polymer/Au ratio is increased from 5/1 to 10/1, the

D_h decreased slightly, from 27.2 ± 4.2 nm to 21.2 ± 3.9 nm (Figure 6.9a, Table 6.2). Moreover, the NIR extinction ratio decreased from 0.676 to 0.542 (Figure 6.9b, Table 6.2). A further increase of the polymer/Au ratio to 20/1 w/w resulted in a dramatic increase in D_h to 52.0 ± 6.7 nm (Figure 6.9a, Table 6.2), while the NIR extinction ratio remained similar to that of the 3-10-95 particles at 0.534 (Figure 6.9b, Table 6.2). The nanocluster zeta potential in all cases remained relatively constant (Table 6.2).

6.4 DISCUSSION

6.4.1 Quenched Equilibrium Formation Mechanism

Previously, the formation of gold nanoclusters was shown to occur *via* a "quenched equilibrium" mechanism, whereby nanoclusters are quenched at essentially an equilibrium size via polymer adsorption on the nanocluster surface.[8-10] According to a free energy model,[10, 26, 27] the nanocluster size is shown to increase with the magnitude of short-ranged attraction between primary particles, and decrease with long-ranged electrostatic repulsion between a charged cluster and a monomeric Au primary particle. Here, the attractive interaction is a combination of short-ranged van der Waals attraction between the gold spheres and depletion attraction produced by the exclusion of polymeric micelles from the gap between two gold nanoparticles. This short-ranged attraction is balanced by long-ranged electrostatic repulsion provided by the charged ligands on the primary nanoparticles.

At the minimum free energy, the equilibrium number of particles n^* in a nanocluster for primary particles each with charge q is:[10, 27]

$$n^* = \frac{5aR}{6\lambda_b kTq^2} \quad (6.1)$$

where a is the attractive short-ranged interaction between particles, R is the primary particle radius, and λ_b is the Bjerrum length.[10] Previously, this model has been used to predict the size of equilibrium Au nanoclusters semi-quantitatively, whereby short-ranged van der Waals and depletion interactions were tuned by varying Au and polymer concentrations, respectively.[10]

As the nanoclusters are assembled, they are quenched in an essentially equilibrium state by irreversible adsorption of the polymer to the nanocluster surface. With PLA(1k)-*b*-PEG(10k)-*b*-PLA(1k), however, the adsorption is relatively weak, due to the relatively small amount of hydrophobic PLA in the polymer relative to the hydrophilic PEG. Thus, the polymer adsorption is slower than the rate of nanocluster growth, ensuring that the polymer does not adsorb on individual gold spheres and preclude the close interparticle spacings necessary for NIR extinction. Moreover, polymer adsorption provides steric stabilization to the nanocluster surface, such that dilution of the quenched equilibrium nanoclusters in water does not change the size. In these previous studies,[10, 16] however, the effects of salt on the electrostatic repulsion between Au primary particles and on polymer adsorption strength and bridging were not explored. Below, we will show that these effects provide additional degrees of freedom to simultaneously obtain very small clusters with close interparticle spacings between primary particles, for strong NIR extinction, and low levels of adsorbed polymer.

6.4.2 Effect of Salt Addition on Pair Potentials

The addition of an electrolyte such as NaCl to a Au nanoparticle dispersion screens the charges and reduces the electrostatic repulsions between particles. The total pair potential V_{total} can be expressed by the equation:

$$V_{total} = V_{vdW} + V_{electrostatic} + V_{depletion} \tag{6.2}$$

where the VDW and depletion terms are described in the supplemental section[10, 28] and the electrostatic potential is given by:[25]

$$V_{electrostatic} = \frac{64\pi R\Gamma_0^2 n_\infty}{\kappa^2} e^{-\kappa H} \tag{6.3}$$

Here, H is the surface-surface separation distance between two spheres of radius R, n_∞ is the bulk ion concentration, and Γ_0 is a function of the nanoparticle surface potential ψ_0 :[25]

$$\Gamma_0 = \frac{exp\left(\frac{e\psi_0}{2kT}\right)-1}{exp\left(\frac{e\psi_0}{2kT}\right)+1} \tag{6.4}$$

where e is the elementary unit of charge. In this case ψ_0 can be derived from the experimental value of nanosphere zeta potential, as is discussed in the Supplemental section.

The inverse Debye length, κ, is given by:

$$\kappa = \sqrt{\frac{1000e^2 N_A}{\epsilon_r \epsilon_0 k_b T} \sum_i z_i M_i} \tag{6.5}$$

where N_A is Avogadro's number, ϵ_r is the dielectric constant of the medium, ϵ_0 is the permittivity of free space, k_b is Boltzmann's constant, T is the temperature, z_i and M_i are the valence and molarities of species *i*. Here, we see that the electrostatic interaction is affected by the salt concentration through the ionic strength dependence of the Debye parameter.

The electrostatic, depletion, and total interaction potentials of two cysteine/citrate capped spheres in for the polymer and NaCl concentrations used to form 3-5-50, 3-5-75, and 3-5-95 nanoclusters are shown in Figure 6.10. The vdW potential which comprises the total interaction potential is shown in Figure E.3. Here, as the NaCl concentration is increased from 1 mM (no nanocluster formation) to 668 mM for 3-5-95 nanoclusters, the decay of the electrostatic repulsion potential becomes sharper (Figure 6.10a). Moreover, as the polymer concentration is increased from 20 mg/ml for 3-5-50 nanoclusters to 200 mg/ml for 3-5-95 nanoclusters, the depletion potential becomes substantially more attractive (Figure 6.10b). The combination of increased NaCl concentration and increased polymer concentrations as the extent of evaporation is increased is depicted in Figure 6.9c. Here, for no added polymer and a negligible NaCl concentration of 1 mM, the total potential is positive, indicating nanoclusters are not formed (Figure 6.10c). For 3-5-50 nanoclusters, the reduction in electrostatic potential combined with the attractive depletion potential makes the total interaction potential attractive, and as the polymer and salt concentration increase for 3-5-75 nanoclusters, the total potential becomes more negative (Figure 6.10c). This potential becomes even more negative for the most concentrated 3-5-95 nanoclusters, where depletion attraction is even stronger (Figure 6.10c). The increase in NIR extinction with added salt indicates more closely spaced Au nanoparticles, which would be consistent with a reduction in the electrostatic repulsion. Even the very small ~20-30 nm nanoclusters formed with NaCl addition exhibit intense

NIR extinction, particularly at the highest evaporation extent and salinity, which was not the case for the experiments without salt present. Moreover, the reduction in charge repulsion leads to closer spacing between primary particles and thus less polymer into the interior of the nanoclusters, as seen by TGA measurements (Figure 6.5).

6.4.3 Effect of Salt Addition on Polymer Adsorption and Bridging

For the triblock PLA-*b*-PEG-*b*-PLA copolymer in the current study, as NaCl is added, the polymer adsorption is reduced, as shown by the TGA results in Figure 6.5.[29] NaCl raises the chemical potential of the polymer in water,[30-32] which alone would enhance the driving force for polymer adsorption. However, salt also screens the charges on bound ligands and thus weakens the charge-dipole interactions and hydrogen bonding with the polymer, which disfavors adsorption. The data indicate this weakening of the ligand-polymer interactions is dominant.

The adsorption of a nonionic polymer such as PLA-*b*-PEG-*b*-PLA to nanoparticle surfaces can induce a short-ranged attractive force between particles, "bridging attraction", between two or more particles.[25, 33, 34] This polymer-induced attraction has been experimentally and computationally observed to contribute to formation of aggregates of nanoparticles[33-36] as well as nanoparticle gels.[37] In the case of adsorption of poly(acrylic acid) (PAA) onto iron oxide nanoparticles,[35, 36] nanoparticle assembly was attributed to an depletion attraction pushing particles together, after which short-ranged bridging irreversibly assembled the particles.[36] Bridging effects have additionally been observed in the case of weakly-adsorbing polymers such as poly(ethylene oxide) (PEO) on silica nanoparticles, whereby nanoparticle aggregates were formed by shear-induced polymer bridging.[38]

During nanocluster growth, the lower polymer adsorption with salt addition minimizes bridging attraction, consistent with the smaller nanocluster size in Table 6.1 and Figure 6.3. This effect appears to be dominant relative to an increase in cluster size that would result from a reduction in electrostatic repulsion upon screening the charges with salt. Even with the reduced adsorption of polymer with added salt, sufficient polymer was adsorbed to quench the size of the nanoclusters against any change upon dilution in DI water.

6.4.4 Assembly of Nanoclusters of Cysteine/Citrate Capped Nanospheres

The effect of tuning Au, polymer, and salt concentrations on the colloidal interactions, along with the expected effects on nanocluster diameter and interparticle spacings, are summarized in Table 6.3. An increase in Au concentration increases van der Waals attractions, which would increase nanocluster diameter and may decrease interparticle spacings within the nanoclusters, (Table 6.3). Additionally, increasing the polymer concentration increases both depletion and polymer bridging attractions. The increase in depletion attraction may decrease interparticle spacings, while increasing nanocluster diameter. In this way, increasing polymer concentration has opposing effects on interparticle spacings, but has synergistic effects on increasing nanocluster diameter (Table 6.3). The addition of NaCl, moreover, decreases both electrostatic repulsions and polymer adsorption, as shown experimentally, which would decrease polymer bridging. Here, both effects may be expected to decrease interparticle spacings. NaCl addition would produce competing effects on nanocluster diameter, however, as the decrease in electrostatic repulsion increases nanocluster diameter, while the decrease in polymer bridging decreases the diameter (Table 6.3). In summary, the nanocluster diameter and

NIR extinction are determined by a combination of van der Waals, depletion, and electrostatic interactions as well as bridging attractions due to adsorbed polymer. The balance between these interactions and their effects on nanocluster properties for various nanocluster formation conditions is described below.

6.4.4.1 Nanoclusters formed without added salt

These mixing and evaporation pathways for cluster formation were regulated in order to produce small ~20 nm nanoclusters which exhibited intense NIR extinction, particularly for the case of 95% evaporation, where the salinity reached 668 mM. The extent of evaporation has a profound effect on nanocluster size, as it simultaneously increases the final polymer, Au, and potentially salt concentrations, as shown in Table 6.1. With no added salt, as the extent of evaporation is increased, the increase in polymer and Au concentrations increases the influence of vdW, bridging, and depletion attractions, thus increasing the nanocluster size markedly in a monotonic fashion. These factors also increased NIR extinction, as was evident particulary from 75 to 95% evaporation, which suggests a decrease in spacings between primary particles, although some of this increase in NIR extinctioin may come from the increase in nanocluster size. Here, the increase in vdW and depletion attraction apparently overcomes the effect of increased bridging, which may otherwise increase interparticle spacings due to excess polymer retained with the nanoclusters (Table 6.3).

6.4.4.2 Effect of NaCl

The addition of salt screens electrostatic charges between primary particles while also decreasing polymer adsorption on the Au surfaces. Thus, the salt may both: (1) increase nanocluster size, due to decreased interparticle repulsions, and (2) decrease

nanocluster size, given lower polymer adsorption and thus lower bridging attraction, as shown in Table 6.3. To illustrate the effect of NaCl on nanocluster size, we plot the reduced decrease in nanocluster diameter versus the final NaCl concentration in Figure 6.11 at constant final Au and final polymer concentrations for each initial salt concentration. Here, the reduced change in diameter ΔD is defined by:

$$\Delta D = \frac{D_{NS} - D_S}{D_{NS}} \quad (2)$$

where D_{NS} and D_S are the nanocluster diameters without and with added salt, respectively. For a salt concentration of 66.7 mM, ΔD is only 0.11, as the effects of dilute electrolyte on the polymer bridging and screening of electrostatic repulsion are either minor or compensate against each other. As the salt concentration is increased to 133 mM, ΔD increases significantly to 0.33, indicating that the effect of lower polymer bridging is dominant. This behavior becomes even more substantial at a salt concentration of 668 mM, where ΔD increases to 0.75.

With added salt, the change in nanoparticle size becomes small with the extent of evaporation, as shown in Figure 6.3c, unlike the case without added salt in Figure 6.3a. Upon evaporation, the final polymer, Au, and salt concentrations increase simultaneously, as shown in Table 6.1. Increasing the Au concentration increases vdW attractions, whereas the increase in polymer concentration increases depletion attraction (Table 6.3). Moreover, the increase in polymer concentration would increase polymer bridging and thus increase the total attraction, which would increase the nanocluster size. However, the increase in salt concentration with evaporation decreases polymer adsorption and bridging attraction, which would decrease the nanocluster size. Additionally, the electrostatic repulsions are screened by the salt, which would tend to

increase the size. Finally , this lower polymer adsorption would tend to decrease the amount of charge neutralization induced by the polymer,[8] which would lower the size. These various interactions, which are summarized in Table 6.3, oppose each other and thus preclude any drastic changes in size with evaporation extent once salt is added. The slight increase in nanocluster size with evaporation in Figure 6.3c suggests a slight dominance of the attractive forces over the decrease in bridging attraction and polymer-induced charge neutralization. In contrast to their effect on size, these attractive forces had a substantial effect on the NIR spectra, especially for the highest salinity at 95% evaporation, producing the large A_{800}/A_{525} of 0.676 for nanoclusters with a diameter of only 27 nm. Clearly, the addition of salt effects many factors that influence size. In this study, it was possible to find domains in concentration and evaporation whereby nanoclusters smaller than 30 nm with strong NIR absorbance could be formed, that we did not achieve without added salt.

6.4.4.3 Effect of initial Au concentration

The nanocluster size decreased only modestly upon decreasing the initial Au concentration prior to solvent evaporation, as shown in Figure 6.6 for 95% evaporation. Decreasing the initial Au concentration from 3 mg/ml to 0.5 mg/ml weakened the vdW forces and lowered the polymer concentration, thus lowering depletion attraction. Both of these factors would lead to smaller clusters as observed (Table 6.3). Moreover, the final salt concentration decreased, resulting in less charge screening, which would favor smaller nanoclusters. Apparently, the greater polymer adsorption at lower salinity, which would otherwise favor larger clusters due to polymer bridging and potential charge neutralization, was not the dominant factor in this case.

6.4.4.4 Effect of polymer/Au ratio

As the polymer/Au ratio increased, the final Au concentration decreased monotonically, as shown in Table 6.2, while the final polymer and salt concentrations increased monotonically. Here the nanocluster properties are governed by a balance of: (1) increased depletion attraction, bridging, and both polymer-induced and salt-induced charge screening as the polymer and salt concentrations are increased, potentially increasing nanocluster diameter, and (2) decreased vdW and polymer bridging as the Au concentration is decreased and the salt concentration is increased, potentially decreasing the nanocluster diameter, as described in Table 6.3. As the polymer/Au ratio was increased from 5/1 to 10/1, the size decreased slightly. In contrast, at the high polymer/Au ratio of 20/1, however, the substantial increase in nanocluster diameter indicated the dominance of depletion attraction, bridging and depletion. The greatest NIR extinction at the lowest polymer/Au ratio is extremely interesting given that these were the smallest nanoclusters. From these NIR data, it appears that the lower polymer adsorption on the Au surfaces, as a consequence of the low polymer/Au ratio and 154 mM salt, allowed for closer spacings of the primary particles.

6.4.5 Comparison to Nanoclusters Made with Lysine/Citrate Nanospheres

The cysteine/citrate capped primary Au nanospheres used in this study have been previously shown to completely resist protein adsorption in undiluted fetal bovine serum.[16] Interestingly, however, these primary nanospheres aggregate and settle immediately after incubation in both 1x phosphate buffered saline (PBS) or 150 mM NaCl at a gold concentration of ~0.04 mg/ml(data not shown), which is approximately

the same salinity as FBS. Here charge screening weakens the electrostatic repulsion. The stability in FBS but not in NaCl nor PBS may be attributed to a potential "depletion stabilization" mechanism, whereby the proteins present in FBS impart stability to the primary nanospheres through creating a stabilizing osmotic pressure gradient without physically adsorbing to the nanosphere surfaces.[28] This mechanism has been previously proposed for the stabilization of Au nanoparticles in solutions of high salinity with PEG as well as iron oxide nanoparticles in fetal calf serum (FCS)-supplemented cellular growth media.[39, 40] In contrast to the primary nanoparticles, the nanoclusters are stable at all of the salinities studied up to 1.3 M, indicating the adsorbed polymer with PEO loops provides steric stabilization provided by PEO.

The use of zwitterionic cysteine instead of cationic lysine as a ligand along with citrate in the mixed monolayer-capped primary nanospheres also significantly affected the nanocluster formation process. The addition of zwitterionic cysteine reduced the charge on the primary particle less than the addition of cationic lysine,[10, 16] resulting in a higher q value in Eq. 6.1 for cysteine/citrate capped nanospheres. Thus, in order to obtain similar nanocluster sizes and morphologies, the attraction a had to be increase to overcome the excess repulsion. Thus, higher evaporation extents (95% vs 50%) were used to achieve nanoclusters with the closely packed Au nanospheres necessary for intense NIR extinction. Moreover, the use of salt in the formation of cysteine/citrate nanoclusters allowed for lower polymer/Au ratios (5/1 compared with 20/1 for lysine/citrate), as a lower polymer/Au was required in order to achieve a similar level of quenching.

Our method of nanocluster assembly, whereby equilibrium Au nanoclusters are quenched by polymer adsorption to the nanocluster surface, provides an alternative to other methods including thermolysis of iron chloride precursors in diethylene glycol,[17]

"self-limiting" assembly of CdSe nanoparticles into clusters upon the reaction of cadmium and selenium precursors in water,[18] and the formation of NIR-active hybrid Au/iron oxide nanoparticles[19, 20] by reaction of Au and iron precursors.

6.4.6 Applications for Biomedical Imaging

Gold nanoparticles which exhibit intense extinction in the NIR region, such as high-aspect ratio nanorods,[41, 42] nanoshells,[43-45] nanocages,[4, 46] and nanoclusters,[8-10] are widely used for biomedical imaging. The intense NIR extinction exhibited by nanoclusters composed of cysteine/citrate-capped Au nanospheres makes them excellent candidates for biomedical imaging applications such as photoacoustic imaging.[3, 5] Moreover, the ~20 nm size of these nanoclusters is optimal for both cellular uptake and long blood residence times necessary for disease treatment. Future studies are warranted to examine biodegradation of these nanoclusters, which is beyond the scope of this study.

6.5 CONCLUSIONS

The concept of the colloidal assembly of gold nanoclusters quenched with a polymer stabilizer[8-10, 16] has been generalized to include primary particles capped with a strongly binding zwitterionic thiol, cysteine, in the presence of citrate. Secondly, the addition of salt to screen charges and weaken polymer adsorption is shown to have a profound effect on nanocluster size and the spacing of the Au primary nanoparticles as characterized by the NIR extinction. Remarkably, a high NIR extinction coefficient of 0.010 $cm^2/\mu g$ was achieved with extremely small ~27 nm Au nanoclusters with added salt, indicating closely spaced primary particles. With the combination of a high salinity

of 668 M NaCl, and a high evaporation extent of 95%, sub-30 nm nanoclusters were formed where the extinction was high at 900 nm and significant even at 1300 nm. Over the conditions studied in this work, this behavior could not be reached without added salt. A general framework has additionally been presented to examine the effect of Au nanoparticle, polymer, and salt concentrations on vdW, electrostatic, depletion, and polymer bridging interactions and thus nanocluster NIR extinction and size, as summarized in Table 6.3. Here, salt addition reduces potential polymer bridging between primary nanospheres, cluster sub-units, and nanoclusters, thus preventing excessive cluster growth and quenches smaller nanoclusters. Furthermore, salt screens electrostatic repulsion between the individual Au spheres, creating denser packing within nanoclusters with smaller primary particle spacing resulting in intense NIR extinction. Additionally, the weaker electrostatic repulsions and lower polymer adsorption with salt addition prevents the excessive retention of polymer within the nanocluster interior. The nanoclusters with a binary monolayer meet a number of criteria of practical interest for optical imaging: small ~4 nm primary particles that would enable the possibility of kidney clearance, lack of protein adsorption on the primary nanospheres,[16] control of nanocluster size, nanoclusters as small as ~20 nm which is beneficial for rapid cellular uptake, and close spacing of the Au nanospheres for strong NIR extinction.

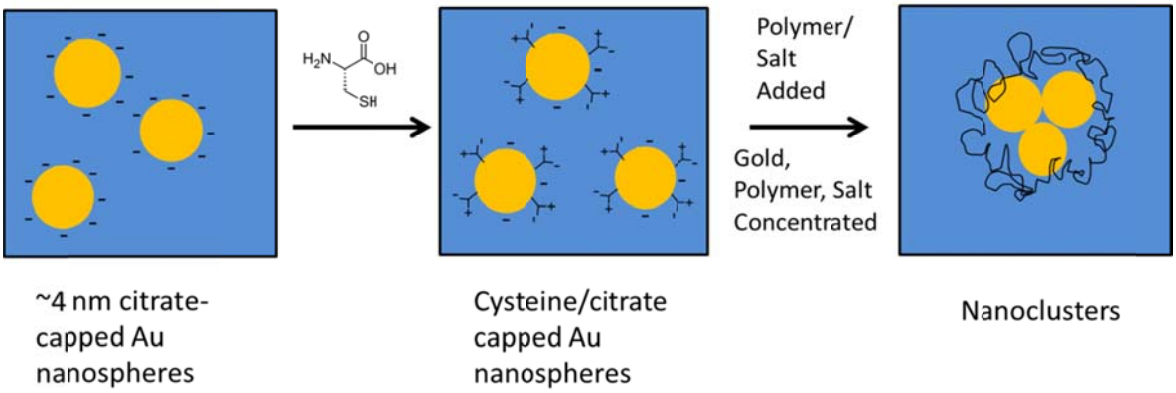

Figure 6.1: Schematic of formation of nanoclusters formed from cysteine/citrate capped Au nanospheres.

Table 6.1: Properties of nanoclusters formed with and without salt addition

Sample Name	**Polymer/Au Ratio (w/w)**	**Evap Extent (%)**	**Final Au Conc (mg/ml)**	**Final Polymer Conc (mg/ml)**	**Final NaCl Conc (mM)**	**D_h (nm)**	**UV-Vis (A_{800}/A_{525})**	**Zeta Potential (mV)**
NS-50	5	95	4	20	0	27.9 ± 3.1	0.376	-17.0 ± 1.0
3-5-50					66.7	24.9 ± 4.9	0.381	-17.6 ± 1.0
NS-75	5	75	8	40	0	38.5 ± 4.9	0.321	-18.5 ± 0.6
3-5-75					133	25.9 ± 4.6	0.421	-18.6 ± 0.9
NS-95	5	95	40	200	0	109.3 ± 9.8	0.673	-14.9 ± 0.6
3-5-95					668	27.2 ± 4.2	0.676	-19.1 ± 0.7

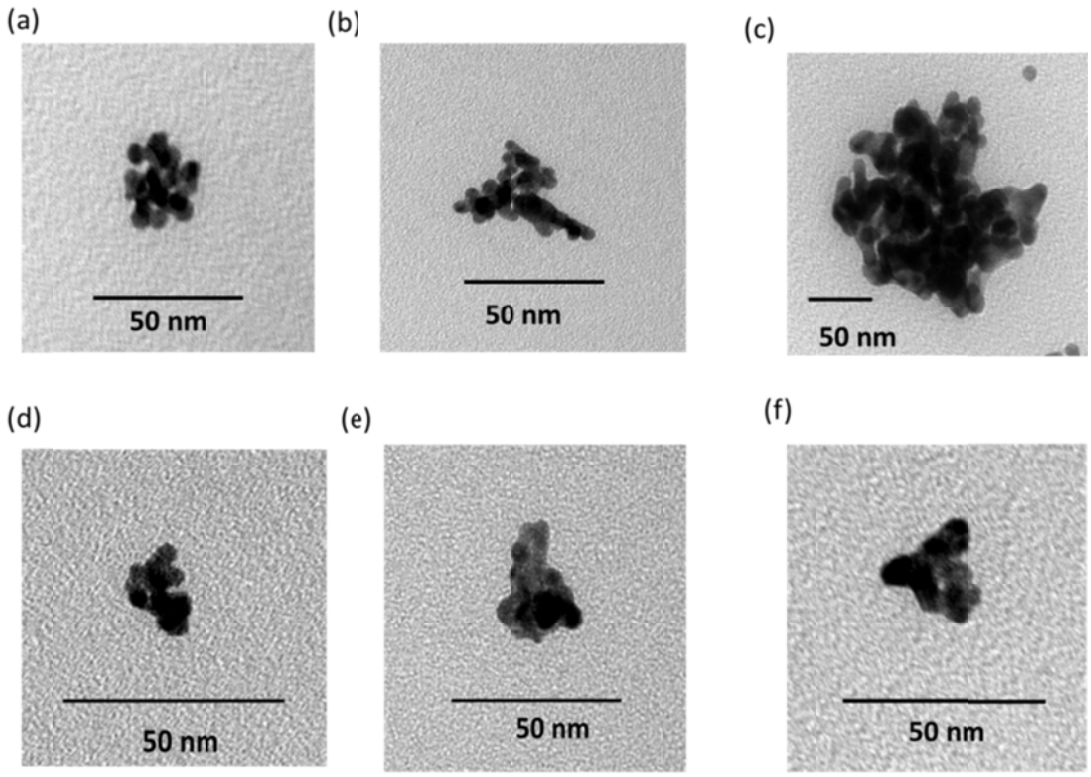

Figure 6.2: TEM images of nanoclusters formed with a 5/1 polymer/Au ratio, 3 mg/ml initial Au concentration, and evaporation extents of (a, d) 50%, (b , e) 75% and (c, f) 95% without (a-c) and with (d-f) salt addition. Samples had final Au, polymer, and NaCl concentrations shown in Table 6.1.

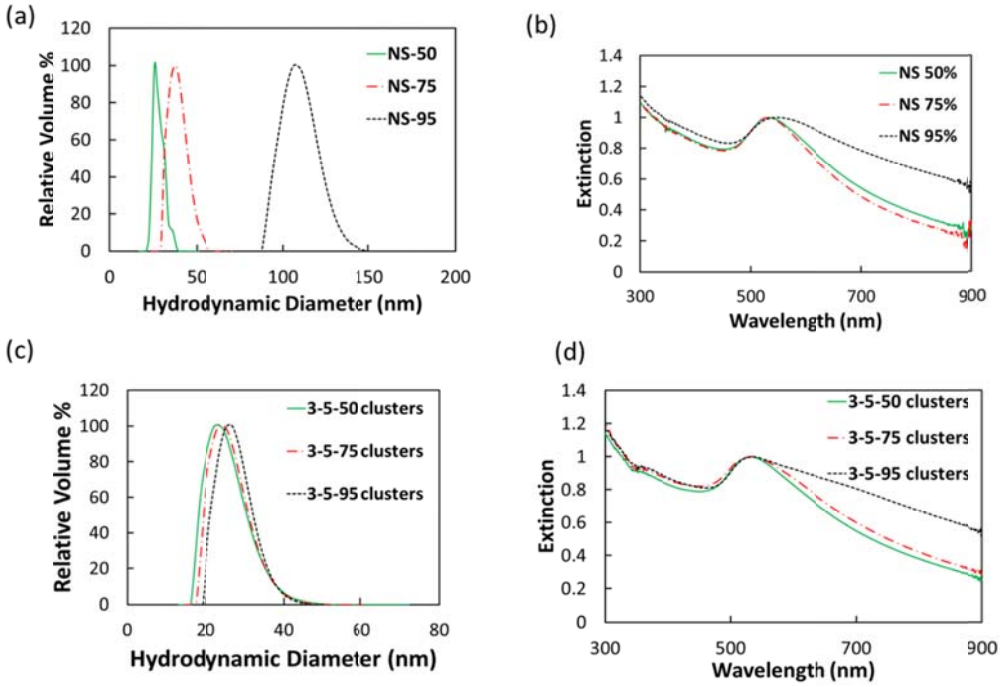

Figure 6.3: (a, c) DLS D_h distributions and (b, d) UV-Vis-NIR extinction spectra for nanoclusters formed with a 3 mg/ml initial Au concentration, 5/1 polymer/Au ratio, and evaporation extents of 50%, 75%, and 95% without (a, b) and with (c, d) salt addition to the polymer solution.

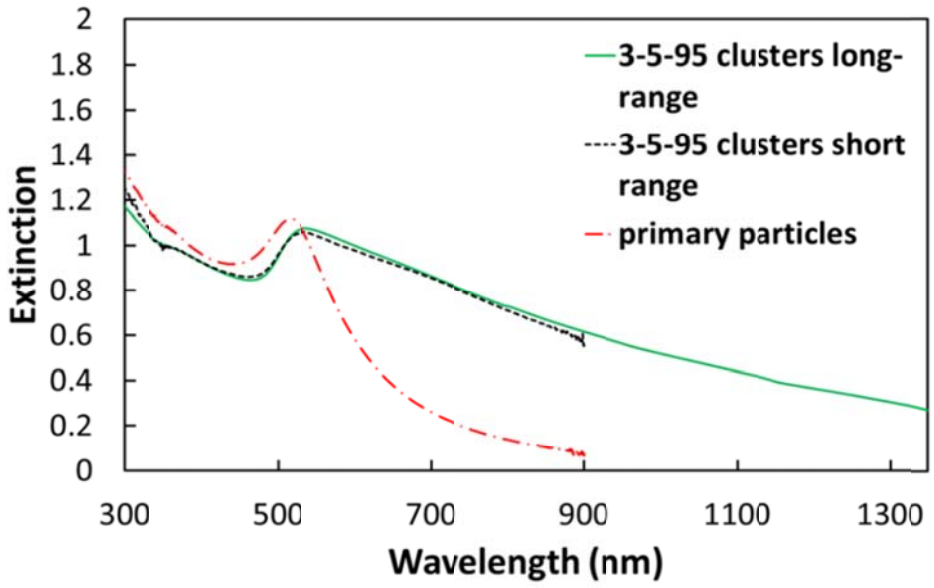

Figure 6.4: Long-ranged (solid green) and short-ranged (dashed black) UV-Vis-NIR extinction spectra of 3-5-95 nanoclusters. Red curve is the extinction spectrum for primary cysteine/citrate capped nanospheres. Here, the Au concentration was ~75 µg/ml for all samples.

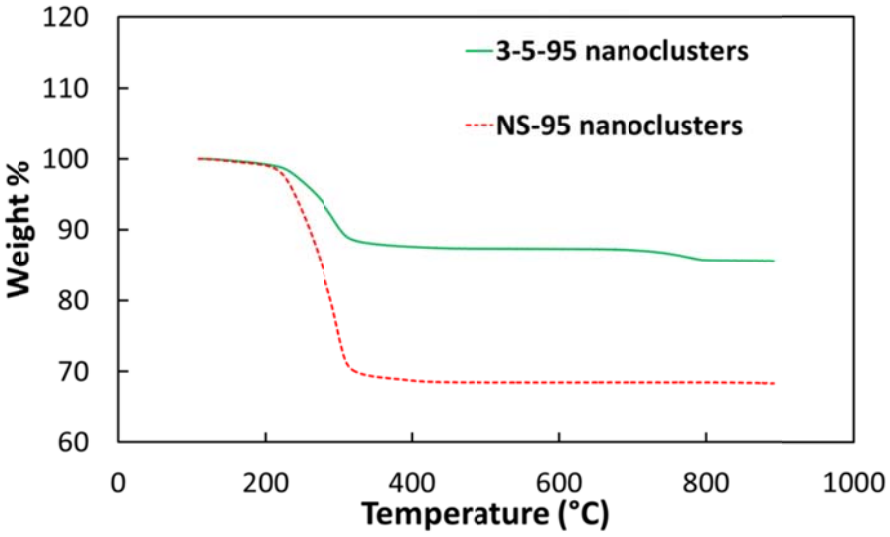

Figure 6.5: TGA results for 3-5-95 nanoclusters (green solid curve) and NS-95 nanoclusters (red dashed curve)

Table 6.2: Properties of nanoclusters formed with added salt and varying starting gold concentrations and polymer/Au ratios.

Sample Name	**Polymer/Au Ratio (w/w)**	**Evap Extent (%)**	**Final Au Conc (mg/ml)**	**Final Polymer Conc (mg/ml)**	**Final NaCl Conc (mM)**	**D_h (nm)**	**UV-Vis (A_{800}/A_{525})**	**Zeta Potential (mV)**
0.5-5-95	5	95	9.2	46.2	154	22.5 ± 4.4	0.718	-24.1 ± 0.7
3-5-95	5	95	40	200	668	27.2 ± 4.2	0.676	-19.1 ± 0.7
3-10-95	10	95	30	300	1000	21.2 ± 3.9	0.542	-22.7 ± 0.7
3-20-95	20	95	20	400	1333	52.0 ± 6.7	0.534	-18.6 ± 0.5

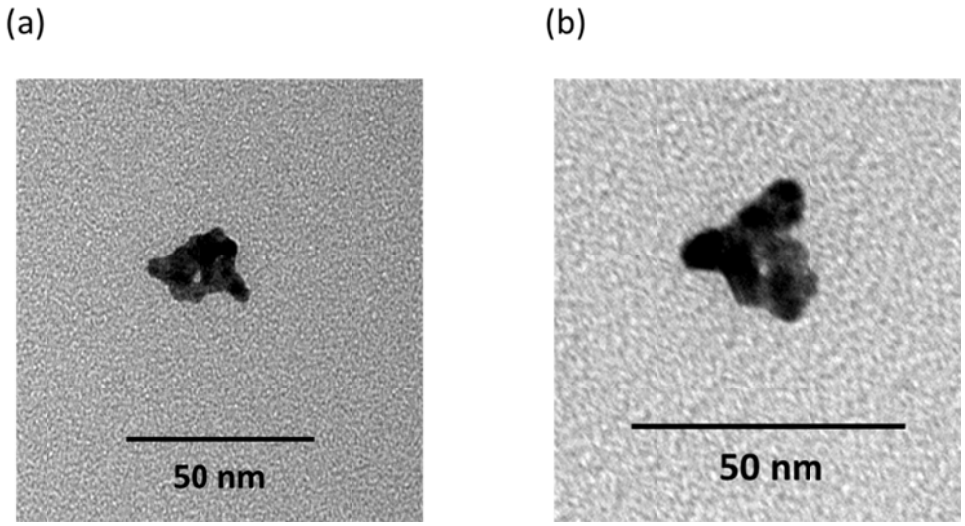

Figure 6.6: TEM images of nanoclusters formed with a 5/1 polymer/Au ratio, 95% evaporation, 100 mM NaCl in the polymer solution, and (a) 0.5 mg/ml initial Au concentration and (b) 3 mg/ml initial Au concentration. Samples had final Au, polymer, and NaCl concentrations given in Table 6.2.

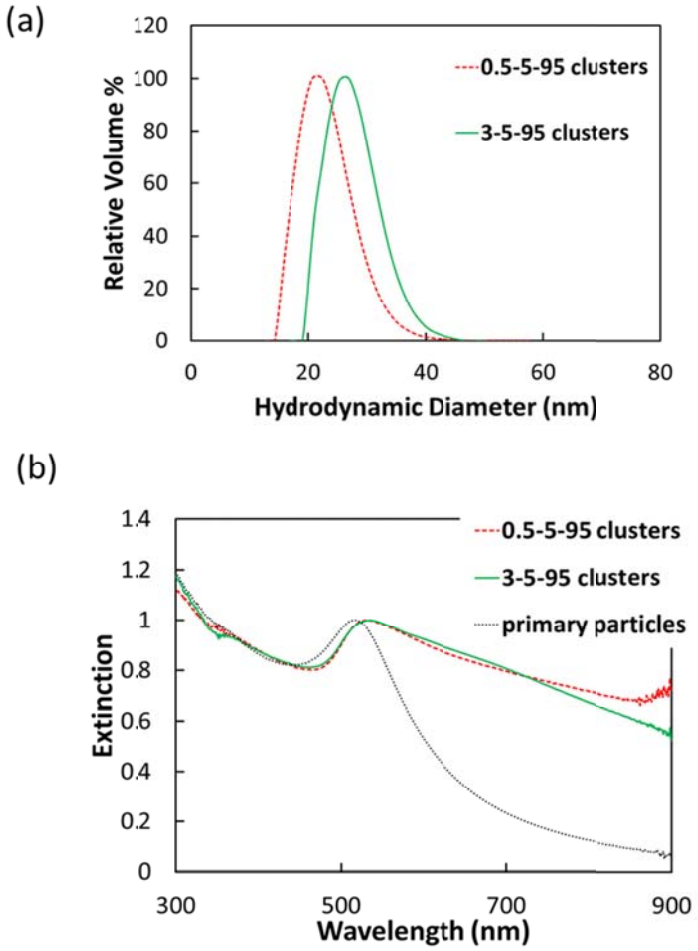

Figure 6.7: (a) DLS D_h distributions and (b) UV-Vis-NIR extinction spectra of nanoclusters formed with initial Au concentrations of 0.5 mg/ml and 3 mg/ml, respectively, for 95% evaporation at a 5/1 polymer/Au ratio

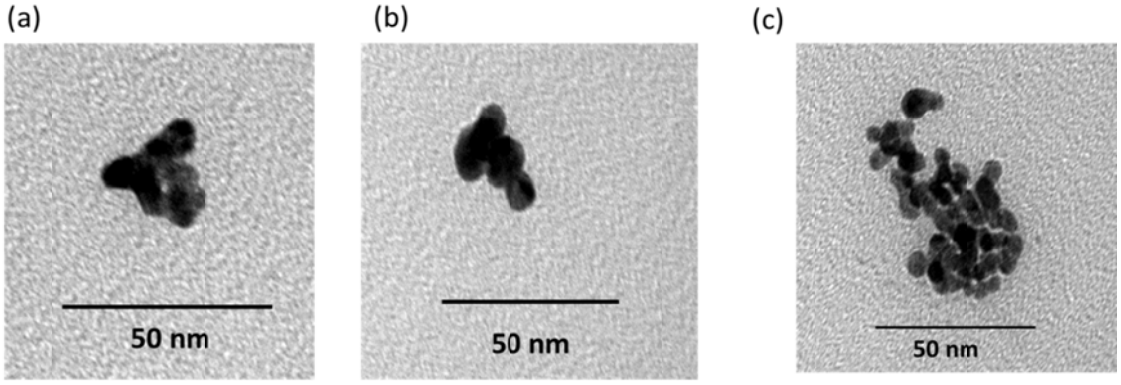

Figure 6.8: TEM images of nanoclusters formed with a 3 mg/ml initial Au concentration, 95% evaporation, 100 mM NaCl concentration in the polymer solution, and (a) 5/1, (b) 10/1, and (c) 20/1 polymer/Au ratios

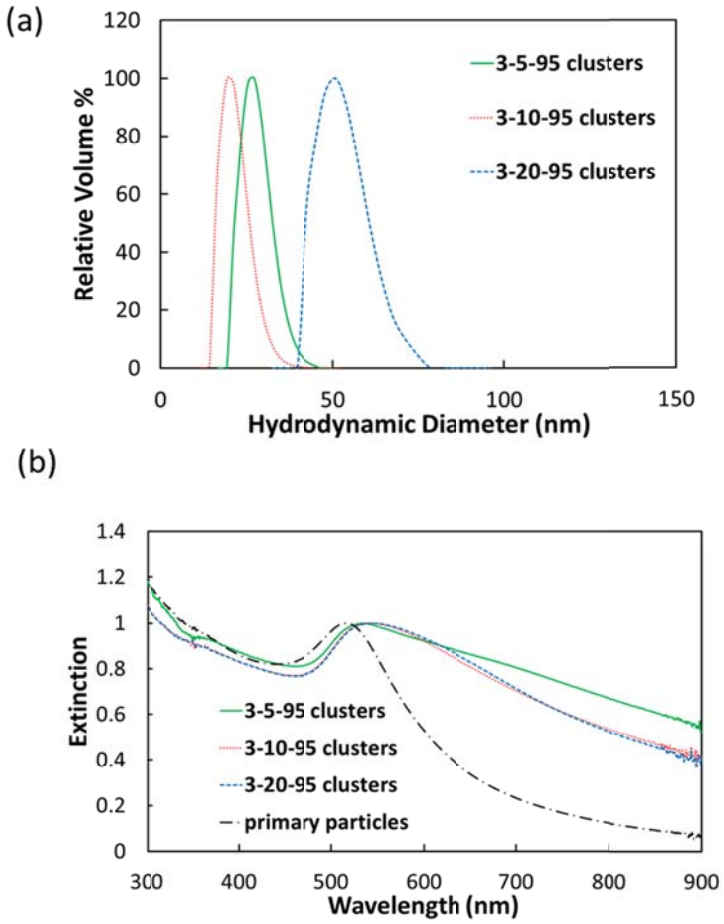

Figure 6.9: (a) DLS D_h distributions and (b) UV-Vis-NIR extinction spectra for nanoclusters formed with polymer/Au ratios of 5/1, 10/1, and 20/1. Samples were formed with an initial Au concentration of 3 mg/ml. The NaCl concentration in the polymer solution was 100 mM in all cases. Evaporation resulted in final Au nanoparticle, polymer, and NaCl concentrations shown in Table 6.2.

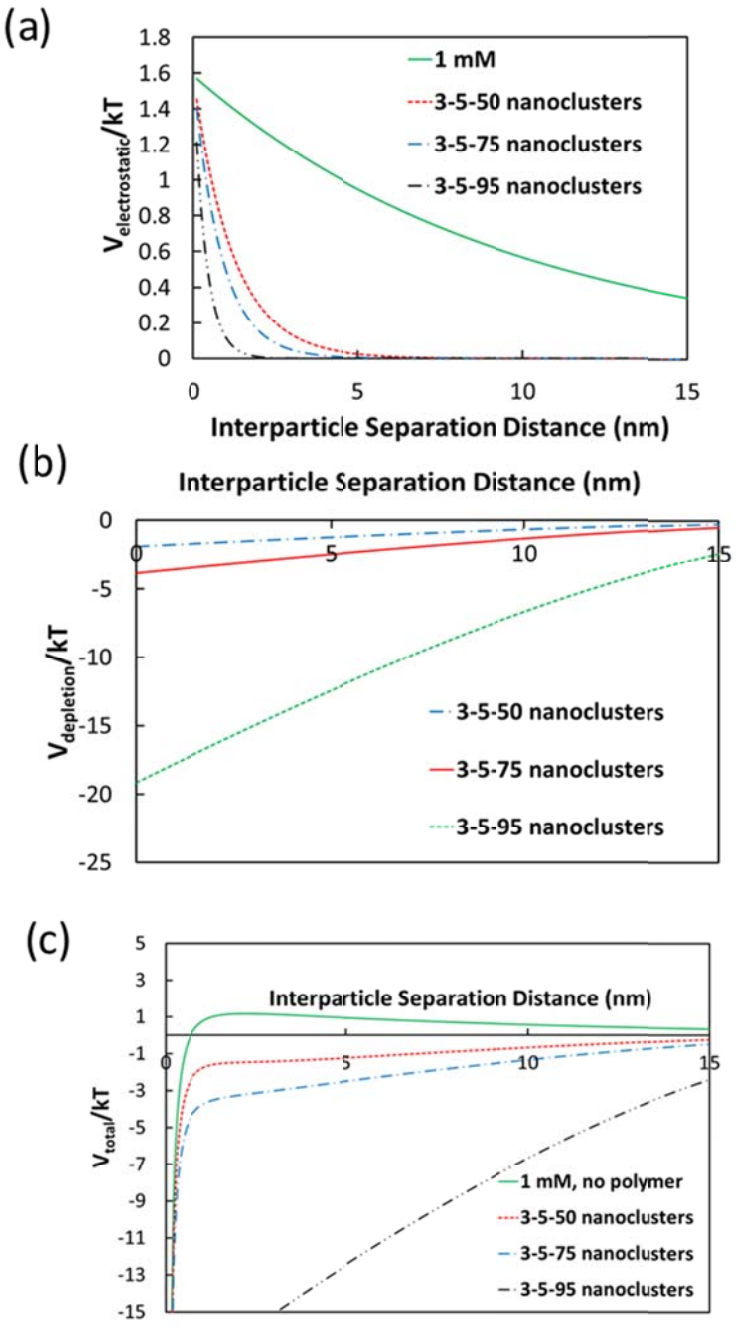

Figure 6.10: (a) Electrostatic, (b) depletion, and (c) total interaction pair potentials of two cysteine/citrate capped nanospheres at polymer and NaCl concentrations used to form 3-5-50, 3-5-75, and 3-5-95 nanoclusters.

Table 6.3: Summary of tunable experimental concentrations and their effect on colloidal interactions, interparticle spacings within nanoclusters, and nanocluster diameters.

Parameter	**Interaction**	**Spacings**	**Diameter**
Increase Au Concentration	Increase vdW attraction	Decrease	Increase
Increase Polymer Concentration	Increase depletion attraction	Decrease	Increase
	Increase polymer bridging	**Increase**	**Increase**
Increase Salinity	**Decrease electrostatic repulsion**	**Decrease**	**Increase**
	Decrease polymer adsorption and bridging	**Decrease**	**Decrease**

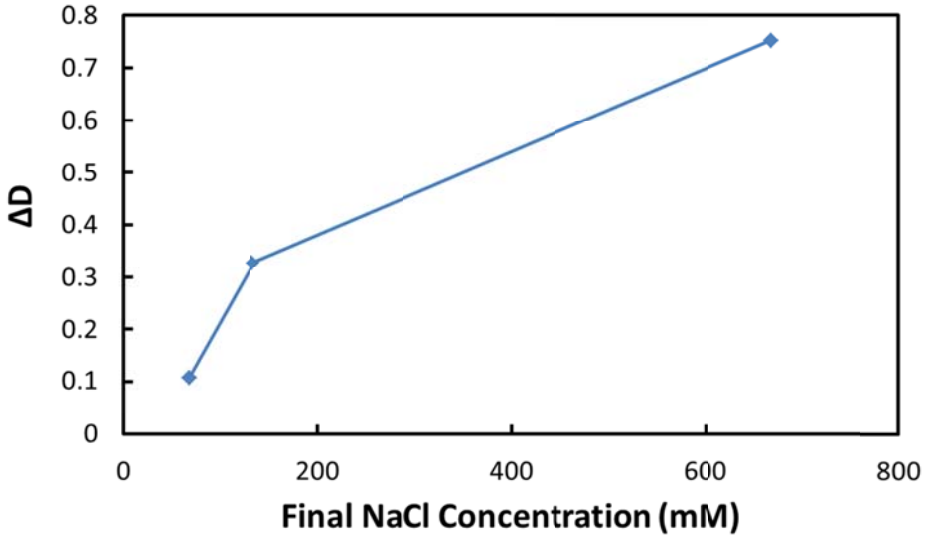

Figure 6.11: Reduced change in nanocluster diameter as a function of final NaCl concentration. Here, the final Au and polymer concentrations are kept constant for nanoclusters formed at each salt concentration. The final Au and polymer concentrations are shown in Table 6.1.

6.6 REFERENCES

1. Weissleder, R. A Clearer Vision for in Vivo Imaging. *Nature Biotechnology* **2001**, *19*.
2. Agarwal, A.; Huang, S. W.; O'Donnell, M.; Day, K. C.; Day, M.; Ashkenazi, S. Targeted Gold Nanorod Contrast Agent for Prostate Cancer Detection by Photoacoustic Imaging. *Journal of Applied Physics* **2007**, *102*, 0647011-0647014.
3. Mallidi, S.; Larson, T.; Tam, J.; Joshi, P. P.; Karplouk, A.; Sokolov, K.; Emelianov, S. Multiwavelength Photoacoustic Imaging and Plasmon Resonance Coupling of Gold Nanoparticles for Selective Detection of Cancer. *Nano Letters* **2009**, *9*, 2825-2831.
4. Song, K. H.; Kim, C.; Cobley, C. M.; Xia, Y.; Wang, L. V. Near-Infrared Gold Nanocages as a New Class of Tracers for Photoacoustic Sentinel Lymph Node Mapping on a Rat Model. *Nano Letters* **2009**, *9*, 183-188.
5. Yoon, S. J.; Mallidi, S.; Tam, J. M.; Tam, J. O.; Murthy, A.; Johnston, K. P.; Sokolov, K. V.; Emelianov, S. Y. Utility of Biodegradable Plasmonic Nanoclusters in Photoacoustic Imaging. *Optics Letters* **2010**, *35*, 3751-3753.
6. Aaron, J.; Nitin, N.; Travis, K.; Kumar, S.; Collier, T.; Park, S. Y.; Jose-Yacaman, M.; Coghlan, L.; Follen, M.; Richards-Kortum, R.*, et al.* Plasmon Resonance Coupling of Metal Nanoparticles for Molecular Imaging of Carcinogenesis in Vivo. *Journal of Biomedical Optics* **2007**, *12*.
7. Aaron, J.; Travis, K.; Harrison, N.; Sokolov, K. Dynamic Imaging of Molecular Assemblies in Live Cells Based on Nanoparticle Plasmon Resonance Coupling. *Nano Letters* **2009**, *9*, 3612-3618.
8. Tam, J. M.; Murthy, A. K.; Ingram, D. R.; Nguyen, R.; Sokolov, K. V.; Johnston, K. P. Kinetic Assembly of near-Ir Active Gold Nanoclusters Using Weakly Adsorbing Polymers to Control the Size. *Langmuir* **2010**, *26*, 8988-8999.
9. Tam, J. M.; Tam, J. O.; Murthy, A.; Ingram, D. R.; Ma, L. L.; Travis, K.; Johnston, K. P.; Sokolov, K. V. Controlled Assembly of Biodegradable Plasmonic Nanoclusters for near-Infrared Imaging and Therapeutic Applications. *ACS Nano* **2010**, *4*, 2178-2184.
10. Murthy, A. K.; Stover, R. J.; Borwankar, A. U.; Nie, G. D.; Gourisankar, S.; Truskett, T. M.; Sokolov, K. V.; Johnston, K. P. Equilibrium Gold Nanoclusters Quenched with Biodegradable Polymers. *ACS Nano* **2013**, *7*, 239-251.
11. Ofir, Y.; Samanta, B.; Rotello, V. M. Polymer and Biopolymer Mediated Self-Assembly of Gold Nanoparticles. *Chemical Society Reviews* **2008**, *37*, 1814-1825.

12. Frankamp, B. L.; Boal, A. K.; Rotello, V. M. Controlled Interparticle Spacing through Self-Assembly of Au Nanoparticles and Poly(Amidoamine) Dendrimers. *Journal of the American Chemical Society* **2002**, *124*, 15146-15147.

13. Zhuang, J.; Wu, H.; Yang, Y.; Cao, Y. C. Controlling Colloidal Superparticle Growth through Solvophobic Interactions. *Angewandte Chemie International Edition* **2008**, *47*, 2208-2212.

14. Larson-Smith, K.; Pozzo, D. C. Scalable Synthesis of Self-Assembling Nanoparticle Clusters Based on Controlled Steric Interactions. *Soft Matter* **2011**, *7*, 5339-5347.

15. Lu, Z.; Yin, Y. Colloidal Nanoparticle Clusters: Functional Materials by Design. *Chemical Society Reviews* **2012**, *41*, 6874-6887.

16. Murthy, A. K.; Stover, R. J.; Hardin, W. G.; Schramm, R.; Nie, G. D.; Gourisankar, S.; Truskett, T. M.; Sokolov, K. V.; Johnston, K. P. Charged Gold Nanoparticles with Essentially Zero Serum Protein Adsorption in Undiluted Fetal Bovine Serum. *Journal of the American Chemical Society* **2013**, *Just Accepted Manuscript*.

17. Ge, J.; Hu, Y.; Biasini, M.; Beyermann, W. P.; Yin, Y. Superparamagnetic Magnetite Colloidal Nanocrystal Clusters. *Angewandte Chemie International Edition* **2007**, *46*, 4342-4345.

18. Xia, Y. S.; Nguyen, T. D.; Yang, M.; Lee, B.; Santos, A.; Podsiadlo, P.; Tang, Z. Y.; Glotzer, S. C.; Kotov, N. A. Self-Assembly of Self-Limiting Monodisperse Supraparticles from Polydisperse Nanoparticles. *Nat. Nanotechnol.* **2011**, *6*, 580-587.

19. Ma, L. L.; Feldman, M. D.; Tam, J. M.; Paranjape, A. S.; Cheruki, K. K.; Larson, T. A.; Tam, J. O.; Ingram, D. R.; Paramita, V.; Villard, J. W.*, et al.* Small Multifunctional Nanoclusters (Nanoroses) for Targeted Cellular Imaging and Therapy. *ACS Nano* **2009**, *3*, 2686-2696.

20. Ma, L. L.; Borwankar, A. U.; Willsey, B. W.; Yoon, K. Y.; Tam, J. O.; Sokolov, K. V.; Feldman, M. D.; Milner, T. E.; Johnston, K. P. Growth of Textured Thin Au Coatings on Iron Oxide Nanoparticles with near Infrared Absorbance. *Nanotechnology* **2013**, *24*.

21. Joshi, H.; Shirude, P. S.; Bansal, V.; Ganesh, K. N.; Sastry, M. Isothermal Titration Calorimetry Studies on the Binding of Amino Acids to Gold Nanoparticles. *Journal of Physical Chemistry B* **2004**, *108*, 11535-11540.

22. Kondoh, H.; Kodama, C.; Sumida, H.; Nozoye, H. Molecular Processes of Adsorption and Desorption of Alkanethiol Monolayers on Au(1 1 1). *Journal of Chemical Physics* **1999**, *111*, 1175-1184.

23. Chompoosor, A.; Han, G.; Rotello, V. M. Charge Dependent of Ligand Release and Monolayer Stability of Gold Nanoparticles by Biogenic Thiols. *Bioconjugate Chemistry* **2008**, *19*, 1342-1345.

24. Hong, R.; Han, G.; Fernandez, J. M.; Kim, B.; Forbes, N. S.; Rotello, V. M. Gluathione-Mediated Delivery and Release Using Monolayer Protected Nanoparticle Carriers. *Journal of the American Chemical Society* **2006**, *128*, 1078-1079.

25. Hiemenz, P. C.; Rajagopalan, R., *Principles of Colloid and Surface Chemistry*. 3 ed.; Taylor & Francis: New York, 1997; p 546-556.

26. Groenewold, J.; Kegel, W. K. Anomalously Large Equilibrium Clusters of Colloids. *Journal of Physical Chemistry B* **2001**, *105*, 11702-11709.

27. Johnston, K. P.; Maynard, J. A.; Truskett, T. M.; Borwankar, A. U.; Miller, M. A.; Wilson, B. K.; Dinin, A. K.; Khan, T. A.; Kaczorowski, K. J. Concentrated Dispersion of Equilibrium Protein Nanoclusters That Reversibly Dissociate into Active Monomers. *ACS Nano* **2012**, *6*, 1357-1369.

28. Lekkerkerker, H. N. W.; Tuinier, R., *Colloids and the Depletion Interaction*. Springer: New York, 2011; Vol. 833, p 12-15.

29. Sakai, T.; Alexandridis, P. Mechanism of Gold Metal Ion Reduction, Nanoparticle Growth and Size Control in Aqueous Amphiphilic Block Copolymer Solutions at Ambient Conditions. *Journal of Physical Chemistry B* **2005**, *109*, 7766-7777.

30. Alexandridis, P.; Holzwarth, J. F. Differential Scanning Calorimetry Investigation of the Effect of Salts on Aqueous Solution Properties of an Amphiphilic Block Copolymer (Poloxamer). *Langmuir* **1997**, *13*, 6074-6082.

31. Su, Y.-L.; Wei, X.-F.; Liu, H.-Z. Effect of Sodium Chloride on Association Behavior of Poly(Ethylene Oxide)-Poly(Propylene Oxide)-Poly(Ethylene Oxide) Block Copolymer in Aqueous Solutions. *Journal of Colloid and Interface Science* **2003**, *264*, 526-531.

32. Tadros, T. F.; Vincent, B. Influence of Temperature and Electrolytes on the Adsorption of Poly(Ethylene Oxide)-Poly(Propylene Oxide) Block Copolymer on Polystyrene Latex and on the Stability of the Polymer-Coated Particles. *Journal of Physical Chemistry* **1980**, *84*, 1575-1580.

33. Hooper, J. B.; Schweizer, K. S. Contact Aggregation, Bridging, and Steric Stabilization in Dense Polymer-Particle Mixtures. *Macromolecules* **2005**, *38*, 8858-8869.

34. Ganesan, V.; Ellison, C. J.; Pryamitsyn, V. Mean-Field Models of Structure and Dispersion of Polymer-Nanoparticle Mixtures. *Soft Matter* **2010**, *6*, 4010-4025.

35. Cohen-Tannoudji, L.; Bertrand, E.; Bressy, L.; Goubault, C.; Baudry, J.; Klein, J.; Joanny, J.-F.; Bibette, J. Polymer Bridging Probed by Magnetic Colloids. *Physical Review Letters* **2005**, *94*.

36. Goubault, C.; Leal-Calderon, F.; Viovy, J.-L.; Bibette, J. Self-Assembled Magnetic Nanowires Made Irreversible by Polymer Bridging. *Langmuir* **2005**, *21*, 3725-3729.

37. Surve, M.; Pryamitsyn, V.; Ganesan, V. Polymer-Bridged Gels of Nanoparticles in Solutions of Adsorbing Polymers. *Journal of Chemical Physics* **2006**, *125*.

38. Kamiayashi, M.; Ogura, H.; Otsubo, Y. Shear-Thickening Flow of Nanoparticle Suspensions Flocculated by Polymer Bridging. *Journal of Colloid and Interface Science* **2008**, *321*, 294-301.

39. Petri-Fink, A.; Steitz, B.; Finka, A.; Salaklang, J.; Hofmann, H. Effect of Cell Media on Polymer Coated Superparamagnetic Iron Oxide Nanoparticles (Spions): Colloidal Stability, Cytotoxicity, and Cellular Uptake Studies. *European Journal of Pharmaceutics and Biopharmaceutics* **2008**, *68*, 129-137.

40. Zhang, X.; Servos, M. R.; Liu, J. Ultrahigh Nanoparticle Stability against Salt, Ph, and Solvent with Retained Surface Accessibility Via Depletion Stabilization. *Journal of the American Chemical Society* **2012**, *134*, 9910-9913.

41. Huang, X.; El-Sayed, I. H.; Qian, W.; El-Sayed, M. A. Cancer Cell Imaging and Photothermal Therapy in the near-Infrared Region by Using Gold Nanorods. *Journal of the American Chemical Society* **2006**, *128*, 2115-2120.

42. Link, S.; Mohamed, M. B.; El-Sayed, M. A. Simulation of the Optical Absorption Spectra of Gold Nanorods as a Function of Their Aspect Ratio and the Effect of the Medium Dielectric Constant. *Journal of Physical Chemistry B* **1999**, *103*, 3073-3077.

43. Gobin, A. M.; Lee, M. H.; Halas, N. J.; James, W. D.; Drezek, R. A.; West, J. L. Near-Infrared Resonant Nanoshells for Combined Optical Imaging and Photothermal Cancer Therapy. *Nano Letters* **2007**, *7*, 1929-1934.

44. Hirsch, L. R.; Stafford, R. J.; Bankson, J. A.; Sershen, S. R.; Rivera, B.; Price, R. E.; Hazle, J. D.; Halas, N. J.; West, J. L. Nanoshell-Mediated near-Infrared Thermal Therapy of Tumors under Magnetic Resonance Guidance. *Proceedings of the National Academy of Sciences* **2003**, *100*, 13549-13554.

45. Loo, C.; Lowery, A.; Halas, N.; West, J.; Drezek, R. Immunotargeted Nanoshells for Integrated Cancer Imaging and Therapy. *Nano Letters* **2005**, *5*, 709-711.

46. Chen, J.; Saeki, F.; Wiley, B. J.; Cang, H.; Cobb, M. J.; Li, Z. Y.; Au, L.; Zhang, H.; Kimmey, M. B.; Li, X.*, et al.* Gold Nanocages: Bioconjugation and Their Potential Use as Optical Imaging Contrast Agents. *Nano Letters* **2005**, *5*, 473-477.

Chapter 7: Conclusions and Recommendations

7.1 CONCLUSIONS

7.1.1 Assembly of Near-IR Active Gold Nanoclusters using Weakly Adsorbing Polymers to Control the Size

A robust, flexible platform has been presented to synthesize gold nanoclusters composed of sub-5 nm constituent gold nanospheres with tunable diameters from ~30 nm to ~100 nm. Both nanocluster size and morphology were controlled by varying nanoparticle and polymer concentrations and thus manipulating colloidal forces such as van der Waals and depletion attraction as well as electrostatic repulsions. Here, the weakly-adsorbing, biodegradable polymer PLA(1k)-*b*-PEG(10k)-*b*-PLA(1k) was used to modulate interparticle interactions and provide steric stabilization to the clusters, preventing uncontrolled cluster growth. Moreover, closely-spaced constituent nanospheres within the nanoclusters provided intense NIR extinction. In contrast to previously reported templated nanocluster assembly methods, the nanoclusters had high gold loadings, due to the exclusion of the weakly-adsorbing polymer to the exterior of the cluster. The generalizable ability to tune the sizes and morphologies, even down to ~30 nm, is of great interest in biomedical applications, as the ability to tune nanoparticle size can have a profound impact on nanoparticle cell uptake and blood circulation time.[1-3] The intense NIR extinction exhibited by these nanoclusters make these particles ideal for biomedical imaging applications. Since this method has been generalized for primary Au nanoparticles of varying surface charge, the controlled assembly of Au nanoclusters

potentially enables the design of nanoclusters for a variety of applications in biomedical imaging and therapy.

7.1.2 Design of Nanospheres with Adsorb Essentially Zero Protein in Undiluted Fetal Bovine Serum

The surface ligands of ~5 nm Au nanospheres were designed such that the nanospheres did not adsorb any protein upon incubation in undiluted fetal bovine serum (FBS). Unexpectedly, these nanospheres were shown to completely resist protein adsorption even with a moderate surface charge, in contrast with previous reports.[4-7] Here, binary mixed monolayers of anionic citrate and either zwitterionic cysteine or cationic lysine ligands were used to resist the adsorption of serum proteins. The ratios of lysine and cysteine to citrate on the nanosphere surface were tuned to 1.4/1 and 1.6/1, respectively, in order to reduce the nanosphere surface charge and thus the possibility of electrostatic interactions between the nanosphere surfaces and the proteins. Moreover, the zwitterionic tips of either the lysine or cysteine ligands were used to bury the charged citrate ligands, thus enabling the nanosphere surfaces to interact weakly with the serum proteins. Furthermore, the 1.4/1 lysine/citrate nanospheres were assembled into ~20 nm biodegradable nanoclusters. The nanoclusters were shown to exhibit intense extinction in the NIR region, and were shown to dissociate back to ~5 nm Au nanospheres upon the degradation of the biodegradable polymeric stabilizer PLA(1k)-*b*-PEG(10k)-*b*-PLA(1k). These dissociated clusters furthermore did not adsorb any serum protein, making the clusters ideal as biomedical contrast agents that have the potential to clear efficiently from the body.

7.1.3 Quenched Colloidal Nanocluster Assembly

The quenched assembly of nanoclusters composed of constituent Au nanospheres which do not adsorb any serum protein has been demonstrated for nanospheres coated with a variety of surface ligands and charges. The equilibrium assembly of quenched nanoclusters has been introduced, whereby gold nanoclusters are quenched at an equilibrium size by the slow, irreversible adsorption of PLA(1k)-*b*-PEG(10k)-*b*-PLA(1k) to the nanocluster surface. Nanocluster size was tuned from ~20 nm to ~40 nm by balancing strong, short-ranged van der Waals and depletion attractions with weak, longer-ranged electrostatic repulsions provided by charged lysine and citrate ligands on the nanosphere surfaces. The polymer adsorbed weakly but irreversibly after nanocluster assembly and quenched nanoclusters at an equilibrium size, such that the size did not change even after cluster dilution. The equilibrium cluster size was predicted semi-quantitatively by using a free energy equilibrium model, in which nanocluster diameter was expressed as a function of the concentrations of polymer and Au nanoparticles. Upon degradation of the polymeric quencher, the nanoclusters were shown to reversibly and completely dissociate to Au monomer. The close spacings between individual lysine/citrate coated nanospheres produced intense NIR extinction for nanoclusters of all sizes.

The concept of quenched nanocluster assembly was further explored by manipulating the ionic strength during nanocluster formation. Here, the addition of a monovalent electrolyte, NaCl, was shown to provide a novel degree of freedom during nanocluster assembly. Salt addition decreased polymer adsorption and thus decreased potential polymer bridging between nanospheres, nanocluster sub-units, and nanoclusters, and thus quenched nanoclusters at smaller sizes. The addition of NaCl additionally screened electrostatic interactions between primary lysine/citrate capped nanospheres,

thus creating close spacings of constituent particles within small nanoclusters which resulted in intense NIR extinction. A general platform for controlling nanocluster size and NIR extinction by manipulating Au nanoparticle, polymer, and salt concentrations in order to regulate van der Waals, depletion, polymer bridging, and electrostatic colloidal interactions was presented. Salt addition was shown not to have an adverse effect on dissociation, as nanoclusters were shown to completely and reversibly dissociate to sub-5.5 nm primary gold nanospheres upon degradation of the polymer quencher PLA(1k)-*b*-PEG(10k)-*b*-PLA(1k), enabling potential renal clearance.

Quenched nanocluster assembly was further generalized by forming nanoclusters composed of primary particles capped with a combination of anionic citrate and a strongly-binding zwitterionic thiol, cysteine, which was shown to completely inhibit serum protein adsorption in Chapter 3. The addition of NaCl increases decreases polymer adsorption and thus decreases polymer bridging between nanospheres, nanocluster sub-units, and nanoclusters. Thus, salt addition quenches smaller clusters, relative to clusters formed without the addition of salt. Salt addition also screened electrostatic repulsion between primary particles and created denser packing within nanoclusters, resulting in intense NIR extinction even for nanoclusters with small sub-30 nm diameters. This extinction was intense at 900 nm and substantial even for wavelengths as long as 1300 nm. A general mechanism has been presented whereby nanocluster size and NIR extinction can be tuned by manipulating Au nanoparticle, polymer, and NaCl concentrations to modulate van der Waals, depletion, and polymer bridging attractions as well as electrostatic repulsions. The quenched nanoclusters were furthermore demonstrated to meet a number of practical criteria: (1) small, ~4 nm constituent particles which do not adsorb serum proteins to enable the possibility of kidney clearance, (2) tunable nanocluster size for rapid cellular uptake and long circulation times, and (3)

closely-spaced constituent nanospheres which produce intense extinction in the NIR region.

7.2 Recommendations and Future Research

7.2.1 Colloidal Nanocluster Assembly

Gold nanoparticles which exhibit intense NIR extinction of interest in biomedical imaging are often synthesized with sizes between ~30 nm and ~100 nm. While this size range is ideal for long circulation times in the body[1] as well as rapid cellular uptake,[1, 2] nanoparticles must be < 5.5 nm in diameter to efficiently clear through the renal system.[7, 8] In this dissertation, this conflict is overcome by assembling biodegradable nanoclusters of tunable size from ~4 nm Au nanospheres. In order for these Au nanoclusters to be used for tumor imaging, however, it is desireable to actively target them to tumors, which is often accomplished by attaching antibodies for sites such as epidermal growth factor receptor (EGFR), which are overexpressed by cancer cells.[9-11] Kumar *et al.* have developed a method of attaching these antibodies to gold nanoparticles directionally, such that much of the antibody activity is preserved and the particles are highly specific to cancer cells.[10] It is thus of great interest to adapt this antibody conjugation approach to the gold nanoclusters presented in this dissertation. Here, antibody conjugation would be evaluated both in cells as well as in animal models.

In addition to gold, iron oxide is widely used for biomedical imaging applications such as magnetic resonance imaging (MRI).[12-14] Moreover, bifunctional particles with both iron oxide and gold moieties have recently been developed which provide both optical and magnetic contrast.[11, 12, 15] However, these bifunctional particles often suffer

from similar size limitations in terms of clearance from the body.[1] It is therefore recommended to expand the quenched colloidal nanocluster assembly approach described in this dissertation to iron oxide as well as gold nanoparticles. In order to preserve the close gold nanoparticle spacings necessary for intense NIR extinction, one approach of forming bifunctional, biodegradable nanoclusters would involve first synthesizing Au nanoclusters, and then decorating the exterior of these nanoclusters with iron oxide particles, either via van der Waals attractions or via electrostatic attractions wherein the iron oxide particles possess an opposite charge relative to the Au nanocluster. Alternatively, ~5 nm core-shell iron oxide-Au nanospheres could be synthesized, and subsequently assembled into biodegradable nanoclusters using the methods described in this dissertation. A biodegradable polymer, such as the PLA(1k)-*b*-PEG(10k)-*b*-PLA(1k) used in this dissertation, could be used in order to promote the biodegradability of these nanoparticle constructs.

The application of quenched colloidal nanoclusters to cancer therapy could also be further investigated, and therapeutic effectiveness could nicely complement the imaging contrast provided by these particles. Thus, it is recommended that the effectiveness of these particles in photothermal therapy be investigated by evaluating the effect of a NIR laser on the thermal properties of the nanoclusters.[12, 15, 16] Additionally, nanoclusters could be formed in the presence of a therapeutic agent, which could then be incorporated either within the nanocluster or tethered to the exterior of the nanocluster. Thus, the broad quenched nanocluster assembly platform introduced in this dissertation has many potential future applications in biomedical imaging and therapy.

7.2.2 Design of Nanoparticles to Resist Serum Protein Adsorption

The design of nanoparticle surfaces in order to completely prevent serum protein adsorption is of great benefit to applications in the biomedical field, as it enables potential efficient kidney clearance of nanoparticles.[7] It is often desirable, however, for nanoparticle surfaces to consist entirely of strongly-bound ligands such as thiols, in order to avoid displacement in the body. It is therefore recommended to extend the binary mixed charge monolayer concept presented in this dissertation to binary groups of thiolated ligands. For example, the thiolated tripeptide glutathione (GSH) adsorbs on and caps Au nanoparticles,[8, 17-19] and is prevalent within cells at high concentrations (~10 mM).[20] Thus, it would be of great interest to use GSH coated Au nanospheres and design the surface with other thiolated ligands of various charge, in order to create nanospheres with thiolated ligands which completely inhibit the adsorption of serum proteins. Furthermore, these nanospheres could be assembled into biodegradable nanoclusters, thus limiting potential ligand displacement by free thiols *in vivo*. Additionally, the binary ligand monolayer concept presented in this dissertation could be extended to other nanoparticle surfaces such as iron oxide, in order to enhance the efficacy of other types of nanoparticle agents. Thus, the mixed charge monolayer concept to prevent serum protein adsorption presented in this dissertation provides a broad platform for inhibiting protein adsorption and promoting efficient clearance of potentially a variety of nanoparticle imaging and therapeutic agents.

7.3 REFERENCES

1. Duan, X.; Li, Y. Physicochemical Characteristics of Nanoparticles Affect Circulation, Biodistribution, Cellular Internalization, and Trafficking. *Small* **2013**, *9*, 1521-1532.
2. Chithrani, B. D.; Ghazani, A. A.; Chan, W. C. W. Determining the Size and Shape Dependence of Gold Nanoparticle Uptake into Mammalian Cells. *Nano Letters* **2006**, *6*, 662-668.
3. Arruebo, M.; Fernandez-Pacheco, R.; Ibarra, R.; Santamaria, J. Magnetic Nanoparticles for Druge Delivery. *Nano Today* **2007**, *2*.
4. Dobrovolskaia, M. A.; Patri, A. K.; Zheng, J.; Clogston, J. D.; Ayub, N.; Aggarwal, P.; Neun, B. W.; Hall, J. B.; McNeil, S. E. Interaction of Colloidal Gold Nanoparticles with Human Blood: Effects on Particle Size and Analysis of Plasma Protein Binding Profiles. *Nanomedicine* **2009**, *5*, 106-117.
5. Casals, E.; Pfaller, T.; Duschl, A.; Oostingh, G. J.; Puntes, V. Time Evolution of the Nanoparticle Protein Corona. *ACS Nano* **2010**, *4*, 3623-3632.
6. De Paoli Lacerda, S. H.; Park, J. J.; Meuse, C.; Pristinski, D.; Becker, M. L.; Karim, A.; Douglas, J. F. Interaction of Gold Nanoparticles with Common Human Blood Proteins. *ACS Nano* **2010**, *4*, 365-379.
7. Choi, H. S.; Liu, W.; Misra, P.; Tanaka, E.; Zimmer, J. P.; Ipe, B. I.; Bawendi, M. G.; Frangioni, J. V. Renal Clearance of Quantum Dots. *Nature Biotechnology* **2007**, *25*, 1165-1170.
8. Zhou, C.; Long, M.; Qin, Y.; Sun, X.; Zheng, J. Luminescent Gold Nanoparticles with Efficient Renal Clearance. *Angewandte Chemie International Edition* **2011**, *50*, 3168-3172.
9. Aaron, J.; Oh, J.; Larson, T. A.; Kumar, S.; Milner, T. E.; Sokolov, K. V. Increased Optical Contrast in Imaging of Epidermal Growth Factor Receptor Using Magnetically Actuated Hybrid Gold/Iron Oxide Nanoparticles. *Optics Express* **2006**, *14*, 12930-12943.
10. Kumar, S.; Aaron, J.; Sokolov, K. Direction Conjugation of Antibodies to Nanoparticles for Synthesis of Multiplexed Optical Contrast Agents with Both Delivery and Targeting Moieties. *Nature Protocols* **2008**, *3*, 314-320.
11. Ma, L. L.; Tam, J. O.; Willsey, B. W.; Rigdon, D.; Ramesh, R.; Sokolov, K.; Johnston, K. P. Selective Targeting of Antibody Conjugated Multifunctional Nanoclusters (Nanoroses) to Epidermal Growth Factor Receptors in Cancer Cells. *Langmuir* **2011**, *27*, 7681-7690.

12. Larson, T. A.; Bankson, J.; Aaron, J.; Sokolov, K. Hybrid Plasmonic Magnetic Nanoparticles as Molecular Specific Agents for Mri/Optical Imaging and Photothermal Therapy of Cancer Cells. *Nanotechnology* **2007**, *18*.

13. Gupta, A. K.; Gupta, M. Synthesis and Surface Engineering of Iron Oxide Nanoparticles for Biomedical Applications. *Biomaterials* **2005**, *26*, 3995-4021.

14. Laurent, S.; Forge, D.; Port, M.; Roch, A.; Robic, C.; Elst, L. V.; Muller, R. N. Magnetic Iron Oxide Nanoparticles: Synthesis, Stabilization, Vectorization, Physicochemical Characterizations, and Biological Applications. *Chemical Reviews* **2008**, *108*, 2064-2110.

15. Ma, L. L.; Feldman, M. D.; Tam, J. M.; Paranjape, A. S.; Cheruki, K. K.; Larson, T. A.; Tam, J. O.; Ingram, D. R.; Paramita, V.; Villard, J. W.*, et al.* Small Multifunctional Nanoclusters (Nanoroses) for Targeted Cellular Imaging and Therapy. *ACS Nano* **2009**, *3*, 2686-2696.

16. Hirsch, L. R.; Stafford, R. J.; Bankson, J. A.; Sershen, S. R.; Rivera, B.; Price, R. E.; Hazle, J. D.; Halas, N. J.; West, J. L. Nanoshell-Mediated near-Infrared Thermal Therapy of Tumors under Magnetic Resonance Guidance. *Proceedings of the National Academy of Sciences* **2003**, *100*, 13549-13554.

17. Zheng, J.; Zhou, C.; Yu, M. X.; Liu, J. B. Different Sized Luminescent Gold Nanoparticles. *Nanoscale* **2012**, *4*, 4073-4083.

18. Yu, M.; Zhou, C.; Liu, J.; Hankins, J. D.; Zheng, J. Luminescent Gold Nanoparticles with Ph-Dependent Membrane Adsorption. *Journal of the American Chemical Society* **2011**, *133*, 11014-11017.

19. Stobiecka, M.; Coopersmith, K.; Hepel, M. Resonance Elastic Light Scattering (Rels) Spectroscopy of Fast Non-Langmuirian Ligand-Exchange in Glutathione-Induced Gold Nanoparticle Assembly. *Journal of Colloid and Interface Science* **2010**, *350*, 168-177.

20. Hong, R.; Han, G.; Fernandez, J. M.; Kim, B.; Forbes, N. S.; Rotello, V. M. Gluathione-Mediated Delivery and Release Using Monolayer Protected Nanoparticle Carriers. *Journal of the American Chemical Society* **2006**, *128*, 1078-1079.

Appendix A: Kinetic Assembly of Near-IR Active Gold Nanoclusters using Weakly Adsorbing Polymers to Control the Size

A.1 Calculation of ligand coverage

The saturation coverage of citrate ligands on ~4 nm gold particles was compared with the experimentally determined citrate/gold ratio obtained by TGA. The saturation coverage of a gold particle by citrate was reported to be 4.6×10^{-10} mol/cm^2 [1], which corresponds to a footprint of 0.36 nm^2/ citrate ligand. The surface area of the particle was divided by the footprint of the ligand to determine the maximum number of citrate ligands that could cover the gold particle was ~140. This amount of citrate coverage on the gold nanoparticle corresponds to 6.3% citrate by weight, which agrees well with the experimentally determined value of 7% obtained by TGA. Therefore, the gold surface was saturated by citrate ligands.

A.2 Calculation of polydispersity index (PDI):

The PDI was calculated as M_w/M_n, where M_w and M_n are the weight averaged and number averaged masses, respectively and may be calculated using[2]

$$M_w = \frac{\sum M_i^2 N_i}{\sum M_i N_i} \qquad \text{(A.1)}$$

$$M_n = \frac{\sum M_i N_i}{\sum N_i} \qquad \text{(A.2)}$$

where M is mass and N is the number of particles. PDI determinations were obtained using number weighted particle size distributions obtained using DLS.

A.3 CALCULATION OF DISPLACEMENT OF CITRATE LIGANDS BY LYSINE:

The displacement of citrate ligands by lysine on gold nanoparticles was estimated using the difference in zeta potentials measured for the citrate-only-capped nanoparticles, -44 mV, versus the citrate/lysine-capped nanoparticles, -30 mV. The charge on the particles, Q, was related to the surface potential, $\psi 0$, using

$$Q = \varepsilon_r \varepsilon_0 \Psi_0 a(1 + \kappa a) \qquad \text{(A.3)}$$

where ε_r, the dielectric constant of the aqueous medium, is 80, ε_0 is the permittivity of free space, a is the particle radius, and κ is the inverse Debye length, which is defined as

$$\kappa = e\sqrt{\frac{2N_A I}{\varepsilon_r \varepsilon_0 k_b T}} \qquad \text{(A.4)}$$

where *e* is the elementary charge of an electron, N_A is Avagadro's number, and I is the ionic strength. I was calculated to be 0.0053M, shown in detail below, using ligand/gold ratios determined from TGA using the following equation:

$$I = 0.5\sum_{i=1}^{n} c_i z_i^2 \qquad \text{(A.5)}$$

where c_i is the molar concentration of ion i and z_i is the charge of an ion. In this system, sodium ions are assumed to be the only free ions in solution. Surface potential was estimated using the experimentally measured zeta potential for this calculation. The ratio

of charge for the citrate-only capped nanoparticles to that for the citrate/lysine capped nanoparticles was used to estimate the displacement of citrate by lysine.

A.4 CALCULATION OF SIZE DISTRIBUTION MOMENTS:

Size distribution moments, μ_1 and μ_3, were used to determine whether cluster formation was dominated by condensation or coagulation.

$$\mu_1 = \frac{r_3}{r_h} = \frac{\sqrt[3]{\sum r_i^3 / N_{Tot}}}{N_{Tot} / \sum \frac{1}{r_i}} \qquad (A.6)$$

$$\mu_3 = \frac{r_1}{r_3} = \frac{\sum r_i / N_{Tot}}{\sqrt[3]{\sum r_i^3 / N_{Tot}}} \qquad (A.7)$$

where r_1 is the arithmetic mean radius, r_3 is the cube mean radius, r_h is the harmonic mean radius, and N_{Tot} is the total number of particles in the system. When $\mu_1 = \mu_3 = 1$, the size distribution moments reflect a monodisperse system where aggregates have been formed by condensation. Size distribution moments where $\mu_1 > 1.25$ and $\mu_3 < 0.905$ suggest that aggregates were formed by coagulation[3].

A.5 CALCULATION OF NANOCLUSTER EXTINCTION CROSS SECTION

For a dilute solution, absorbance, *A*, follows Beer–Lambert's Law:

$$A = \varepsilon(\lambda)\, C\ell \qquad (A.8)$$

where ε is the extinction coefficient, *C* is the dispersion concentration, and □ ℓ □is the path length through which light travels. For a path length of 1 cm, and a gold concentration of 56 μg/mL, the maximum absorbance, found at a wavelength of 700 nm, was 1.10. Using Eq. S8, we determined that the average $\varepsilon_{700\ nm}$ was 0.017±0.003 $cm^2/\mu g$ for three dispersions. Assuming that the nanoclusters are spherical, 100 nm in diameter,

and in a closest-packed state, the particle extinction cross section was calculated by, $\varepsilon_{700\ nm}$ x M_{Au}, where $M_{Au}$is the mass of gold per nanocluster, and was estimated to be 1.0×10^{-5} ng/cluster ($M_{Au} = V_p\times\rho_p\times0.72$, where V_p and ρ_p are the particle volume and density, respectively). The average particle extinction cross section was calculated to be ~9.0 x 10^{-15} m^2.

A.6 CALCULATION OF TOTAL INTERACTION POTENTIALS AND THEORETICAL STABILITY RATIOS

Total interaction potentials were calculated by summing van der Waals (VDW), electrostatic, and depletion contributions. The VDW attractive component is described by [2]:

$$V_{VDW} = \frac{-A}{6}\left[\frac{2a^2}{H(4a+H)} + \frac{2a^2}{(2a+H)^2} + \ln\left(\frac{H(4a+H)}{(2a+H)^2}\right)\right] \qquad (A.9)$$

where A is the Hamaker constant of particles interacting in an aqueous medium and H is the surface to surface separation distance between particles. The electrostatic interaction contribution is described by[2]:

$$V_{electrostatic} = \frac{64\pi a k_b T \Gamma_0^2 n_\infty}{\kappa^2}\exp[-\kappa H] \qquad (A.10)$$

where n_∞ is the bulk ion concentration, and Γ_0 is a ratio of constants related to the surface potential, defined as[2]:

$$\Gamma_0 = \frac{\exp\left[\frac{ze\psi_0}{2k_bT}\right] - 1}{\exp\left[\frac{ze\psi_0}{2k_bT}\right] + 1} \qquad \text{(A.11)}$$

where z is the valence of the electrolyte, taken to be 1 in this model, e is the elementary charge unit of an electron, and ψ_0 is the surface potential of the gold nanoparticle.

To construct the interaction potential curves, the necessary input parameters were calculated as described below. In order to determine the bulk ion concentration, n_∞, the number of citrate ligands per gold particle was estimated based on an experimentally observed W of ~7×10^9 for a colloidal gold suspension with no added polymer (Table 2.2). Using Eq. 6, the stability ratio W may be related to the interaction potential, V_{total}, and thus surface potential, ψ_0. Therefore, values for ψ_0.were obtained by matching experimentally determined W values to an interaction potential. The corresponding ψ_0 was calculated to be -95 mV. This value was then used to calculate the charge on the particle using Eq. S3[4]. The calculated particle charge was used to determine the number of charged citrate ligands per particle, which resulted in an estimated value of 11 charged citrate ligands per gold nanoparticle. By using an initial gold concentration of approximately 3 mg/ml, the number density of gold particles can be determined. From this value and the estimated charged citrate ligand coverage, the initial n_∞ was approximately 5.1×10^{22} charged citrate molecules per cubic meter. In order to determine κ, electro-neutrality was assumed, such that the ionic strength of the solution balances the charge on the gold particles. Therefore, κ is defined as[5]

$$\kappa = e\sqrt{\frac{z_{particle} n_{particle}}{\varepsilon_r \varepsilon_0 k_b T}} \qquad \text{(A.12)}$$

where $z_{particle}$ is the valence of the gold nanoparticle, equivalent to the number of citrate ligands per particle, $n_{particle}$ is the number density of gold particles, and ε_r is 80 in this case.

The depletion contribution to the total potential is described in the text (Eq. 5). The number density of micelles, required for the depletion calculation, was dependent on the polymer concentration in the system[6].

$$\rho_\infty = \frac{(C_p - CMC)N_A}{N_{agg}} \qquad \text{(A.13)}$$

where C_p is the polymer concentration, CMC is the critical micelle concentration for the PLA(2k)-PEG(10k)-PLA(2k) triblock copolymer, which was reported as 7 μg/ml[7], and N_{agg} is the aggregation number for the polymer, reported as 165 [8]. The summation of the potentials determines the total interaction potential (V_{total}), which was normalized by k_bT and then plotted as a function of surface to surface separation distance for various evaporation extents in Fig. 9. In order to calculate the potential for a dispersion of nanoclusters, the reduction in surface potential due to ion pairing caused by polymer adsorption was regressed from experimentally determined W values using Eq. 6, taking into account the electrostatic, VDW and depletion terms for V_{total}. Since it was not possible to perform a regression for evaporation extents greater than 50% because of the excessive turbidity of the solutions, the experimental W value corresponding to 50% solvent evaporation, obtained from the observed time required to elicit a change in the dispersion color after 50% evaporation, was chosen. The surface potential reduction

from ion pairing was thus determined to be approximately 1.6. This value was then used to calculate the interaction potential and W values at other evaporation extents.

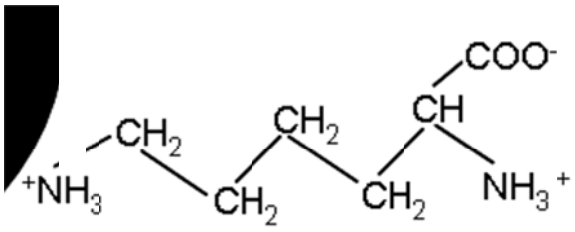

Figure A.1: Schematic of lysine ligand

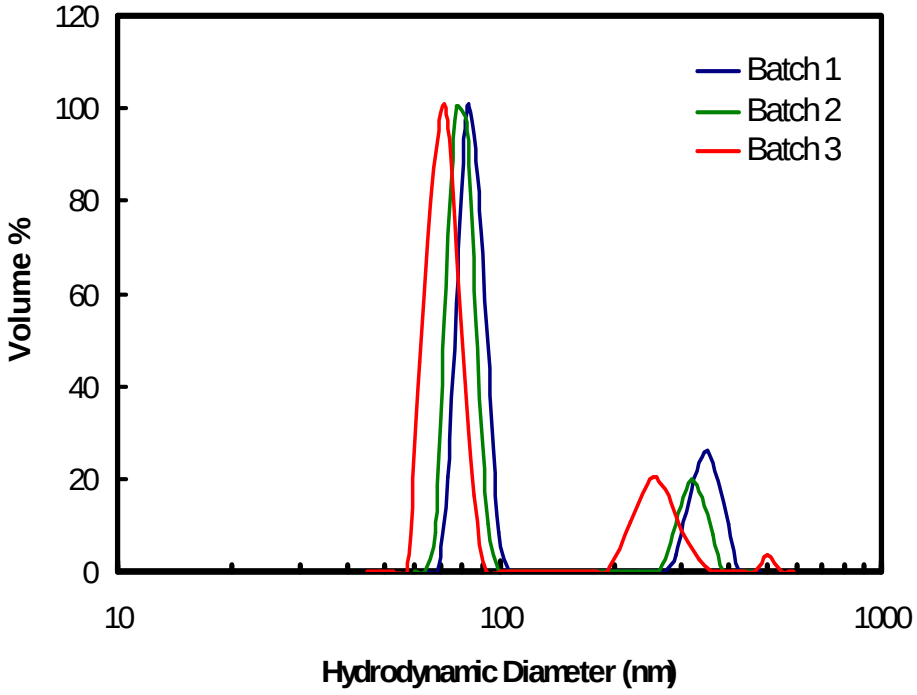

(a)

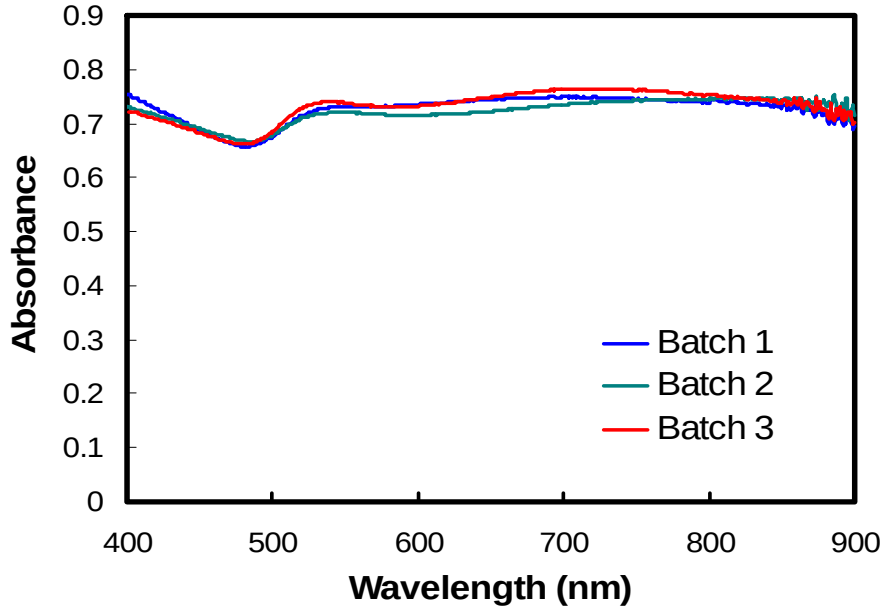

(b)

Figure A.2: Reproducibility of nanoclusters of citrate/lysine-capped gold nanoparticles in terms of (a) size and (b) optical properties. Starting gold and PLA-*b*-PEG-*b*-PLA concentrations were 3 and 50 mg/mL, respectively. Nanoclusters were produced after 100% solvent evaporation.

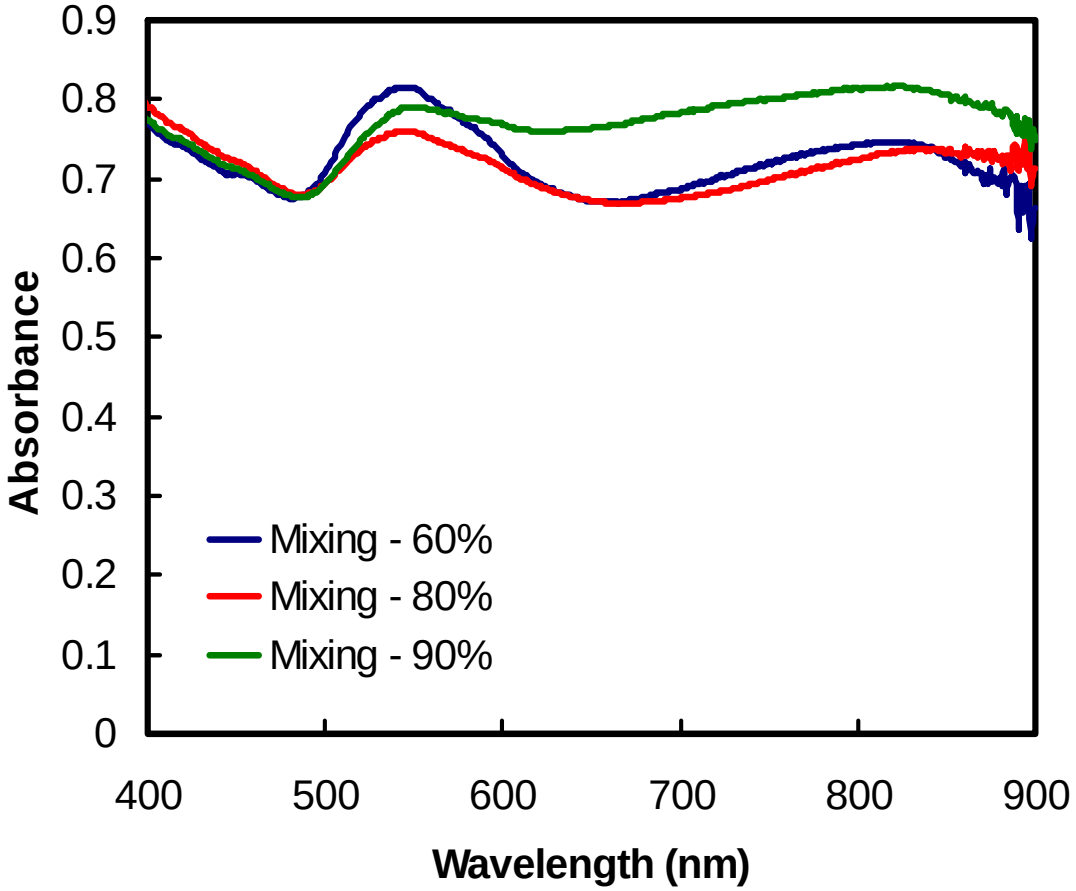

Figure A.3: UV-vis spectra of clusters of citrate-capped nanoparticles made with the mixing protocol. The starting gold concentration was 3 mg/mL and the PLA-*b*-PEG-*b*-PLA /Au ratio was 16/1.

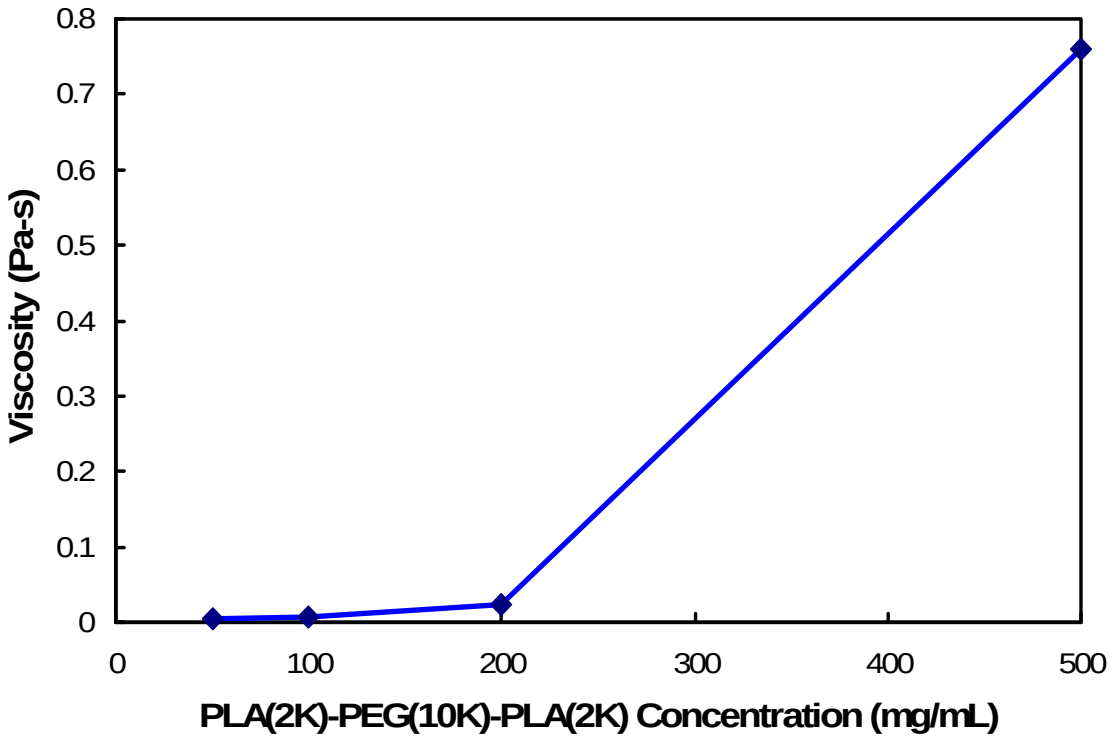

Figure A.4: Viscosity of PLA-*b*-PEG-*b*-PLA as a function of concentration. Viscosity measurements were performed using a cone and plate viscometer (TA Instruments AR 2000ex with a Peltier plate base and aluminum cone, with a diameter of 40 mm, angle of 1^{o} 59 minutes and 56 seconds and a truncation distance of 55 μm).

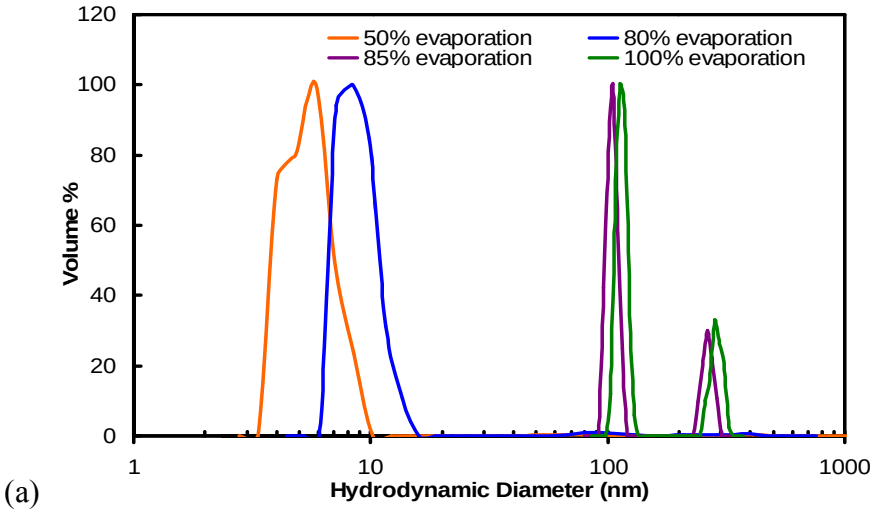

(a)

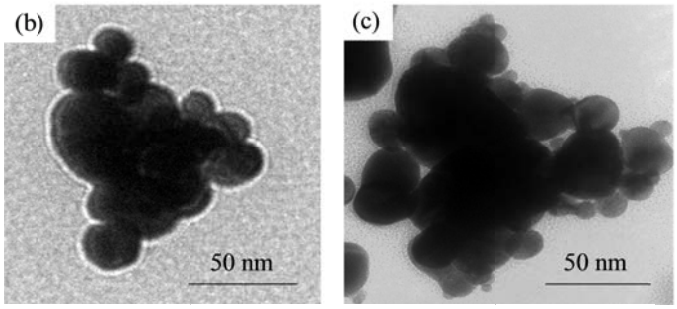

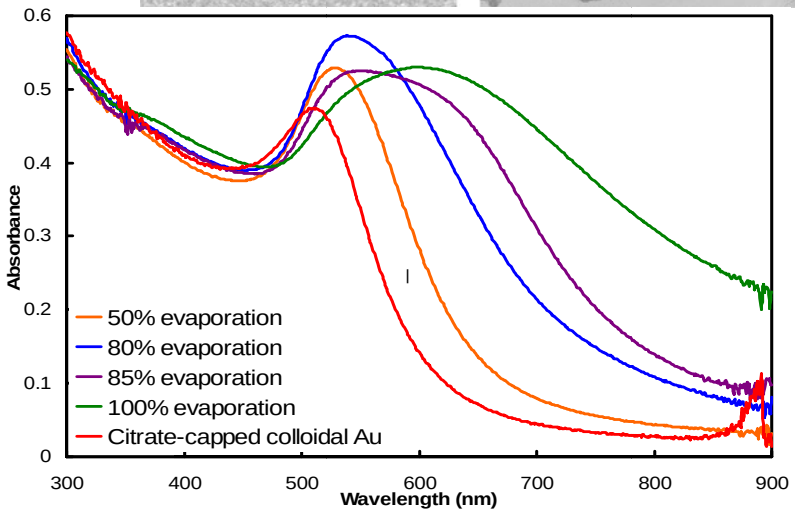

(d)

Figure A.5: (a) DLS measurements, TEM images after (b) 85% and (c) 100% solvent evaporation, respectively, and (d) UV-vis, absorbance spectra for nanoclusters composed of citrate-capped gold nanoparticles produced after different extents of evaporation with a starting gold concentration of 3 mg/mL and a PLA-*b*-PEG-*b*-PLA/gold ratio of 16/1.

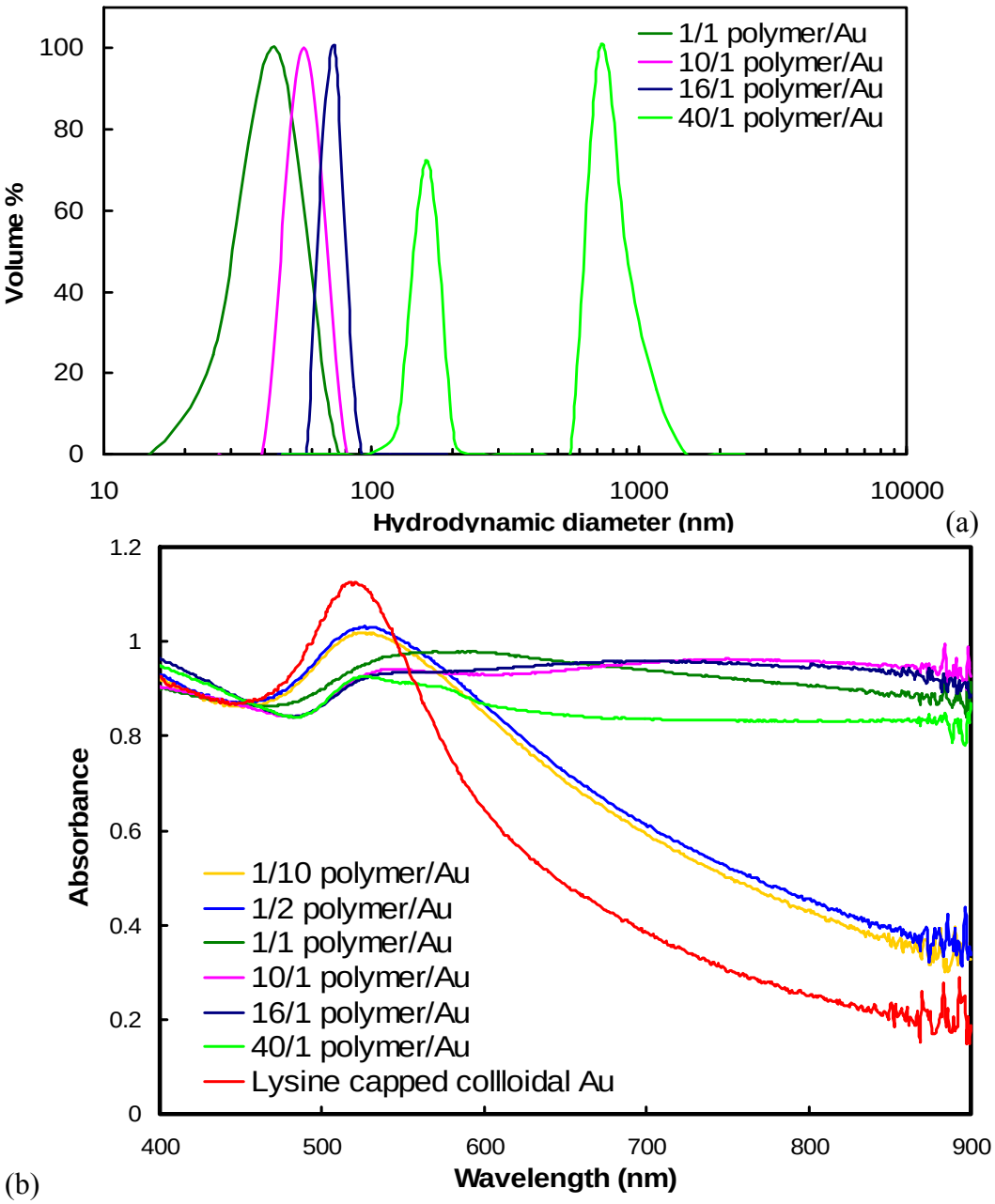

Figure A.6: (a) Particle size measurements by DLS and (b) UV-vis absorbance spectra of clusters of citrate/lysine-capped nanoparticles formed when varying the PLA-*b*-PEG-*b*-PLA /Au ratio. The starting gold concentration was 3 mg/mL and the clusters were formed under 100% solvent evaporation.

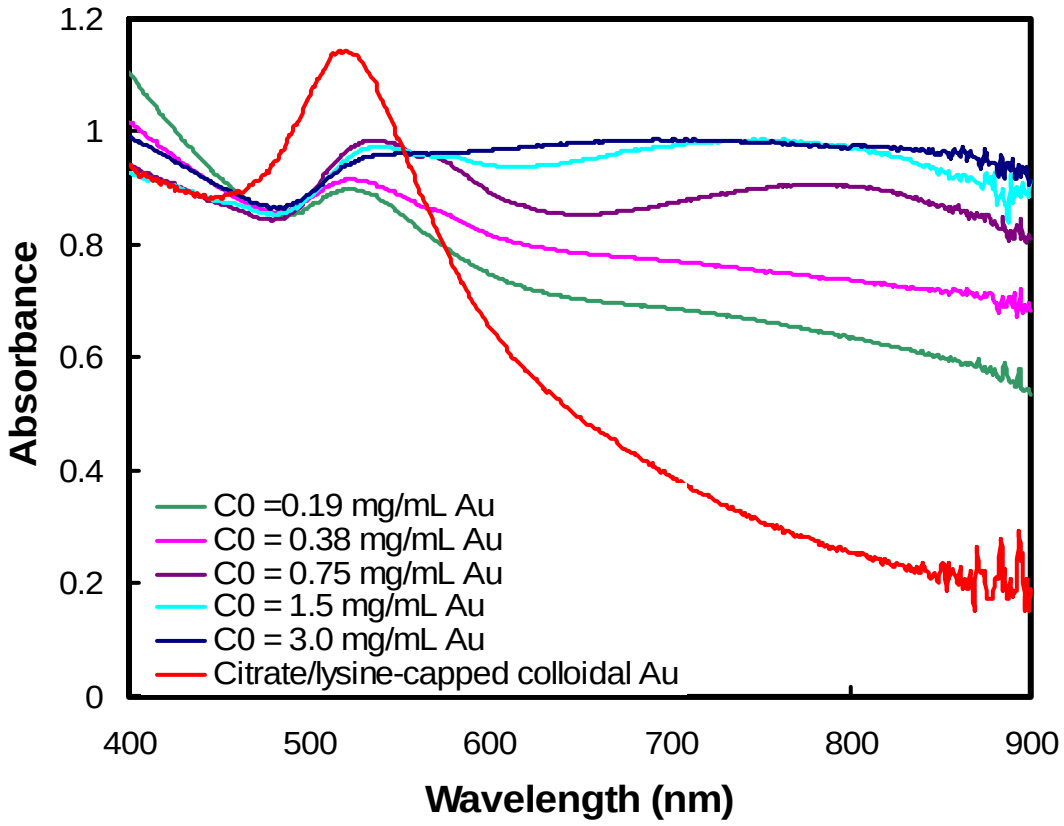

Figure A.7: UV-vis absorbance spectra of citrate/lysine-capped nanoclusters formed when varying the starting concentration of the colloidal gold solution. The starting PLA-*b*-PEG-*b*-PLA concentration was 50 mg/mL.

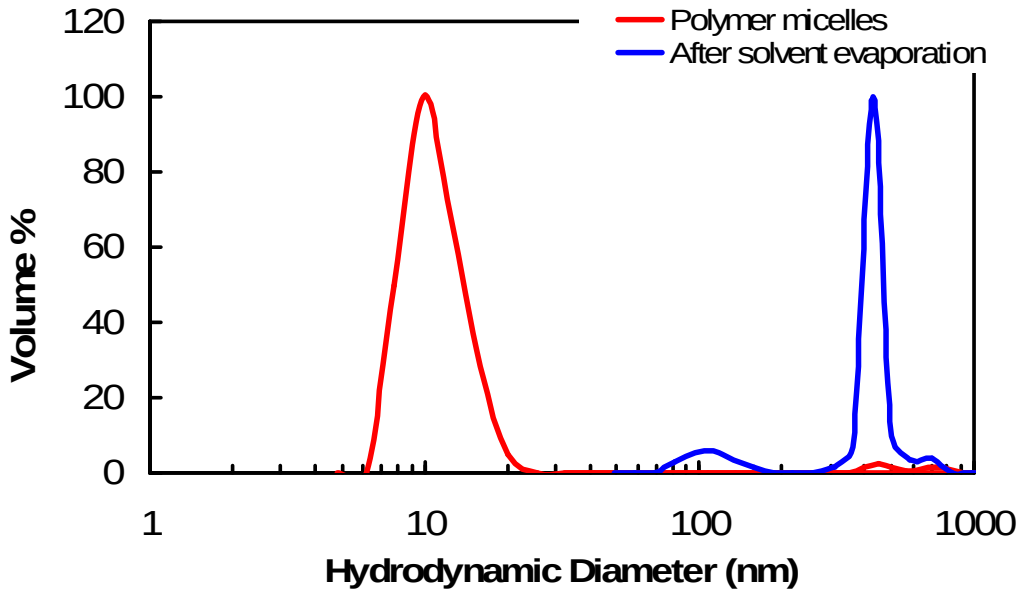

Figure A.8: DLS measurement of PLA-*b*-PEG-*b*-PLA micelles prior to solvent evaporation and after solvent evaporation. A 50 mg/mL polymer solution was prepared. To measure the micelle size, the solution was diluted to 1 mg/mL for analysis by DLS. To determine the effect of solvent evaporation on the polymer, the solution was evaporated to dryness and then redispersed in DI water to a concentration of 5 mg/mL.

Table A.1: Particle sizes, as determined by DLS, of citrate/lysine-capped nanoclusters formed when varying the starting concentration of the colloidal gold solution. The starting PLA-*b*-PEG-*b*-PLA concentration was 50 mg/mL.

Sample	Particle Size Range (nm)
C_0 = 0.19 mg/mL Au	74-118 (12%), 380-608 (80%)
C_0 = 0.38 mg/mL Au	82-122 (62%), 502-613 (38%)
C_0 = 0.75 mg/mL Au	44-57 (68%), 250-377 (32%)
C_0 = 1.5 mg/mL Au	56-100 (89%), 316-562 (11%)
C_0 = 3.0 mg/mL Au	54-101 (82%), 236-359 (18%)

A.7 SUPPLEMENTARY REFERENCES

1. Kunze, J.; Burgess, I.; Nichols, R.; Buess-Herman, C.; Lipkowski, J., Electrochemical evaluation of citrate adsorption on Au(111) and the stability of citrate-reduced gold colloids. *J. Electroanal. Chem.* **2007,** *599*, 147-159.
2. Hiemenz, P. C.; Rajagopalan, R.; Editors, *Principles of Colloid and Surface Chemistry, Third Edition, Revised and Expanded*. 1997; p 688 pp.
3. Friedlander, S. K., *Smoke, dust, and haze : fundamentals of aerosol dynamics* Oxford University Press: New York, NY, 2000.
4. Hunter, R. J., *Zeta Potential in Colloid Science*. Academic Press: 1981.
5. Smith, P. G.; Patel, M. N.; Kim, J.; Milner, T. E.; Johnston, K. P., Effect of Surface Hydrophilicity on Charging Mechanism of Colloids in Low-Permittivity Solvents. *J. Phys. Chem. C* **2007,** *111*, 840-848.
6. Mondain-Monval, O.; Leal-Calderon, F.; Phillip, J.; Bibette, J., Depletion Forces in the Presence of Electrostatic Double Layer Repulsion. *Phys. Rev. Lett.* **1995,** *75*, 3364-3367.
7. Venkatraman, S. S.; Jie, P.; Min, F.; Freddy, B. Y. C.; Leong-Huat, G., Micelle-like nanoparticles of PLA-PEG-PLA triblock copolymer as chemotherapeutic carrier. *Int. J. Pharm.* **2005,** *298*, 219-232.
8. Agrawal, S. K.; Sanabria-DeLong, N.; Tew, G. N.; Bhatia, S. R., Structural Characterization of PLA-PEO-PLA Solutions and Hydrogels: Crystalline vs Amorphous PLA Domains. *Macromolecules* **2008,** *41*, 1774-1784.

Appendix B: Charged Gold Nanoparticles with Essentially Zero Serum Protein Adsorption in Undiluted Fetal Bovine Serum

B.1 Determination of Lysine/Citrate and Cysteine/Citrate Ratios by XPS

The lysine/citrate ratios on the surface of Au nanospheres with lysine/citrate feed ratios of 4.5/1 and 9/1 were determined from the integration of the N 1s and O 1s peaks in the XPS spectrum. Lysine contains 2 N and 2 O atoms, while citrate has 7 O and 0 N atoms. As a result, we set up the following system of simultaneous equations:

$$2y_L = y_N \quad \text{(B.1)}$$

$$2y_L + 7y_C = y_O \quad \text{(B.2)}$$

Here, y_L is the molar fraction of lysine, y_N is the molar fraction of nitrogen, y_c is the molar fraction of citrate, and y_O is the molar fraction of oxygen. For the nanospheres synthesized with a feed ratio of 4.5/1, integration of the N 1s and O 1s spectra yielded an average N/O ratio of 0.12, and thus a lysine/citrate ratio of 0.5. From the integration of the N 1s and O 1s spectra shown in Figure 3.2, we get an average N/O ratio of 0.28, and thus a lysine/citrate ratio of 1.4.

The cysteine/citrate ratios on the surface of the Au nanospheres synthesized with cysteine/citrate feed ratios of 0.3/1 and 0.7/1 were determined from the integration of the N 1s and O 1s peaks in the XPS spectrum, in a manner similar to that of lysine/citrate nanospheres. Cysteine contains 1 N and 2 O atoms, while citrate has 7 O and 0 N atoms. Thus, Equations B.1 and B.2 become:

$$y_{cys} = y_N \quad \text{(B.3)}$$

$$2y_{cys} + 7y_{cit} = y_O \quad \text{(B.4)}$$

Here, y_{cys} is the molar fraction of cysteine, and y_{cit} is the molar fraction of citrate. For a cysteine/citrate feed ratio of 0.3/1, integration of the N 1s and O 1s spectra yielded an average N/O ratio of 0.11, corresponding to a cysteine/citrate ratio of 1.0. For the 0.7/1 cysteine/citrate feed ratio, the average N/O ratio was 0.15, corresponding to a cysteine/citrate ratio of 1.6. In both cases, the ratios of N and O to Au were not quantified, due to the fact that the X-ray beam in XPS does not uniformly penetrate the entire Au sphere.[4]

B.2 Correlation of XPS and Zeta Potential Results

The reduction in nanosphere zeta potential after ligand exchange can be correlated to the XPS results on the mixed charge monolayers, as shown in Table B.1. Approximately 196 citrate ligands are present on the surface of the citrate-capped nanospheres,[3] which corresponds to 196 × 3 = 588 negative charges. Ligand exchange with lysine replaces 3 negative charges with one positive charge, and ligand exchange with cysteine replaces 3 negative charges with a net neutral charge. Thus, for the lysine/citrate nanospheres, the number of charges N on the nanosphere was determined by:

$$N = 3x - y \quad \text{(B.5)}$$

where x is the number of citrate ligands and y is the number of lysine ligands. For the cysteine/citrate monolayers, the number of charges N is determined by:

$$N = 3x \qquad \text{(B.6)}$$

The calculated values of N is then compared to the value of 588 for citrate-capped nanospheres, in order to determine the percentage of negative charge retained on the nanosphere for each mixed charge monolayer. This number compares exceptionally well with the percentage of negative charge retained as determined by zeta potential measurements, as shown in Table B.1.

B.3 DESCRIPTION OF PREVIOUS CELLULAR STUDIES

Solid gold nanoparticles have been shown to aggregate within cellular endosomes.[5,6] In a previous study, however, we have demonstrated the cellular dissociation of ~80 nm nanoclusters within J477A murine macrophage cells.[2] Hyperspectral imaging indicated that over a period of 168 h, the scattering spectra shifted significantly out of the NIR region. Moreover, TEM analysis of cells indicated that dissociation of nanoclusters occurred, as ~80 nm nanoclusters which were visible in TEM images after 24 h, but only sub 5 nm Au nanoparticles were visible in cells after 168 h of incubation. As a result, this previous study provided proof of dissociation of nanoclusters within macrophage cells.

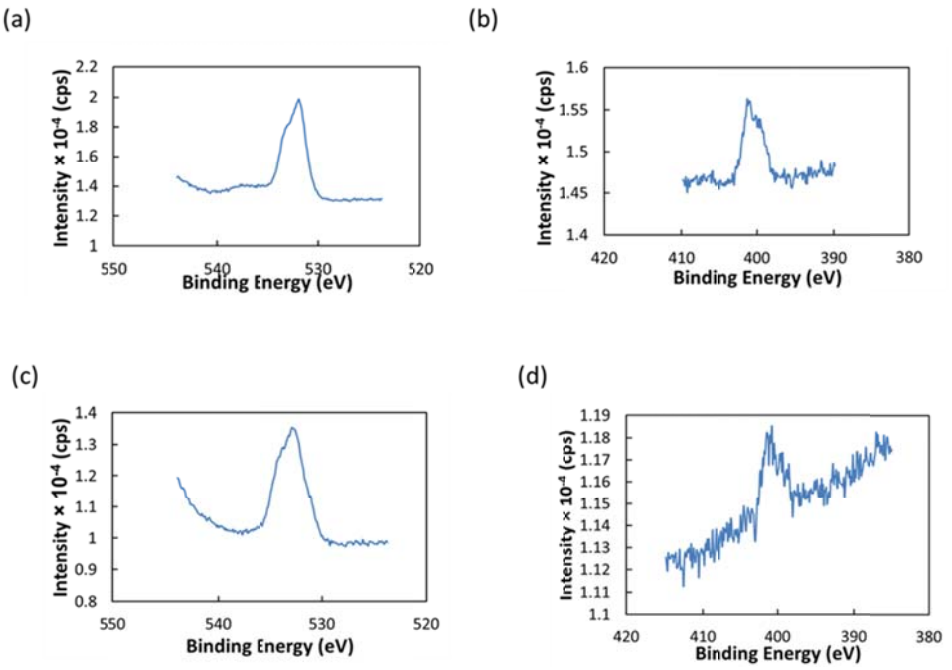

Figure B.1 XPS spectra of (a) O 1s for 1.4/1 lysine/citrate nanospheres, (b) N 1s for lysine/citrate, (c) O 1s for 1.6/1 cysteine/citrate nanospheres, and (d) N 1s for 1.6/1 cysteine/citrate nanospheres.

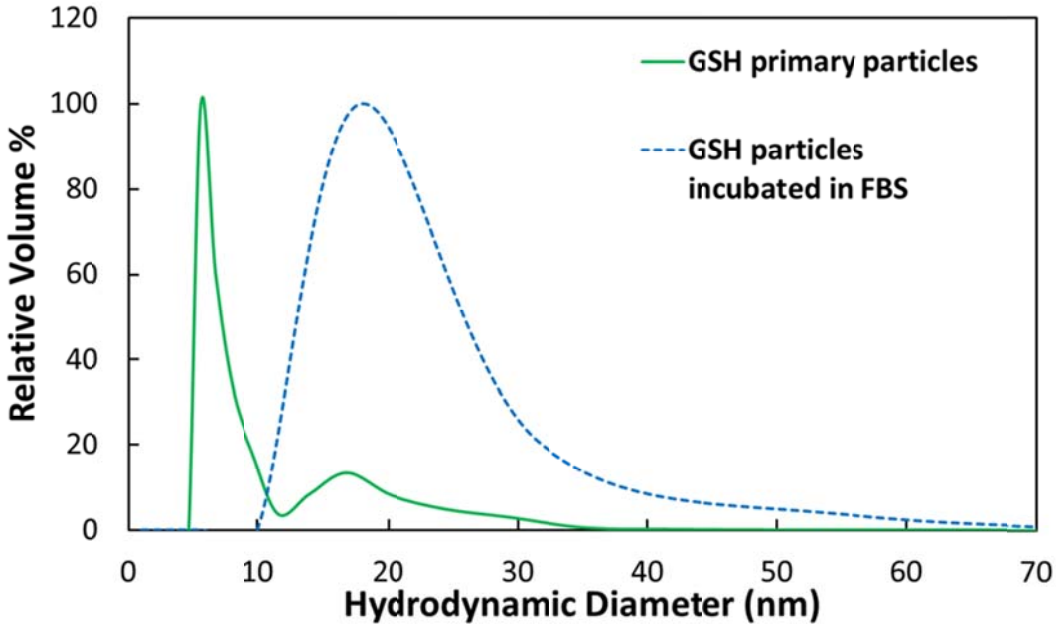

Figure B.2 DLS size distributions of GSH-capped nanospheres before (solid green curve) and after (dashed blue curve) incubation in 100% FBS for 4 h at 37 °C.

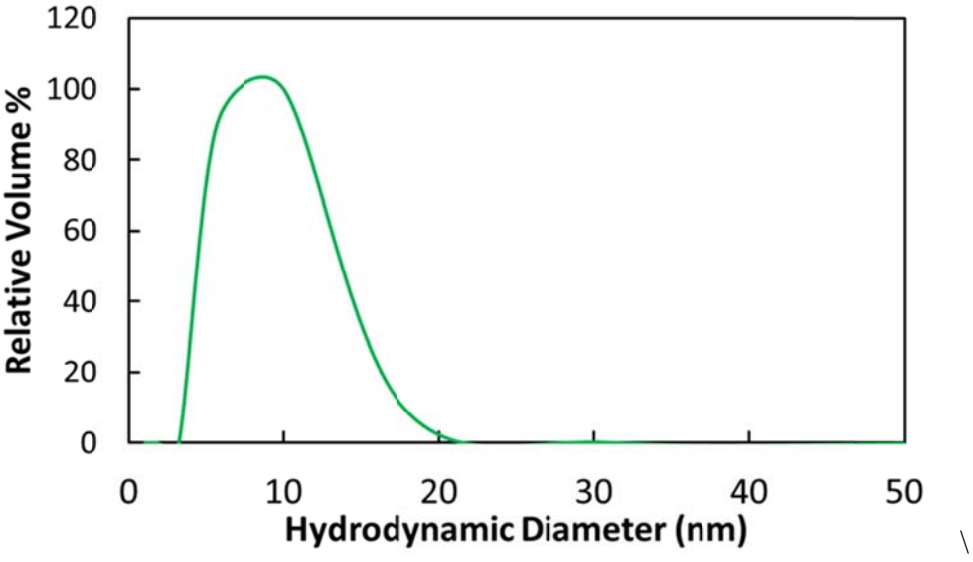

Figure B.3 DLS distribution of pure FBS.

(a)

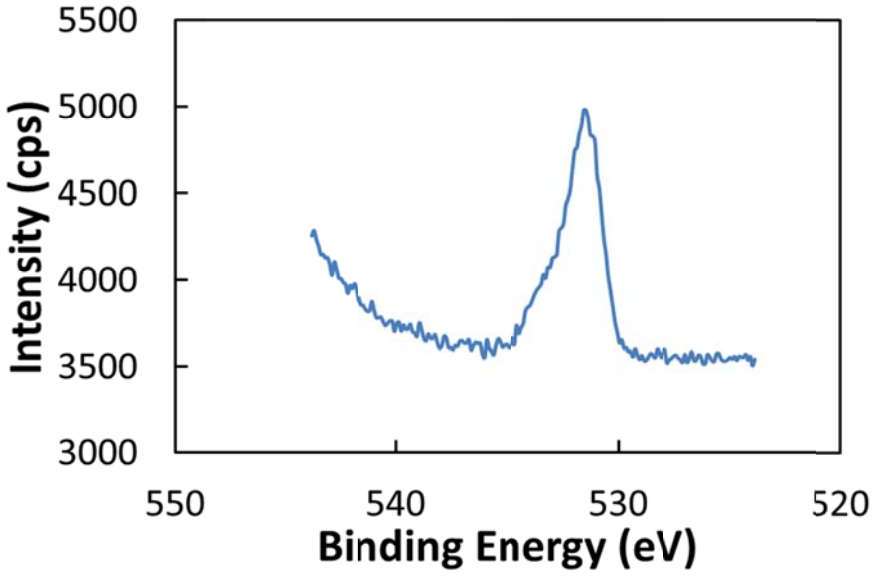

(b)

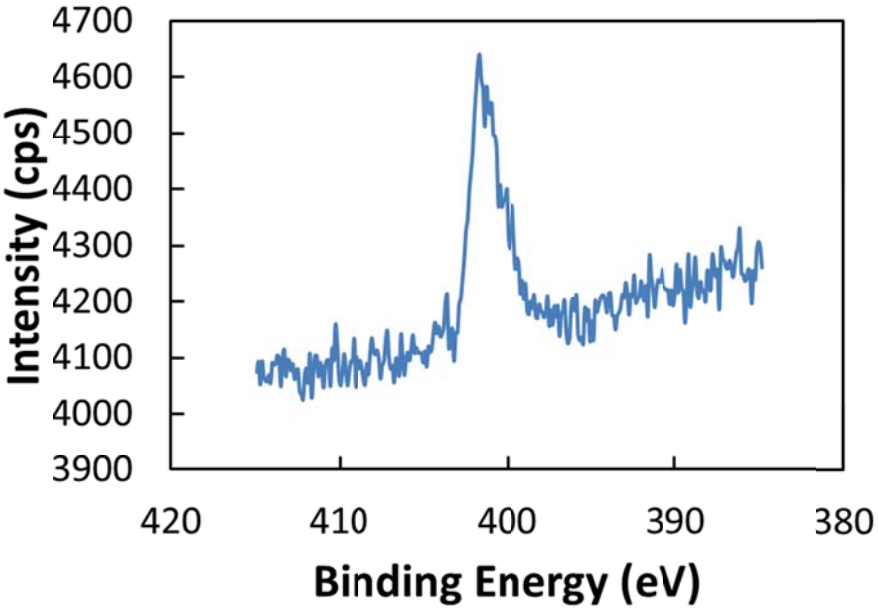

Figure B.4 (a) O 1s and (b) N 1s XPS spectra for nanospheres synthesized with a lysine/citrate feed ratio of 4.5/1.

(a)

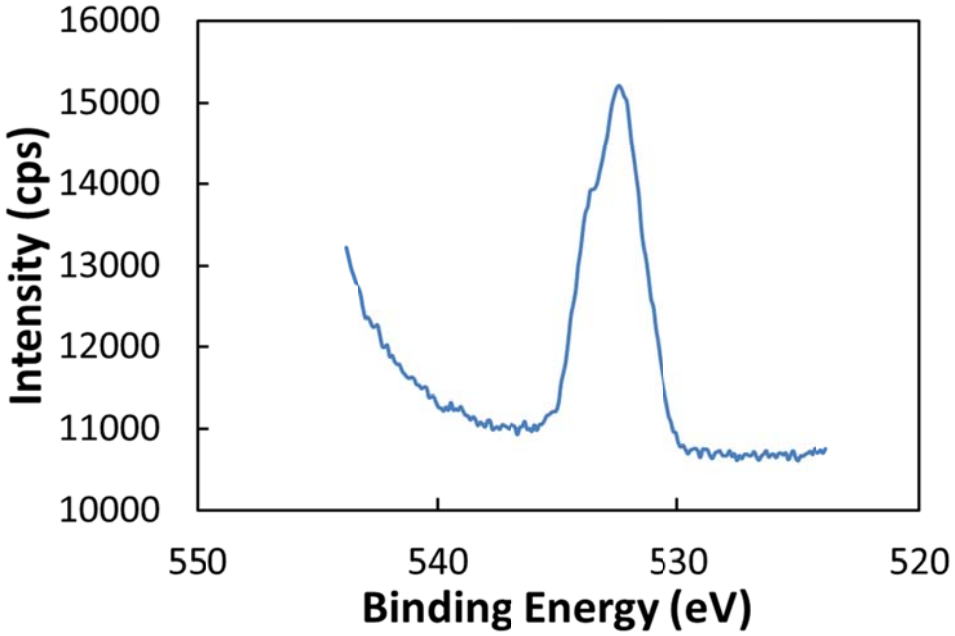

(b)

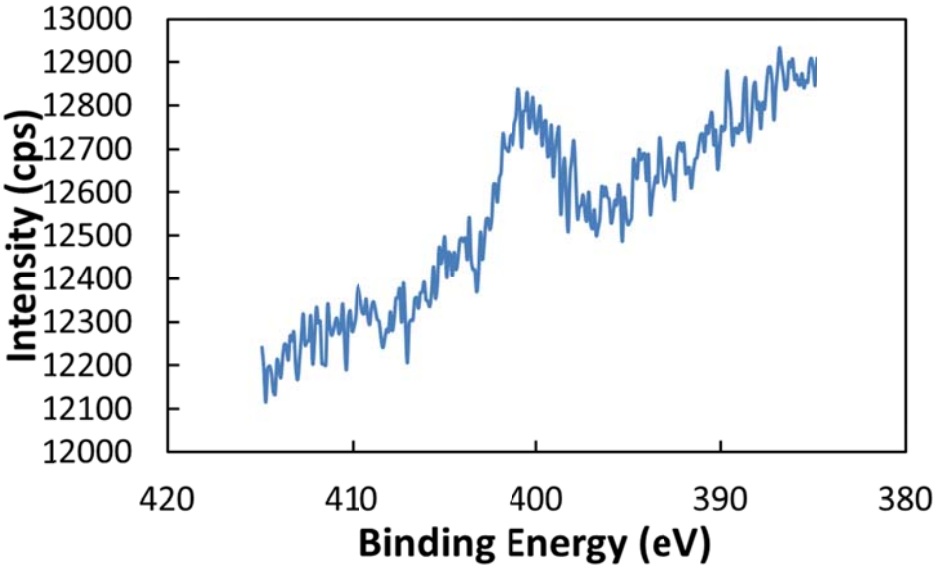

Figure B.5 (a) O 1s and (b) N 1s XPS spectra for nanospheres synthesized with a cysteine/citrate feed ratio of 0.3/1.

(a)

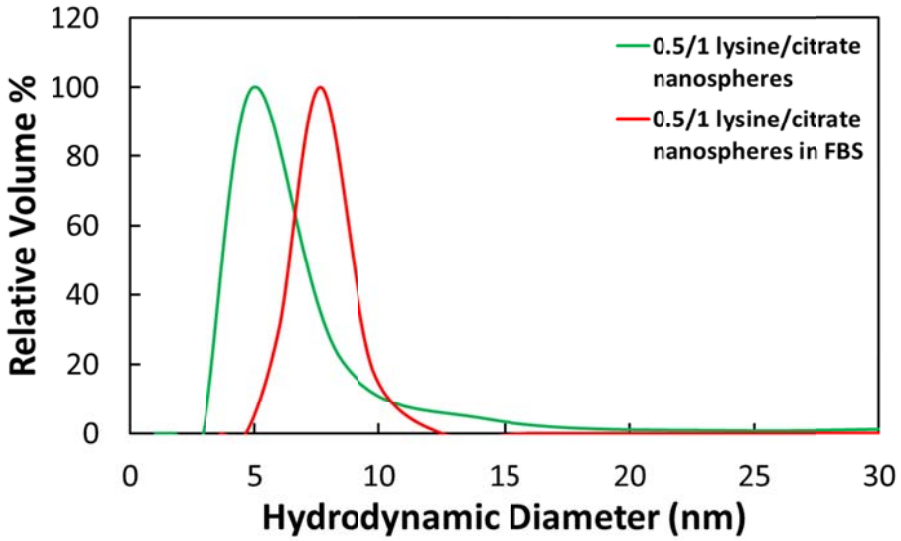

(b)

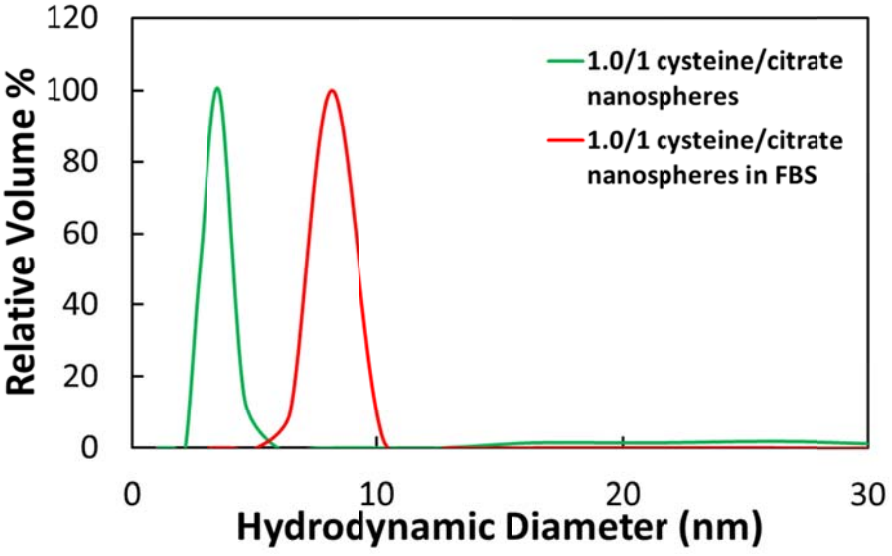

Figure B.6 DLS size distributions before and after incubation in 100% FBS for (a) 0.5/1 lysine/citrate nanospheres and (b) 1.0/1 cysteine/citrate nanospheres

Table B.1 Correlation of XPS and zeta potential results for nanospheres capped with mixed-charge monolayers.

Ligand (s)	**XPS Ligand Ratio**	**Number of Charges from XPS**	**% of Charge Retained from XPS**	**Zeta Potential (mV)**	**% of Charge Retained from Zeta Potential**
Citrate	n/a	588	100%	-58.4 ± 5.3	100%
Lysine/Citrate	0.5	327	56%	-28.9 ± 3.9	49%
Lysine/Citrate	1.4	131	22%	-16.1 ± 2.9	28%
Cysteine/Citrate	1.0	290	49%	-28.8 ± 3.2	49%
Cysteine/Citrate	1.6	228	39%	-21.6 ± 1.7	37%

Table B.2 Centrifugation yields for mixed-monolayer capped nanospheres after incubation in 100% FBS for 4 h at 37 °C.

Ligands	**XPS Ligand Ratio**	**D_h in FBS (nm)**	**Au mass yield in pellet (%)**
Lysine/Citrate in FBS	0.5	7.7 ± 3.8	53.9 ± 13.1
Lysine/Citrate in FBS	1.4	3.9 ± 2.1	26.3 ± 5.8
Cysteine/Citrate in FBS	1.0	8.8 ± 5.8	39.2 ± 13.0
Cysteine/Citrate in FBS	1.6	3.4 ± 2.7	21.3 ± 13.1

Table B.3 Centrifugation yields for mixed-monolayer capped nanospheres in water

Ligands	**XPS Ligand Ratio**	**Au mass yield in pellet (%)**
Lysine/Citrate in FBS	0.5	22.7
Cysteine/Citrate in FBS	1.0	24.1

Table B.4 Reproducibility of 0.5/1 lysine/citrate nanospheres

Sample	Zeta Potential (mV)	DLS (nm)
1	-28.8 ± 5.0	4.7 ± 1.1
2	-26.4 ± 0.4	5.4 ± 1.3
3	-31.6 ± 6.3	4.8 ± 1.2

Table B.5 Reproducibility of 1.4/1 lysine/citrate nanospheres

Sample	Zeta Potential (mV)	DLS (nm)
1	-16.0 ± 6.6	4.6 ± 1.0
2	-15.3 ± 1.2	4.4 ± 1.1
3	-17.0 ± 0.9	4.7 ± 1.2

Table B.6 Reproducibility of 1.0/1 cysteine/citrate nanospheres

Sample	Zeta Potential (mV)	DLS (nm)
1	-29.9 ± 4.3	4.5 ± 3.4
2	-27.6 ± 2.0	5.6 ± 4.4

Table B.7 Reproducibility of 1.6/1 cysteine/citrate nanospheres

Sample	Zeta Potential (mV)	DLS (nm)
1	-22.2 ± 2.7	3.6 ± 2.2
2	-21.0 ± 0.6	3.1 ± 2.8

Table B.8 Full DLS distribution data for 1.4 lysine/citrate nanospheres in 100% FBS

Diameter (nm)	Relative Volume %	Cumulative Volume %
1	0	0
2	0	0
3	100	81
6	19	97
10	4	99
18	1	100
32	0	100
56	0	100

Table B.9 Full DLS distribution data for 1.6 cysteine/citrate nanospheres in 100% FBS

Diameter (nm)	Relative Volume %	Cumulative Volume %
1	0	0
2	32	20
3	100	85
6	19	97
10	4	99
18	1	100
32	0	100
56	0	100

B.4 SUPPLEMENTARY REFERENCES

(1) Tam, J. M.; Murthy, A. K.; Ingram, D. R.; Nguyen, R.; Sokolov, K. V.; Johnston, K. P. *Langmuir* **2010**, *26*, 8988.

(2) Tam, J. M.; Tam, J. O.; Murthy, A.; Ingram, D. R.; Ma, L. L.; Travis, K.; Johnston, K. P.; Sokolov, K. V. *ACS Nano* **2010**, *4*, 2178.

(3) Murthy, A. K.; Stover, R. J.; Borwankar, A. U.; Nie, G. D.; Gourisankar, S.; Truskett, T. M.; Sokolov, K. V.; Johnston, K. P. *ACS Nano* **2013**, *7*, 239.

(4) Watts, J. F.; Wolstenholme, J. *An Introduction to Surface Analysis by XPS and AES*; John Wiley & Sons: West Sussex, England, 2003.

(5) Aaron, J.; Travis, K.; Harrison, N.; Sokolov, K. *Nano Lett.* **2009**, *9*, 3612.

(6) Kneipp, J.; Kneipp, H.; McLaughlin, M.; Brown, D.; Kneipp, K. *Nano Lett.* **2006**, *6*, 2225.

Appendix C: Equilibrium Gold Nanoclusters Quenched with Biodegradable Polymers

C.1 Synthesis of Citrate-Capped Gold Nanospheres

Citrate-coated gold nanospheres were synthesized by adapting a synthesis route which has been described previously.[1, 2] Here, 3 L of deionized water was heated to ~ 97 °C. Aqueous solutions of 1% (w/v) $HAuCl_4 \cdot H_2O$, 1% (w/v) $Na_3C_3H_5O(COO)_3 \cdot 2H_2O$, and 0.075% (w/v) $NaBH_4$ were prepared. 30 mL of each solution was added successively to the deionized water in 1 min intervals, while the solution was stirred vigorously. The resulting gold nanoparticle solution was allowed to cool to room temperature, and was then centrifuged in 250 ml centrifuge tubes at 8500 rpm for 10 min at 4 °C in an Avanti J-E centrifuge (Beckman Coulter, Brea, CA), in order to remove ~100 ml of the 3 L solution as large particles. The remaining supernatant (~0.02 mg Au/ml) was passed through a tangential flow filtration (TFF) setup (KrosFlo Research II, Spectrum Labs, Rancho Domingo, CA), using a polystyrene filter with a pore size of 10 kDa and a filter surface area of 1050 cm^2. TFF processing removed water and excess reaction reagents from the nanoparticle solution, and resulted in ~100 ml of ~1 mg Au/ml solution. 15 ml centrifugal filter devices with a 30 kDa MW cutoff (Ultracel YM-30, Millipore, Billerica, MA) were used to additionally concentrate the nanoparticle solution. After centrifugation at 6000 rpm for 5 min, the resulting gold nanoparticle solution was adjusted with DI water to a concentration of 3.0 ± 0.1 mg Au/ml. Synthesis resulted in ~30 ml of 3 mg/ml Au nanospheres.

C.2 Citrate and Citrate/Lysine Monolayer Calculations

The theoretical weight of a monolayer coverage of citrate ligands, as well as the theoretical weight of a citrate/lysine mixed monolayer, was compared to experimental data determined by TGA. In this calculation, the lysine/citrate ratio was 1.4, as determined experimentally by XPS. The saturation monolayer coverage of citrate on a gold nanoparticle surface was reported to be 4.6×10^{-10} mol/cm^2 .[3] This value correlates to a citrate footprint value of 0.36 nm^2/ligand. The number of citrate ligands comprising a monolayer on the gold nanoparticle surface is given by

$$n = \frac{4\pi\left(\frac{D}{2}\right)^2 \times 0.9}{f} \qquad \text{(C.1)}$$

where *n* is the number of citrate ligands, D is the diameter of the nanoparticle, and f is the ligand footprint. Here, *D* is taken to be 5 nm and *f* is 0.36 nm^2. The factor of 0.9 in the numerator of Equation S1 arises from the approximation of ligand attachment as close-packed circles on a planar surface.[4] Here, n is determined to be 196 citrate ligands/nanoparticle, which corresponds to ~4.7% w/w on a 5 nm gold particle, in reasonable agreement with the TGA result of 4%. In order to calculate the theoretical weight of monolayer coverage after lysine exchange with citrate, the lysine/citrate ratio of 1.4 determined by XPS was used. Since the TGA ligand weight % does not increase from 4% upon the addition of lysine, we can rule out any electrostatic binding between the anionic citrate and cationic lysine, and thus assume that one lysine ligand displaces one citrate ligand, such that the effective footprint for a lysine ligand is also 0.36 nm^2/ligand. Assuming that n remains constant at 196, a lysine/citrate ratio of 1.4 indicates

that the nanoparticle surface contains 114 lysine ligands and 82 citrate ligands, which translates to 4.1% w/w of a 5 nm gold nanoparticle, in very good agreement with the TGA result of 4% w/w. Thus, a monolayer of citrate/lysine may be assumed to be present on the nanoparticles after ligand exchange.

C.3 Calculation of Extinction Coefficients

The relationship between extinction and the extinction coefficient is given by the Beer-Lambert law:

$$A(\lambda) = \varepsilon(\lambda)Cl \qquad \text{(C.2)}$$

where A is the measured extinction at a given wavelength λ, ε is the extinction coefficient at that wavelength, in cm^2/mg, C is the concentration in mg/ml, and l is the path length in cm. For all measurements in this study, the path length is 1 cm. Extinction and extinction coefficient values in this study are determined for a wavelength of 800 nm.

C.4 XPS Determination of Ligand Ratio

In order to determine the ratio of lysine/citrate ligands, XPS spectra were recorded for primary gold nanospheres after ligand exchange. Integration of N 1s and O 1s peaks was conducted in order to determine the atomic percentages of N and O atoms on the surface of the gold nanospheres. Lysine contains 2 N atoms and 2 O atoms (and has been shown to have a XPS N/O intensity ratio which corresponds favorably to $1/1^5$), whereas citrate contains 7 O atoms and no N atoms. Thus, the following system of simultaneous equations can be set up:

$$2y_L = y_N \qquad \text{(C.3)}$$

$$2y_L + 7y_C = y_O \qquad \text{(C.4)}$$

where y_L is the molar fraction of lysine, y_N is the molar fraction of nitrogen, y_C is the molar fraction of citrate, and y_O is the molar fraction of oxygen. We then define the N/O atomic ratio $R_{N/O}$ as y_N/y_O, and we obtain:

$$\frac{y_L}{y_C} = \frac{7R_{N/O}}{2-2R_{N/O}} \qquad \text{(C.5)}$$

Equation C.4 thus provides a simple algebraic expression for the lysine/citrate ratio. From the N 1s and O 1s peak integrations, we have a N/O ratio of 0.28, and thus a lysine/citrate ratio of 1.4. We did not attempt to determine ratios of N and O to Au, as the X-ray beam in XPS did not uniformly penetrate the entire Au sphere.[6]

C.5 Charge Screening Calculation

In order to determine the percentage of charge retained in the nanoclusters, the number of negative charges in a cluster of *n* primary particles was determined from zeta potential measurements. This value was then compared to the total theoretical number of negative charges on *n* primary particles, derived from the primary particle zeta potential. In order to determine the number of negative charges in a cluster, the charge on a nanocluster was related to the zeta potential by the equation[7]:

$$Q = 4\pi\epsilon_r\epsilon_0\zeta R_C(1 + \kappa R_C) \qquad \text{(C.6)}$$

Here, Q is the charge on the nanocluster (in C), ϵ_r is the dielectric constant of the medium (80 for aqueous solvents), ϵ_0 is the permittivity of free space, ζ is the zeta potential, R_c is the nanocluster radius, and κ is the inverse Debye length. For a salt concentration of 1 mM, κ is 10^8 m^{-1}. In order to calculate the number of charges in a nanocluster, Q was divided by e, the unit of elementary charge. The relationship presented in Equation C.6 can explain the increase in number of charges per cluster even when the measured zeta potential magnitude decreases, as shown in Table 4.4. Since Q is quadratically proportional to the cluster radius, but only directly proportional to the zeta potential, an increase in cluster radius can result in an increase in nanocluster charge even when the zeta potential magnitude is decreased.

The theoretical number of charges was calculated by first determining the number of primary particles in a nanocluster, using the equation:

$$n = \left(\frac{R_C}{R}\right)^3 \times 0.72 \tag{C.7}$$

where n is the number of primary particles in a nanocluster, R_c is the nanocluster radius, R is the primary particle radius (2.5 nm in our case), and 0.72 is the packing fraction assuming closely-packed primary particles within a cluster. The charge on a primary particle is calculated by using Equation C.5, with values for zeta potential and radius for the primary particles. The percentage of charge retained was calculated by dividing the number of negative charges on a nanocluster by the theoretical number of charges for n particles, and these results are presented in Table 4.4.

C.6 EQUILIBRIUM MODEL DETAILS

In order to generate the size contours presented in Figure 4.9, gold and polymer concentrations, and thus volume fractions, were related to the equilibrium cluster size n^* through Equation 4.5. Here, the attraction magnitude a within a nanocluster was calculated from the sum of the van der Waals attractive interaction potential and the depletion interaction potential. The van der Waals interaction potential is given by[7]:

$$V_{vdw} = -\frac{A_{gwg}}{6}\left[\frac{2R^2}{H(2R+H)} + \frac{2R^2}{(2R+H)^2} + ln\left(\frac{H(4R+H)}{(2R+H)^2}\right)\right] \quad \text{(C.8)}$$

Here, R is the primary nanoparticle radius, H is the interparticle surface-surface separation distance, and A_{gwg} is the Au-Au Hamaker constant in an aqueous medium.[8] An interparticle distance of 1 nm is assumed within a nanocluster, and thus V_{vdw} is -3.01k_bT. The interparticle distance of 1 nm is a reasonable assumption given that the sensitivity of the free energy model is relatively low for interparticle distances up to 5 nm. Here, 5 nm is the maximum assumed interparticle distance given the strong NIR extinction exhibited by the nanoclusters. When the interparticle distance is increased from 1 nm to 5 nm, the predicted size at, for example, a c_p of 20 mg/ml and a c_{Au} of 1 mg/ml decreases from 38.9 nm to 35.9 nm, and the predicted size at a c_p of 80 mg/ml and a c_{Au} of 4 mg/ml decreases from 19.2 nm to 18.4 nm. Thus, the decrease in size is ~4-8% due to the increase in assumed interparticle spacing, within the error of DLS measurements.

In order to determine the molecular weight and R_g in Equation 4.6, we use the relationship:[9]

$$R_g = 0.0215M^{0.583} \quad \text{(C.9)}$$

where $R_g = R_h/0.64$.[9]

The depletion potentials calculated for different experimental polymer concentrations are shown in Figure C.3. The depletion component of the attraction *a* in Equation 4.4 is calculated by assuming an interparticle distance of 1 nm. Thus, *a* is the sum of the depletion and van der Waals attractions.

The entropic contributions of counterion dissociation from the charges on the gold nanoparticles is accounted for using the expression:[10, 11]

$$F_E = 2n_c q\left[ln\left(\frac{q}{q_0}\right) - 1\right] \quad \text{(C.10)}$$

where q_0 represents the charge on the gold particle where the cluster free energy is minimized for weakly-charged systems[10, 11] and can be related to the number of dissociable ion sites per gold primary particle and gold volume fraction, as described below.

Nanocluster charge q (or q_0) depends on both the number of dissociable sites σs and on the particle volume fraction ϕ_{Au}, due to the greater entropic gains upon counterion dissociation in more dilute systems.[10, 11] The relationship between q_0, σs, and ϕ_{Au} is given by:[10]

$$q_0^2 = \frac{4\pi R^3 \sigma s}{b^3 e^{\Delta\epsilon + 2}\phi_{Au}} \quad \text{(C.11)}$$

In Equation C.11, R is the radius of the primary nanoparticle, b is the distance between opposite charges in an ionic bond, σ is the density of dissociable ion sites on a primary particle, equivalent to the effective charge density on a primary gold nanoparticle, s is the surface area of a primary nanoparticle, and $\Delta\epsilon$ is the dissociation energy of an ion pair, which can be expressed as $\Delta\epsilon = \lambda_b/b$, where λ_b is the Bjerrum length. At room temperature, $\lambda_b = 56/\epsilon_r$ nm, where ϵ_r is the dielectric constant.[10] The value of σs was determined to be 2.78, using Equation C.5. Equation C.11 is used to calculate the charge per particle in a cluster, which is then fed into Equation 4.4. The size contours in Figure 4.9 are subsequently generated. The parameters used to generate these contours are given in Table C.1.

C.7 REDUCED DIELECTRIC CONSTANT OF WATER IN CLUSTERS

The dielectric constant of liquid water is known to be significantly reduced when it is confined to nanometer length scales.[11-14] This should be especially true in the small channels (less than ~1nm) between the closely spaced primary particles in the Au nanoclusters. A recent simulation study[12] found that water's dielectric constant is reduced to approximately a third of water's bulk value in highly crowded systems, which is consistent with our choice of 25 for the model calculations in the present study. This has important energetic implications, *e.g.* enhancing ion pairing between the ligand charges on the gold nanoparticle surface and the counterions and hence decreasing the effective charge per particle q. With the low local dielectric constant, the Debye length is sufficiently large for long ranged repulsion to balance short ranged attraction and favor nanocluster formation, as shown in Equation 4.4.

(a)

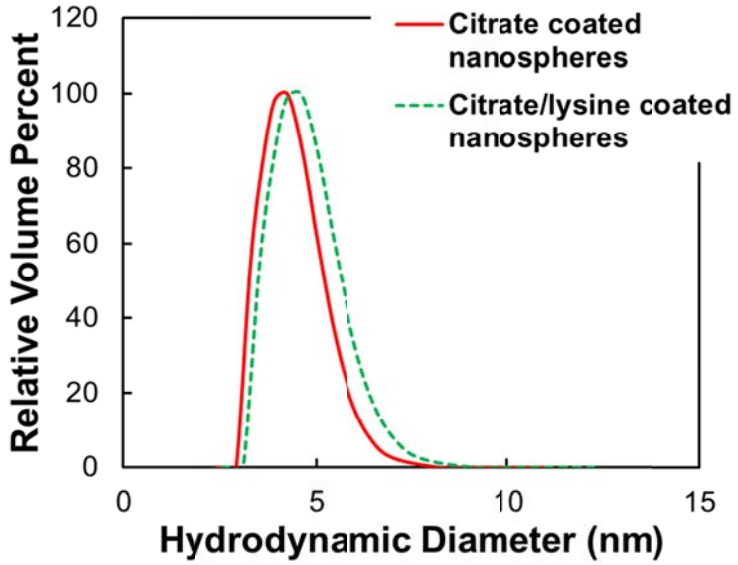

(b)

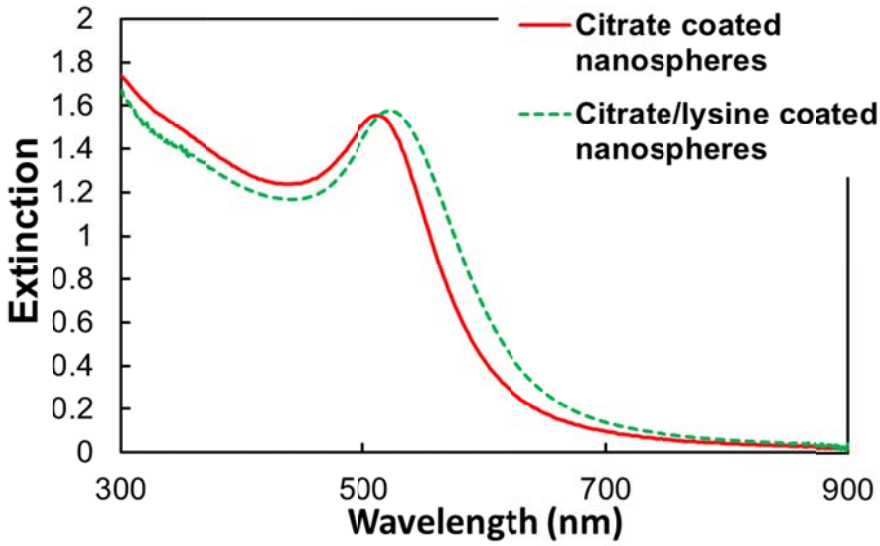

Figure C.1: (a) DLS size distributions and (b) UV-Vis-NIR extinction spectra of citrate-coated nanospheres (red, solid) and citrate/lysine coated nanospheres (green, dashed) after ligand exchange. UV-Vis-NIR spectra were taken at a gold concentration of ~90 μg/ml.

(a)

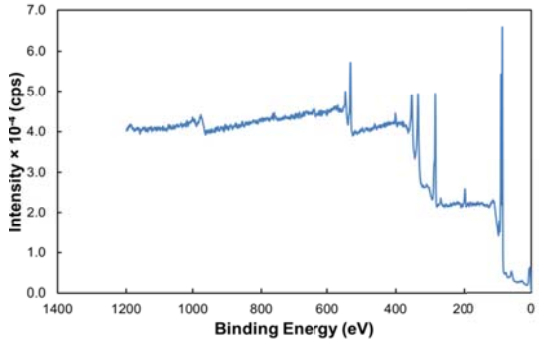

(b)

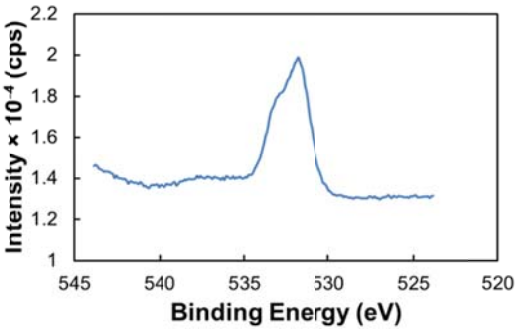

(c)

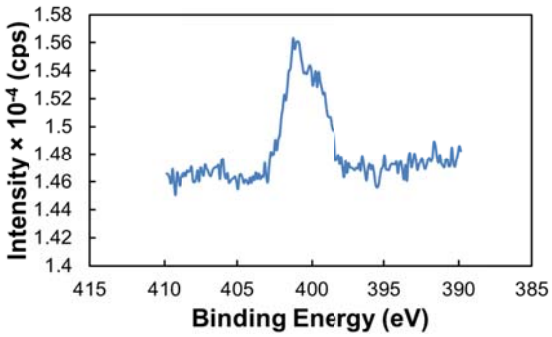

Figure C.2: (a) XPS survey scan, (b) O 1s peak and (c) N 1s peak of lysine/citrate capped Au nanospheres.

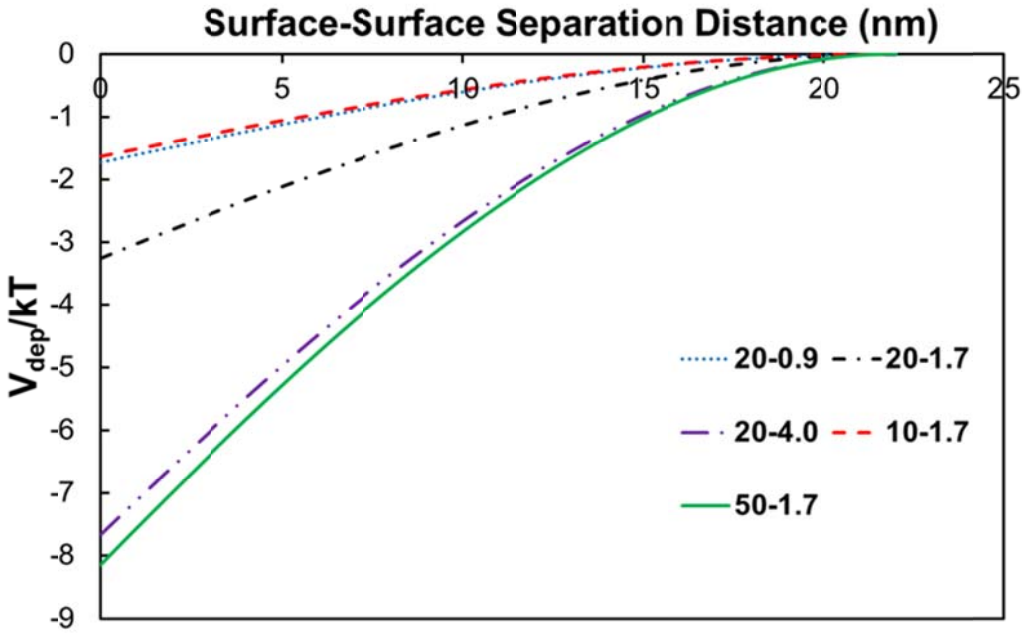

Figure C.3: Depletion potentials calculated for polymer concentrations identical to the indicated experimental samples.

(a)

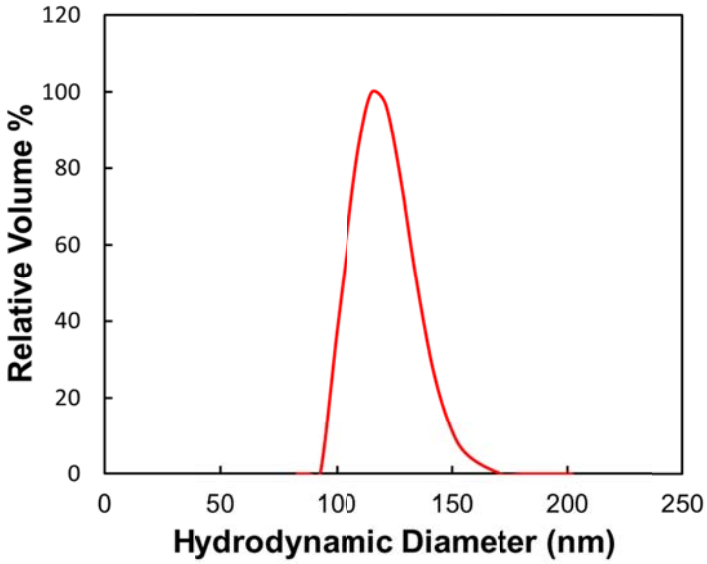

(b)

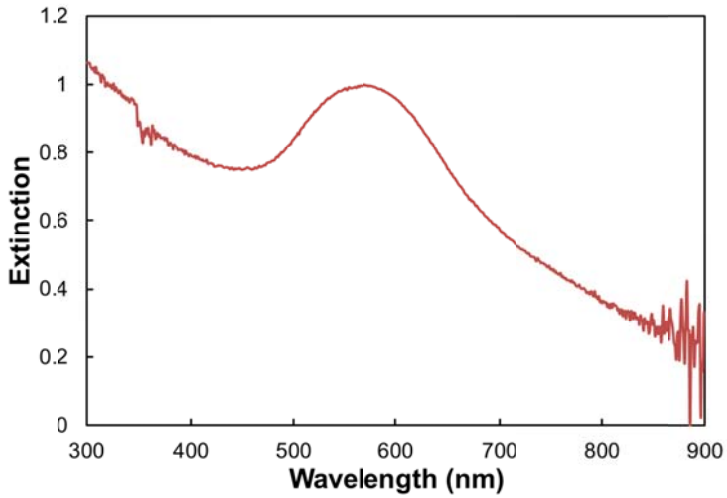

Figure C.4: (a) DLS size distribution and (b) UV-Vis-NIR extinction spectrum of nanoclusters formed with a 6 mg/ml initial Au concentration and a 16/1 polymer/Au ratio. Here, all polymer solution was added in one step instead of iteratively.

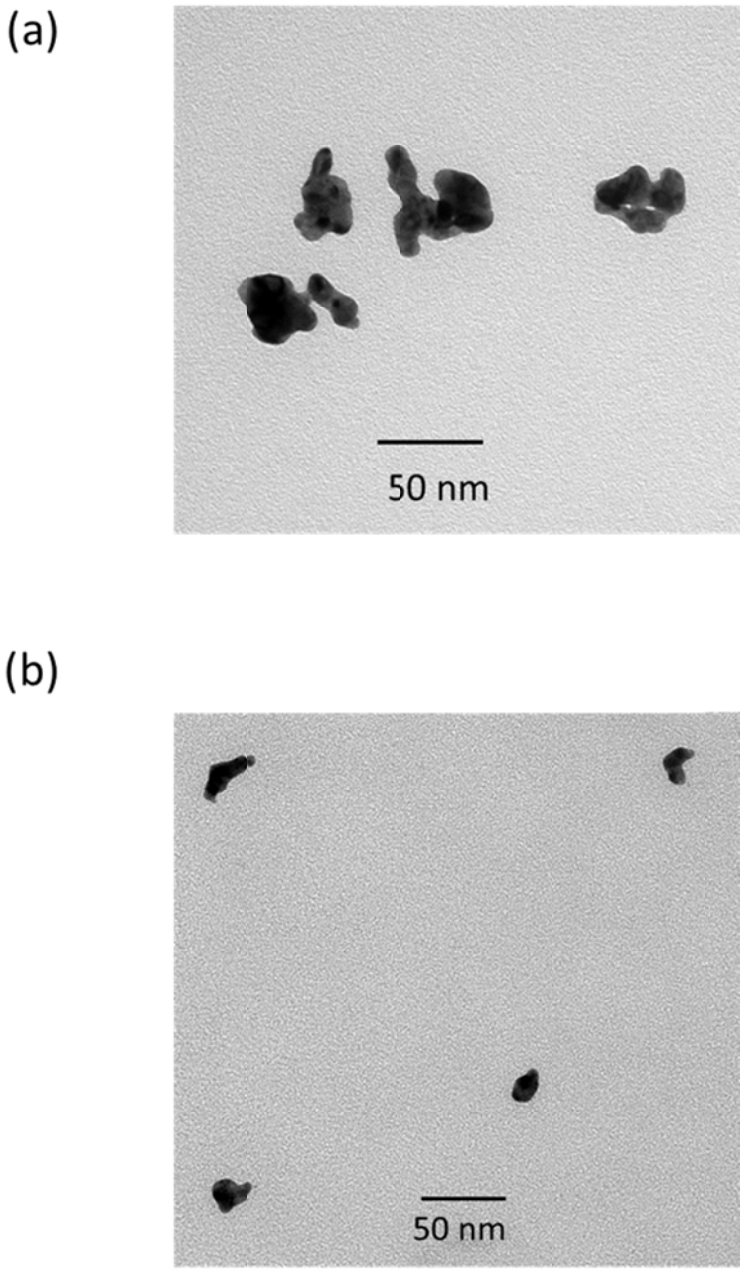

Figure C.5: TEM images showing multiple nanoclusters of (a) 20-4.0 particles and (b) 20-0.9 particles.

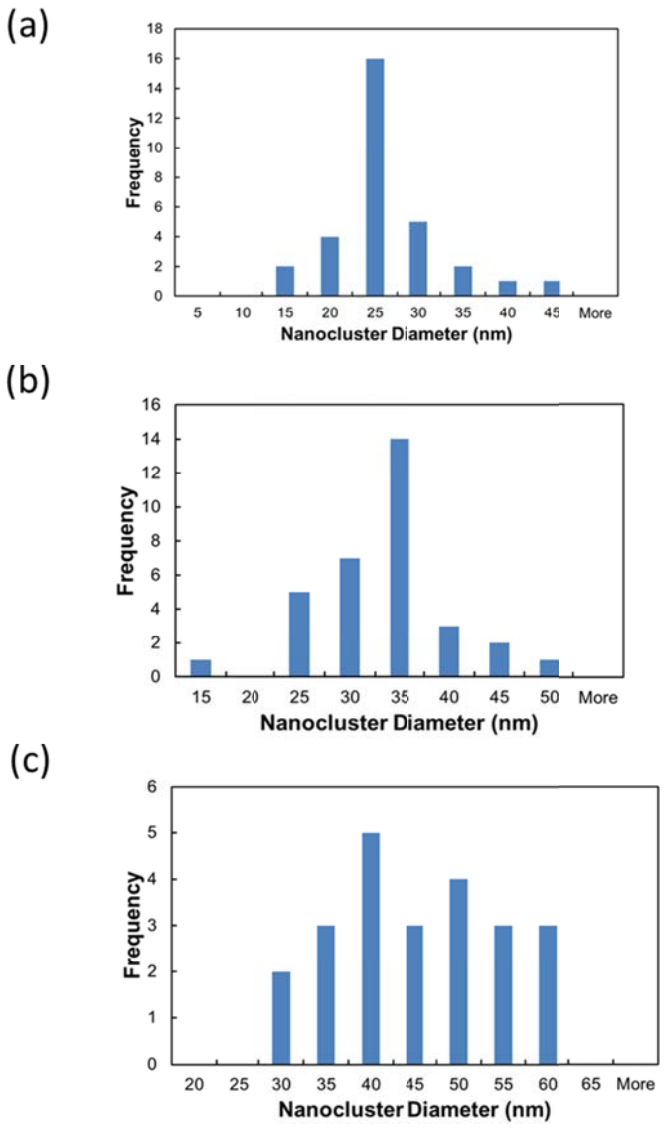

Figure C.6: Histograms of nanocluster diameters obtained from TEM image analysis of (a) 20-0.9 particles, where 31 particles were analyzed from 14 separate images from one grid (b) 20-1.7 particles, where 33 particles were analyzed from 18 separate images from one grid and (c) 20-4.0 particles, where 23 particles were analyzed from 15 separate images from one grid. TEM images were taken of clusters with discernible boundaries. Grids in all cases showed minimal unclustered particles or exceedingly large clusters (relative to the sizes shown in histograms).

(a)

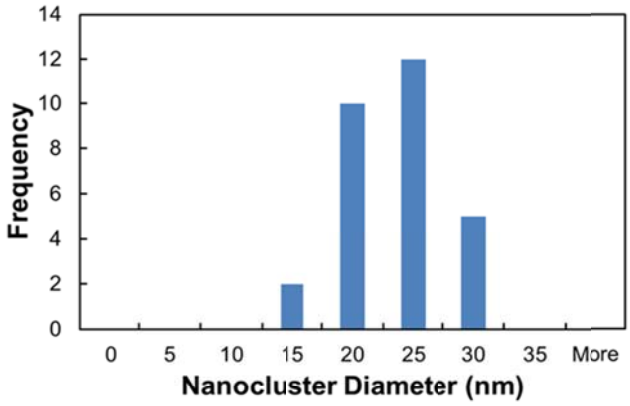

(b)

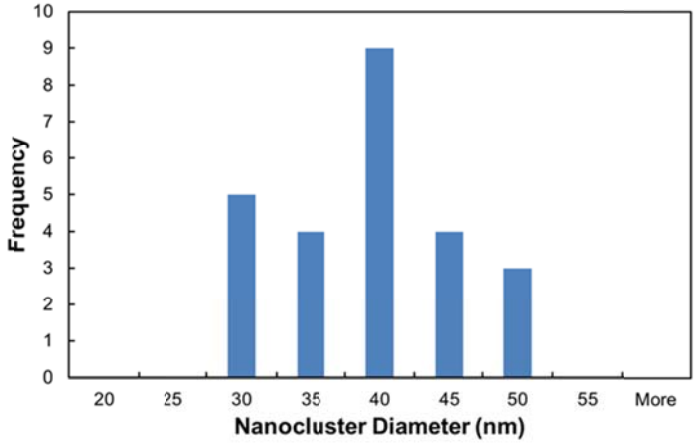

Figure C.7: Histograms obtained from TEM image analysis of (a) 10-1.7 particles, where 29 particles were analyzed from 19 separate images of one grid and (b) 50-1.7 particles, where 25 particles were analyzed from 23 separate images of one grid. TEM images were obtained in the same manner as in Figure C.6 above.

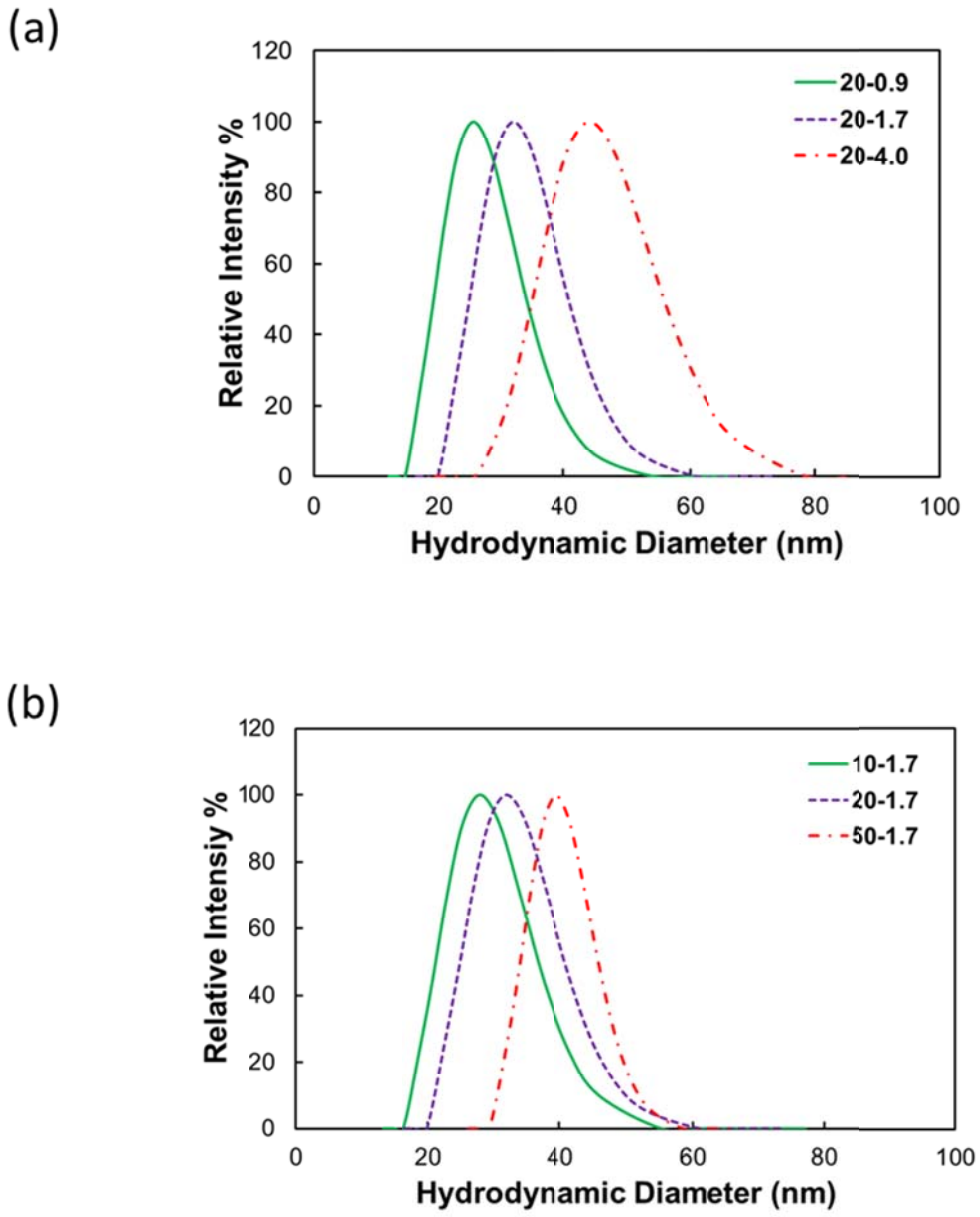

Figure C.8: Intensity-weighted DLS D_H distributions of (a) 20-0.9, 20-1.7, and 20-4.0 particles, and (b) 10-1.7, 20-1.7, and 50-1.7 particles.

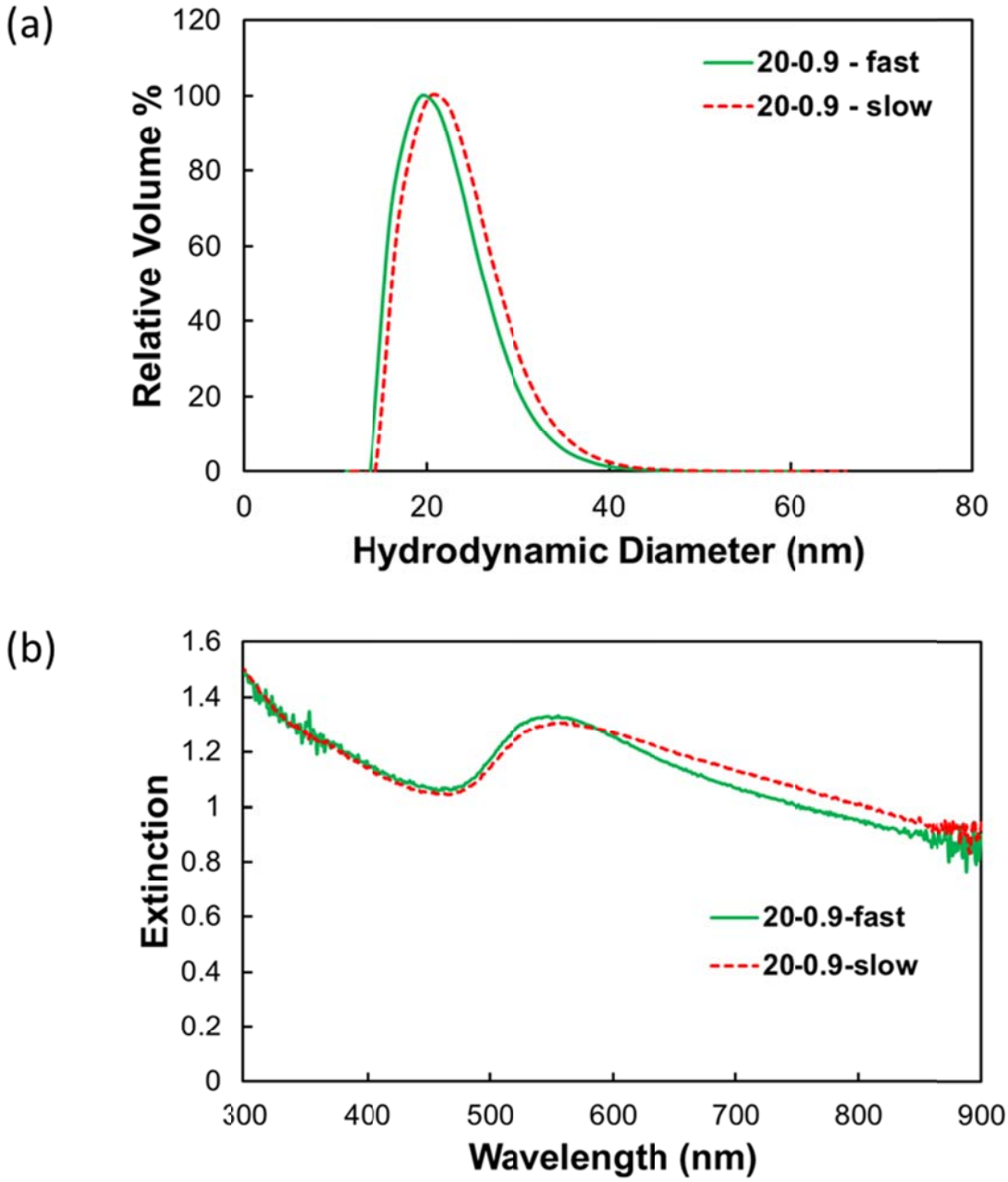

Figure C.9: (a) DLS D_H distributions and (b) UV-Vis-NIR extinction spectra for 20-0.9 particles synthesized over 40 min (fast) and 4.5 hr (slow).

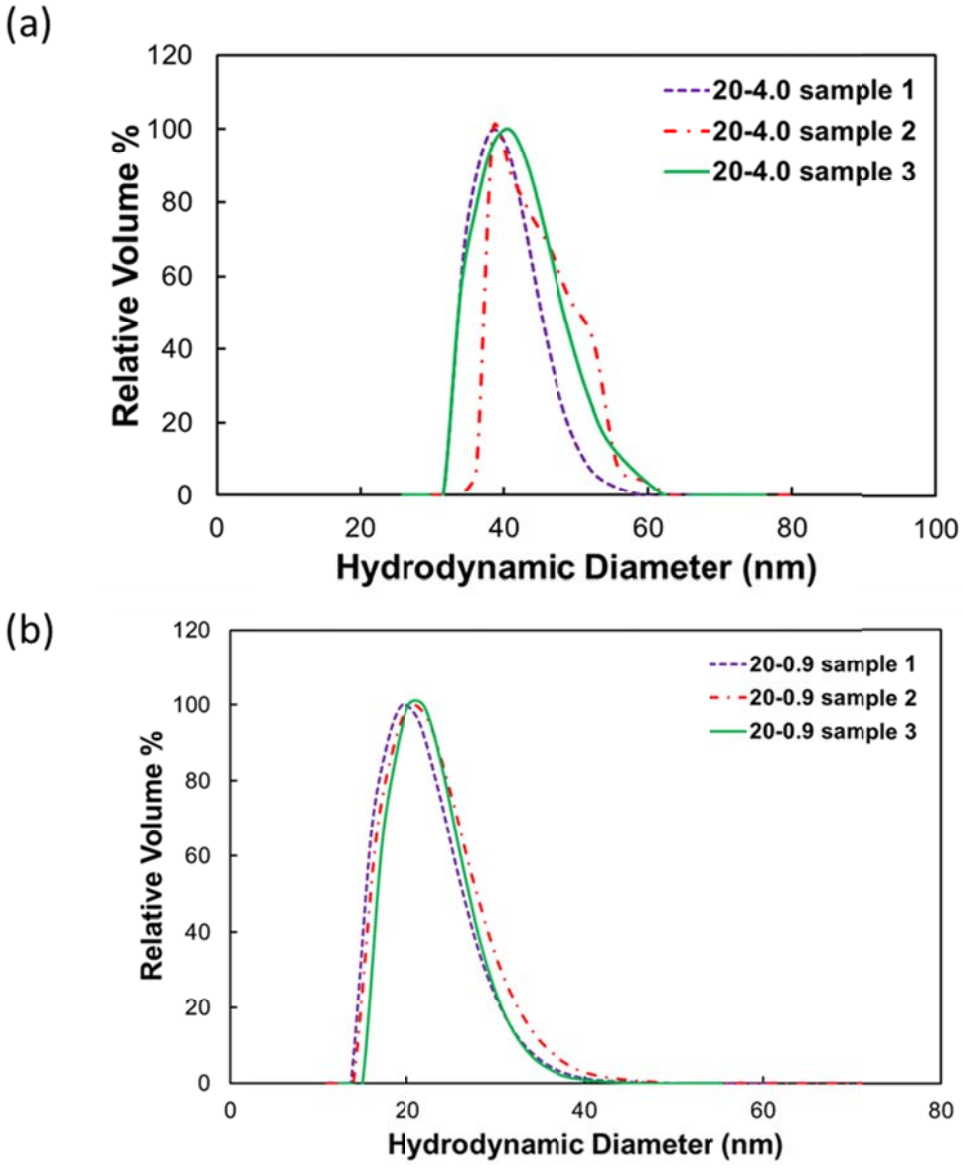

Figure C.10: Reproducibility of D_H distributions for three separate samples each of (a) 20-4.0 particles and (b) 20-0.9 particles.

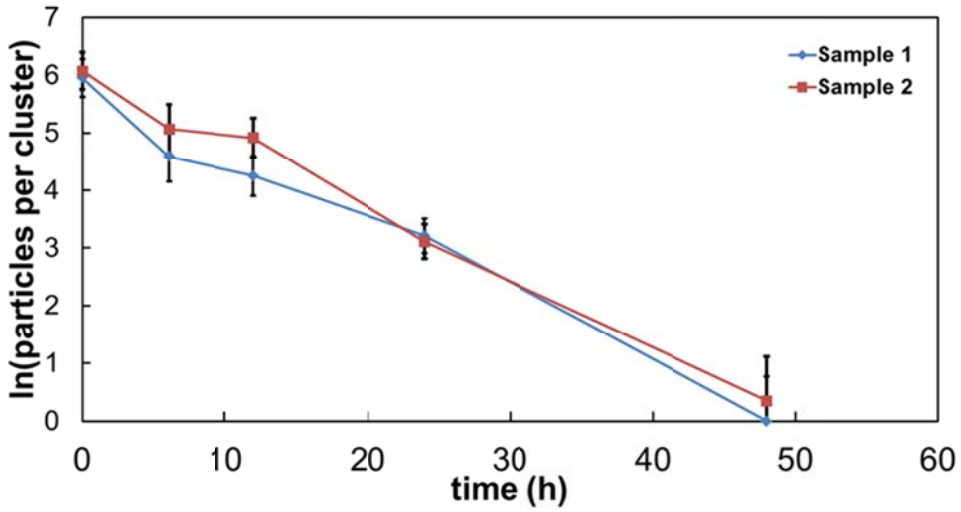

Figure C.11: Reproducibility of dissociation kinetics of 20-4.0 particles.

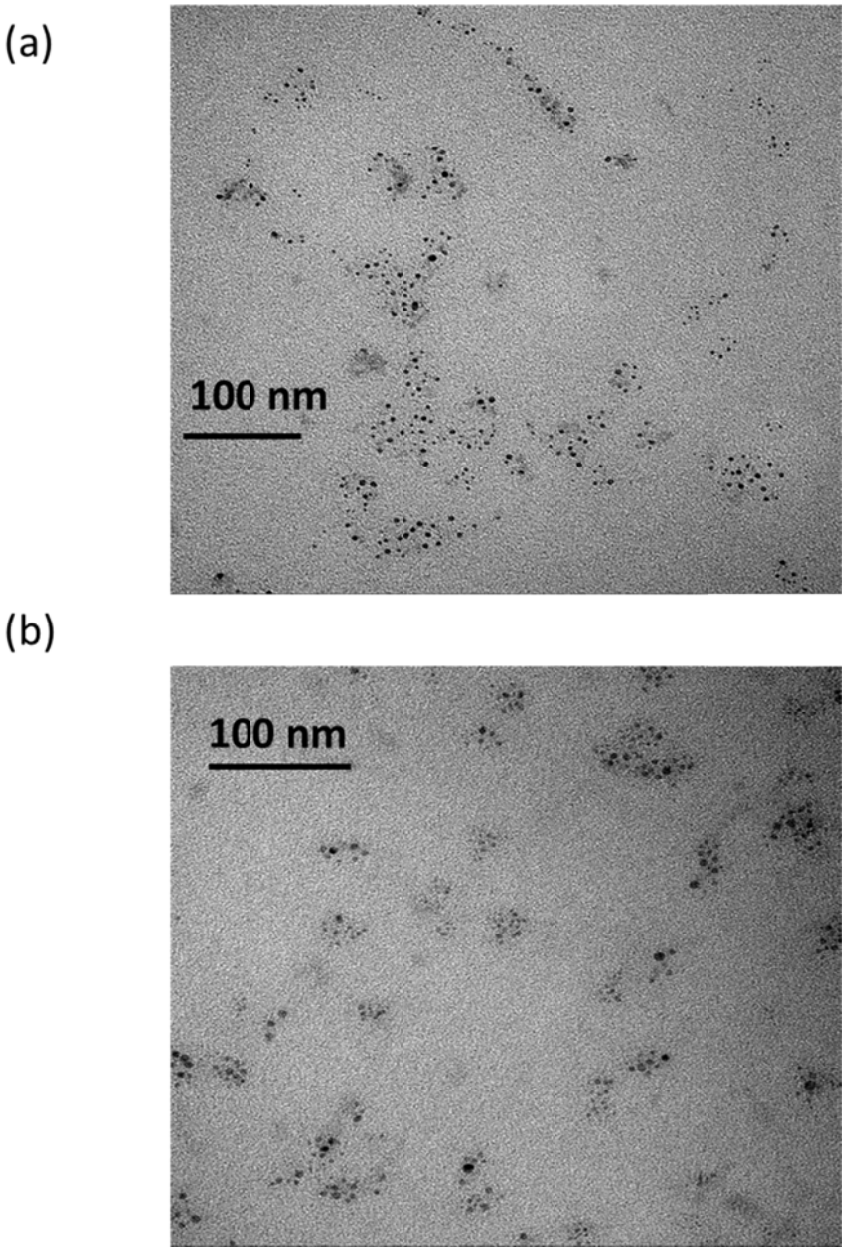

Figure C.12: TEM images of (a) Dissociated 20-4.0 particles after 48 h in pH 5 HCl and (b) dissociated 20-1.7 particles after 24 h in pH 5 HCl

Table C.1: TGA results reporting the organic mass content of 20-0.9, 20-1.7, and 20-4.0 particles, as determined from the amount of mass loss.

Sample	**Organic Mass Content (w/w)**
20-0.9	46.5%
20-1.7	50%
20-4.0	31.8%

Table C.2: Parameters used to generate theoretical size contours in Figure 4.9

Parameter	**Value**
A_{gwg} (J)	4.0×10^{-19}
Attractive VDW potential ($-a_{vdw}/k_bT$)	3.01
b (bond distance in ionic bond, nm)	0.1
σs(number of dissociable sites per particle)	2.78
R (radius of primary particle, nm)	2.0
ϵ_r (dielectric constant within nanocluster)	25

C.8 SUPPLEMENTARY REFERENCES

1. Tam, J. M.; Tam, J. O.; Murthy, A.; Ingram, D. R.; Ma, L. L.; Travis, K.; Johnston, K. P.; Sokolov, K. V. Controlled Assembly of Biodegradable Plasmonic Nanoclusters for Near-Infrared Imaging and Therapeutic Applications. *ACS Nano* **2010**, *4*, 2178-2184.
2. Tam, J. M.; Murthy, A. K.; Ingram, D. R.; Nguyen, R.; Sokolov, K. V.; Johnston, K. P. Kinetic Assembly of Near-IR Active Gold Nanoclusters Using Weakly Adsorbing Polymers to Control the Size. *Langmuir* **2010**, *26*, 8988-8999.
3. Kunze, J.; Burgess, I.; Nichols, R.; Buess-Herman, C.; Lipkowski, J. Electrochemical Evaluation of Citrate Adsorption on Au(1 1 1) and the Stability of Citrate-Reduced Gold Colloids. *J. Electroanal. Chem.* **2007**, *599*, 147-159.
4. Bezdek, K. Circle Packings into Convex Domains of the Euclidean and Hyperbolic Plane and the Sphere. *Geometriae Dedicata* **1986**, *21*, 249-255.
5. Bozack, M. J.; Zhou, Y.; Worley, S. D. Structural Modifications in the Amino Acid Lysine Induced by Soft Xray Irradiation. *J. Chem. Phys.* **1994**, *100*, 8392-8398.
6. Watts, J. F.; Wolstenholme, J., *An Introduction to Surface Analysis by Xps and Aes*. John Wiley & Sons: West Sussex, England, 2003.
7. Hiemenz, P. C.; Rajagopalan, R., *Principles of Colloid and Surface Chemistry*. 3 ed.; Taylor & Francis: New York, 1997.
8. Israelachvili, J. N., *Intermolecular and Surface Forces*. 3 ed.; Elsevier: New York, 2011.
9. Linegar, K. L.; Adeniran, A. E.; Kostko, A. F.; Anisimov, M. A. Hydrodynamic Radius of Polyethylene Glycol in Solution Obtained by Dynamic Light Scattering. *Colloid J.* **2010**, *72*, 279-281.
10. Groenewold, J.; Kegel, W. K. Anomalously Large Equilibrium Clusters of Colloids. *J. Phys. Chem. B* **2001**, *105*, 11702-11709.
11. Johnston, K. P.; Maynard, J. A.; Truskett, T. M.; Borwankar, A. U.; Miller, M. A.; Wilson, B. K.; Dinin, A. K.; Khan, T. A.; Kaczorowski, K. J. Concentrated Dispersion of Equilibrium Protein Nanoclusters That Reversibly Dissociate into Active Monomers. *ACS Nano* **2012**, *6*, 1357-1369.
12. Harada, R.; Sugita, Y.; Feig, M. Protein Crowding Affects Hydration Structure and Dynamics. *J. Am. Chem. Soc.* **2012**, *134*, 4842-4849.
13. Despa, F.; Fernandez, A.; Berry, R. S. Dielectric Modulation of Biological Water. *Phys. Rev. Lett.* **2004**, *93*, 228104.

14. Tjong, H.; Zhou, H.-X. Prediction of Protein Solubility from Calculation of Transfer Free Energy. *Biophys. J.* **2008**, *95*, 2601-2609.

Appendix D: Effect of Salt Addition on the Formation of Biodegradable Gold Nanoclusters of Controlled Size with Intense NIR Extinction

D.1 Calculation of Number of Particles per Nanocluster

In order to estimate the number of primary particles in a nanocluster with diameter *D*, we use the equation:

$$n = \left(\frac{D}{D_{primary}}\right)^3 \times 0.72 \qquad \text{(D.1)}$$

where *n* is the number of primary particles per cluster, $D_{primary}$ is the diameter of the primary particles (4 nm), and 0.72 is the packing fraction assuming that the clusters have a close-packed morphology.

D.2 Calculation of vdW and Depletion Interaction Potentials

The vdW attractive potential between two lysine/citrate-capped Au nanospheres is given by:[1]

$$V_{vdw} = \frac{-A}{6}\left[\frac{2R^2}{H(4R+H)} + \frac{2R^2}{(2R+H)^2} + \ln\frac{H(4R+H)}{(2R+H)^2}\right] \qquad \text{(D.2)}$$

where *A* is the Au-Au Hamaker constant in water, *R* is the radius of the nanospheres, and H is the surface-surface separation distance between particles. The Hamaker constant for Au in water has been determined previously,[2, 3] and the nanosphere radius is 2 nm, as determined from DLS measurements shown in Figure D.1. The vdW potential for two 4 nm Au nanospheres is shown in Figure D.3a.

In addition to van der Waals attraction, depletion attraction is induced between two nanoparticles by the osmotic pressure gradient produced from the exclusion of micelles of PLA-*b*-PEG-*b*-PLA from the gap between Au nanospheres.[2] The depletion potential between two spheres in the presence of a polymer with concentration c_p is given by:[2, 4-6]

$$\frac{V_{depletion}}{kT} = -\left(\frac{R_g}{R}\right)^{-3}\left(\frac{c_p}{c^*}\right)\left(\frac{R_g}{R}-\frac{H}{2R}\right)^2\left(\frac{3}{2}+\frac{R_g}{R}+\frac{H}{4R}\right) \qquad \text{(D.3)}$$

In Eq. D.3, R_g is the radius of gyration of the polymer, R is the nanosphere radius, H is the surface-surface separation distance, and c^* is the concentration at which the polymer chains begin to overlap, defined as:

$$c^* = \frac{3M}{4\pi R_g^3 N_A} \qquad \text{(D.4)}$$

where M is the polymer molecular weight and N_A is Avogadro's number. In this work, we approximate the radius of gyration from the hydrodynamic radius of a micelle of PLA(1k)-*b*-PEG(10k)-*b*-PLA(1k), which has been determined to be 7 nm.[2, 3]

D.3 Calculation of Nanosphere Surface Potential

The surface potential ψ_0 of the primary cysteine/citrate capped nanospheres was calculated from experimental zeta potential measurements. Here, the zeta potential was first related to a nanosphere surface charge using the equation:[1, 7]

$$\zeta = \frac{q}{4\pi\epsilon_r\epsilon_0 R_s(1+\kappa R_s)} \quad \text{(D.5)}$$

where ζ is the zeta potential, q is the nanosphere surface charge, ε_r is the dielectric constant of the medium, ε_0 is the permittivity of free space, R_s is the nanosphere radius, and κ is the Debye parameter, which is defined in the main text. Here, the surface of shear is approximated to be equal to the surface of the nanosphere. [7] The nanosphere surface charge q can also be related to the surface potential ψ_0:

$$\psi_0 = \frac{q}{4\pi\epsilon_r\epsilon_0 R_s} \quad \text{(D.6)}$$

Combining Equations D.5 and D.6, we obtain from a measured zeta potential of -14 mV for cysteine/citrate capped nanospheres in 1 mM KCl a surface potential of -17 mV, which is then used to generate the electrostatic and total interaction potentials shown in Figure 5.8 in Chapter 5.

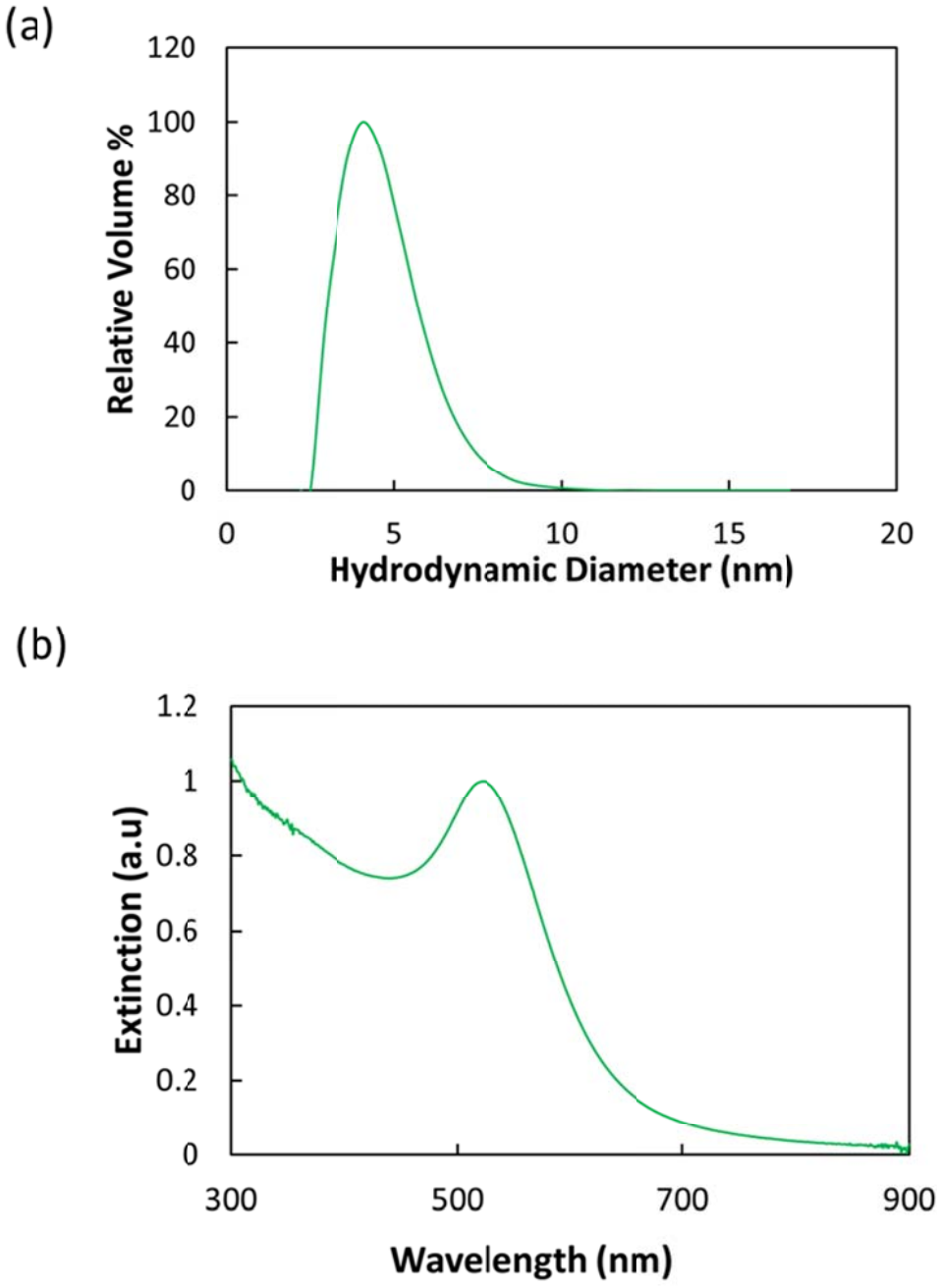

Figure D.1: (a) DLS D_h distribution and (b) UV-Vis-NIR extinction spectrum for lysine/citrate capped Au nanospheres used in this study.

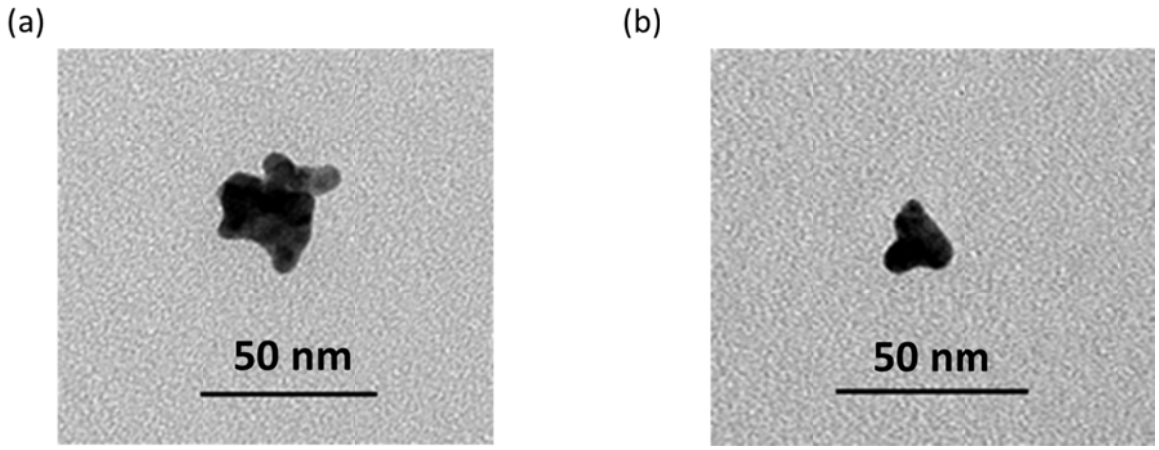

Figure D.2: TEM images obtained for (a) 2-20-0 and (b) 2-20-67 nanoclusters.

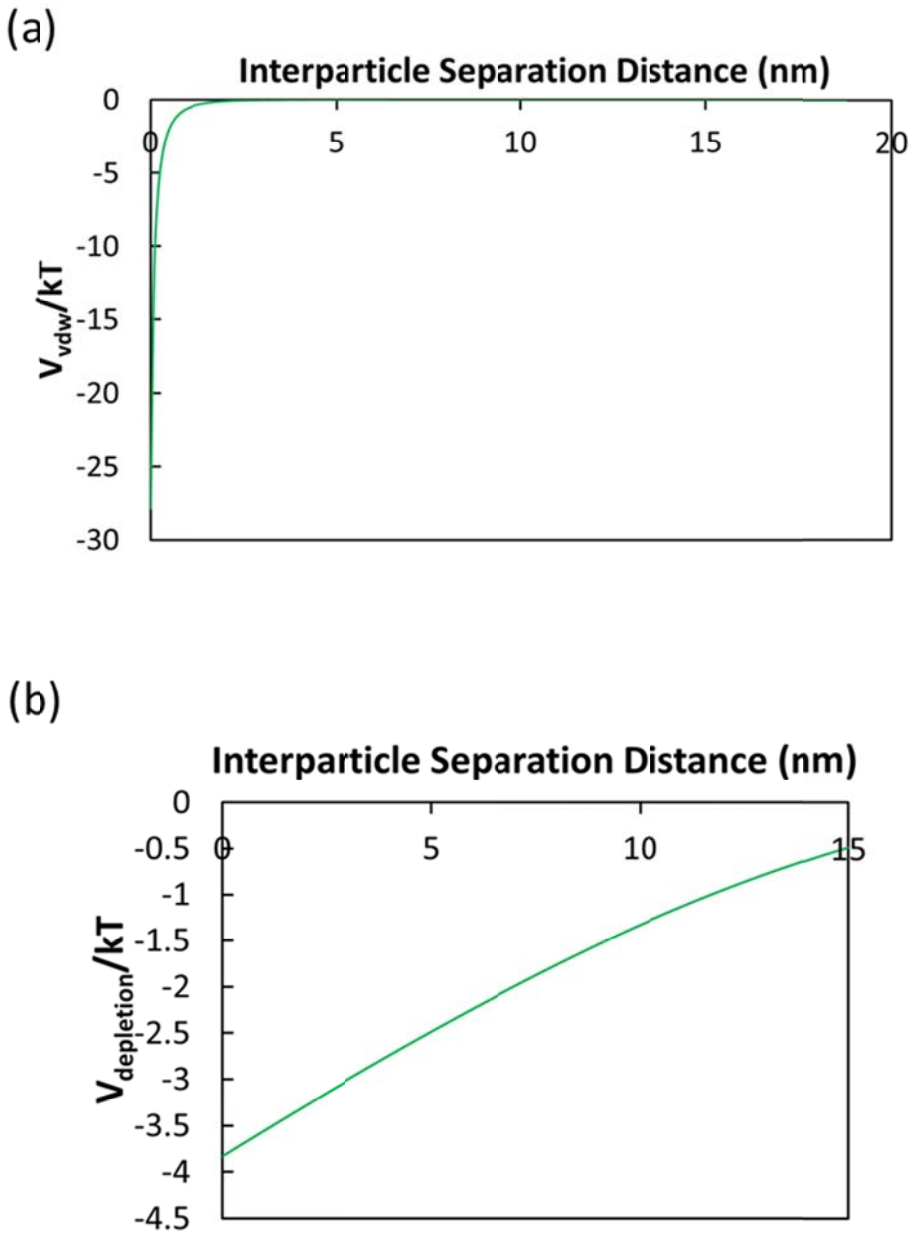

Figure D.3: (a) vdW interaction potential and (b) depletion interaction potential for 2-40-0, 2-40-67, and 2-40-133 nanoclusters.

Table D.1: Experimental conditions used to synthesize nanocluster samples.

Sample Name	**Final Polymer Conc (mg/ml)**	**Final Au conc (mg/ml)**	**Final Salt Conc (mM)**	**Initial Au Conc (mg/ml)**	**Polymer/ Au Ratio (w/w)**	**Evaporation Extent (%)**	**NaCl conc in polymer solution (mM)**
2-40-0	40	2	0	3	20	50	0
4-40-0	40	4	0	1.5	10	75	0
8-40-0	40	8	0	3	5	75	0
2-20-0	20	2	0	1.5	10	50	0
2-40-67	40	2	67	3	20	50	50
4-40-67	40	4	67	1.5	10	75	50
8-40-67	40	8	67	3	5	75	50
2-20-67	20	2	67	1.5	10	50	100
2-40-133	40	2	133	3	20	50	100
4-40-133	40	4	133	1.5	10	75	100
8-40-133	40	8	133	3	5	75	100
2-20-133	20	2	133	1.5	10	50	200

D.4 SUPPLEMENTARY REFERENCES

1. Hiemenz, P. C.; Rajagopalan, R., *Principles of Colloid and Surface Chemistry*. 3 ed.; Taylor & Francis: New York, 1997; p 546-556.
2. Murthy, A. K.; Stover, R. J.; Borwankar, A. U.; Nie, G. D.; Gourisankar, S.; Truskett, T. M.; Sokolov, K. V.; Johnston, K. P. Equilibrium Gold Nanoclusters Quenched with Biodegradable Polymers. *ACS Nano* **2013**, *7*, 239-251.
3. Tam, J. M.; Murthy, A. K.; Ingram, D. R.; Nguyen, R.; Sokolov, K. V.; Johnston, K. P. Kinetic Assembly of near-Ir Active Gold Nanoclusters Using Weakly Adsorbing Polymers to Control the Size. *Langmuir* **2010**, *26*, 8988-8999.
4. Lekkerkerker, H. N. W.; Tuinier, R., *Colloids and the Depletion Interaction*. Springer: New York, 2011; Vol. 833, p 12-15.
5. Asakura, S.; Oosawa, F. On Interaction between 2 Bodies Immersed in a Solution of Macromolecules. *Journal of Chemical Physics* **1954**, *22*, 1255-1256.
6. Asakura, S.; Oosawa, F. Interaction between Particles Suspended in Solutions of Macromolecules. *Journal of Polymer Science* **1958**, *33*, 183-192.
7. Johnston, K. P.; Maynard, J. A.; Truskett, T. M.; Borwankar, A. U.; Miller, M. A.; Wilson, B. K.; Dinin, A. K.; Khan, T. A.; Kaczorowski, K. J. Concentrated Dispersion of Equilibrium Protein Nanoclusters That Reversibly Dissociate into Active Monomers. *ACS Nano* **2012**, *6*, 1357-1369.

Appendix E: Nanoclusters of Gold Nanospheres with Binary Monolayers of Cysteine and Citrate Formed by Quenched Assembly with Strong NIR Extinction

E.1 Calculation of vdW and Depletion Interaction Potentials

The vdW attractive potential between two Au nanoparticles is given by:[1]

$$V_{vdw} = \frac{-A}{6}\left[\frac{2R^2}{H(4R+H)} + \frac{2R^2}{(2R+H)^2} + \ln\frac{H(4R+H)}{(2R+H)^2}\right] \quad \text{(E.1)}$$

where A is the Au-Au Hamaker constant in water, R is the nanosphere radius, and H is the surface-surface separation distance between particles. The vdW potential for two 4 nm Au nanospheres is shown in Figure E.2.

In addition to van der Waals attraction, an attractive force (depletion attraction) is created by the osmotic pressure gradient produced from the exclusion of micelles of PLA-*b*-PEG-*b*-PLA from the gap between Au nanospheres.[2] The depletion attractive potential between two spheres in the presence of a polymer with concentration c_p is given by:[2-5]

$$\frac{V_{depletion}}{kT} = -\left(\frac{R_g}{R}\right)^{-3}\left(\frac{c_p}{c^*}\right)\left(\frac{R_g}{R} - \frac{H}{2R}\right)^2\left(\frac{3}{2} + \frac{R_g}{R} + \frac{H}{4R}\right) \quad \text{(E.2)}$$

where R_g is the radius of gyration of the polymer, R is the nanosphere radius, H is the surface-surface separation distance, and c^* is the concentration at which the polymer chains begin to overlap, defined as:

$$c^* = \frac{3M}{4\pi R_g^3 N_A} \quad \text{(E.3)}$$

where M is the polymer molecular weight and N_A is Avogadro's number. In this work, we approximate the radius of gyration from the hydrodynamic radius of a micelle of PLA(1k)-*b*-PEG(10k)-*b*-PLA(1k), which has been determined to be 7 nm.[2, 6] In order to generate the total interaction potentials shown in Figure 6.10, we choose polymer concentrations of the 3-5-50, 3-5-75, and 3-5-95 samples, which are given in Table 6.1 of Chapter 6.

E.2 Calculation of Nanosphere Surface Potential

The surface potential ψ_0 of the primary cysteine/citrate capped nanospheres was calculated from experimental zeta potential measurements. Here, the zeta potential was first related to a nanosphere surface charge using the equation:[1, 7]

$$\zeta = \frac{q}{4\pi\epsilon_r\epsilon_0 R_s(1+\kappa R_s)} \quad \text{(E.4)}$$

where ζ is the zeta potential, q is the nanosphere surface charge, ε_r is the dielectric constant of the medium, ε_0 is the permittivity of free space, R_s is the nanosphere radius, and κ is the Debye parameter, which is defined in the main text. Here, the surface of shear is approximated to be equal to the surface of the nanosphere. [7] The nanosphere surface charge q can also be related to the surface potential ψ_0:

$$\psi_0 = \frac{q}{4\pi\epsilon_r\epsilon_0 R_s} \quad \text{(E.5)}$$

Combining Equations E.4 and E.5, we obtain from a measured zeta potential of -23 mV for cysteine/citrate capped nanospheres in 1 mM KCl a surface potential of -28 mV, which is then used to generate the electrostatic and total interaction potentials shown in Figure 6.10 in Chapter 6.

E.3 Calculation of Extinction Coefficient

The extinction coefficient of the 3-5-95 nanoclusters can be calculated from Beer-Lambert's law:

$$A(\lambda) = \varepsilon(\lambda)Cl \quad \text{(E.6)}$$

where *A(λ)* is the measured extinction (absorbance) at a particular wavelength, ε(λ) is the extinction coefficient at a particular wavelength, *C* is the solution concentration, and l is the cuvette path length. For a concentration of 70 μg/ml and a path length of 1 cm, the measured extinction of 3-5-95 nanoclusters was 0.731 at 800 nm and 0.305 at 1300 nm. Thus, the corresponding extinction coefficient was 0.010 $cm^2/\mu g$ at 800 nm and 0.004 $cm^2/\mu g$ at 1300 nm.

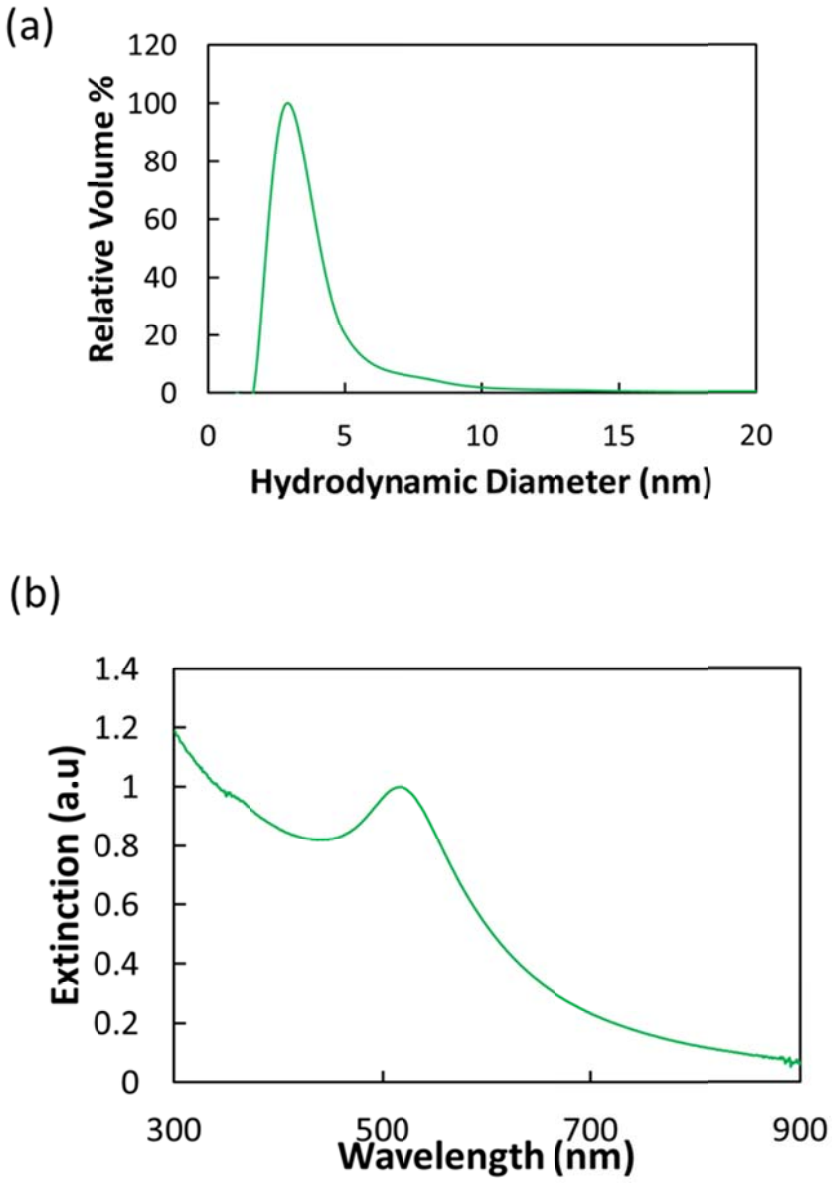

Figure E.1: (a) DLS D_h distribution and (b) UV-Vis-NIR spectrum of primary cysteine/citrate capped nanospheres used in this study.

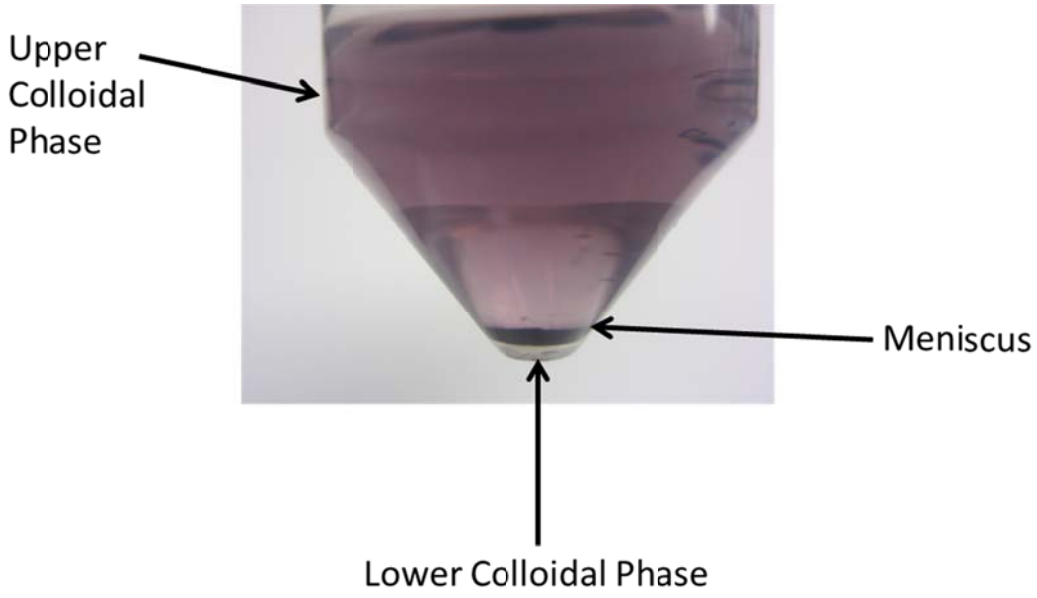

Figure E.2: Photograph of upper and lower colloidal phases of a 3-5-95 nanocluster sample. The meniscus between the lower phase (containing dense nanoclusters) and upper phase (containing unclustered nanospheres, loosely bound aggregates, and excess polymer) is marked. The white object which appears near the bottom of the centrifuge tube is an artifact due to light reflections and is not part of the pellet.

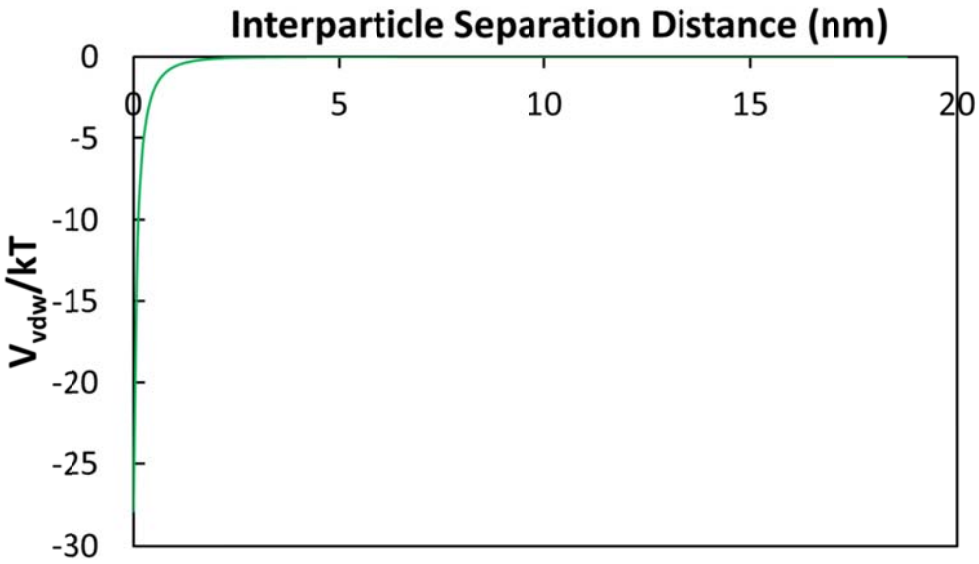

Figure E.3: vdW interaction potential for primary Au nanospheres.

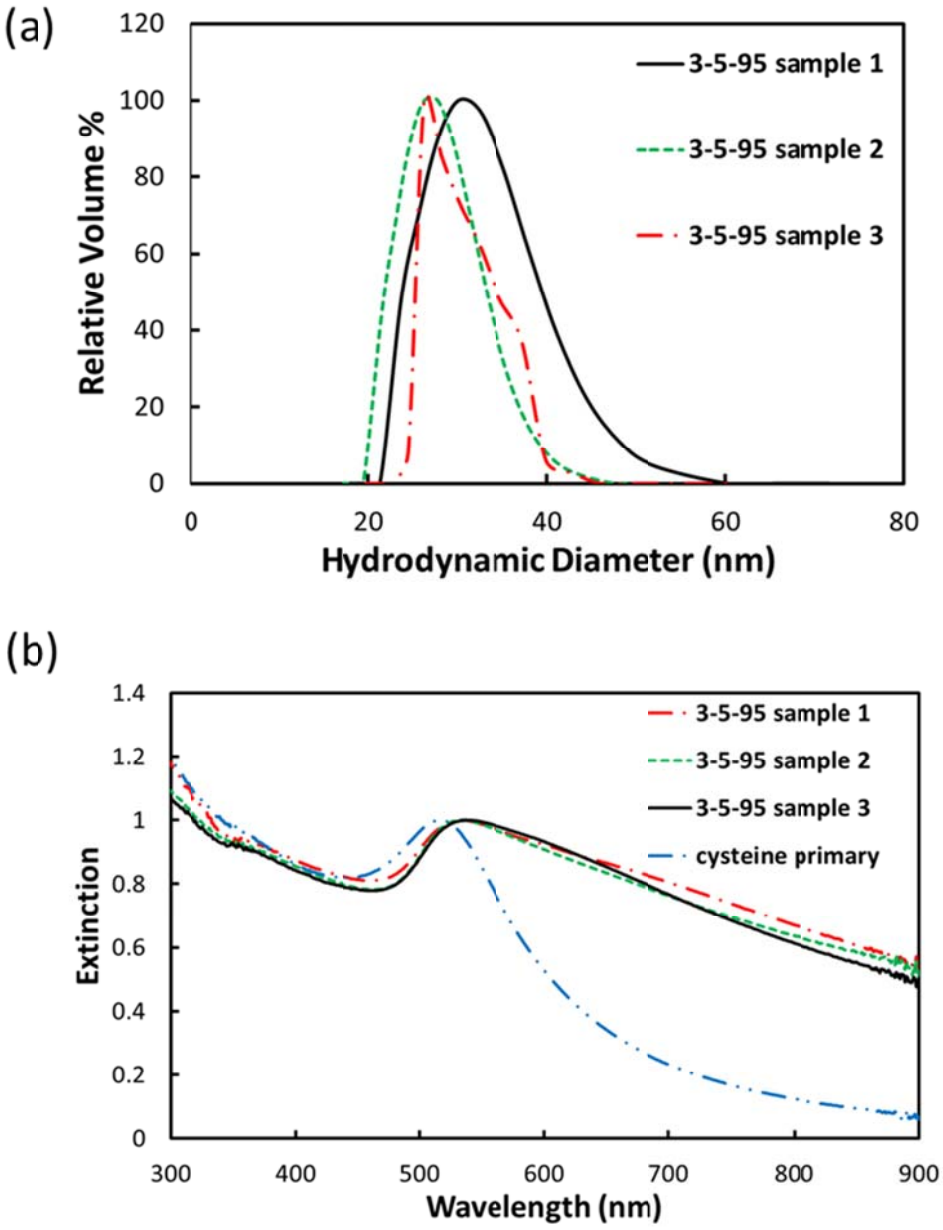

Figure E.4: Reproducibility of (a) DLS D_h distributions and (b) UV-Vis-NIR extinction curves of 3 separate samples of 3-5-95 particles.

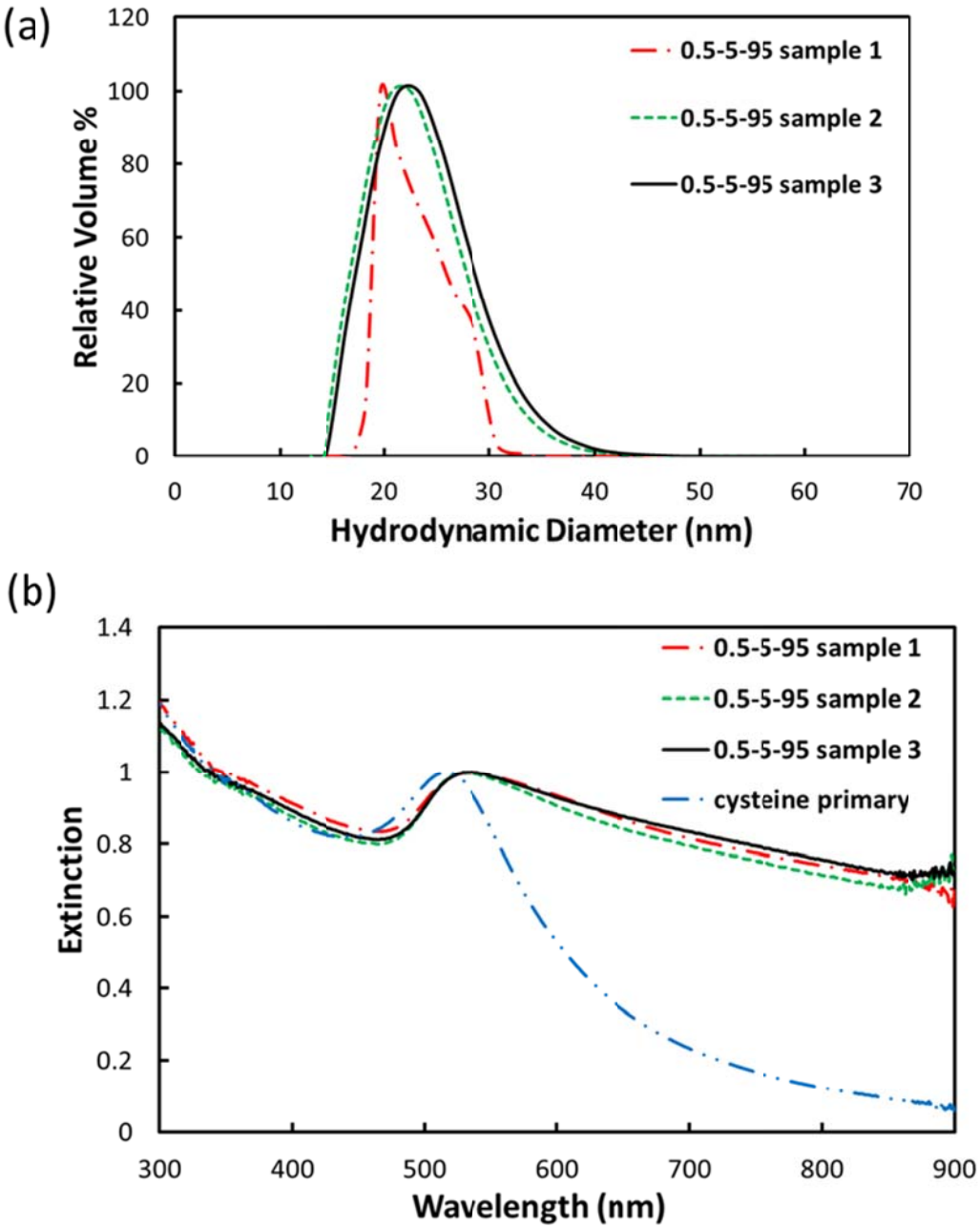

Figure E.5: Reproducibility of (a) DLS D_h distributions and (b) UV-Vis-NIR extinction curves for 3 separate samples of 0.5-5-95 particles.

E.4 SUPPLEMENTARY REFERENCES

1. Hiemenz, P. C.; Rajagopalan, R., *Principles of Colloid and Surface Chemistry*. 3 ed.; Taylor & Francis: New York, 1997; p 546-556.
2. Murthy, A. K.; Stover, R. J.; Borwankar, A. U.; Nie, G. D.; Gourisankar, S.; Truskett, T. M.; Sokolov, K. V.; Johnston, K. P., Equilibrium Gold Nanoclusters Quenched with Biodegradable Polymers. *ACS Nano* **2013**, *7*, 239-251.
3. Lekkerkerker, H. N. W.; Tuinier, R., *Colloids and the Depletion Interaction*. Springer: New York, 2011; Vol. 833, p 12-15.
4. Asakura, S.; Oosawa, F., On Interaction Between 2 Bodies Immersed in a Solution of Macromolecules. *Journal of Chemical Physics* **1954**, *22*, 1255-1256.
5. Asakura, S.; Oosawa, F., Interaction Between Particles Suspended In Solutions of Macromolecules. *Journal of Polymer Science* **1958**, *33*, 183-192.
6. Tam, J. M.; Murthy, A. K.; Ingram, D. R.; Nguyen, R.; Sokolov, K. V.; Johnston, K. P., Kinetic Assembly of Near-IR Active Gold Nanoclusters Using Weakly Adsorbing Polymers to Control the Size. *Langmuir* **2010**, *26*, 8988-8999.
7. Johnston, K. P.; Maynard, J. A.; Truskett, T. M.; Borwankar, A. U.; Miller, M. A.; Wilson, B. K.; Dinin, A. K.; Khan, T. A.; Kaczorowski, K. J., Concentrated Dispersion of Equilibrium Protein Nanoclusters That Reversibly Dissociate Into Active Monomers. *ACS Nano* **2012**, *6*, 1357-1369.

Bibliography

Aaron, J.; Nitin, N.; Travis, K.; Kumar, S.; Collier, T.; Park, S. Y.; Jose-Yacaman, M.; Coghlan, L.; Follen, M.; Richards-Kortum, R., Sokolov, K., Plasmon resonance coupling of metal nanoparticles for molecular imaging of carcinogenesis in vivo. *Journal of Biomedical Optics* **2007,** *12* (3), 034007/1-034007/11.

Aaron, J.; Oh, J.; Larson, T. A.; Kumar, S.; Milner, T. E., Sokolov, K. V., Increased optical contrast in imaging of epidermal growth factor receptor using magnetically actuated hybrid gold/iron oxide nanoparticles. *Optics Express* **2006,** *14* (26), 12930-12943.

Aaron, J.; Travis, K.; Harrison, N., Sokolov, K., Dynamic Imaging of Molecular Assemblies in Live Cells Based on Nanoparticle Plasmon Resonance Coupling. *Nano Letters* **2009,** *9* (10), 3612-3618.

Adler, D. C.; Huang, S.-W.; Huber, R., Fujimoto, J. G., Photothermal detection of gold nanoparticles using phase-sensitive optical coherence tomography. *Optics Express* **2008,** *16* (7), 4376-4393.

Agarwal, A.; Huang, S. W.; O'Donnell, M.; Day, K. C.; Day, M., Ashkenazi, S., Targeted gold nanorod contrast agent for prostate cancer detection by photoacoustic imaging. *J. Appl. Phys.* **2007,** *102*, 0647011-0647014.

Agrawal, S. K.; Sanabria-DeLong, N.; Tew, G. N., Bhatia, S. R., Structural Characterization of PLA-PEO-PLA Solutions and Hydrogels: Crystalline vs Amorphous PLA Domains. *Macromolecules* **2008,** *41*, 1774-1784.

Alexandridis, P., Holzwarth, J. F., Differential Scanning Calorimetry Investigation of the Effect of Salts on Aqueous Solution Properties of an Amphiphilic Block Copolymer (Poloxamer). *Langmuir* **1997,** *13* (23), 6074-6082.

Armstrong, J. K.; Chowdhry, B. Z.; Snowden, M. J., Leharne, S. A., Effect of Sodium Chloride upon Micellization and Phase Separation Transitions in Aqueous Solutions of Triblock Copolymers: A High-Sensitivity Differential Scanning Calorimetry Study. *Langmuir* **1998,** *14*, 2004-2010.

Arruebo, M.; Fernandez-Pacheco, R.; Ibarra, R., Santamaria, J., Magnetic nanoparticles for druge delivery. *Nano Today* **2007,** *2* (3).

Asakura, S., Oosawa, F., On Interaction Between 2 Bodies Immersed in a Solution of Macromolecules. *Journal of Chemical Physics* **1954,** *22* (7), 1255-1256.

Asakura, S., Oosawa, F., Interaction Between Particles Suspended In Solutions of Macromolecules. *Journal of Polymer Science* **1958,** *33* (126), 183-192.

Aslan, K.; Luhrs, C. C., Perez-Luna, V. H., Controlled and Reversible Aggregation of Biotinylated Gold Nanoparticles with Streptavidin. *Journal of Physical Chemistry B* **2004,** *108* (40), 15631-15639.

Bae, K. H.; Choi, S. H.; Park, S. Y.; Lee, Y., Park, T. G., Thermosensitive Pluronic Micelles Stabilized by Shell Cross-Linking with Gold Nanoparticles. *Langmuir* **2006,** *22* (14), 6380-6384.

Berret, J.-F., Stoichiometry of Electrostatic Complexes Determined by Light Scattering. *Macromolecules* **2007,** *40* (12), 4260-4266.

Betancourt, T.; Brown, B., Brannon-Peppas, L., Doxorubicin-loaded PLGA nanoparticles by nanoprecipitation: preparation, characterization and *in vitro* evaluation. *Nanomedicine* **2007,** *2* (2), 220-232.

Beurer, E.; Venkataraman, N. V.; Sommer, M., Spencer, N. D., Protein and Nanoparticle Adsorption on Orthogonal, Charge-Density-Versus-Net-Charge Surface-Chemical Gradients. *Langmuir* **2012,** *28*, 3159-3166.

Bezdek, K., Circle packings into convex domains of the Euclidean and hyperbolic plane and the sphere. *Geometriae Dedicata* **1986,** *21* (3), 249-255.

Blatchford, C. G.; Campbell, J. R., Creighton, J. A., Plasma Resonance- Enhanced Raman Scattering by Adsorbates on Gold Colloids: The Effects of Aggregation. *Surface Science* **1982,** *120*, 445-455.

Boal, A. K.; Ilhan, F.; DeRouchey, J. E.; Thurn-Albrecht, T.; Russell, T. P., Rotello, V. M., Self-assembly of nanoparticles into structured spherical and network aggregates. *Nature* **2000,** *404*, 746-748.

Bozack, M. J.; Zhou, Y., Worley, S. D., Structural modifications in the amino acid lysine induced by soft xray irradiation. *Journal of Chemical Physics* **1994,** *100* (11), 8392-8398.

Brewer, S. H.; Glomm, W. R.; Johnson, M. C.; Knag, M. K., Franzen, S., Probing BSA Binding to Citrate-Coated Gold Nanoparticles and Surfaces. *Langmuir* **2005,** *21* (20), 9303-9307.

Buitenhuis, J.; Dhont, J. K. G., Lekkerkerker, H. N. W., Static and Dynamic Light Scattering by Concentrated Colloidal Suspensions of Polydisperse Sterically Stabilized Boehmite Rods. *Macromolecules* **1994,** *27* (25), 7267-7277.

Casals, E.; Pfaller, T.; Duschl, A.; Oostingh, G. J., Puntes, V., Time Evolution of the Nanoparticle Protein Corona. *ACS Nano* **2010,** *4* (7), 3623-3632.

Cedervall, T.; Lynch, I.; Lindman, S.; Berggard, T.; Thulin, E.; Nilsson, H.; Dawson, K. A., Linse, S., Understanding the nanoparticle-protein corona using methods to quantify exchange rates and affinities of proteins for nanoparticles. *Proceedings of the National Academy of Sciences* **2006,** *104* (7), 2050-2055.

Chen, J.; Saeki, F.; Wiley, B. J.; Cang, H.; Cobb, M. J.; Li, Z.-Y.; Au, L.; Zhang, H.; Kimmey, M. B.; Li, X., Xia, Y., Gold Nanocages: Bioconjugation and Their Potential Use as Optical Imaging Contrast Agents. *Nano Letters* **2005,** *5* (3), 473-477.

Chen, S.; Cao, Z., Jiang, S., Ultra-low fouling peptide surfaces derived from natural amino acids. *Biomaterials* **2009,** *30*, 5893-5896.

Chen, S.; Li, L.; Zhao, C., Zheng, J., Surface hydration: Principles and applications toward low-fouling/nonfouling biomaterials. *Polymer* **2010,** *51*, 5283-5293.

Chen, S.; Yu, F.; Yu, Q.; He, Y., Jiang, S., Strong Resistance of a Thin Crystalline Layer of Balanced Charged Groups to Protein Adsorption. *Langmuir* **2006,** *22* (19), 8186-8191.

Chen, S.; Zhen, J.; Li, L., Jiang, S., Strong Resistance of Phosphorylcholine Self-Assembled Monolayers to Protein Adsorption: Insights into Nonfouling Properties of Zwitterionic Materials. *Journal of the American Chemical Society* **2005,** *127*, 14473-14478.

Chen, S. F.; Cao, Z. Q., Jiang, S. Y., Ultra-low fouling peptide surfaces derived from natural amino acids. *Biomaterials* **2009,** *30* (29), 5892-5896.

Cheng, C.; Wen, Y.; Xu, X., Gu, H., Tunable synthesis of carboxyl-functionalized magnetite nanocrystal clusters with uniform size. *J. Mater. Chem.* **2009,** *19*, 8782-8788.

Chithrani, B. D.; Ghazani, A. A., Chan, W. C. W., Determining the Size and Shape Dependence of Gold Nanoparticle Uptake into Mammalian Cells. *Nano Letters* **2006,** *6* (4), 662-668.

Choi, H. S.; Liu, W.; Misra, P.; Tanaka, E.; Zimmer, J. P.; Ipe, B. I.; Bawendi, M. G., Frangioni, J. V., Renal clearance of quantum dots. *Nat. Biotechnol.* **2007,** *25* (10), 1165-1170.

Chompoosor, A.; Han, G., Rotello, V. M., Charge Dependent of Ligand Release and Monolayer Stability of Gold Nanoparticles by Biogenic Thiols. *Bioconjugate Chemistry* **2008,** *19* (7), 1342-1345.

Chow, M. K., Zukoski, C. F., Gold sol formation mechanisms: role of colloidal stability. *Journal of Colloid and Interface Science* **1994,** *165* (1), 97-109.

Cohen-Tannoudji, L.; Bertrand, E.; Bressy, L.; Goubault, C.; Baudry, J.; Klein, J.; Joanny, J.-F., Bibette, J., Polymer Bridging Probed by Magnetic Colloids. *Physical Review Letters* **2005,** *94*.

De Paoli Lacerda, S. H.; Park, J. J.; Meuse, C.; Pristinski, D.; Becker, M. L.; Karim, A., Douglas, J. F., Interaction of Gold Nanoparticles with Common Human Blood Proteins. *ACS Nano* **2010,** *4* (1), 365-379.

Despa, F.; Fernandez, A., Berry, R. S., Dielectric Modulation of Biological Water. *Physical Review Letters* **2004,** *93*, 228104.

DeVries, G. A.; Brunnbauer, M.; Hu, Y.; Jackson, A. M.; Long, B.; Neltner, B. T.; Uzun, O.; Wunsch, B. H., Stellacci, F., Divalent Metal Nanoparticles. *Science* **2007,** *315* (5810), 358-361.

Ditsch, A.; Laibinis, P. E.; Wang, D. I. C., Hatton, T. A., Controlled Clustering and Enhanced Stability of Polymer-Coated Magnetic Nanoparticles. *Langmuir* **2005,** *21* (13), 6006-6018.

Dobrovolskaia, M. A.; Patri, A. K.; Zheng, J.; Clogston, J. D.; Ayub, N.; Aggarwal, P.; Neun, B. W.; Hall, J. B., McNeil, S. E., Interaction of colloidal gold nanoparticles with human blood: effects on particle size and analysis of plasma protein binding profiles. *Nanomedicine* **2009,** *5*, 106-117.

Dominguez-Medina, S.; McDonough, S.; Swanglap, P.; Landes, C. F., Link, S., In Situ Measurement of Bovine Serum Albumin Interaction with Gold Nanospheres. *Langmuir* **2012,** *28*, 9131-9139.

Duan, X., Li, Y., Physicochemical Characteristics of Nanoparticles Affect Circulation, Biodistribution, Cellular Internalization, and Trafficking. *Small* **2013,** *9*, 1521-1532.

Edwards, T. D., Bevan, M. A., Polymer Mediated Depletion Attraction and Interfacial Colloidal Phase Behavior. *Macromolecules* **2012,** *45* (1), 585-594.

Estephan, Z. G.; Jaber, J. A., Schlenoff, J. B., Zwitterion-Stabilized Silica Nanoparticles: Toward Nonstick Nano. *Langmuir* **2010,** *26* (22), 16884-16889.

Ferrari, M., Cancer nanotechnology: opportunities and challenges. *Nature Reviews Cancer* **2005,** *5* (3), 161-171.

Frankamp, B. L.; Boal, A. K., Rotello, V. M., Controlled Interparticle Spacing through Self-Assembly of Au Nanoparticles and Poly(amidoamine) Dendrimers. *Journal of the American Chemical Society* **2002,** *124*, 15146-15147.

Frankamp, B. L.; Uzun, O.; Ilhan, F.; Boal, A. K., Rotello, V. M., Recognition-Mediated Assembly of Nanoparticles into Micellar Structures with Diblock Copolymers. *Journal of the American Chemical Society* **2002,** *124* (6), 892-893.

Fresnais, J.; Lavelle, C., Berret, J.-F., Nanoparticle Aggregation Controlled by Desalting Kinetics. *Journal of Physical Chemistry C* **2009,** *113* (37), 16371-16379.

Friedlander, S. K., *Smoke, dust, and haze : fundamentals of aerosol dynamics* Oxford University Press: New York, NY, 2000.

Ganesan, V.; Ellison, C. J., Pryamitsyn, V., Mean-field models of structure and dispersion of polymer-nanoparticle mixtures. *Soft Matter* **2010,** *6*, 4010-4025.

Gavrilenko, V. I., *Optics of Nanomaterials*. Pan Stanford Publishing: Singapore, 2011; p 63-66.

Ge, J.; Hu, Y.; Biasini, M.; Beyermann, W. P., Yin, Y., Superparamagnetic Magnetite Colloidal Nanocrystal Clusters. *Angewandte Chemie International Edition* **2007,** *46*, 4342-4345.

Gindy, M. E.; Panagiotopoulos, A. Z., Prud'homme, R. K., Composite Block Copolymer Stabilized Nanoparticles: Simultaneous Encapsulation of Organic Actives and Inorganic Nanostructures. *Langmuir* **2008,** *24* (1), 83-90.

Gindy, M. E.; Prud'homme, R. K.; Ji, S.; Hoye, T. R., Macosko, C. W., Functional block copolymer nanoparticles for targeted drug delivery and imaging. *PMSE Preprints* **2006,** *95*, 989-990.

Gobin, A. M.; Lee, M. H.; Halas, N. J.; James, W. D.; Drezek, R. A., West, J. L., Near-Infrared Resonant Nanoshells for Combined Optical Imaging and Photothermal Cancer Therapy. *Nano Lett.* **2007,** *7* (7), 1929-1934.

Gögelein, C.; Nägele, G.; Buitenhuis, J.; Tuinier, R., Dhont1, J. K. G., Polymer depletion-driven cluster aggregation and initial phase separation in charged nanosized colloids. *The Journal of Chemical Physics* **2009,** *130* (20), 204905-1 - 204905-15.

Gopidas, K. R.; Whitesell, J. K., Fox, M. A., Nanoparticle-Cored Dendrimers: Synthesis and Characterization. *Journal of the American Chemical Society* **2003,** *125*, 6491-6502.

Goubault, C.; Leal-Calderon, F.; Viovy, J.-L., Bibette, J., Self-Assembled Magnetic Nanowires Made Irreversible by Polymer Bridging. *Langmuir* **2005,** *21* (9), 3725-3729.

Grabar, K. C.; Allison, K. J.; Baker, B. E.; Bright, R. M.; Brown, K. R.; Freeman, R. G.; Fox, A. P.; Keating, C. D.; Musick, M. D., Natan, M. J., Two-dimensional arrays of colloidal gold particles: a flexible approach to macroscopic metal surfaces. *Langmuir* **1996,** *12*, 23535-2361.

Groenewold, J., Kegel, W. K., Anomalously Large Equilibrium Clusters of Colloids. *J. Phys. Chem. B* **2001,** *105*, 11702-11709.

Groenewold, J., Kegel, W. K., Colloidal cluster phases, gelation and nuclear matter. *J. Phys.-Condes. Matter* **2004,** *16* (42), S4877-S4886.

Guo, Y.; Ma, Y.; Xu, L.; Li, J., Yang, W., Conformational Change Induced Reversible Assembly/Disassembly of Poly-L-lysine-Functionalized Gold Nanoparticles. *Journal of Physical Chemistry C* **2007,** *111* (26), 9172-9176.

Gupta, A. K., Gupta, M., Synthesis and surface engineering of iron oxide nanoparticles for biomedical applications. *Biomaterials* **2005,** *26*, 3995-4021.

Halas, N. J.; Lal, S.; Chang, W.-S.; Link, S., Nordlander, P., Plasmons in Strongly Coupled Metallic Nanostructures. *Chemical Reviews* **2011,** *111*, 3913-3961.

Han, X.; Goebl, J.; Lu, Z., Yin, Y., Role of Salt in the Spontaneous Assembly of Charged Gold Nanoparticles in Ethanol. *Langmuir* **2011,** *27*, 5282-5289.

Harada, R.; Sugita, Y., Feig, M., Protein Crowding Affects Hydration Structure and Dynamics. *Journal of the American Chemical Society* **2012,** *134* (10), 4842-4849.

Harada, T., Hatton, T. A., Formation of Highly Ordered Rectangular Nanoparticle Superlattices by the Cooperative Self-Assembly of Nanoparticles and Fatty Molecules. *Langmuir* **2009,** *25* (11), 6407-6412.

Hiemenz, P. C., Rajagopalan, R., *Principles of Colloid and Surface Chemistry*. 3 ed.; Taylor & Francis: New York, 1997; p 546-556.

Hiemenz, P. C.; Rajagopalan, R., Editors, *Principles of Colloid and Surface Chemistry, Third Edition, Revised and Expanded*. 1997; p 688 pp.

Hirsch, L. R.; Stafford, R. J.; Bankson, J. A.; Sershen, S. R.; Rivera, B.; Price, R. E.; Hazle, J. D.; Halas, N. J., West, J. L., Nanoshell-mediated near-infrared thermal therapy of tumors under magnetic resonance guidance. *Proceedings of the National Academy of Sciences of the United States of America* **2003,** *100* (23), 13549-13554.

Holmlin, R. E.; Chen, X.; Chapman, R. G.; Takayama, S., Whitesides, G. M., Zwitterionic SAMs that Resist Nonspecific Adsorption of Protein from Aqueous Buffer. *Langmuir* **2001,** *17* (9), 2841-2850.

Hong, R.; Han, G.; Fernandez, J. M.; Kim, B.; Forbes, N. S., Rotello, V. M., Gluathione-Mediated Delivery and Release Using Monolayer Protected Nanoparticle Carriers. *Journal of the American Chemical Society* **2006,** *128* (4), 1078-1079.

Hooper, J. B., Schweizer, K. S., Contact Aggregation, Bridging, and Steric Stabilization in Dense Polymer-Particle Mixtures. *Macromolecules* **2005,** *38*, 8858-8869.

Hopp, T. P., Woods, W. R., Prediction of protein antigenic determinants from amino acid sequences. *Proceedings of the National Academy of Sciences* **1981,** *78* (6), 3824-3828.

Horovitz, O.; Mocanu, A.; Tomoaia, G.; Bobos, L.; Dubert, D.; Daian, I.; Yusanis, T., Tomoaia-Cotisel, M., Lysine mediated assembly of gold nanoparticles. *Studia Universitatis Babes-Bolyai, Chemia* **2007,** *52* (1), 97-108.

Hu, Y.; Noelck, S. J., Drezek, R. A., Symmetry Breaking in Gold-Silica-Gold Multilayer Nanoshells. *ACS Nano* **2010,** *4* (3), 1521-1528.

Huang, C.-M.; Wei, K.-H.; Jeng, U. S., Liang, K. S., Structural Evolution of Poly(styrene-b-4-vinylpyridine) Diblock Copolymer/Gold Nanoparticle Mixtures from Solution to Solid State. *Macromolecules* **2007,** *40* (14), 5067-5074.

Huang, X.; El-Sayed, I. H.; Qian, W., El-Sayed, M. A., Cancer Cell Imaging and Photothermal Therapy in the Near-Infrared Region by Using Gold Nanorods. *Journal of the American Chemical Society* **2006,** *128* (6), 2115-2120.

Huang, X.; Peng, X.; Wang, Y.; Wang, Y.; Shin, D. M.; El-Sayed, M. A., Nie, S., A Reexamination of Active and Passive Tumor Targeting by Using Rod-Shaped Gold Nanocrystals and Covalently Conjugated Peptide Ligands. *ACS Nano* **2010,** *4* (10), 5887-5896.

Hunter, R. J., *Zeta Potential in Colloid Science*. Academic Press: 1981.

Iacovella, C. R.; Horsch, M. A., Glotzer, S. C., Local ordering of polymer-tethered nanospheres and nanorods and the stabilization of the double gyroid phase. *The Journal of Chemical Physics* **2008,** *129*, 044902-1 - 0440902-10.

Isojima, T.; Lattuada, M.; Vander Sande, J. B., Hatton, T. A., Reversible Clustering of pH- and Temperature-Responsive Janus Magnetic Nanoparticles. *ACS Nano* **2008,** *2* (9), 1799-1806.

Isojima, T.; Suh, S. K.; Vander Sande, J. B., Hatton, T. A., Controlled Assembly of Nanoparticle Structures: Spherical and Toroidal Superlattices and Nanoparticle-Coated Polymeric Beads. *Langmuir* **2009,** *25* (14), 8292-8298.

Israelachvili, J. N., *Intermolecular and Surface Forces*. 3 ed.; Elsevier: New York, 2011.

Ivanova, T.; Panaiotov, I.; Proust, J. E.; Benoit, J. P., Verger, R., Hydrolysis kinetics of poly(D,L-lactide) monolayers spread on basic or acidic aqueous subphases. *Colloids and Surfaces B: Biointerfaces* **1997,** *8*, 217-225.

Jackson, A. M.; Myerson, J. W., Stellacci, F., Spontaneous assembly of subnanometre-ordered domains in the ligand shell of monolayer-protected nanoparticles. *Nature Materials* **2004,** *3*, 330-336.

Jain, N. J.; George, A., Bahadur, P., Effect of salt on the micellization of pluronic P65 in aqueous solution. *Colloids and Surfaces A* **1999,** *157*, 275-283.

Jain, P. K.; Lee, K. S.; El-Sayed, I. H., El-Sayed, M. A., Calculated Absorption and Scattering Properties of Gold Nanoparticles of Different Size, Shape, and Composition: Applications in Biological Imaging and Biomedicine. *Journal of Physical Chemistry B* **2006,** *110* (14), 7238-7248.

Jia, G.; Cao, Z.; Xue, H.; Xu, Y., Jiang, S., Novel Zwitterionic-Polymer-Coated Silica Nanoparticles. *Langmuir* **2009,** *25* (5), 3196-3199.

Jiang, S. Y., Cao, Z. Q., Ultralow-Fouling, Functionalizable, and Hydrolyzable Zwitterionic Materials and Their Derivatives for Biological Applications. *Advanced Materials* **2010,** *22* (9), 920-932.

Jiang, W.; Kim, B. Y. S.; Rutka, J. T., Chan, W. C. W., Nanoparticle-mediated cellular response is size-dependent. *Nature Nanotechnology* **2008,** *3* (3), 145-150.

Johnston, K. P.; Maynard, J. A.; Truskett, T. M.; Borwankar, A. U.; Miller, M. A.; Wilson, B. K.; Dinin, A. K.; Khan, T. A., Kaczorowski, K. J., Concentrated Dispersion of Equilibrium Protein Nanoclusters That Reversibly Dissociate Into Active Monomers. *ACS Nano* **2012,** *6* (2), 1357-1369.

Joshi, H.; Shirude, P. S.; Bansal, V.; Ganesh, K. N., Sastry, M., Isothermal Titration Calorimetry Studies on the Binding of Amino Acids to Gold Nanoparticles. *Journal of Physical Chemistry B* **2004,** *108* (31), 11535-11540.

Kamiayashi, M.; Ogura, H., Otsubo, Y., Shear-thickening flow of nanoparticle suspensions flocculated by polymer bridging. *Journal of Colloid and Interface Science* **2008,** *321*, 294-301.

Kaufman, E. D.; Belyea, J.; Johnson, M. C.; Nicholson, Z. M.; Ricks, J. L.; Shah, P. K.; Bayless, M.; Pettersson, T.; Feldoto, Z.; Blomberg, E.; Claesson, P., Franzen, S., Probing Protein Adsorption onto Mercaptoundecanoic Acid Stabilized Gold Nanoparticles and Surfaces by Quartz Crystal Microbalance and Z-Potential Measurements. *Langmuir* **2007,** *23* (11), 6053-6062.

Kelly, K. L.; Coronado, E.; Zhao, L. L., Schatz, G. C., The optical properties of metal nanoparticles: The influence of size, shape, and dielectric environment *Journal of Physical Chemistry B* **2003,** *107* (3), 668-677.

Khlebtsov, B.; Zharov, V.; Melnikov, A.; Tuchin, V., Khlebtsov, N., Optical amplification of photothermal therapy with gold nanoparticles and nanoclusters. *Nanotechnology* **2006,** *17* (20), 5167-5179.

Khlebtsov, N., Dykman, L., Biodistribution and toxicity of engineered gold nanoparticles: a review of *in vitro* and *in vivo* studies. *Chemical Society Reviews* **2011,** *40*, 1647-1671.

Khoury, C. G., Vo-Dinh, T., Gold Nanostars For Surface-Enhanced Raman Scattering: Synthesis, Characterization and Optimization. *J. Phys. Chem. C* **2008,** *112* (48), 18849-18859.

Kim, T.; Lee, C.-H.; Joo, S.-W., Lee, K., Kinetics of gold nanoparticle aggregation: Experiments and modeling. *Journal of Colloid and Interface Science* **2008,** *318* (2), 238-243.

Kleshchanok, D.; Tuinier, R., Lang, P. R., Direct measurements of polymer-induced forces. *Journal of Physics: Condensed Matter* **2008,** *20* (7), 073101/1-073101/25.

Kline, S. R., Kaler, E. W., Aggregation of Colloidal Silica by n-Alkyl Sulfates. *Langmuir* **1996,** *12*, 2402-2407.

Kneipp, J.; Kneipp, H.; McLaughlin, M.; Brown, D., Kneipp, K., In Vivo Molecular Probing of Cellular Compartments with Gold Nanoparticles and Nanoaggregates. *Nano Letters* **2006,** *6* (10), 2225-2231.

Kondoh, H.; Kodama, C.; Sumida, H., Nozoye, H., Molecular processes of adsorption and desorption of alkanethiol monolayers on Au(1 1 1). *Journal of Chemical Physics* **1999,** *111* (3), 1175-1184.

Kooi, M. E.; Cappendijk, V. C.; Cleutjens, K. B. J. M.; Kessels, A. G. H.; Kitslaar, P. J. E. H. M.; Borgers, M.; Frederik, P. M.; Daemen, M. J. A. P., van Engelshoven, J. M. A., Accumulation of Ultrasmall Superparamagnetic Particles of Iron Oxide in Human Atherosclerotic Plaques Can Be Detected by In Vivo Magnetic Resonance Imaging. *Circulation* **2003,** *107*, 2453-2458.

Kreibig, U., Vollmer, M., *Optical Properties of Metal Clusters* Springer: Berlin, Germany, 1995 Vol. 25.

Kulkarni, A. M.; Chatterjee, A. P.; Schweizer, K. S., Zukoski, C. F., Depletion Interactions in the Protein Limit: Effects of Polymer Density Fluctuations. *Physical Review Letters* **1999,** *83* (22), 4554-4557.

Kumar, S.; Aaron, J., Sokolov, K., Direction conjugation of antibodies to nanoparticles for synthesis of multiplexed optical contrast agents with both delivery and targeting moieties. *Nature Protocols* **2008,** *3* (2), 314-320.

Kumar, S.; Harrison, N.; Richards-Kortum, R., Sokolov, K., Plasmonic Nanosensors for Imaging Intracellular Biomarkers in Live Cells. *Nano Letters* **2007,** *7* (5), 1338-1343.

Kunze, J.; Burgess, I.; Nichols, R.; Buess-Herman, C., Lipkowski, J., Electrochemical evaluation of citrate adsorption on Au(1 1 1) and the stability of citrate-reduced gold colloids. *J. Electroanal. Chem.* **2007,** *599*, 147-159.

Ladd, J.; Zhang, Z.; Chen, S.; Hower, J. C., Jiang, S., Zwitterionic Polymers Exhibiting High Resistance to Nonspecific Protein Adsorption from Human Serum and Plasma. *Biomacromolecules* **2008,** *9* (5), 1357-1361.

Larson-Smith, K., Pozzo, D. C., Scalable synthesis of self-assembling nanoparticle clusters based on controlled steric interactions. *Soft Matter* **2011,** *7*, 5339-5347.

Larson, T. A.; Bankson, J.; Aaron, J., Sokolov, K., Hybrid plasmonic magnetic nanoparticles as molecular specific agents for MRI/optical imaging and photothermal therapy of cancer cells. *Nanotechnology* **2007,** *18* (32), 325101/1-325101/8.

Larson, T. A.; Joshi, P. P., Sokolov, K., Preventing Protein Adsorption and Macrophage Uptake of Gold Nanoparticles via a Hydrophobic Shield. *ACS Nano* **2012,** *6* (10), 9182-9190.

Lattuada, M., Hatton, T. A., Preparation and Controlled Self-Assembly of Janus Magnetic Nanoparticles. *Journal of the American Chemical Society* **2007,** *129* (42), 12878-12889.

Laurent, S.; Forge, D.; Port, M.; Roch, A.; Robic, C.; Elst, L. V., Muller, R. N., Magnetic Iron Oxide Nanoparticles: Synthesis, Stabilization, Vectorization, Physicochemical Characterizations, and Biological Applications. *Chemical Reviews* **2008,** *108* (6), 2064-2110.

Lazarides, A. A., Schatz, G. C., DNA-Linked Metal Nanosphere Materials: Structural Basis for the Optical Properties. *Journal of Physical Chemistry B* **2000,** *104* (3), 460-467.

Lekkerkerker, H. N. W., Tuinier, R., *Colloids and the Depletion Interaction*. Springer: New York, 2011; Vol. 833, p 12-15.

Li, J.; He, W.-D., Sun, X.-L., Preparation of poly(styrene-b-N-isopropylacrylamide) micelles surface-linked with gold nanoparticles and thermo-responsive ultraviolet-visible absorbance. *Journal of Polymer Science, Part A: Polymer Chemistry* **2007,** *45* (22), 5156-5163.

Li, L.; Chen, S.; Zheng, J.; Ratner, B. D., Jiang, S., Protein Adsorption on Oligo(ethylene glycol)-Terminated Alkanethiolate Self-Assembled Monolayers: The Molecular Basis for Nonfouling Behavior. *Journal of Physical Chemistry B* **2005,** *109* (7), 2934-2941.

Li, L., Weng, J., Enzymatic synthesis of gold nanoflowers with trypsin. *Nanotechnology* **2010,** *21*.

Lim, I. I. S.; Ip, W.; Crew, E.; Njoki, P. N.; Mott, D.; Zhong, C.-J.; Pan, Y., Zhou, S., Homocysteine-mediated reactivity and assembly of gold nanoparticles. *Langmuir* **2007,** *23* (2), 826-833.

Linegar, K. L.; Adeniran, A. E.; Kostko, A. F., Anisimov, M. A., Hydrodynamic Radius of Polyethylene Glycol in Solution Obtained by Dynamic Light Scattering. *Colloid Journal* **2010,** *72* (2), 279-281.

Link, S.; Mohamed, M. B., El-Sayed, M. A., Simulation of the Optical Absorption Spectra of Gold Nanorods as a Function of Their Aspect Ratio and the Effect of the Medium Dielectric Constant. *Journal of Physical Chemistry B* **1999,** *103*, 3073-3077.

Liu, W.; Choi, H. S.; Zimmer, J. P.; Tanaka, E.; Frangioni, J. V., Bawendi, M., Compact Cysteine-Coated CdSe(ZnCdS) Quantum Dots for in Vivo Applications. *Journal of the American Chemical Society* **2007,** *129*, 14530-14531.

Liu, X.; Huang, H.; Jin, Q., Ji, J., Mixed Charged Zwitterionic Self-Assembled Monolayers as a Facile Way to Stabilize Large Gold Nanoparticles. *Langmuir* **2011,** *27* (9), 5242-5251.

Loo, C.; Lowery, A.; Halas, N.; West, J., Drezek, R., Immunotargeted Nanoshells for Integrated Cancer Imaging and Therapy. *Nano Letters* **2005,** *5* (4), 709-711.

Lu, P. J.; Zaccarelli, E.; Ciulla, F.; Scholfield, A. B.; Sciortino, F., Weitz, D. A., Gelation of particles with short-range attraction. *Nature* **2008,** *453*, 499-504.

Lu, Z., Yin, Y., Colloidal nanoparticle clusters: functional materials by design. *Chemical Society Reviews* **2012,** *41*, 6874-6887.

Lundqvist, M.; Stigler, J.; Elia, G.; Lynch, I.; Cedervall, T., Dawson, K. A., Nanoparticle size and surface properties determine the protein corona with possible implications for biological impacts. *Proceedings of the National Academy of Sciences* **2008,** *105* (38), 14265-14270.

Ma, L. L.; Borwankar, A. U.; Willsey, B. W.; Yoon, K. Y.; Tam, J. O.; Sokolov, K. V.; Feldman, M. D.; Milner, T. E., Johnston, K. P., Growth of textured thin Au coatings on iron oxide nanoparticles with near infrared absorbance. *Nanotechnology* **2013,** *24*.

Ma, L. L.; Feldman, M. D.; Tam, J. M.; Paranjape, A. S.; Cheruki, K. K.; Larson, T. A.; Tam, J. O.; Ingram, D. R.; Paramita, V.; Villard, J. W.; Jenkins, J. T.; Wang, T.; Clarke, G. D.; Asmis, R.; Sokolov, K.; Chandrasekar, B.; Milner, T. E., Johnston, K. P., Small Multifunctional Nanoclusters (Nanoroses) for Targeted Cellular Imaging and Therapy. *ACS Nano* **2009,** *3* (9), 2686-2696.

Ma, L. L.; Tam, J. O.; Willsey, B. W.; Rigdon, D.; Ramesh, R.; Sokolov, K., Johnston, K. P., Selective Targeting of Antibody Conjugated Multifunctional Nanoclusters (Nanoroses) to Epidermal Growth Factor Receptors in Cancer Cells. *Langmuir* **2011,** *27*, 7681-7690.

Mahmoudi, M.; Lynch, I.; Ejtehadi, M. R.; Monopoli, M. P.; Bombelli, F. B., Laurent, S., Protein-Nanoparticle Interactions: Opportunities and Challenges. *Chemical Reviews* **2011,** *111* (9), 5610-5637.

Mallidi, S.; Larson, T.; Aaron, J.; Sokolov, K., Emelianov, S., Molecular specific optoacoustic imaging with plasmonic nanoparticles. *Optics Express* **2007,** *15* (11), 6583-6588.

Mallidi, S.; Larson, T.; Tam, J.; Joshi, P. P.; Karplouk, A.; Sokolov, K., Emelianov, S., Multiwavelength Photoacoustic Imaging and Plasmon Resonance Coupling of Gold Nanoparticles for Selective Detection of Cancer. *Nano Letters* **2009,** *9* (8), 2825-2831.

Markarucha, A. J.; Todorova, N., Yarovsky, I., Nanomaterials in biological environment: a review of computer modelling studies. *European Biophysics Journal* **2011,** *40*, 103-115.

Mata, J. P.; Majhi, P. R.; Guo, C.; Liu, H. Z., Bahadur, P., Concentration, temperature, and salt-induced micellization of a triblock copolymer Pluronic L64 in aqueous media. *Journal of Colloid and Interface Science* **2005,** *292*, 548-556.

Miles, W. C. G., J.D.;Huffstetler, P.P.; Reinhold, C.M.; Pothayee, N.; Caba, B.L.; Boyd, J.S.; Davis, R.M.; Riffle, J.S., Synthesis and Colloidal Properties of Polyether-Magnetite Complexes in Water and Phosphate-Buffered Saline. *Langmuir* **2009,** *25*, 803-813.

Mirkin, C. A.; Letsinger, R. L.; Mucic, R. C., Storhoff, J. J., A DNA-based method for rationally assembling nanoparticles into macroscopic materials. *Nature (London)* **1996,** *382* (6592), 607-609.

Mondain-Monval, O.; Leal-Calderon, F.; Phillip, J., Bibette, J., Depletion Forces in the Presence of Electrostatic Double Layer Repulsion. *Phys. Rev. Lett.* **1995,** *75*, 3364-3367.

Murthy, A. K.; Stover, R. J.; Borwankar, A. U.; Nie, G. D.; Gourisankar, S.; Truskett, T. M.; Sokolov, K. V., Johnston, K. P., Equilibrium Gold Nanoclusters Quenched with Biodegradable Polymers. *ACS Nano* **2013,** *7* (1), 239-251.

Murthy, A. K.; Stover, R. J.; Hardin, W. G.; Schramm, R.; Nie, G. D.; Gourisankar, S.; Truskett, T. M.; Sokolov, K. V., Johnston, K. P., Charged Gold Nanoparticles with Essentially Zero Serum Protein Adsorption in Undiluted Fetal Bovine Serum. *Journal of the American Chemical Society* **2013,** *135*, 7799-7802.

Murthy, A. K.; Stover, R. J.; Nie, G. D.; Gourisankar, S.; Martinez, M.; Truskett, T. M.; Sokolov, K. V., Johnston, K. P., Nanoclusters of Gold Nanospheres with Binary Monolayers of Cysteine and Citrate Formed by Quenched Assembly. *Langmuir* **2013,** *in prep*.

Murthy, V. S.; Cha, J. N.; Stucky, G. D., Wong, M. S., Charge-Driven Flocculation of Poly(L-lysine)-Gold Nanoparticle Assemblies Leading to Hollow Microspheres. *Journal of the American Chemical Society* **2004,** *126* (16), 5292-5299.

Mutch, K. J.; Duijneveldt, J. S. v., Eastoe, J., Colloid–polymer mixtures in the protein limit. *Soft Matter* **2007,** *3*, 155-167.

Mutch, K. J.; Duijneveldt, J. S. v.; Eastoe, J.; Grillo, I., Heenan, R. K., Small-Angle Neutron Scattering Study of Microemulsion Polymer Mixtures in the Protein Limit. *Langmuir* **2008,** *24*, 3053-3060.

Nehl, C. L.; Liao, H., Hafner, J. H., Optical Properties of Star-Shaped Gold Nanoparticles. *Nano Letters* **2006,** *6* (4), 683-688.

Ofir, Y.; Samanta, B., Rotello, V. M., Polymer and biopolymer mediated self-assembly of gold nanoparticles. *Chemical Soceity Reviews* **2008,** *37* (9), 1814-1825.

Ostuni, E.; Chapman, R. G.; Holmlin, R. E.; Takayama, S., Whitesides, G. M., A Survey of Structure-Property Relationships of Surfaces that Resist the Adsorption of Protein. *Langmuir* **2001,** *17*, 5605-5620.

Petri-Fink, A.; Steitz, B.; Finka, A.; Salaklang, J., Hofmann, H., Effect of cell media on polymer coated superparamagnetic iron oxide nanoparticles (SPIONs): Colloidal

stability, cytotoxicity, and cellular uptake studies. *European Journal of Pharmaceutics and Biopharmaceutics* **2008,** *68*, 129-137.

Piech, M., Walz, J. Y., Direct measurement of depletion and structural forces in polydisperse, charged systems. *Journal of Colloid and Interface Science* **2002,** *253* (1), 117-129.

Pissuwan, D.; Valenzuela, S. M.; Killingsworth, M. C.; Xu, X., Cortie, M. B., Targeted destruction of murine macrophage cells with bioconjugated gold nanorods. *Journal of Nanoparticle Research* **2007,** *9* (6), 1109-1124.

Porcar, L.; Falus, P.; Chen, W.-R.; Faraone, A.; Fratini, E.; Hong, K.; Baglioni, P., Liu, Y., Formation of the Dynamic Clusters in Concentrated Lysozyme Protein Solutions. *Journal of Physical Chemistry Letters* **2010,** *1*, 126-129.

Rechberger, W.; Hohenau, A.; Leitner, A.; Krenn, J. R.; Lamprecht, B., Aussenegg, F. R., Optical properties of two interacting gold nanoparticles. *Optics Communications* **2003,** *220*, 137-141.

Reddy, S. T. S., M. A.; Hubbell, J. A., Targeting dendritic cells with biomaterials: developing the next generation of vaccines. *Trends in Immunology* **2006,** *27* (12), 573-579.

Ren, Y.; Xu, C.; Wu, M.; Niu, M., Fang, Y., Controlled synthesis of gold nanoflowers assisted by poly(vinylpyrrolidone)-sodium dodecyl sulfate aggregations. *Colloids and Surfaces A: Physicochemical and Engineering Aspects* **2011,** *380*, 222-228.

Riley, T.; Stolnik, S.; Heald, C. R.; Xiong, C. D.; Garnett, M. C.; Illum, L., Davis, S. S., Physicochemical Evaluation of Nanoparticles Assembled from Poly(lactic acid)-Poly(ethylene glycol) (PLA-PEG) Block Copolymers as Drug Delivery Vehicles. *Langmuir* **2001,** *17*, 3168-3174.

Ryoo, W.; Webber, S. E., Johnston, K. P., Water-in-Carbon Dioxide Microemulsions with Methylated Branched Hydrocarbon Surfactants. *Industrial and Engineering Chemistry Research* **2003,** *42* (25), 6348-6358.

Sakai, T., Alexandridis, P., Mechanism of Gold Metal Ion Reduction, Nanoparticle Growth and Size Control in Aqueous Amphiphilic Block Copolymer Solutions at Ambient Conditions. *Journal of Physical Chemistry B* **2005,** *109* (16), 7766-7777.

Sakai, T., Alexandridis, P., Metal nanoparticle synthesis and organization in 1D, 2D and 3D structures formed by amphiphilic block copolymers. *PMSE Preprints* **2005,** *93*, 798-799.

Sedgwick, H.; Egelhaaf, S. U., Poon, W. C. K., Clusters and gels in systems of sticky particles. *J. Phys.-Condes. Matter* **2004,** *16* (42), S4913-S4922.

Selvakannan, P. R.; Mandal, S.; Phadtare, S.; Pasricha, R., Sastry, M., Capping of Gold Nanoparticles by the Amino Acid Lysine Renders Them Water-Dispersible. *Langmuir* **2003,** *19* (8), 3545-3549.

Shenhar, R.; Norsten, T. B., Rotello, V. M., Polymer-Mediated Nanoparticle Assembly: Structural Control and Applications. *Advanced Materials* **2005,** *17* (6), 657-669.

Skrabalak, S. E.; Chen, J.; Au, L.; Lu, X.; Li, X., Xia, Y., Gold nanocages for biomedical applications. *Advanced Materials* **2007,** *19* (20), 3177-3184.

Smith, P. G.; Patel, M. N.; Kim, J.; Milner, T. E., Johnston, K. P., Effect of Surface Hydrophilicity on Charging Mechanism of Colloids in Low-Permittivity Solvents. *J. Phys. Chem. C* **2007,** *111*, 840-848.

Sokolov, K. V.; Follen, M.; Aaron, J.; Pavlova, I.; Malpica, A.; Lotan, R., Richards-Kortum, R., Real-time vital optical imaging of precancer using anti-epidermal growth factor receptor antibodies conjugated to gold nanoparticles. *Cancer Research* **2003,** *63*, 1999-2004.

Song, K. H.; Kim, C.; Cobley, C. M.; Xia, Y., Wang, L. V., Near-Infrared Gold Nanocages as a New Class of Tracers for Photoacoustic Sentinel Lymph Node Mapping on a Rat Model. *Nano Letters* **2009,** *9* (1), 183-188.

Srivastava, S.; Frankamp, B. L., Rotello, V. M., Controlled Plasmon Resonance of Gold Nanoparticles Self-Assembled with PAMAM Dendrimers. *Chemistry of Materials* **2005,** *17* (3), 487-490.

Srivastava, S.; Samanta, B.; Arumugam, P.; Han, G., Rotello, V. M., DNA-mediated assembly of iron platinum (FePt) nanoparticles. *Journal of Materials Chemistry* **2007,** *17* (1), 52-55.

Stobiecka, M.; Coopersmith, K., Hepel, M., Resonance elastic light scattering (RELS) spectroscopy of fast non-Langmuirian ligand-exchange in glutathione-induced gold nanoparticle assembly. *Journal of Colloid and Interface Science* **2010,** *350*, 168-177.

Stradner, A.; Sedgwick, H.; Cardinaux, F.; Poon, W. C. K.; Egelhaaf, S. U., Schurtenberger, P., Equilibrium cluster formation in concentrated protein solutions and colloids. *Nature* **2004,** *432* (7016), 492-495.

Striemer, C. C.; Gaborski, T. R.; McGrath, J. L., Fauchet, P. M., Charge- and size-based separation of macromolecules using ultrathin silicon membranes. *Nature* **2007,** *445*, 749-753.

Su, Y.-L.; Wei, X.-F., Liu, H.-Z., Effect of sodium chloride on association behavior of poly(ethylene oxide)-poly(propylene oxide)-poly(ethylene oxide) block copolymer in aqueous solutions. *Journal of Colloid and Interface Science* **2003,** *264*, 526-531.

Surve, M.; Pryamitsyn, V., Ganesan, V., Polymer-bridged gels of nanoparticles in solutions of adsorbing polymers. *Journal of Chemical Physics* **2006,** *125*.

Tadros, T. F., Vincent, B., Influence of Temperature and Electrolytes on the Adsorption of Poly(ethylene oxide)-Poly(propylene oxide) Block Copolymer on Polystyrene

Latex and on the Stability of the Polymer-Coated Particles. *Journal of Physical Chemistry* **1980,** *84*, 1575-1580.

Tam, J. M.; Murthy, A. K.; Ingram, D. R.; Nguyen, R.; Sokolov, K. V., Johnston, K. P., Kinetic Assembly of Near-IR Active Gold Nanoclusters Using Weakly Adsorbing Polymers to Control the Size. *Langmuir* **2010,** *26* (11), 8988-8999.

Tam, J. M.; Tam, J. O.; Murthy, A.; Ingram, D. R.; Ma, L. L.; Travis, K.; Johnston, K. P., Sokolov, K. V., Controlled Assembly of Biodegradable Plasmonic Nanoclusters for Near-Infrared Imaging and Therapeutic Applications. *ACS Nano* **2010,** *4* (4), 2178-2184.

Tirumalai, R. S.; Chan, K. C.; Prieto, D. A.; Issaq, H. J.; Conrads, T. P., Veenstra, T. D., Characterization of the Low Molecular Weight Human Serum Proteome. *Molecular & Cellular Proteomics* **2003,** *2* (10), 1096-1103.

Tjong, H., Zhou, H.-X., Prediction of Protein Solubility from Calculation of Transfer Free Energy. *Biophysical Journal* **2008,** *95* (6), 2601-2609.

Trigari, S.; Rindi, A.; Margheri, G.; Sottini, S.; Dellepiane, G., Giorgetti, E., Synthesis and modelling of gold nanostars with tunable morphology and extinction spectrum. *Journal of Materials Chemistry* **2011,** *21*, 6531-6540.

Troutman, T. S.; Barton, J. K., Romanowski, M., Biodegradable plasmon resonant nanoshells. *Advanced Materials* **2008,** *20* (13), 2604-2608.

Uzun, O.; Frankamp, B. L.; Sanyal, A., Rotello, V. M., Recognition-Mediated Assembly of Nanoparticle-Diblock Copolymer Micelles with Controlled Size. *Chemistry of Materials* **2006,** *18* (23), 5404-5409.

Vaisocherova, H. Z., Z.; Yang,W.; Cao,Z.; Cheng,G.; Taylor,A.D; Piliarik,M.; Homola,J.; Jiang,S., Functionalizable surface platform with reduced nonspecific protein adsorption from full blood plasma - Material selection and protein immobilization optimization. *Biosensors and Bioelectronics* **2008,** *24*, 1924-1930.

Varun, K., Robert, K. P. h., Thermodynamic limits on drug loading in nanoparticle cores. *Journal of Pharmaceutical Sciences* **2008,** *97* (11), 4904-4914.

Venkatraman, S. S.; Jie, P.; Min, F.; Freddy, B. Y. C., Leong-Huat, G., Micelle-like nanoparticles of PLA-PEG-PLA triblock copolymer as chemotherapeutic carrier *Int. J. Pharm.* **2005,** *298*, 219-232.

Verma, A.; Uzun, O.; Hu, Y.; Hu, Y.; Han, H.-S.; Watson, N.; Chen, S.; Irvine, D. J., Stellacci, F., Surface-structure-regulated cell-membrane penetration by monolayer-protected nanoparticles. *Nature Materials* **2008,** *7*, 588-595.

von Maltzahn, G.; Park, J.-H.; Agrawal, A.; Bandaru, N. K.; Das, S. K.; Sailor, M. J., Bhatia, S. N., Computationally Guided Photothermal Tumor Therapy Using Long-Circulating Gold Nanorod Antennas. *Cancer Research* **2009,** *69* (9), 3892-3900.

Vrij, A., Polymers at Interfaces and the Interactions in Colloidal Dispersions *Pure and Applied Chemistry* **1976,** *48*, 471-483

Walkey, C. D.; Olsen, J. B.; Guo, H.; Emili, A., Chan, W. C. W., Nanoparticle Size and Surface Chemistry Determine Serum Protein Adsorption and Macrophage Uptake. *Journal of the American Chemical Society* **2012,** *134*, 2139-2147.

Wang, A. Z. B., V.; Vasilliou, C. C;Gu, F.;Alexis, F.; Zhang, L.; Shaikh, M.; Yuet, K.;Cima, M. J.; Langer, R.; Kantoff, P.W.;Bander, N.H; Jon, S.;Farokhzad, O.C., Superparamagnetic iron oxide nanopartilc-aptamer bioconjugates for combined prostate cancer imaging and therapy. *ChemMedChem* **2008,** *3* (9), 1311-1315.

Wang, W.; Yang, X., Cui, H., Growth Mechanism of Flowerlike Gold Nanostructures: Surface Plasmon Resonance (SPR) and Resonance Rayleigh Scattering (RRS) Approaches to Growth Monitoring. *Journal of Physical Chemistry C* **2008,** *112* (42), 16348-16353.

Wang, Z.; Zhang, J.; Ekman, J. M.; Kenis, P. J. A., Lu, Y., DNA-Mediated Control of Metal Nanoparticle Shape: One-Pot Synthesis and Cellular Uptake of Highly Stable and Functional Gold Nanoflowers. *Nano Letters* **2010,** *10*, 1886-1891.

Watts, J. F., Wolstenholme, J., *An Introduction to Surface Analysis by XPS and AES*. John Wiley & Sons: West Sussex, England, 2003.

Wei, H.; Insin, N.; Lee, J.; Han, H.-S.; Cordero, J. M.; Liu, W., Bawendi, M. G., Compatct Zwitterion-Coated Iron Oxide Nanoparticles for Biological Applications. *Nano Letters* **2011,** *12*, 22-25.

Weissleder, R., A clearer vision for in vivo imaging. *Nature Biotechnology* **2001,** *19*.

Weissleder, R., Molecular Imaging in Cancer. *Science* **2006,** *312* (5777), 1168-1171.

Wilcoxon, J. P.; Martin, J. E., Schaefer, D. W., Aggregation in colloidal gold. *Physical Review A: Atomic, Molecular, and Optical Physics* **1989,** *39* (5), 2675-2688.

Xia, Y. In *Gold nanocages: A new class of plasmonic nanostructures for biomedical applications*, ACS National Meeting, Boston, MA, United States, August 19-23, 2007 Boston, MA, United States, 2007; pp COLL-528.

Xia, Y. S.; Nguyen, T. D.; Yang, M.; Lee, B.; Santos, A.; Podsiadlo, P.; Tang, Z. Y.; Glotzer, S. C., Kotov, N. A., Self-assembly of self-limiting monodisperse supraparticles from polydisperse nanoparticles. *Nat. Nanotechnol.* **2011,** *6* (9), 580-587.

Xu, L.; Guo, Y.; Xie, R.; Zhuang, J.; Yang, W., Li, T., Three-dimensional assembly of Au nanoparticles using dipeptides. *Nanotechnology* **2002,** *13* (6), 725-728.

Yang, W.; Xue, H.; Li, W.; Zhang, J., Jiang, S., Pursuing "Zero" Protein Adsorption of Poly(carboxybetaine) from Undiluted Blood Serum and Plasma. *Langmuir* **2009,** *25* (19), 11911-11916.

Yang, W.; Zhang, L.; Wang, S.; White, A. D., Jiang, S., Functionalizable and ultra stable nanoparticles coated with zwitterionic poly(carboxybetaine) in undiluted blood serum. *Biomaterials* **2009,** *30*, 5617-5621.

Yoon, S. J.; Mallidi, S.; Tam, J. M.; Tam, J. O.; Murthy, A.; Johnston, K. P.; Sokolov, K. V., Emelianov, S. Y., Utility of biodegradable plasmonic nanoclusters in photoacoustic imaging. *Optics Letters* **2010,** *35* (22), 3751-3753.

Yoon, S. J.; Murthy, A.; Johnston, K. P.; Sokolov, K. V.; Emelianov, S. Y. Thermal Stability of Biodegradable Plasmonic Nanoclusters in Photoacoustic Imaging. *Optics Express* **2012**, *20*, 29479-29487.

You, C.-C.; De, M.; Han, G., Rotello, V. M., Tunable Inhibition and Denaturation of a-Chymotrypsin with Amino Acid-Functionalized Gold Nanoparticles. *Journal of the American Chemical Society* **2005,** *127* (37), 12873-12881.

Yu, M.; Zhou, C.; Liu, J.; Hankins, J. D., Zheng, J., Luminescent Gold Nanoparticles with pH-Dependent Membrane Adsorption. *Journal of the American Chemical Society* **2011,** *133*, 11014-11017.

Zaccarelli, E., Colloidal gels: equilibrium and non-equilibrium routes. *J. Phys.-Condes. Matter* **2007,** *19*, 1-50.

Zhang, C.; Pansare, V. J.; Prud'homme, R. K., Priestley, R. D., Flash nanoprecipitation of polystyrene nanoparticles. *Soft Matter* **2012,** *8*, 86-93.

Zhang, X.; Servos, M. R., Liu, J., Ultrahigh Nanoparticle Stability against Salt, pH, and Solvent with Retained Surface Accessibility via Depletion Stabilization. *Journal of the American Chemical Society* **2012,** *134*, 9910-9913.

Zheng, J.; Zhou, C.; Yu, M. X., Liu, J. B., Different sized luminescent gold nanoparticles. *Nanoscale* **2012,** *4* (14), 4073-4083.

Zhou, C.; Long, M.; Qin, Y.; Sun, X., Zheng, J., Luminescent Gold Nanoparticles with Efficient Renal Clearance. *Angew. Chem. Int. Ed.* **2011,** *50*, 3168-3172.

Zhou, Y.; Jiang, K.; Chen, Y., Liu, S., Gold nanoparticle-incorporated core and shell crosslinked micelles fabricated from thermoresponsive block copolymer of N-isopropylacrylamide and a novel primary-amine containing monomer. *Journal of Polymer Science, Part A: Polymer Chemistry* **2008,** *46* (19), 6518-6531.

Zhuang, J.; Wu, H.; Yang, Y., Cao, Y. C., Controlling Colloidal Superparticle Growth Through Solvophobic Interactions. *Angew. Chem. Int. Ed.* **2008,** *47*, 2208-2212.

Vita

Avinash Krishna Murthy was born in New York, NY. After graduating from Hoover High School (Hoover, AL) in May 2004, he attended Princeton University (Princeton, NJ), where he obtained a Bachelor of Science in Engineering degree and a Certificate in Engineering Biology from the Chemical Engineering Department in June 2008. During his undergraduate tenure, he conducted senior thesis research on the modeling of the collective oscillation of neural networks under the guidance of Prof. Yannis Kevrikidis. Additionally, he conducted research on a novel chemotherapeutic agent under the direction of Prof. M Tino Unlap at the University of Alabama at Birmingham during the summer of 2006, while participating the UAB Summer in Biomedical Sciences program. After graduation from Princeton, he enrolled in the graduate program in the Chemical Engineering Department at the University of Texas at Austin in August 2008. He performed graduate work under the guidance of Prof. Keith P. Johnston and Prof. Konstantin V. Sokolov, and obtained a Doctor of Philosophy in Chemical Engineering in August 2013.

Permanent address: 5751 Willow Lake Drive, Hoover, AL 35244

This dissertation was typed by the author.